THERMAL PERFORMANCE EVALUATION OF INTEGRAL ABUTMENT BRIDGES

A THESIS SUBMITTED TO
GRADUATE SCHOOL OF NATURAL AND APPLIED SCIENCES
OF
KOCAELI UNIVERSITY

BY

HANAN RIFAI

IN PARTIAL FULFILLMENT OF THE REQUIREMENTS
FOR
THE DEGREE OF MASTER OF SCIENCE
IN
CIVIL ENGINEERING

KOCAELI 2024

THERMAL PERFORMANCE EVALUATION OF INTEGRAL ABUTMENT BRIDGES

A THESIS SUBMITTED TO
GRADUATE SCHOOL OF NATURAL AND APPLIED SCIENCES
OF
KOCAELI UNIVERSITY

BY

HANAN RIFAI

IN PARTIAL FULFILLMENT OF THE REQUIREMENTS
FOR
THE DEGREE OF MASTER OF SCIENCE
IN
CIVIL ENGINEERING

Prof. Dr. SAMI ARSOY
Supervisor, Kocaeli University ……………………..
Prof. Dr. SEVAL PINARBAŞI ÇUHADAROĞLU
Jury Member, Kocaeli University ……………………..
Assoc. Prof. Dr. MEHMET ÖZGÜR
Jury Member, Çanakkale Onsekiz Mart University ……………………

Thesis Defense Date: 25.06.2024

ETHICAL DECLARATION AND RESEARCH FUND SUPPORT

According to the thesis writing rules of the Graduate School of Natural and Applied Sciences, Kocaeli University, in this thesis that I have prepared:

- I declare that this thesis is my original work.
- I affirm that I have adhered to scientific ethical principles and rules throughout all stages of preparation, data collection, analysis, and information presentation.
- I acknowledge and provide references for all data and information obtained in this study, and I have included these sources in the references section.
- I affirm that this work meets the criteria set by the Graduate School of Natural and Applied Sciences at Kocaeli University through the use of plagiarism detection software subscribed to by the university.
- I confirm that there has been no manipulation of the data used.
- I declare that I have not submitted any part of this thesis as part of another thesis at this university or any other university.

No stage of this thesis has been financially or infrastructurally supported by any institution/organization.

I hereby acknowledge that if any contradiction to this statement is identified in relation to my work at any time, I accept all moral and legal consequences that may arise as a result.

Hanan RIFAI

PUBLICATION AND INTELLECTUAL PROPERTY RIGHTS

I declare that I grant permission to Kocaeli University to archive and make available for use, in both printed and electronic formats, my entire master's thesis, or any part thereof, under the following conditions, as approved by the Graduate School of Natural and Applied Sciences. With this permission, all intellectual property rights will remain mine except for the usage rights granted to the university. The future use of my thesis, either in its entirety or in part, in works such as articles, books, presentations, licenses, patents, or similar endeavors, will be subject to my discretion and the acknowledgement of my supervisor's contribution.

I affirm and guarantee that the thesis is my original work, does not violate the rights of others, and that I am the sole owner of the thesis. I further declare that any copyrighted material used in my thesis has been obtained with written permission from the respective copyright holders, and I undertake to provide copies of these permissions to the university upon request.

In accordance with the guidelines published by the Council of Higher Education regarding the collection, organization, and accessibility of an electronic thesis, my thesis will be made accessible in the YOK National Thesis Center/Kocaeli University Libraries Open Access System, except under the condition specified below.

The access to my thesis has been postponed for 6 months from the graduation date with the decision of the Institute Board of Directors.

Hanan RIFAI

PREFACE AND ACKNOWLEDGEMENTS

It is with great pleasure and a sense of accomplishment that I present this thesis, which marks the culmination of my graduate studies at Kocaeli University. The journey to complete this study has been both challenging and rewarding, and I am grateful for the support and guidance I have received throughout the process.

I would like to express my deepest gratitude to my supervisor, Dr. Sami Arsoy, for his support, valuable insights, and expert guidance throughout the entire duration of this research program. His encouragement and mentorship have been instrumental in shaping the direction and success of this research.

Most importantly, I would like to extend my heartfelt thanks to my family and for their unwavering support, love, and understanding throughout my academic journey. I am forever grateful to my father, Emad Rifai, my late mother, Amna Rifai, my eldest sister, Tagrid Rifai, and my ex-husband, Abdulhady Alsmaeel, for their constant encouragement, belief in my abilities, and the sacrifices they have made to ensure my success. This thesis is dedicated to them as a token of my deepest appreciation and gratitude for their unconditional love and support.

It is my utmost wish that this thesis contributes to the existing sea of knowledge in the field of integral abutment bridges and serves as a foundation for future research endeavors.

June – 2024 Hanan RIFAI

CONTENTS

LIST OF FIGURES

LIST OF TABLES

INDEX OF SYMBOLS AND ABBREVIATIONS

A(t) : Time-dependent daily temperature difference parameter
A_{max} : maximum time-dependent daily temperature difference
A_{min} : minimum time-dependent daily temperature difference
Avg. Max : Average maximum temperature
Avg. Min : Average minimum temperature
C_E : England coefficient depends on the elastic modulus of the subgrade
cm : Centimeters
C_S : Sweden method coefficient
D : Dead load
d : Pile diameter
E_0 : At-rest earth pressure
E_a : Active earth pressure
EBT : Effective bridge temperature
EI_P : Flexural stiffness of the pile
E_P : Normalized resultant earth pressure force
E_p : Passive earth pressure
E_{Pile} : Modulus of elasticity of the pile
E_{Pmax} : Resultant earth pressure force at plastic equilibrium
Es : Modulus of elasticity of backfill soil
H : Height of the abutment
I_p : Moment of inertia of the pile
K : Earth pressure coefficient
K* : England earth pressure coefficient
K_B : Barker earth pressure coefficient
k_h : Modulus of sub-grade reaction
kN : Kilonewton
kN/m : Kilonewtons per meter
kN/m^2 : Kilonewtons per square meter
L_b : Length of bridge
m : Meters
mm : Millimeters
p : Soil reaction at a point on the pile per unit of the length
P_x : Axial load
Rec. Max : Record maximum temperature
Rec. Min : Record minimum temperature
T_{Const} : Construction temperature
$T_{Const.max}$: Maximum construction temperature
$T_{Const.min}$: Minimum construction temperature
$T_{e.amp}$: Amplitude of the temperature variation
$T_{e.max}$: Maximum effective bridge temperature
$T_{e.min}$: Minimum effective bridge temperature
T_F : Temperature full
$T_{Freq.max}$: Frequent maximum effective bridge temperature
$T_{Freq.min}$: Frequent minimum effective bridge temperature

$\dot{T}_{max}$: Maximum (minimum) shade air temperature with an annual probability of being exceeded 0.02.
T_{max} : Maximum shade air temperatures
T_{maxp} : Maximum shade air temperatures with an annual probability of being exceeded p (equivalent to a mean return period of 1/p)
$\dot{T}_{min}$: Minimum shade air temperature with an annual probability of being exceeded 0.02.
T_{min} : Minimum shade air temperatures
T_{minp} : Minimum shade air temperatures with an annual probability of being exceeded p (equivalent to a mean return period of 1/p)
T_R : Temperature rise
x : Length along the pile
y : Pile deflection
Z : Depth
α : Coefficient of thermal expansion
β : Inclination angle of the backfill soil surface in reference to the horizontal.
γ : Soil unit weight
Δ : Bridge displacement whether expansion or contraction
Δ' : Displacement of the abutment at H/2.
δ : Friction angle between the backfill material and the face of the abutment
ΔT (±) : Change in temperature of the superstructure.
$\Delta T_{M,cool}$: Temperature component for cooling conditions
$\Delta T_{M,heat}$: Temperature component for heating conditions
ΔT_N : Overall range of the uniform bridge temperature component
$\Delta T_{N,con}$: Uniform temperature component for contraction
$\Delta T_{N,exp}$: Uniform temperature component for expansion
θ : Angle from the face of the wall to the vertical
ν : Poisson's ratio
σ_h : Lateral (horizontal) earth pressure
σ_v : Vertical earth pressure
ϕ : Variation of the passive earth pressure coefficient under a unit of displacement (m^{-1})
K_0 : At-rest earth pressure coefficient
K_a : Active earth pressure coefficient
K_p : Passive earth pressure coefficient
φ : Internal friction angle of the backfill

Abbreviations

2D-SA : Two-Dimensional Static Analysis
2D-TH : Two-Dimensional Time-History Analysis
3D-SA : Three-Dimensional Static Analysis
3D-TH : Three-Dimensional Time-History Analysis
AASHTO : American Association of State Highway and Transportation Officials
CEN : European Committee for Standardization
DOT : Iowa State Department of Transportation

EBT	: Effective Bridge Temperature
IAB	: Integral Abutment Bridge
MassDOT	: Massachusetts Department of Transportation
NCHRP	: National Cooperative Highway Research Program
PennDOT DM4	: Design Manual Part 4 by Pennsylvania Department of Transportation
PSC	: Pre-Stressed Concrete.

THERMAL PERFORMANCE EVALUATION OF INTEGRAL ABUTMENT BRIDGES

ABSTRACT

Integral Abutment Bridges (IABs) face significant geotechnical challenges due to thermal effects that induce cyclic displacements in backfill soil. This research enhances the understanding of IABs' thermal behavior by investigating the impact of secondary loads on bridge performance, critically evaluating current design assumptions, and proposing strategies to mitigate adverse thermal effects. A comprehensive finite element analysis was conducted to assess the individual and combined effects of primary and secondary loads, identifying both beneficial and detrimental impacts. Various methods for calculating earth pressure behind abutments were examined and validated using field monitoring data, with finite element modeling assessing their influence on IAB behavior. The research emphasizes the often-overlooked role of construction temperature in design practices, proposing a specific temperature range for consideration during design and construction. A parametric study explored the effects of construction temperature on both steel and prestressed concrete IABs, considering factors such as bridge length, soil stiffness, and abutment height. Findings reveal that secondary loads can either amplify or mitigate structural responses. Additionally, they highlight the variability among earth pressure behind abutment calculation methods and underscore the importance of accounting for soil ratcheting effects. The study established construction temperature guidelines designed to be applicable year-round and to ensure symmetrical temperature variations during expansion and contraction phases. This enhances predictions of thermal displacements and internal forces and minimizes the negative effects of thermal loading, as emphasized in the parametric study for various design parameters. This research offers practical recommendations to enhance the reliability and efficiency of IAB infrastructure development.

Keywords: Finite Element Modeling, Integral Abutment Bridges, Soil-Structure Analysis, Thermal Loadings, Thermal Response.

DERSİZ KÖPRÜLERİN TERMAL PERFORMANS DEĞERLENDİRMESİ

ÖZET

Dersiz köprüler, geri dolgu topraklarında döngüsel deplasmanlara neden olan termal etkiler nedeniyle önemli jeoteknik zorluklarla karşılaşmaktadır. Bu araştırma, dersiz köprülerin termal davranışını anlamayı geliştirerek köprü performansı üzerindeki ikincil yüklerin etkisini incelemekte, mevcut tasarım varsayımlarını eleştirel bir şekilde değerlendirmekte ve olumsuz termal etkileri azaltma stratejileri önermektedir. Birincil ve ikincil yüklerin bireysel ve birleşik etkilerini değerlendirmek için kapsamlı bir sonlu elemanlar analizi yapılmış ve hem yararlı hem de zararlı etkiler belirlenmiştir. Ayaklar arkasındaki toprak basıncını hesaplama için çeşitli yöntemler incelenmiş ve saha izleme verileri kullanılarak doğrulanmıştır; sonlu elemanlar modellemesi yöntemlerinin dersiz köprülerin davranışı üzerindeki etkisi değerlendirilmiştir. Araştırma, tasarım uygulamalarında genellikle göz ardı edilen inşaat sıcaklığının rolünü vurgulayarak, tasarım ve inşaat sırasında dikkate alınması gereken belirli bir sıcaklık aralığı önermektedir. Bir parametrik çalışması, köprü uzunluğu, zemin sertliği ve ayak yüksekliği gibi faktörleri göz önünde bulundurarak, hem çelik hem de gerilme beton dersiz köprüleri üzerindeki inşaat sıcaklığının etkilerini araştırmıştır. Bulgular, ikincil yüklerin yapısal tepkileri artırabileceğini veya azaltabileceğini ortaya koymaktadır. Ayrıca, ayak arkasındaki toprak basıncını hesaplama yöntemleri arasındaki değişkenliği vurgulamakta ve zemin ratcheting etkilerini dikkate almanın önemini belirtmektedir. Çalışma, yıl boyunca uygulanabilir ve genişleme ile daralma aşamalarında simetrik sıcaklık değişimlerini sağlamak üzere tasarlanmış inşaat sıcaklığı yönergelerini belirlemiştir. Bu, termal deplasmanları ve iç kuvvet tahminlerini geliştirir ve termal yüklemenin olumsuz etkilerini en aza indirir; bu durum, çeşitli tasarım parametreleri için yapılan parametrik çalışmada vurgulanmıştır. Bu araştırma, dersiz köprü altyapı geliştirme sürecinin güvenilirliğini ve verimliliğini artırmak için pratik öneriler sunmaktadır.

Anahtar Kelimeler: Derzsiz Köprüler, Sonlu Elemanlar Modellemesi, Termal Tepkiler, Termal Yükler, Zemin-Yapı Analizi.

1. INTRODUCTION

1.1. Background

Bridges without expansion joints or sliding bearings are referred to as integral abutment bridges (IABs). In these structures, the bridge superstructure and abutment function as a single structural unit. Figure 1.1 illustrates the differences in the connections between the bridge superstructure and abutment in a traditional bridge versus an IAB. IABs are alternatively referred to as integral bridges, jointless bridges, integral bent bridges, and rigid-frame bridges. Semi-integral abutment bridges typically have sliding bearings, but no expansion joints. Expansion joints and bearings have traditionally been used to accommodate the seasonal thermal expansion and contraction of bridge decks, typically of the order of tens of millimeters.

(a) (b)

Figure 1.1. Connection between bridge superstructure and abutment of: (a) a traditional bridge and (b) an IAB.

A survey conducted in the United Kingdom, covering around 200 concrete highway bridges, and commissioned by the Department of Transport, brought attention to the significant issues associated with expansion joints. This survey, as reported by Wallbank in 1989, highlighted expansion joints as a major source of costly and maintenance work. In response to this issue, the Highways Agency took action by releasing Advice Note BA 42 in 1996, which recommended the design of IABs. The note stated that all bridges with lengths up to 60 should be designed as integral structures with their supports.

The vulnerability of expansion joints is attributed to their adverse effect on the durability of the superstructure. The issue arises due to the potential leakage of water and corrosive chemicals, such as deicing salts onto structural elements. Expansion joints, by necessity, are located above abutments, bearings, beams, and piers. It is these critical structural elements of a bridge that suffer most from corrosion. Figure 1.2 illustrates an example of an expansion joint leakage issue. Furthermore, the accumulation of debris, including dirt and rocks, within the joints restricts the deck's movement. Consequently, the limitations in movement can lead to an elevation in the earth pressure behind the abutment, leading to unanticipated internal forces in the bridge elements. These factors can ultimately pose a risk of bridge failure. (Springman et al., 1996).

Figure 1.2. Exemplification of Expansion Joint Leakage Issue.

Despite the IAB concept being proven to be cost-effective during initial construction for various span lengths and technically successful in eliminating problems associated with expansion joints and bearings, it is exposed to different issues of a geotechnical nature. These problems are likely due to a complex soil–structure interaction mechanism involving relative movement between the bridge abutments and the backfill soil. The seasonal and daily cycles of expansion and contraction in the bridge deck can lead to an elevation in the earth pressure behind the abutment. This phenomenon, known as soil ratcheting (England and Dunstan, 1994 and England et al., 2000), leads to a substantial increase in the horizontal resultant earth pressure force acting on each abutment. These forces present a potential and significant long-term challenge in the context of IAB problems.

However, the behaviors of IABs under thermal loadings have not been completely understood. Thus, this study aims to enhance a better understanding of thermal behavior in IABs by investigating the effects of secondary loads on bridge performance, discussing the assumptions of these loads in current design practices, and proposing strategies to mitigate the associated negative effects of thermal loadings.

1.2. Statement of the Problem

Daily and seasonal temperature variations cause bridge superstructures to expand and contract. This thermal-induced displacement applies lateral loading and unloading forces on the substructure and the backfill soil behind the abutment. These cyclic thermal displacements significantly affect the internal forces within IAB elements and affect earth pressure variations behind the abutment. Depending on the magnitude and direction of these displacements, pressures can range from minimum active to maximum passive. Thus, alongside primary loads such as dead load and traffic load, this type of bridge also experiences secondary loads, including temperature load and varying earth pressure load.

Despite extensive research involving field monitoring, laboratory experiments, and numerical modeling, a significant gap remains in understanding how secondary loads, particularly when combined with primary loads, affect the overall behavior of IABs. Investigating the assumptions related to these secondary loads and their interactions with primary loads is crucial for assessing their overall effect on IAB behavior.

Regarding temperature loads and thermal displacement calculations, bridge design specifications typically recommend a uniform temperature range to account for temperature changes in the bridge superstructure, based on climate, materials, and an assumed construction temperature. However, these specifications often overlook the potential variability in construction temperature during the construction phase. While construction temperature is generally assumed in the design process, it is not explicitly addressed in the recommendations, and specific upper or lower bounds for construction temperature during the construction phase are not provided. As a result, actual temperature changes in the bridge superstructure may exceed the assumed values, leading to potential inaccuracies in predicting thermal displacements.

Additionally, there is a notable gap in the literature concerning the influence of construction temperature on the structural response of IABs. Moreover, while various methods exist for calculating passive earth pressure behind abutments, significant variations in outcomes have been observed. These variations can substantially affect the overall behavior of IABs, underscoring the need for further investigation.

1.3. Research Purpose

The objective of this research is to enhance understanding of the thermal behavior of IABs and propose novel approaches to address associated challenges. The study encompasses several key goals. Firstly, it aims to investigate the influence of various loads on the overall response of IABs to gain a deeper understanding of their behavior. This involves a direct comparison of the structural response of bridge elements under individual load conditions such as dead load, backfill pressure, and temperature load. Additionally, the study examines the combined effects of these loads to fully capture their effect on bridge behavior, reflecting real-world conditions and enhancing the understanding of how secondary loads interact with primary loads to affect the behavior of IABs. Another key goal is to highlight the varied outcomes resulting from different methods used to calculate passive earth pressure and their subsequent effect on the overall response of IABs. Additionally, it seeks to validate the accuracy of these methods through comparison with both long-term and short-term field monitoring data.

Significant emphasis was placed on considering construction temperature, a parameter often overlooked in design practices. By incorporating construction temperature as a design parameter in construction practices, the accuracy of thermal displacement and internal force predictions can be improved, thereby enhancing overall design outcomes. The study aims to propose a construction temperature range [$T_{Const.min}$, $T_{Const.max}$] to be selected during the design phase and managed and monitored during the construction phase. Although specifying an exact construction temperature range [$T_{Const.min}$, $T_{Const.max}$] poses challenges due to environmental variations, insights from the Arsoy model (2004) were utilized to address this issue. The Arsoy model (2008) can assist in selecting a suitable year-round range for local conditions and ensuring balanced temperature variations during both expansion and contraction phases, minimizing the negative effects of thermal loading.

Furthermore, the study investigates the effect of construction temperature on the structural response of both steel and prestressed concrete (PSC) IABs through a parametric study. Key parameters such as bridge length, foundation soil stiffness, and abutment height are considered. The primary objective is to emphasize that by identifying the recommended construction temperature range [$T_{Const.min}$, $T_{Const.max}$], it is possible to mitigate the adverse effects associated with thermal loading conditions across different design parameters. This approach offers innovative solutions to overcome the challenges presented by the limited length of IABs.

Overall, this research provides valuable insights and practical recommendations for the design and construction of IABs, promoting more reliable and efficient infrastructure development.

1.4. Research Methodology

To achieve the objectives outlined earlier in this research study, the following tasks have been performed.

Task 1. A literature review has been conducted, initially covering the introduction to IABs, including their classifications, advantages, and disadvantages. Additionally, critical considerations in thermal analysis of IABs were investigated, focusing on aspects such as soil–structure interaction and thermal-induced displacements. In addition, a brief review of general information regarding temperature variations in IABs will be provided. An overview of the structural response of IABs to varied load conditions will also be provided. Additionally, a summary of the effects of different parameters on the structural response of IABs will be discussed. Finally, the literature review explored finite element modeling of IABs, and structural analysis methods for IABs.

Task 2 involved investigating the influence of various loads—specifically secondary loads (temperature load and earth pressure) and the primary load (dead load)—on the overall response of IABs to gain a deeper understanding of their behavior. To achieve this, a simple 3D finite element model was created using MIDAS CIVIL software. The analysis results were categorized based on the influence of three loads: dead load alone, backfill pressure alone, and temperature load alone. This categorization allowed for a direct comparison of the bridge elements' response under each individual load condition. Additionally, results were analyzed under the combined influence of dead load, backfill pressure, and temperature load, considering states of contraction and expansion. The proportional value of the secondary loads relative to the dead load was determined, providing insight into the magnitude and direction of the secondary load effects compared to the primary dead load response. Furthermore, the proportional value of load combinations, including those with secondary loads (expansion case, contraction case) and at-rest load effects, will be determined to understand how these secondary loads interact with the dead load. This analysis will assess whether these interactions amplify or mitigate the overall structural responses, helping to identify their beneficial or detrimental effects. The bridge's response was evaluated by measuring the bending moment and displacement across the girder, pile, and abutment.

Task 3 encompassed several key components aimed at investigating the various calculations of earth pressure behind the abutment and their influence on the overall behavior of IABs. Firstly, a comparative analysis was performed to calculate earth pressure behind the abutment using different methods across various displacements. The aim was to highlight the varied outcomes resulting from different methods. Furthermore, validation was conducted to ensure the accuracy of these methods through comparison with both long-term and short-term field monitoring data. Subsequently, a simple 3D finite element model was created using MIDAS CIVIL software. Within this model, five different methods for calculating the passive earth pressure behind the abutment were investigated across different thermal displacement scenarios to assess their subsequent effects on the overall response of IABs. The results of the analyses performed for this research only included backfill pressure to facilitate a direct comparison of the effects of methods used to calculate passive earth pressure. Additionally, a combination of passive earth pressure and dead load was investigated to fully account for the effect of passive earth pressure on overall behavior, reflecting real-world conditions. The proportional values of bridge response under dead load and passive earth pressure, using various methods, were compared to the responses from the at-rest case. This comparison highlights how different methods of calculating passive earth pressure affect the overall IAB structural response and underscores their significant effect on IAB design. The response was evaluated by measuring the bending moment and displacement across the girder, pile, and abutment.

Task 4 focused on evaluating construction temperature considerations in the design practices for IABs. Initially, the study examined the consideration of construction temperature in bridge design specifications across the United States, Canada, and Europe, identifying key weaknesses in these approaches. Examples were provided to demonstrate potential discrepancies between construction temperature implied by design specifications and the actual variability encountered. Furthermore, a new approach has been proposed to incorporate construction temperature as a design parameter, offering an innovative consideration in the design process. It recommended defining a construction temperature range [$T_{Const.min}$, $T_{Const.max}$] to be selected during the design phase and actively managed and monitored throughout the construction phase. Despite the inherent challenges in specifying an exact construction temperature range due to environmental variability, the study used insights from the Arsoy (2008) model to address this challenge. By incorporating daily and seasonal temperature variations, the research established construction temperature range guidelines designed to be applicable year-round, ensuring symmetrical temperature variation during both expansion and contraction phases, thereby minimizing the negative effects of thermal loading. Finally, a new parameter, the effective construction temperature, is proposed to represent the actual construction temperature at which the integral connection between the bridge deck and abutment is established. This parameter has been determined for both steel and concrete bridges, acknowledging that it varies due to the different times and natures of the integral connection for various bridge superstructure materials.

Task 5 involved conducting a parametric study considering three key parameters: (1) bridge length, (2) foundation soil stiffness, and (3) abutment height. The objective was to examine the influence of construction temperature on the structural response of both steel and PSC IABs across various design parameters. The task commenced with a discussion to establish the magnitudes for the parametric study. A series of analyses were then performed using MIDAS CIVIL software to assess the thermal performance of IABs. The analyses involved applying different construction temperatures to understand their effect on the thermal behavior of these bridges. The response was evaluated by measuring the bending moment and displacement over the top of the abutment and pile, as well as the bending moment at the end of the main girder and the displacement at the middle of the span near the abutment. The results were presented from two different perspectives: Firstly, the relationship between construction temperature and structural responses was illustrated considering various key parameters such as different bridge lengths, abutment heights, and foundation soil stiffnesses. Secondly, the relationship between various key parameters such as bridge length, abutment height, and foundation soil stiffness, and structural responses was illustrated considering different construction temperature. Both approaches were conducted under the combined effect of dead load, temperature load, and backfill pressure in both expansion and contraction conditions. These analyses provided a comprehensive understanding of how different parameters and construction temperature affect the structural response of IABs.

1.5. Limitations

This section outlines the assumptions and simplifications involved in the 3D finite element models used in this research, as well as the sources of some design specifications data, which constitute the study's limitations.

During the literature review, it was observed that the bridge design specifications provided by the American Association of State Highway and Transportation Officials (AASHTO) and the Canadian Highway Bridge Design Code (CHBDC) impose certain constraints on the extent of available information. Consequently, data from these codes utilized in this study were drawn from previously published theses and articles.

Regarding the assumptions and simplifications made in the 3D finite element models, the following points are notable:

- The stiffness of the connections between elements and the elasticity modulus of the elements were computed using the finite element modeling software.
- The 3D model was simplified to include only the primary components of the bridge to reflect its general behavior, rather than to provide a detailed design. Therefore, no specific design codes were applied in this study
- Cross-sectional details and material strengths were obtained from prior research, which will be discussed in detail later.
- All models were evaluated for failure before analyzing the results, ensuring that the behavior of all elements remained within the linear domain and did not transition to the nonlinear domain.
- This study focused on specific loads affecting IABs: dead load as the primary load, temperature loads (excluding vertical temperature gradients), and earth pressure as secondary loads. Notably, the soil stiffness of the backfill behind the abutment was not considered in the model.

These limitations should be taken into account when interpreting the results and conclusions of this study.

2. LITERATURE REVIEW

Integral bridges, also known as integral abutment bridges (IABs), are designed without expansion joints, or sliding bearings. In these structures, the abutment and the superstructure function as a single structural unit. This section provides a general literature review, starting with the classification of IAB types and their advantages and disadvantages. Furthermore, it explores critical considerations in the thermal analysis of IABs, such as soil–structure interaction, focusing on backfill-abutment interaction and soil-pile interaction. The review of backfill-abutment interaction includes limit equilibrium approach, subgrade reaction, and continuum approach. For soil-pile interaction, the subgrade reaction approach, continuum, and equivalent cantilever approach will be discussed. The section will also address thermal-induced displacements in IABs, considering factors such as bridge temperature, shade air temperature variation, and effective bridge temperature. In addition, a brief review of general information regarding temperature variations in IABs will be provided. This includes a discussion on a uniform temperature range affecting the entire structure and temperature gradients within the girder. An overview of the structural response of IABs to varied load conditions will also be provided. Additionally, a summary of the effects of different parameters on the structural response of IABs will be discussed, such as construction temperature, superstructure material, bridge length, foundation soil stiffness, and abutment height. Finally, the finite element modeling of IABs will be reviewed, covering the modeling of deck-beam and slab bridges, abutment pile types, considerations for modeling, and structural analysis methods for IABs

2.1. Introduction to IABs

IAB lacks expansion joints, which are typically used to accommodate thermal-induced displacements. Instead, the spans are cast as a continuous, solid structure extending from one abutment to the other. Consequently, displacements due to thermal expansion, contraction, or braking loads are absorbed and managed by the abutments and, if present, the piers. Figure 2.1 illustrates the Brisbane Gateway bridge, an example of an IAB.

Figure 2.1. Brisbane Gateway bridge, an example of an IAB.

By eliminating expansion joints and bearings, IABs reduce maintenance costs and enhance structural efficiency, integrating the abutments with the superstructure to create a more cohesive and resilient design. Figure 2.2 illustrates the differences between an IAB and a conventional bridge.

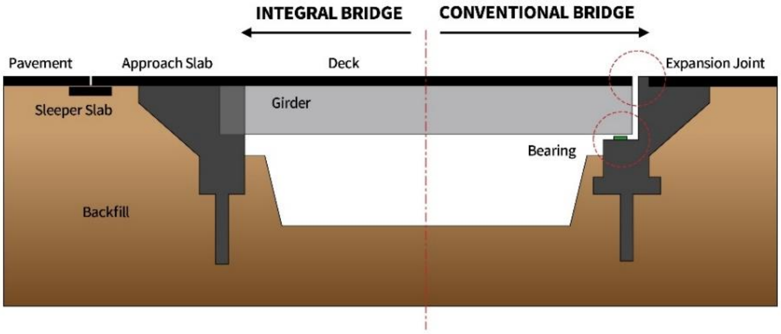

Figure 2.2. IAB and conventional bridge (Norlan De Vera, 2022).

The main concern for IABs is the effect of varying temperatures as it causes the bridge deck to deform either contraction or expansion. These repeated contractions and expansion of the deck have a significant effect on the backfill adjacent to the abutment which causes a cycle of soil compaction and soil slide, which in effect causes the modulus of subgrade reaction and pressure distribution of the backfill to vary with depth.

2.2. Classification of IAB Types:

PD 6694-1 published by the British Standards Institution (BSI) classifies the types of integral and semi-integral abutments for the integral construction of the IABs. PD 6694-1 categorizes three types of abutments for integral construction: full height frame abutments as shown in Figure 2.3 (a–c), embedded wall abutments as shown in Figure 2.3 (d), and end screen abutments as shown in Figure 2.3 (e–i). The movements in full height frame abutments are accommodated by rotation or flexure of the abutment wall—whereas, in end screen abutments, the abutments can translate in and out of the fill to compensate for the deck movements. PD 6694-1 provides further subclassifications for end screen abutments: bank pad abutments including those supported on the ground or piles as shown in Figure 2.3 (e–g), flexible support abutments as shown in Figure 2.3 (h), and semi-integral abutments as shown in Figure 2.3 (i). According to PD 6694-1, semi-integral abutments consist of the displacement bearings at the connection between the vertical support at the end of the bridge deck and conventional or embedded walls or reinforced soil abutments. The displacement bearing connection accommodates the deck expansion and contraction without transferring the effect to the bridge abutment.

A) Frame abutments

The transmission of bending moments, shears, and axial forces occurs through the structural connection between the abutment and the deck. This specific bridge type is supported either on spread footings or piled foundations, as depicted in Figure 2.3 (a–c). The frame type abutment not only supports the vertical loads from the bridge deck but also serves as a retaining wall for the backfill and the earth pressures from the embankment.

B) Embedded wall abutments

The Embedded Abutment, as depicted in Figure 2.3 (d), includes bored pile, sheet pile, or diaphragm wall abutments, extending to different depths below the ground fill surface. The depth of wall embedment provides stability to the system, preventing rocking, while ensuring that the walls are inherently integrated with the bridge deck.

C) End Screen Abutment

These types of abutments primarily serve as retaining walls for transmitting longitudinal loads and embankment earth pressures. Vertical loads from the deck are supported by independent columns positioned within 2 from the end screen. This positioning aims to minimize the vertical displacement of the end screen during end span deflection. The supports at the ends can either be structurally isolated from the horizontal displacements of the end screen or connected to the deck. If connected, they must be designed to withstand or prevent the earth pressures resulting from their displacement relative to the embankment.

i. Bank pad abutments

The bank pad abutment design serves as an extension to the deck, forming a footing seated on the backfill, functioning as an end support for the bridge, as shown in Figure 2.3 (e) and (f)). It allows the deck and footing to slide on the foundation material, accommodating thermal expansion and contraction, and permitting rotation under live loading. For stability, the bank pad should possess sufficient self-weight. In multi-span designs, it is crucial for the end spans to exhibit adequate flexibility to accommodate potential differential settlement while preventing uplift caused by traffic loading.

ii. Bank pad abutments on piles

The pad abutment relies on a single row of individual vertical piles for its foundation, which are either driven or bored through the embankment. The tops of these piles are integrated into the deck's structure. As the deck expands, its ends move into the backfill, causing the piles to flex backward into the fill.

iii. Flexible support abutments

In this case, the bridge is supported by flexible columns or piles. Only the end screen, connected to the deck end, moves into the fill. The supporting columns or piles might be enclosed in sleeves, enabling them to bend without disturbing the adjacent soil. Alternatively, they may be positioned in front of a reinforced earth wall or a similar type of abutment.

iv. Semi-integral abutments

These abutments therefore act in a similar manner to flexible support abutments in regard to the lateral earth forces loading the end screen wall. Further integral schemes for multi-span bridges and deck ends are elaborated on in Figure 2.3, which gives an idea of the range of options available to the bridge designer. In a semi-integral structure, vertical support at the end of the deck is facilitated by bearings situated either on conventional abutment walls or reinforced soil abutments that remain stationary during deck expansion. These abutments function similarly to flexible support abutments concerning the lateral earth forces exerted on the end screen wall.

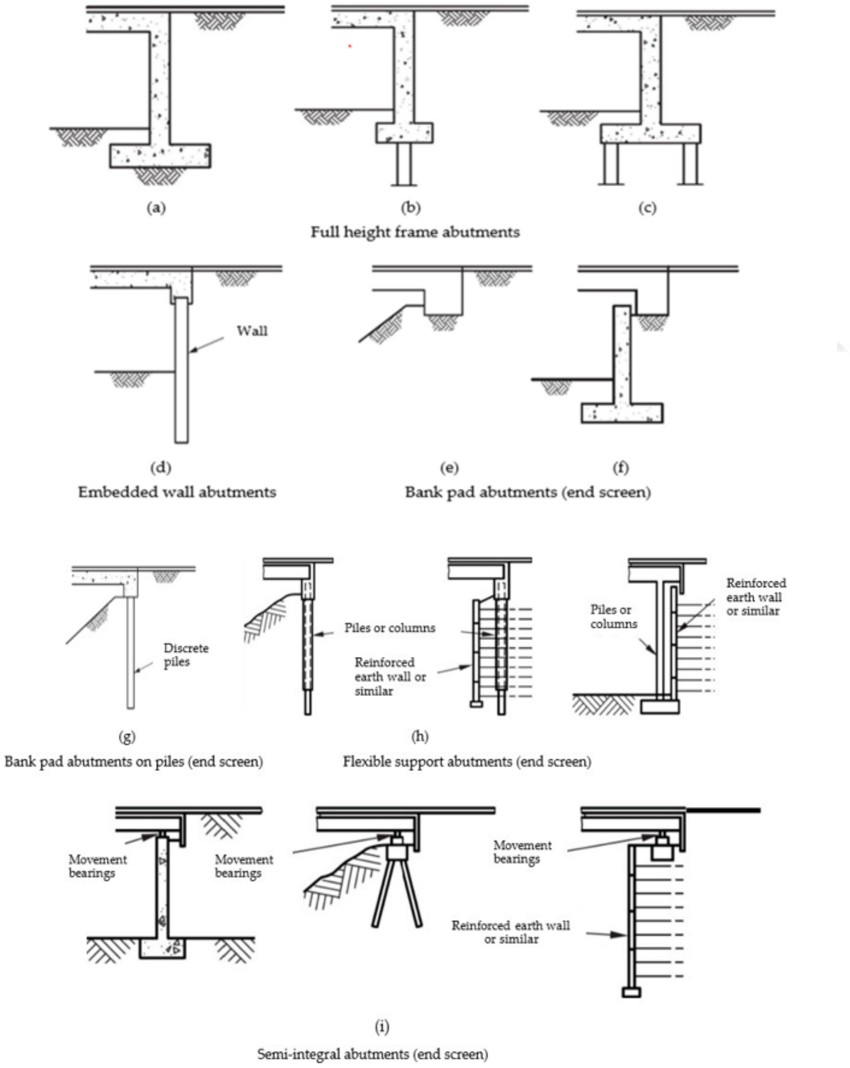

Figure 2.3. Types of integral and semi-integral abutments (PD 6694-1).

2.3. IABs Advantages and Disadvantages:

Principal advantages of IABs have been summarized by Arsoy et al. (2004) and include the following:

- Lower construction costs due to elimination of expansion joints (Yang et al. (1985), Greimann et al. (1987), Soltani and Kukreti (1992)). the reduction in initial costs is linked to the elimination of expensive deck joints, anchor bolts, bearings, and their time and money consuming assembly and integral abutments will generally provide some uplift capacity.
- Lower maintenance costs due to elimination of expansion joints (Yang et al. (1985), Soltani and Kukreti (1992), Hoppe and Gomez (1996)). Integrated structures have the capability to eliminate damage associated with joints caused by the use of deicing chemicals and restricted displacement of rigid structures. In conventional bridges, a significant portion of maintenance costs are connected to repairing joint damage. Even waterproof joints deteriorate over time, permitting water, including salt-laden substances, to seep through, accelerating corrosion damage to girder ends, bearings, and supporting reinforced concrete substructures. Accumulation of dirt, rocks, and debris in the elastomeric glands further contributes to failures. Furthermore, Bearings are especially expensive to replace. Over time, steel bearings may tip over and/or seize up due to loss of lubrication or buildup of corrosion. Elastomeric bearings can split due to unanticipated displacements or ratchet out of position. Eliminating bearings can effectively avoid a significant source of maintenance problems in bridges.
- Seismic performance has improved. (Hoppe and Gomez (1996), Kreger and Talbott (2009). Performance under seismic actions is improved due to the interaction of more substructure elements and damping within the system.
- Fewer piles are required for foundation support (Soltani and Kukreti (1992), Hoppe and Gomez (1996), and no battered piles are needed (Burke (1996).
- Construction is simple and rapid (Burke (1996), Wasserman and Walker (1996)). An IAB can be regarded, for analysis and design purposes, as a continuous frame consisting of a single horizontal member and two or more vertical members. this eliminates the need for a separate design process for both the superstructure and

foundations.

- Greater end-span ratios are achievable (Burke (1996), Wasserman and Walker (1996), GangaRao et al. (1996)).
- The smooth, uninterrupted deck of the IAB is aesthetically pleasing and improves vehicular riding quality (Loveall 1996), Soltani and Kukreti (1996)).

Moreover, in high-speed railway bridge applications, structural elements such as the superstructure and abutment support can be made slenderer compared to traditional jointed railway bridges (Marx, 2011). This is attributed to the consequential participation of all load-bearing elements in load distribution. IABs offer several structural advantages as well. They feature increased reserve load capacity and improved load distribution, providing greater resistance against potentially damaging overloads. Additionally, integral abutments help avoid the risk of abutment instability. Consequently, IABs are increasingly seen as attractive options in cold climates, including the northern United States, Canada, and northern Europe.

Despite the significant advantages of IABs, some problems and uncertainties are associated with their use. These are potentially due to a complex soil–structure interaction mechanism involving relative displacement between the bridge abutments and backfill soil. This displacement is caused by the cyclic expansion and contraction of the bridge superstructure due to daily and seasonal thermal variations. Figure 2.4. illustrates the thermal displacements of the bridge superstructure.

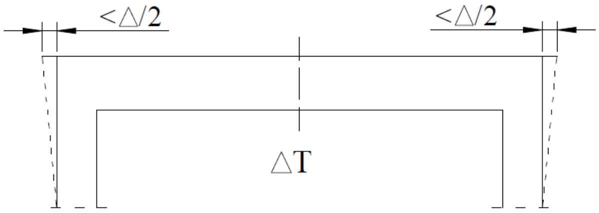

Figure 2.4. Thermal displacements of the bridge superstructure (Tlustochowicz, 2005).

Research conducted by Horvath (2004) emphasizes these challenges, highlighting that problems associated with IABs are fundamentally geotechnical in the nature, potentially manifesting both structurally and geotechnically at any point during the bridge's lifespan. He noted that resulting issues include irreversible subsidence behind the abutments and the progressive accumulation of lateral earth pressures on the abutments. Any of these outcomes, individually or combined, can lead to compromised serviceability, or even collapse failures of the bridge components, signifying serious concerns. Furthermore, the thermal displacement experienced by the abutments can transfer to the piles supporting these abutments, potentially subjecting them to fatigue and high service stresses as a consequence of the continuous cyclical displacement of the bridge deck. These stresses have the capacity to create plastic hinges in the piles, thereby potentially diminishing their axial load capacities. Studies conducted by Soltani and Kukreti (1996), Yang et al. (1985), and Krauthammer et al. (1994) emphasize this concern.

In addition, IABs with a skew tend to cause plan rotations due to cyclical earth pressure changes influencing the abutment wall (Hoppe and Gomez (1996)). Another disadvantage is the potential for water to enter the bridge end backfills, causing undermining of the bridge abutments (Wolde-Tinsae and Klinger (1987)). Furthermore, the elimination of intermediate expansion joints in multiple spans results in a structural continuity that may induce secondary stresses in the superstructure. These forces due to shrinkage, creep, thermal gradients, differential settlement, differential deflections, and earth pressure can cause cracks in concrete bridge abutments (Soltani and Kukreti, 1992). Since wing-walls are linked into the integral system, they may also exhibit cracking due to incompatibility with the rotations and contractions of the deck superstructure (Wolde-Tinsae and Klinger (1987).

The application of the IAB concept has several limitations. IABs are not compatible with weak embankments or subsoils, and their usage is restricted to specific lengths, although the maximum allowable length remains somewhat unclear. These bridges are deemed suitable only when the expected temperature-induced moment at each abutment aligns with predefined values specified by relevant authorities in different countries. However, they might tolerate slightly larger moments in some cases.

2.4. Soil–Structure Interaction in the IABs

Although the IAB concept offers several benefits and helps overcome various structural challenges, the primary uncertainty in analyzing and designing an IAB lies in predicting the soil's response behind the abutment and around the piles. These soil forces can become significant, especially during thermal expansion of the bridge girder, significantly affecting the overall structural design of the bridge-abutment-pile system.

The lateral soil reaction is nonlinear and depends on the magnitude and nature of the abutment movement, which can involve both translation and rotation. This presents a soil–structure interaction problem, where the magnitudes and characteristics of soil and structural deformations and stresses are mutually interdependent. (Faraji et al., 2001).

The interaction between the structures, especially foundation and soil medium have potential to alter the actual behavior of any structure considerably compared to the analysis of the structure alone. Since, IABs behavior is interdependent between its structural components and soil medium, it is vital to determine the relevant parameters of soil to represent its behavior. In general modelling of the structural element i.e., superstructure and foundation piles are rather simple and straightforward compared to soil medium. The complex behavior of soil due to its heterogeneous, anisotropic, and nonlinear in force displacement characteristics need to be accounted for in its modelling. (David and Forth, 2011).

2.4.1. Backfill–Abutment Interaction

IABs accommodate the thermal expansion and contraction of the superstructure by displacement of the abutments or end screens, which are retaining structures. Often retaining structures are analyzed representing the soil as merely a load – the stiffness of the soil is not modelled (limiting equilibrium approach). The design proceeds considering only limiting active and passive lateral earth pressures. However, if displacements/ deflections of the structure are insufficient to mobilize the limiting values, intermediate values of earth pressure occur, as illustrated in Figure 2.5.

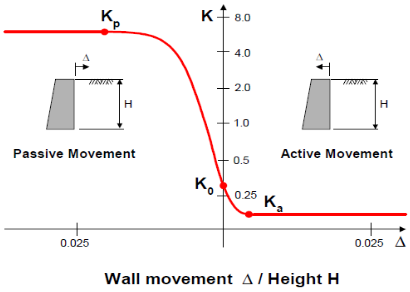

Figure 2.5. Pressure/ deflection curve (Rhodes and Moses, 2014).

The lateral earth pressure depends on the strain in the soil, which in turn depends on displacements in the structure. Structural displacements depend on the stiffness of both structure and soil, and on lateral earth pressures. In cases where the stiffness of the soil and its interaction with the structure significantly determine the structural system's behavior, the limiting equilibrium approach is considered inadequate. Consequently, an analysis incorporating the behavior of both soil and structure, known as soil–structure interaction analysis, becomes necessary. This analysis must encompass the intricate nature of soil, acknowledging its heterogeneous, anisotropic, and nonlinear force-displacement characteristics. In this context, the soil can be represented using continuum-type elements or Winkler springs positioned behind the abutment to address soil–structure interaction.

In this section, an overview of analytical and numerical models employed in backfill-abutment design will be provided. Firstly, conventional models, based on limit equilibrium principles, will be outlined. These models commonly disregard soil stiffness and encompass classical theories for earth pressure behind the abutment and include displacement-dependent Methods. In cases where the stiffness of the soil and structural interaction significantly dictate the structural system's behavior, the conventional limiting equilibrium approach may not be suitable. In such instances, the soil–structure interaction can be represented using approaches like the subgrade reaction approach or the elastic continuum approach.

2.4.1.1. Limiting Equilibrium Approach

‘Limiting equilibrium’ approach for the design of IABs generally use an assumed lateral earth pressure distribution and earth pressure coefficient, commonly denoted K. This coefficient signifies the ratio between lateral (horizontal) pressure and vertical pressure ($K = \sigma_h / \sigma_v$), as illustrated in Figure 2.6. Thus horizontal earth pressure is assumed to be directly proportional to the vertical pressure at any given point in the soil profile. Earth pressure coefficient can depend on the soil properties and the stress history of the soil. There are three categories of horizontal earth compression coefficients: at-rest pressure coefficient (K_0), active pressure coefficient (K_a) and passive pressure coefficient (K_p). The at-rest lateral earth pressure load can be calculated using the equation developed by Jaky in 1944. The at-rest lateral earth pressure coefficient (K_0) is provided below as Equation (2.1),

$$K_0 = 1 - \sin(\varphi) \tag{2.1}$$

There are many theories, empirically based or analytically derived approaches, used for predicting active and passive lateral earth pressure coefficient. Some of these will be listed in the following sections.

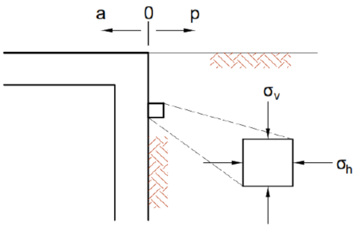

Figure 2.6. Stress state behind the abutment (Vahedifard et al., 2015).

A) Classical Theories for Earth Pressure Behind the Abutment:

Classical earth pressure theories deal with the limit equilibrium state of the soil, where soil parameters at failure are known or easily obtainable. Most earth pressure theories require only the soil friction (φ) and the wall friction (δ) at failure to calculate an earth pressure coefficient. It is assumed that the soil mass has undergone enough deformation so that the soil friction is fully mobilized.

The lateral earth pressures on abutments are calculated by first evaluating the coefficient of passive earth pressure. The most common methods to evaluate passive earth pressure coefficient use Rankine (1857) or Coloumb (1776) theories. Another conventional method was developed by Caquot and Kerisel (1948), which evaluated passive earth pressure coefficient by assuming a curved failure surface and earth pressure coefficient tables summarize the results of their analysis.

a) Coulomb Theory (1776)

The Coulomb theory offers an analytical method for determining the resultant horizontal force acting on a retaining system, considering various factors such as the slope of the wall, wall friction, and backfill slope. This theory operates on the assumption that soil shear resistance develops along the wall and the failure plane. The equations for the active earth pressure and passive earth pressure coefficients are provided below as Equations (2.2a) and (2.2b), respectively,

$$K_{aC} = \frac{\cos^2(\varphi - \theta)}{\cos^2\theta\cos(\delta+\theta)\left(1+\sqrt{\frac{\sin(\delta+\varphi)\sin(\varphi-\beta)}{\cos(\delta+\theta)\cos(\beta-\theta)}}\right)^2} \tag{2.2a}$$

$$K_{pC} = \frac{\cos^2(\varphi + \theta)}{\cos^2\theta\cos(\delta-\theta)\left(1-\sqrt{\frac{\sin(\delta+\varphi)\sin(\varphi+\beta)}{\cos(\delta-\theta)\cos(\beta-\theta)}}\right)^2} \tag{2.2b}$$

δ represents the friction angle between the backfill material and the face of the wall, while β denotes the angle from the backfill surface to the horizontal. Additionally, θ represents the angle from the face of the wall to the vertical, and φ signifies the internal friction angle of the backfill, as illustrated in Figure 2.7.

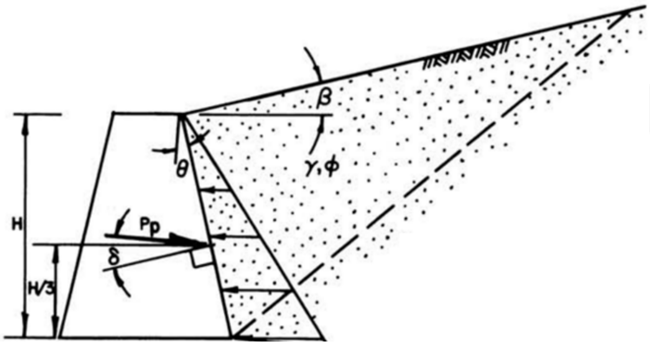

Figure 2.7. Coulomb’s passive wedge (Coulomb,1776).

Regarding the earth pressure distribution, a simple triangular pressure distribution is assumed, as illustrated in Figure 2.8. The lateral earth pressure (σ_h) at any depth Z can be calculated using Equation (2.3). The maximum lateral earth pressure occurs at depth H (σ_{hmax} = K γ H), and the resultant force (E_{Pmax}) acts at a height of H/3 from the bottom and is determined by the total area of the triangular pressure diagram (E_{Pmax} = 0.5 K γ H^2).

$$\sigma_h = K\,\sigma_v = K\,\gamma\,Z \tag{2.3}$$

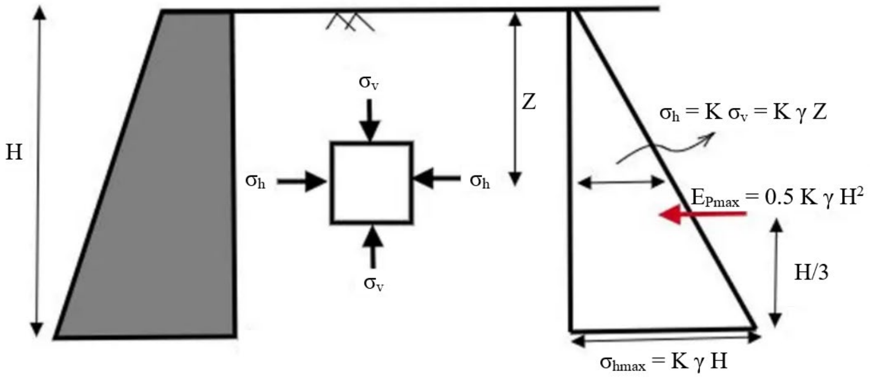

Figure 2.8. The simple triangular earth pressure distribution.

b) Rankine Theory (1857).

In 1857, Rankine developed a theory for predicting active pressure and passive pressure. The assumptions made include no cohesion in the soil, no friction on the wall, a vertical soil-wall interface, a planar failure surface for the soil to move on, and the angle of the generated force parallel to the surface of the backfill. The equations for active earth pressure and passive earth pressure coefficients are provided below as given in Equations (2.4a) and (2.4b), respectively,

$$K_{aR} = \cos\beta \, \frac{\cos\beta - \sqrt{\cos^2\beta - \cos^2\varphi}}{\cos\beta + \sqrt{\cos^2\beta - \cos^2\varphi}} \tag{2.4a}$$

$$K_{pR} = \cos\beta \, \frac{\cos\beta + \sqrt{\cos^2\beta - \cos^2\varphi}}{\cos\beta - \sqrt{\cos^2\beta - \cos^2\varphi}} \tag{2.4b}$$

The angle φ is the internal friction angle of the backfill, and β is the inclination angle of the backfill soil surface in reference to the horizontal. For the case where β is 0, the above equations are simplified to Equations (2.5a) and (2.5b) for active earth pressure and passive earth pressure coefficient, respectively,

$$K_{aR} = \tan^2\left(45 - \frac{\varphi}{2}\right) \tag{2.5a}$$

$$K_{pR} = \tan^2\left(45 + \frac{\varphi}{2}\right) \tag{2.5b}$$

Regarding the earth pressure distribution, a simple triangular pressure distribution is assumed. (refer to Section 2.4.1.1, Figure 2.8).

c) Caquot and Kerisel theory (1948)

In 1948 Albert Caquot and Jean Kerisel introduced an advanced theory that adapted Muller-Breslau's equations to accommodate a non-planar rupture surface by employing a logarithmic spiral. This modification holds significant importance, particularly in scenarios involving passive earth pressure with soil-wall friction. Mayniel and Muller-Breslau's equations prove to be non-conservative in such situations. For active earth pressure, the logarithmic spiral rupture surface yields negligible differences compared to Muller-Breslau's approach. However, due to the complexity of these logarithmic equations, tables or computers are often utilized instead of manual calculations.

Caquot and Kerisel's log spiral theory finds broader applicability in cases where wall displacements are substantial enough to fully mobilize the shear strength of the backfill soil and where the properties of the backfill can be accurately estimated. These calculation methods for active earth pressure and passive earth pressure serve practical purposes. Coulomb method proves useful for irregular backfill configurations, while Rankine's theory and log spiral analysis are more suitable for regular configurations.

B) Displacement-Dependent Methods for Passive Earth Pressure Behind the Abutment:

Classical earth pressure theories assume that the soil mass experiences sufficient displacement for full mobilization of soil friction, leading to the earth pressure reaching its limiting active and passive values. While traditional theories are generally applicable for active earth pressure, where limit values can occur under minimal displacement, passive earth pressure may not always fully mobilize soil friction due to insufficient displacement of the soil mass behind the abutment. Consequently, the resulting passive earth pressure may not reach the expected limiting values. The determination of the resulting passive lateral pressure behind the abutments for a specific displacement cannot be simply derived from static calculations alone. Consequently, numerous experimental investigations were conducted by bridge engineers and geologists to establish empirical relationships between passive lateral pressure and the displacement of the abutment. Some of these will be listed in the following sections.

a) Modified Coefficients based on Rankine' theory (1857).

Some researchers argue that employing the full passive pressure without considering displacement is not conservative, as it reduces the flexural effects of dead and live loads on the bridge girders. Consequently, they have proposed modified coefficients based on Rankine's law. Broms and Ingelson (1971) suggested that horizontal earth pressures behind the abutment should increase linearly from zero at the abutment top to Rankine's passive horizontal earth pressure at two-thirds of abutment height, and then decrease linearly to Rankine's active earth pressure at the abutment base. Furthermore, Sandford and Elgaaly (1993) suggested that the horizontal earth pressure should decrease linearly from Rankine's passive earth pressure at two-thirds of the abutment height to the at-rest earth pressure at the abutment base. In addition, Burke, and Chen et al. (1993, 1997) modified the Rankine earth pressure theory for calculating the coefficient of passive earth pressure behind the abutment, by multiplying 2/3 on Rankine's passive coefficients. It recommended to be applied in most IABs with single span, or 2-3 small and medium spans. This simplified method is not widely used and has been found differences from others analyses (Hong, 2006).

b) Barker (1991) method.

Barker et al. (1991) indicated that the coefficient of horizontal earth pressure behind the abutment depended on the ratio of the abutment top displacement to the abutment height and the backfill relative density. In other words, the horizontal earth pressure coefficient is the same no matter whether the abutment top displacement is induced by abutment rotation or translation. The coefficient of earth pressure (K_B) proposed by Barker et al. (1991) had a linear relationship with the abutment displacement and is calculated by following Equation (2.6),

$$K_B = K_0 + \phi\Delta \leq K_p \tag{2.6}$$

Δ is the displacement of the abutment (m). ϕ is the variation of the passive earth pressure coefficient under a unit of displacement (m^{-1}) and is taken as 35 m^{-1} according to Barker et al.(1991), regarding the earth pressure distribution, a simple triangular pressure distribution is assumed. (refer to Section 2.4.1.1, Figure 2.8).

However, the experimental studies (Terzaghi, 1936; Rowe, 1954; Sherif et al., 1982; Fang et al., 1994) showed that the magnitude and the distribution of horizontal earth pressures behind the abutment depended on both the abutment deformation mode and magnitude and the horizontal earth pressures behind the abutment did not increase linearly along the whole abutment.

c) NCHRP Method (Clough and Duncan, 1991).

The National Cooperative Highway Research Program (NCHRP) categorizes the backfill soil behind abutments into three types: dense sandy soil, medium dense sandy soil, and loose sandy soil. Based on finite element analyses conducted by Clough and Duncan (1991), they developed a relationship curve to determine the earth pressure coefficient as a function of the displacement to abutment height ratio (Δ/H). This curve can be found in various style manuals, such as NCHRP Report No. 343, illustrated in Figure 2.9. Regarding the earth pressure distribution, a simple triangular pressure distribution is assumed. (refer to Section 2.4.1.1, Figure 2.8).

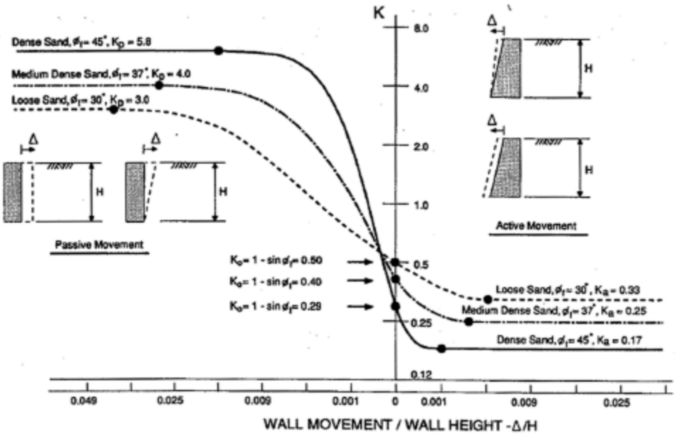

Figure 2.9. Relationship between wall displacement and earth pressure sand in NCHR (Clough and Duncan, 1991).

d) Arsoy (2004) method.

Arsoy (2004) introduced design charts for estimating the magnitude and position of the resultant passive earth pressure force for cohesionless backfill. These charts consider both medium dense and dense granular backfill materials and depend on the mode of abutment movement: translation or rotation. Figure 2.10 presents the response of displacement-dependent resultant forces (E_P) normalized by the resultant force at plastic equilibrium (E_{Pmax}) as a function of normalized wall displacement (Δ/H). The resultant force at plastic equilibrium, which represents the point where full passive forces are mobilized, can be computed using classical passive earth pressure theories such as Rankine (1857) or Coulomb (1776).

The application point of the resultant force can be estimated from Figure 2.11, by referring to the ratio indicated for the given wall displacement that depends on the mode of abutment movement.

Regarding the earth pressure distribution, for pure translation, it can be inferred from Figure 2.11 that the abutment (y/H) ratio is equal to 1/3, indicating that the resultant force acts at one-third of the abutment height from the base. Thus, the earth pressure distribution is assumed to be a simple triangular distribution (refer to Section 2.4.1.1, Figure 2.8).

However, for other modes of abutment movement, the earth pressure distribution behind the abutment is not available for this approach. Therefore, the resultant force could be modeled as a one-dimensional force applied at a determined point of application.

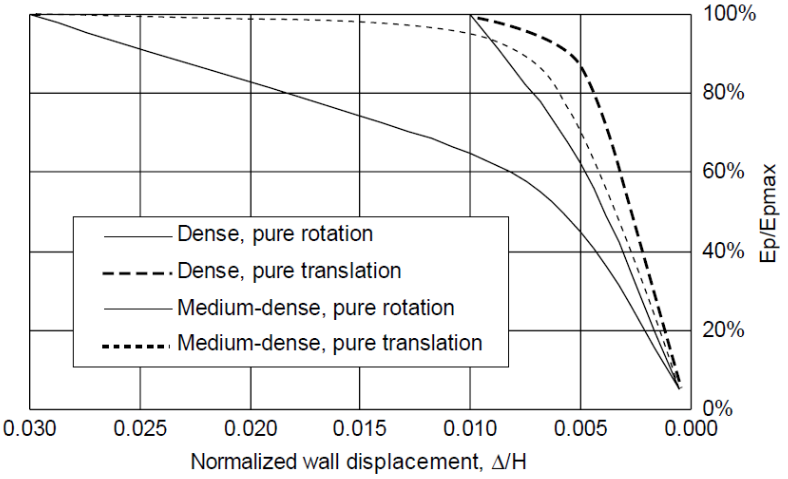

Figure 2.10. Magnitude of resultant passive earth pressure force (Arsoy, 2004).

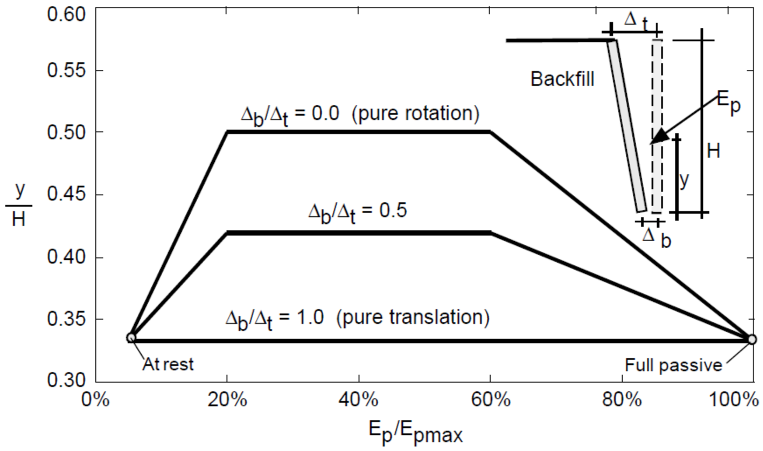

Figure 2.11. Position of resultant passive earth pressure force on IABs (Arsoy, 2004).

e) Sweden (Bro, 2002) method.

Swedish design standards (Bro 2002) propose Equation (2.7) to calculate the additional horizontal earth pressures behind the abutment induced by the abutment displacement toward the backfill. Equation (2.7) can be used to determine the additional horizontal earth pressures within the upper half-height of the abutment, with these pressures decreasing linearly from the mid-height to zero at the abutment base, as illustrated in Figure 2.12 (Flener, 2004; Vägverket, 2002).

$$\Delta P = C_S \gamma \frac{\Delta}{H} \left(\frac{\Delta}{H} \leq 0.005\right) \tag{2.7}$$

Cs is 300 or 600 depending on whether the forces are advantageous or not. γ represents the soil unit weight, Δ is the horizontal displacement of the abutment, and H is the abutment height. The earth pressure coefficients are provided in Table 2.1.

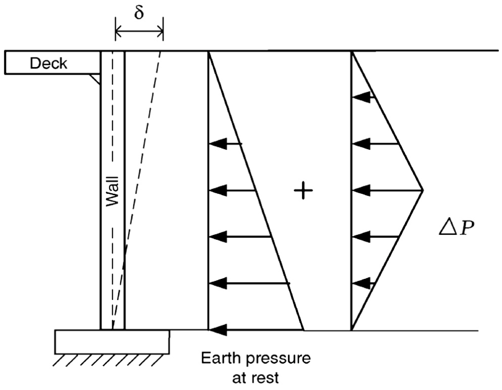

Figure 2.12. Design earth pressures according to Swedish bridge code (Bro, 2002).

Table 2.1. Lateral earth pressure coefficients of different materials (Bro, 2002).

Material	K_0	K_a	K_p
Crushed stone	0.34	0.17	5.83
Subbase material	0.36	0.22	4.60
Clinker	0.43	0.27	3.70
Plastic cell	0.40	0	-

f) Massachusetts method (2007).

Results from full-scale wall tests performed at the University of Massachusetts, shown there is reasonable agreement between the predicted average passive earth pressure response of standard compacted gravel borrow and the curves of earth pressure coefficient against the displacement to abutment height ratio (Δ/H) found in design manuals, that is displayed in Figure 2.13. When using compacted gravel borrow backfill the Massachusetts earth pressure coefficient (K_M) shall be estimated using Equation (2.8).

$$K_M = 0.43 + 5.7\left[1 - e^{-190\left(\frac{\Delta}{H}\right)}\right] \tag{2.8}$$

H is the height of the abutment, Δ is the displacement of the abutment. Regarding the earth pressure distribution, a simple triangular pressure distribution is assumed. (refer to Section 2.4.1.1, Figure 2.8).

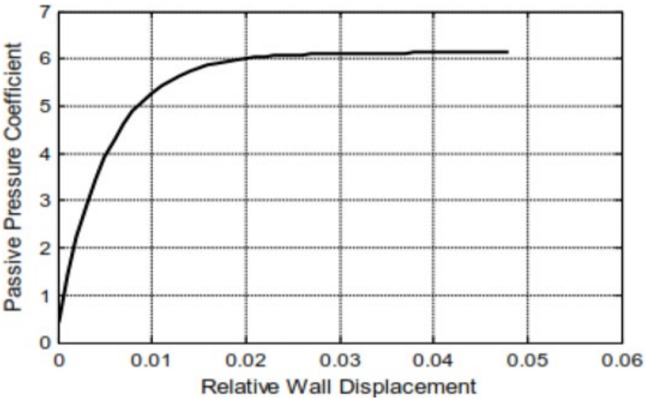

Figure 2.13. Earth pressure coefficient against the displacement to abutment height ratio (Δ/H) based on Massachusetts department of transportation (MassDOT, 2007).

g) England Method (2011).

The PD6694-1 (2011) uses a single equation for all abutments that accommodate thermal displacement by rotation and/or flexure that was originally derived from England et al (2000) but modified. The England earth pressure coefficient (K*) over the upper half of the abutment is given by Equation (2.9),

$$K^{*} = \mathrm{K_0} + \left(\frac{\mathrm{C_E}\ \grave{\Delta}}{\mathrm{H}}\right)^{0.6} \mathrm{K_p} \qquad (2.9)$$

H represents the height of the abutment, and Δ' denotes the displacement of the abutment at H/2 when the end of the deck displacement Δ. As depicted in Figure 2.14, the ratio Δ'/ Δ varies depending on the boundary conditions at the top and bottom of the abutment. It is also influenced by the stiffness of the abutment and the magnitude of the earth pressure applied to it. For instance, in the scenario of a stiff abutment hinged or fixed at both the top and bottom, Δ' is approximately 0.5 times Δ. Additionally, K_0 is the coefficient of at-rest earth pressure, while K_p is the coefficient of passive earth pressure determined using the design value of the triaxial effective stress. Additionally, the coefficient C_E, which depends on the elastic modulus of the subgrade Es in MPa, is determined by Equation (2.10), where C_E falls within the range of 20 to 66.

$$\mathrm{C_E} = 0.051\mathrm{E_S} + 14.9 \qquad (2.10)$$

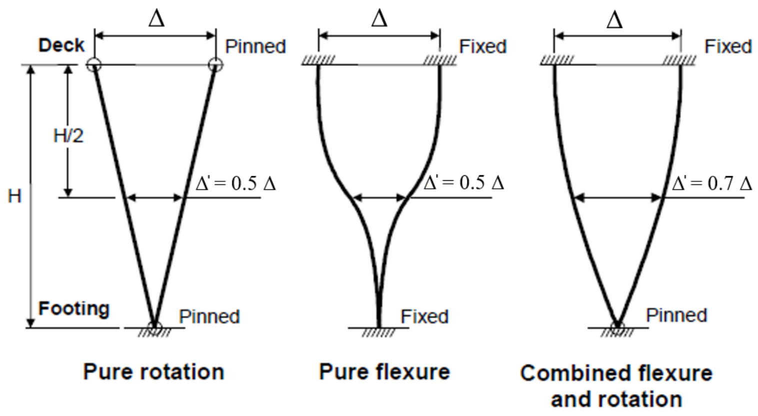

Figure 2.14. Comparison of various types of rotational and flexural abutment displacements and the associated values for the ratio Δ'/Δ (PD6694-1, 2011)

Figure 2.15 below shows the assumed pressure distribution given by PD6694-1 (2011) for a full height abutment on flexible foundations.

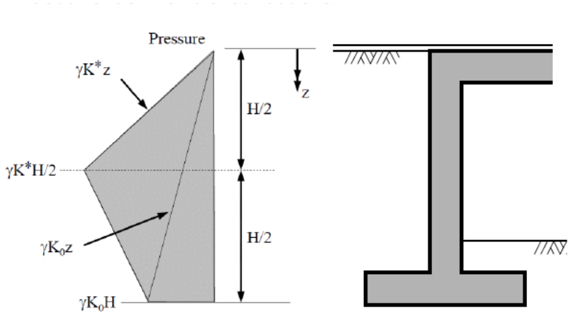

Figure 2.15. Assumed earth pressure distribution for full height abutments on flexible foundations (PD6694-1, 2011).

For shorter height bank pad abutments that accommodate thermal displacements through translation without rotation, PD6694-1 provides an Equation (2.11) for the earth pressure coefficient (K^*) as follows, regarding the earth pressure distribution, a simple triangular pressure distribution is assumed. (refer to Section 2.4.1.1, Figure 2.8).

$$K^* = K_0 + \left(\frac{d_d}{H}\right)^{0.4} K_p \qquad (2.11)$$

2.4.1.2. Overview of Variations in Passive Earth Pressure Calculation Methods in Literature

The following section provides an overview of variations in passive earth pressure calculation methods based on the limit equilibrium approach, along with an assessment of their accuracy and their impact on IAB behavior, as documented in the literature through field monitoring, experimental studies, and theoretical analyses. The existing literature reveals a noticeable gap in studies that specifically investigate the differences between various earth pressure methods, highlighting the need for further research in this area.

According to Huntley et al. (2013), their study was centered on field data obtained from pressure cells installed behind abutments of a 76 m long, two-span, pile-supported IAB over the monitoring period of three years. The primary focus of this study was to evaluate the suitability of common theoretical passive earth pressure coefficients. Overall, they concluded that none of the passive earth pressure coefficients included in this study (Rankine 1857, Coulomb 1776, Caquot and Kerisel 1948, Broms and Ingelson 1971, Modified Broms and Ingelson, England and Tsang, 2005) suitably predict the passive earth pressure behind the abutments. Table 2.2 presents the differences in the earth pressure coefficients calculated from various methods as presented in the study. Additionally, Figure 2.16 illustrates these values plotted and compared with the ratio of horizontal pressure to vertical pressure throughout the monitoring period for the abutment pressure cells.

Table 2.2. Theoretical passive earth pressure coefficients, K_P. (Huntley et al.,2013).

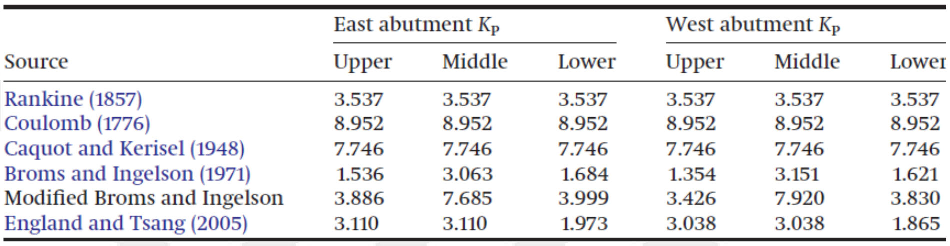

	East abutment K_P			West abutment K_P		
Source	Upper	Middle	Lower	Upper	Middle	Lower
Rankine (1857)	3.537	3.537	3.537	3.537	3.537	3.537
Coulomb (1776)	8.952	8.952	8.952	8.952	8.952	8.952
Caquot and Kerisel (1948)	7.746	7.746	7.746	7.746	7.746	7.746
Broms and Ingelson (1971)	1.536	3.063	1.684	1.354	3.151	1.621
Modified Broms and Ingelson	3.886	7.685	3.999	3.426	7.920	3.830
England and Tsang (2005)	3.110	3.110	1.973	3.038	3.038	1.865

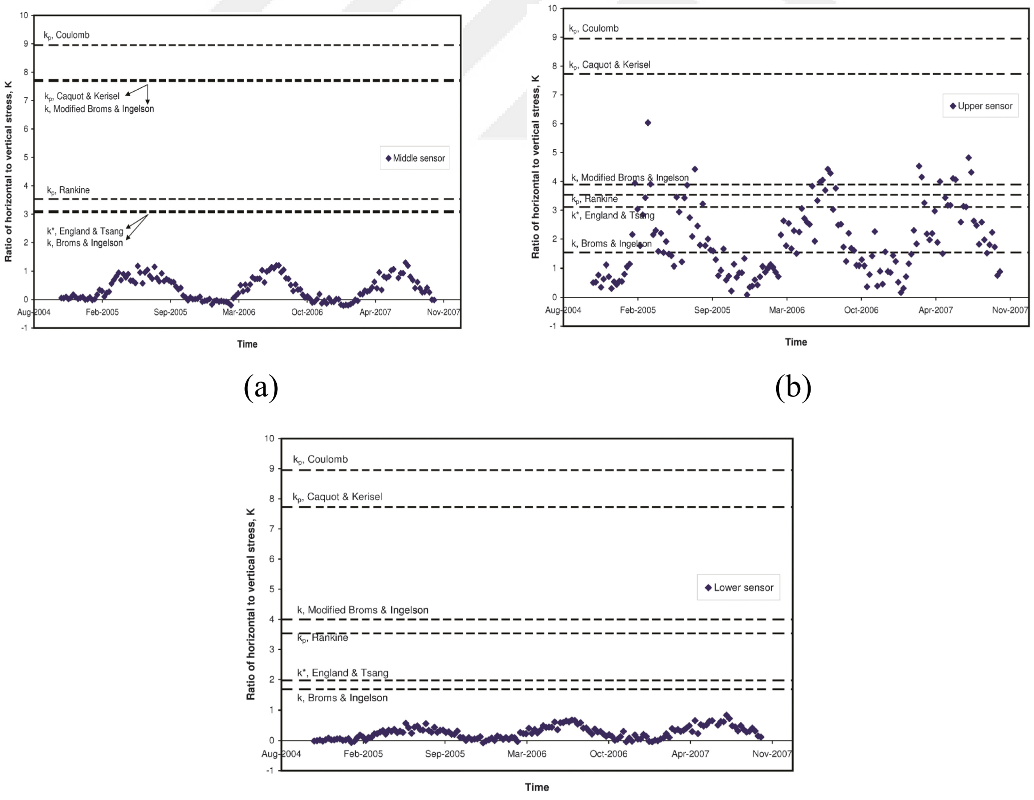

(a)

(b)

(c)

Figure 2.16. Ratio of horizontal to vertical stress (K) at: (a) middle, (b) upper, and (c) lower pressure cell locations on the bridge abutment (Huntley et al., 2013).

In the study conducted by Huang et al. (2020), they investigated the soil-abutment-pile interaction through a low-cycle pseudo-static test under horizontal displacement loads. They compared the passive earth pressure coefficient obtained from various methods proposed by Burke-Chen (1993,1997), England at al. (2000), Barker et al. (1991) and NCHRP (1991), Dicleli (2000), Massachusetts (2007), Rankine (1857), and Coulomb (1776), with the test results. Their findings revealed that the passive earth pressure coefficient obtained from the test was significantly larger than all of the calculated values, which they attributed to the ratcheting effect in the soil. They concluded that the existing calculation methods of earth pressure behind abutments were found to be inaccurate for predicting the earth pressure behind the abutment. Figure 2.17 shows the relationships between the relative displacement Δ/H (Δ is the displacement at the top of the abutment) and the passive earth pressure coefficient K_p.

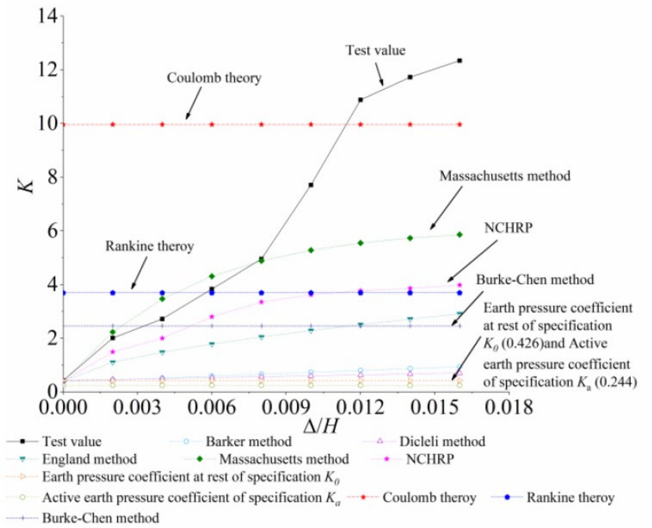

Figure 2.17. The relationships between the relative displacement Δ/H and the earth pressure coefficient (K) (Huang et al. (2020).

Liu et al. (2022) conducted a comparison of passive earth pressures behind an abutment for loose and dense backfills using methods that are independent of abutment displacement (Rankine 1857, Coulomb 1776, Broms and Ingelson 1971, and Sandford and Elgaaly, 1993)) and methods that take abutment displacement into account (MassDOT 2007, Bro 2004, UK Highways Agency, 2003), as illustrated in Figure 2.18. Their findings revealed that the methods proposed by Rankine (1857), Coulomb (1776), Broms and Ingelson (1971), and Sandford and Elgaaly (1993) are not appropriate, because these methods do not consider the factor of abutment displacement magnitude on the passive earth pressures behind the abutment. Additionally, the study showed that the predicted passive earth pressures, according to the MassDOT, (2007), significantly exceeded predictions made using design methods commonly adopted in Sweden (Bro, 2004) and the United Kingdom (UK Highways Agency, 2003).

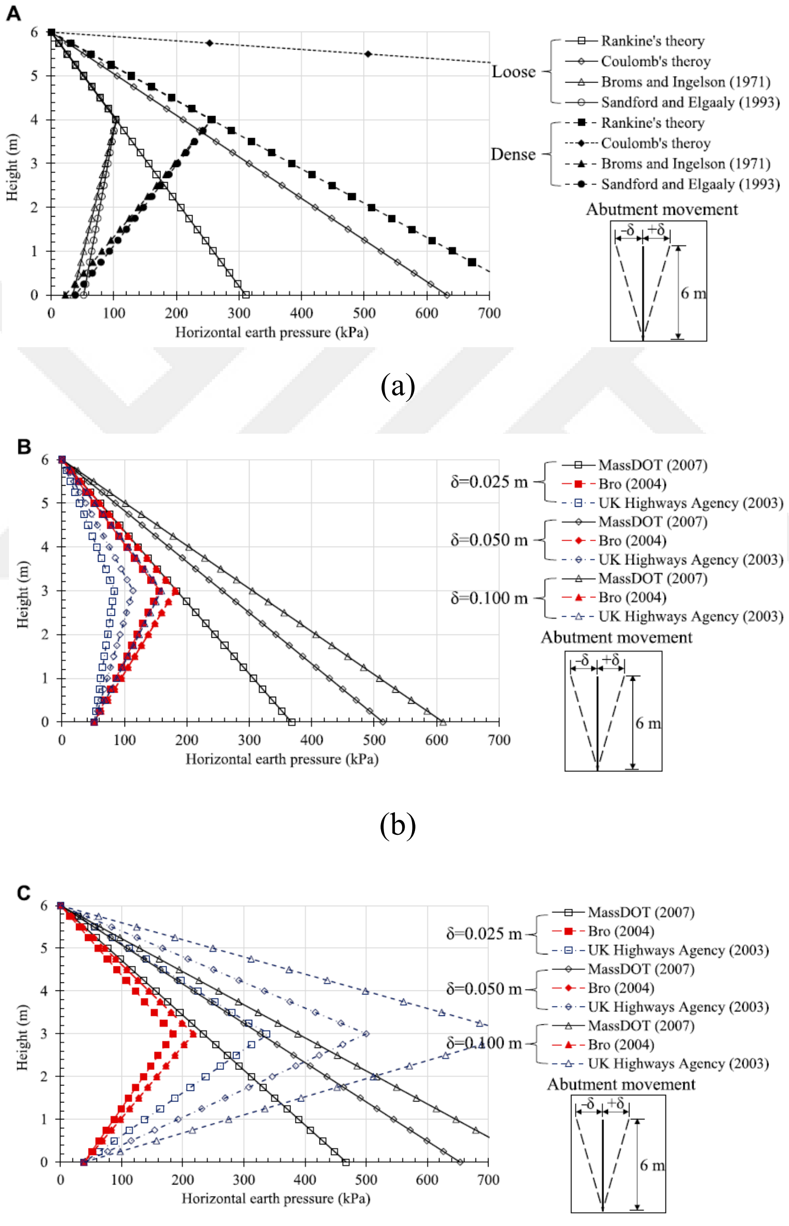

(a)

(b)

(c)

Figure 2.18. Earth pressures behind the abutment predicted based on methods: (a) displacement-independent for loose and dense backfills, (b) displacement-dependent for loose backfill, and (c) displacement-dependent for dense backfill (Liu et al., 2022).

Huang et al. (2022) conducted a quasi-static cyclic test on a scaled specimen to understand the behavior of backfill earth pressure and internal forces of the abutment and the pile during expansion and contraction of the bridge, considering the soil-structure interaction. They proposed a modified method for calculating the backfill earth pressure coefficient, which was examined for accuracy against test results and compared with existing methods proposed by Rankine (1857), Coulomb (1776), Burke-Chen (1993, 1997), Barker et al. (1991), England et al. (2000), Massachusetts (2020), NCHRP (1991), and the Design of Highway Bridges and Culverts (JTG D60-2015) code of China (K_R, K_C, K_{BC}, K_B, K_E, K_M, K_{NCHRP}, K_a, respectively, as noted in the study). They concluded that the existing calculation methods of earth pressure behind abutments were found to be inaccurate. Additionally, the study indicates that the calculation method of earth pressure behind the abutment has a significant influence on the bending moment of the pile. The internal forces of the pile calculated by the existing earth pressure theories were much different from the test results. Meanwhile, the internal forces of the pile calculated by the proposed method were more accurate. Figure 2.20 demonstrates a comparison of the pile bending moment calculated from test results and the calculated by the existing earth pressure methods, and Figure 2.19 compares the earth pressure coefficient behind the abutment obtained by the proposed method (K_{MN}), test results (K_{T-H}, K_{T-C}, K_{T-Z}), and existing earth pressure methods.

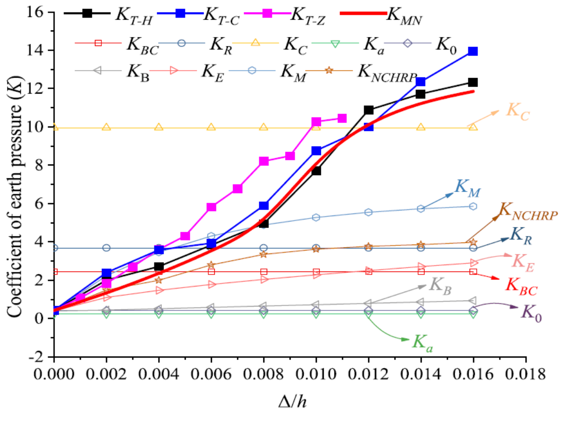

Figure 2.19. Comparison of the earth pressure coefficient calculated by the modified method and other methods (Huang et al., 2022).

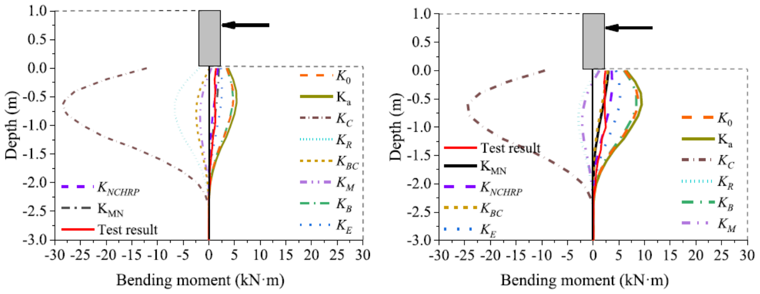

(a) Δ= +2*mm* (b) Δ= +4*mm*

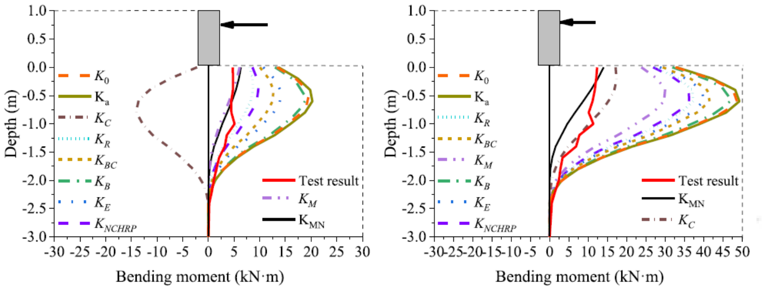

(c) Δ= +8*mm* (d) Δ= +16*mm*

Figure 2.20. Comparison of the pile bending moment under earth pressure calculated by the proposed method, test results, and existing methods. (Huang et al., 2022).

2.4.1.3. Subgrade Reaction Approach and Continuum Mechanics Approach

The distribution of soil reaction on the abutment is basically nonlinear, varying in depth, quantity, and type of abutment movement. Factors such as the relative flexural stiffness of the composite bridge deck and foundation piles, as well as the horizontal stiffness of the soil adjacent to the abutment and piles, can significantly influence the extent and nature of abutment movement. Consequently, this variation influences the magnitude and distribution of soil pressure behind the abutment. In cases where the stiffness of the soil and structural interaction significantly dictate the structural system's behavior, the conventional limiting equilibrium approach may not be suitable. In such instances, the soil–structure interaction can be represented using approaches like the subgrade reaction approach or the elastic continuum approach.

The subgrade reaction approach, rooted in the Winkler soil model (1867), treats the foundation as a beam resting on an elastic foundation. In this approach, the elastic medium is replaced by a series of infinitely closely spaced independent elastic springs. The model illustrating this soil idealization is depicted in Figure 2.21. Discrete nonlinear springs are commonly employed to simulate backfill–abutment interaction.

Various types of nonlinear force-deflection relations for these springs are widely utilized in finite element analysis.

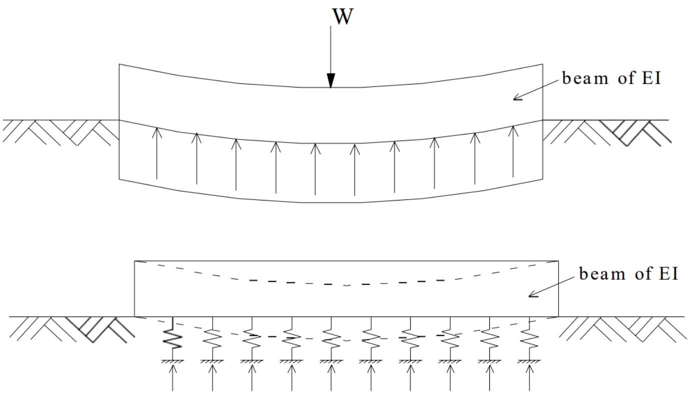

Figure 2.21. Winkler Spring Approach (1867).

2.4.2. Soil–Pile Interaction

The interaction between soil and pile under lateral displacement due to thermal loading is very complex, because of nonuniform distribution of stresses on the pile surface, where the stresses will have decreased on the backside of the pile and increased on the front, where some unit stresses contain both normal and shearing components as the displaced soil tries to move around the pile, as illustrated in Figure 2.22, so it is not acceptable to calculate the earth pressure around the pile surface by using traditional methods.

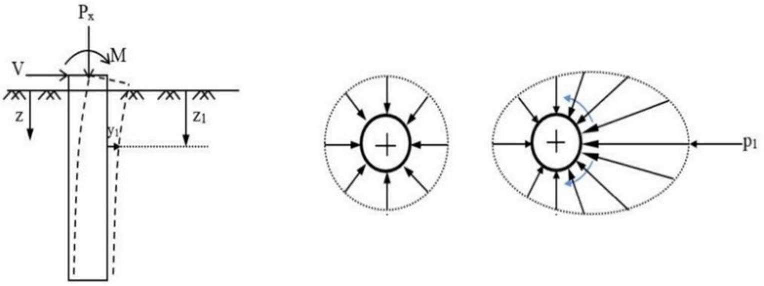

Figure 2.22. The interaction between a laterally loaded pile and the surrounding soil.

The formulation of the laterally loaded pile problem is based on either the subgrade reaction approach or the elastic continuum approach (Horvath, 1992). In addition to these methods, the equivalent cantilever approach is another useful method in pile design. These approaches will be briefly described in the following section.

2.4.2.1. Subgrade Reaction Approach

The subgrade reaction approach is based on the Winkler hypothesis (1867) and is the most widely used method in the subject area. With this approach, a laterally loaded pile is treated as a beam resting on an elastic subgrade. A series of closely spaced independent elastic springs replaces the subgrade. For vertical piles there can be made similar idealization and the predicted behavior of the laterally loaded piles according to Winkler's idealization is shown on Figure 2.23.

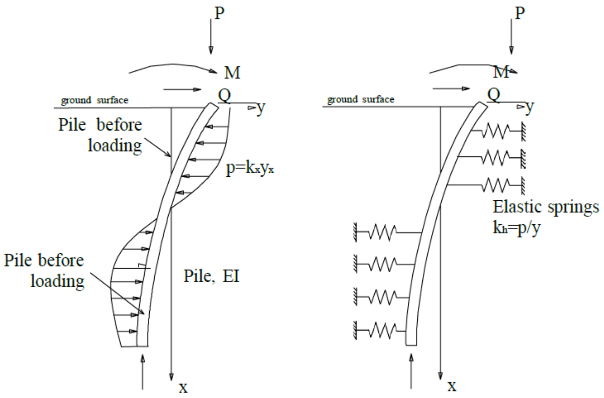

Figure 2.23. Laterally loaded pile in soil (on the left), laterally loaded pile on springs (right).

For design purposes, it is necessary to determine the soil stiffness, which is represented by the spring constants. The stiffness of these springs can be expressed using the modulus of horizontal subgrade reaction, as given in Equation (2.12).

$$k_h = \frac{p}{y} \tag{2.12}$$

p is the soil reaction at a point on the pile per unit of the length along the pile, and y is the pile deflection at this point. Various methods are available for deriving p-y curves. Some of these will be discussed in the following sections.

A) Curves Differential Equation

Prakash and Sharma (1990) provided the governing differential Equation (2.13),

$$EI_P \frac{d^4y}{dx^4} + P_x \frac{d^2y}{dx^2} + k_h y = 0 \tag{2.13}$$

EI_P represents the flexural stiffness of the pile, y is the lateral deflection, x denotes the length along the pile, P_x signifies the axial load, and k_h represents the spring constant used to represent the soil.

The solution of the above differential equation is obtained by appropriately representing the soil with a spring constant and considering the proper boundary conditions. Solutions can be obtained either in closed form (exact) or using approximate methods. While closed-form solutions are preferred, they can be time-consuming and limited in their applicability. In practice, approximate solutions are more commonly used as they often provide satisfactory results. These approximate methods include series expansion method, finite difference method, finite element method, and other approaches based on some or all of the above techniques.

B) Empirical p-y Curves

The essential of this method is to introduce a series of p-y curves to represent the true behavior of soils by considering the non-linearity of the soil modulus. The main purpose of the method is to obtain a representative value of the spring constant used to represent the soil (k_h) for the desired depth and lateral deflection values (y). This is accomplished through an iterative process by assuming a deflection (y) and calculating the value of the spring constant used to represent the soil (k_h). The iterations are continued until the assumed and calculated deflections are the same within a tolerance limit. When representative p-y curves are used, the method is capable of reflecting the real deflection behavior of the pile and the moment distribution along the pile. The challenge is to obtain a representative set of p-y curves for each site.

The concept of empirical p-y curves was first developed by Mclelland and Focht in 1956. Matlock proposed a well-known family of p-y curves (Matlock, 1970), illustrated in Figure 2.24, which was based on extensive research on laterally loaded piles in soft clay. This research included field testing with instrumented piles, experiments with laboratory models, and the development of analytical methods and correlations.

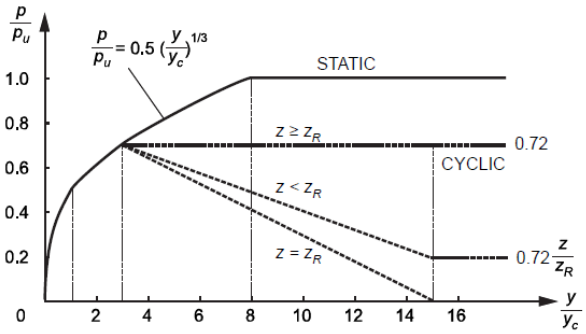

Figure 2.24. Family of p-y curves for laterally loaded piles in soft clay by Matlock (1970).

Reese et al. (1975) developed a family of p-y curves for sand, based on experimental field testing of piles installed at a site where the soils consisted of clean fine sand to silty fine sand, and they also developed a family of p-y curves for piles in stiff clay in 1974, as illustrated in Figure 2.25. Additionally, Sullivan et al. (1979) and Hong (2006) introduced a unified curve for both soft and stiff clays, illustrated in Figures (2.26).

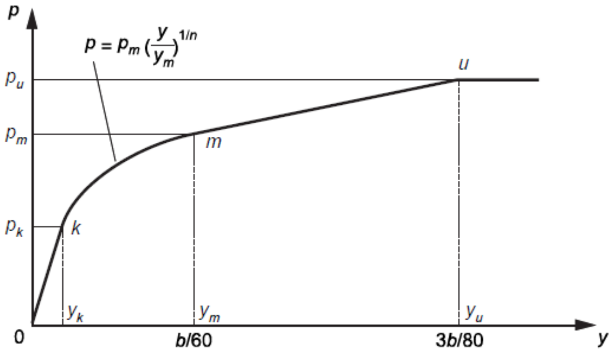

Figure 2.25. Family of p-y curves for piles in stiff clay by Reese (1974).

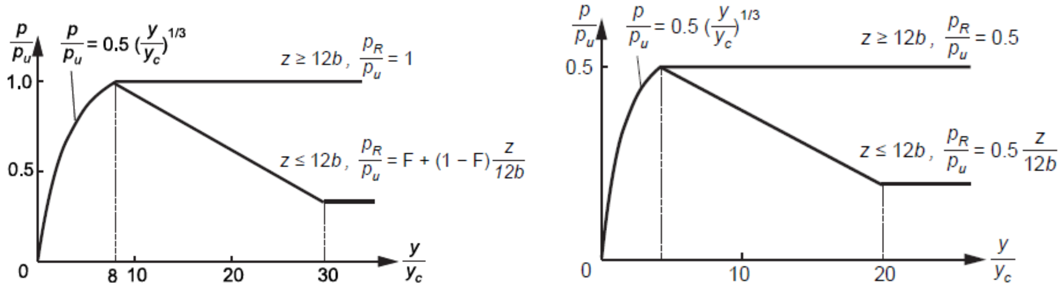

(a) (b)

Figure 2.26. Family of p-y curves for piles in clay, (a) static loading, (b) cyclic loading (Sullivan et al. (1979) and Hong (2006)).

C) Elasto-Plasticity Models for p-y Curves

To account for nonlinear behavior, a simplified elastic and perfectly plastic model can be assumed. For this design method, only the ultimate resistance and initial stiffness of the soil springs are needed (Greimann et al., 1987). Additionally, researchers have developed the modified Ramberg-Osgood model to accommodate loading and unloading of the pile during cyclic loading. This model is used to approximate the p-y soil resistance and displacement curves for use in finite element solutions (Greimann et al., 1984, Greimann et al., 1987). For example, the model for p-y curves could be expressed as illustrated in Figure 2.27.

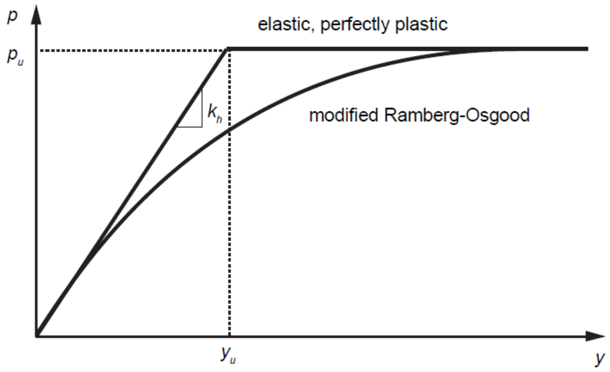

Figure 2.27. Elasto-plasticity models for p-y curves.

2.4.2.2. Continuum Mechanics Approach

As an alternative to the Winkler spring approach, the continuum mechanics approach is generally viewed as being more rational yet versatile. This approach is usually based on finite-element or finite-difference numerical formulations. The finite-element method requires discretization of the pile and surrounding soil. The differential equations that quantify the behavior of the pile and soil are solved by minimizing the potential energy within the system. The finite element method can capture the most important features of complex pile-soil interactions, but it is rarely used in the design of laterally loaded bridge structures owing to the high computation time required (Gerolymos et al. 2009).

2.4.2.3. Equivalent Cantilever Approach

The equivalent cantilever method is proposed for designing piles of IABs by Greimann and Wolde-Tinsea (1988) and Abendroth, Greimann and Ebner (1989). This method appears to be widely accepted by bridge engineers. The method is based on analytical and finite element studies. An equivalent cantilever column is used to replace the actual pile. In other words, the soil-pile system is reduced down to an equivalent cantilever column. Two alternatives are provided, one involving elastic behavior, and the other involving inelastic behavior of the piles. Finite element simulations indicated that both alternatives were conservative. Both alternatives are concerned with the vertical load carrying capacity of piles under lateral displacements induced by temperature changes. A worked-out example on the design of an integral abutment using the equivalent cantilever method is given by Barker et al. (1990). Girton et al. (1991) who evaluated this method experimentally, concluded that the equivalent cantilever column model is sufficiently accurate for design purposes. The method does not consider the effects of the backfill-abutment interactions and the effects of the induced stresses in the superstructure.

2.5. Thermal Induced Displacements in IABs

Changes in temperature cause materials to undergo length variations, a fundamental property leading to the expansion and contraction of bridge superstructures. As temperatures rise, bridges expand, while cooling induces contraction. Conventional bridges include expansion joints between the superstructure and abutments to accommodate these thermal displacements. However, IABs eliminate these joints, causing the superstructure to displace the bridge abutments. This displacement imposes lateral loading and unloading forces on the pile and backfill. In bridge design specifications, thermal displacement is often determined using Equation (2.14), proposed by Boley and Weiner in 1960.

$$\Delta = \alpha \ L_b \, \Delta T(\pm) \tag{2.14}$$

Δ is the bridge deformation whether expansion or contraction (m), α is the coefficient of thermal expansion (1/C°), L_b is the length of bridge segment from neutral point (usually center of bridge) to abutment (m), and ΔT (±) is the change in temperature of the superstructure.

The magnitude of thermal displacement is influenced by the coefficient of thermal expansion, which is a material-specific property of the superstructure. It is also affected by the length of the bridge superstructure and the maximum temperature fluctuations experienced by the bridge superstructure.

2.5.1. Bridge Temperature

Bridge temperatures and subsequent thermal displacements in a specific location undergo continuous fluctuations due to the intricate and cyclic nature of climatic events and meteorological conditions. The primary factors influencing structural temperatures could be summarized as follows, diurnal temperature variations, solar fluctuations, wind speed, precipitation, and the thermal properties as well as the geometry of the structures. Figure 2.28 illustrates the environmental effects influencing bridge temperatures.

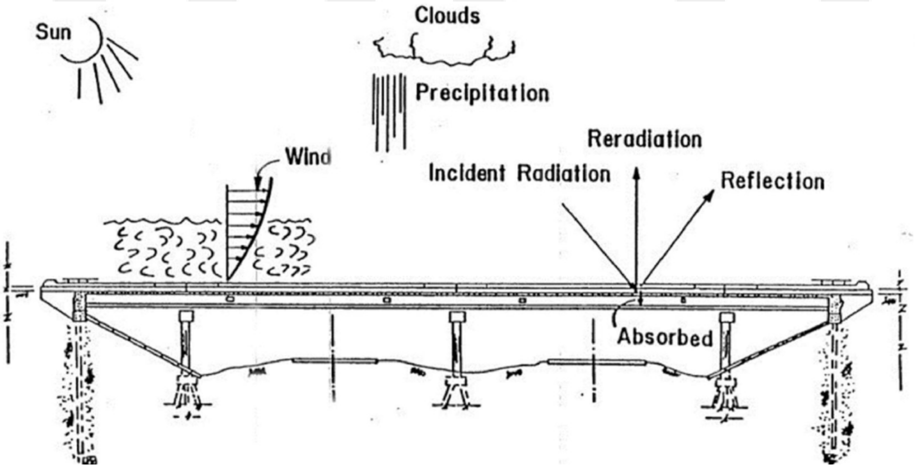

Figure 2.28. Environmental effects affecting bridge temperatures (England, 2000).

Diurnal temperature variation plays an important role in determining the temperature of a bridge. Meteorological institutions worldwide employ a standardized method to measure air temperature known as shade air temperature. This method is specifically designed to mitigate the effect of wind and other weather conditions, ensuring more accurate temperature readings for analysis. Notably, shade air temperature emerges as the most significant factor affecting bridge temperatures.

Solar radiation levels vary between sunny and cloudy days and are measured globally at solar stations. Generally, higher solar radiation corresponds to elevated structure temperatures, while lower solar radiation leads to reduced structure temperatures. Solar stations employ various methods: some directly measure solar radiation, while others gather relevant meteorological data to indirectly estimate solar radiation levels.

Wind speed, a recorded metric by meteorological institutions, influences the temperature at a given locality. It plays a crucial role in dissipating heat from the structure. Generally, higher wind speed results in lower structure temperatures.

Precipitation holds importance due to its effect on the heat transfer between a structure and the precipitating moisture. Evaporation during precipitation reduces heat stored in the superstructure, contributing to lower temperatures. In general, precipitation tends to decrease structure temperatures.

Additionally, the thermal properties of a bridge superstructure significantly affect heat transfer within it. Steel structures, characterized by thin plate elements, conduct heat more rapidly than concrete structures, which typically feature heavier construction. This difference in thermal properties affects how heat is transferred within the superstructure. (Arsoy, 2008).

2.5.2. Shade Air Temperature Variation

For a bridge, predicting the variation in shade air temperature involves estimating future events based on historical data. Meteorological stations measure shade air temperatures consistently and compile this information into databases. To determine the expected maximum and minimum temperatures for a specific location, statistical analysis of past data is crucial, typically spanning a considerable period, such as 40 years. This analysis includes assessing record highs and lows, mean high and low temperatures, average high and low values, as well as mean average temperatures. For instance, Figure 2.29 illustrates the mean high, mean low, and average mean values of shade air temperatures recorded between 1948 and 1998 in Charlottesville, Virginia, as outlined by Arsoy (2008). This historical data visualization aids in understanding the temperature variations over the specified period, facilitating future temperature estimations for the region.

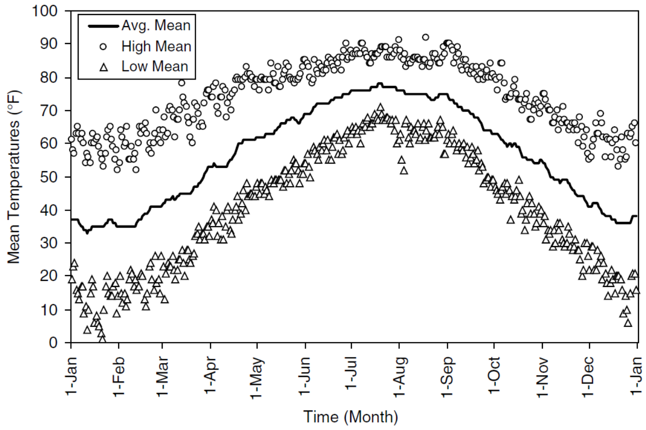

Figure 2.29. Temperature variation patterns in Charlottesville, Virginia, between 1948 and 1998. (Arsoy, 2008).

According to the Eurocode (European Committee for Standardization – (CEN, 2003a)), it is recommended to obtain characteristic values for the minimum and maximum shade air temperatures (T_{maxp} and T_{minp}) for a specific site location from national isotherm maps. Here, T_{maxp} and T_{minp} represent the maximum and minimum shade air temperatures with an annual probability of being exceeded p (equivalent to a mean return period of 1/p).

These values should represent the shade air temperatures at mean sea level in open country environments, with an annual probability of being exceeded set at 0.02. In scenarios where the annual probability of exceeding these temperatures differs from 0.02, adjustments are necessary, considering factors like elevation above sea level and local conditions, such as frost pockets.

In such scenarios, determining the new values for the maximum or minimum shade air temperatures (T_{maxp} or T_{minp}) depends on the ratio of $T_{maxp}/\dot{T}_{max}$ or $T_{minp}/\dot{T}_{min}$, Here, $\dot{T}_{max}$ ($\dot{T}_{min}$) is the value of the maximum (minimum) shade air temperature with an annual probability of being exceeded of 0.02. This can be referenced from Figure A.1 within the Eurocode (EN 1991-1-5: 2003), as illustrated in Figure 2.30.

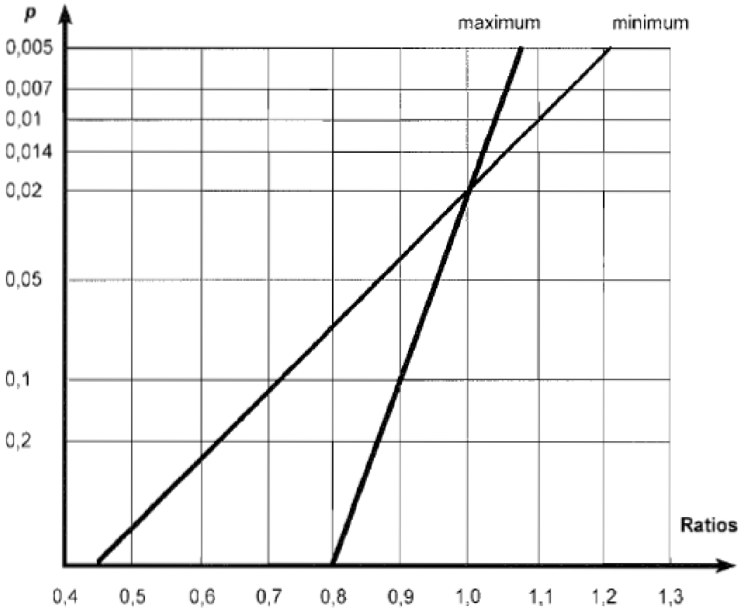

Figure 2.30. Ratios maximum and minimum shade air temperature (EN 1991-1-5: 2003).

2.5.3. Effective Bridge Temperature

The displacements of bridge girders primarily occur due to fluctuations in environmental temperature and solar radiation, which continuously change. Variations in the thermal properties and distinct thermal inertias of bridge materials cause different types of bridges to respond differently to these environmental changes. Moreover, the temperature distribution within a structure is generally non-uniform. Consequently, predicting longitudinal displacements of bridge girders solely from surrounding shade temperatures is challenging. Considerable theoretical and practical research, as conducted by Emerson (1973, 1976, 1977), aimed to determine a representative bridge temperature for making design calculations. A parameter known as the effective bridge temperature (EBT) has been defined for this purpose. EBT values fluctuate throughout the year, showing maximum and minimum daily changes as well as seasonal variations for both composite and concrete decks, as illustrated in Figure 2.31. (England, 2000).

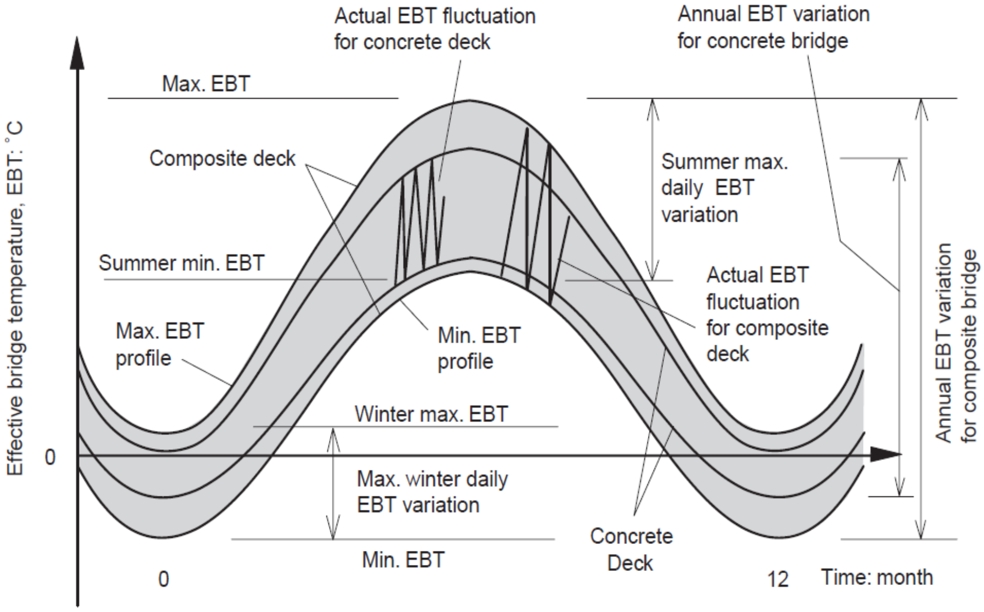

Figure 2.31. Daily and seasonal EBT variations for both composite and concrete decks (England, 2000).

The recommendations for EBT primarily follow a deterministic approach, although some methodologies incorporate a probabilistic perspective. In the deterministic approach, the maximum and minimum anticipated values of EBT for both concrete and steel bridges are determined based on historical data, accumulated experience, and engineering expertise. However, it is worth noting that the probabilistic approach, which incorporates statistical probabilities and uncertainty analysis, is not widely adopted in practice. (Arsoy, 2008).

As previously discussed, differences in the thermal properties and thermal inertia of bridge superstructure materials are influential factors contributing to variations in the EBT observed among different types of bridge.

According to research conducted by England in 2000, the EBTs associated with three different bridge deck types—specifically steel decks, concrete decks, and composite decks (comprising steel beams with a concrete slab)—across four different geographical locations in the UK, are presented in a Table 2.3.

Table 2.3. EBTs variations associated with three different bridge deck types (England, 2000).

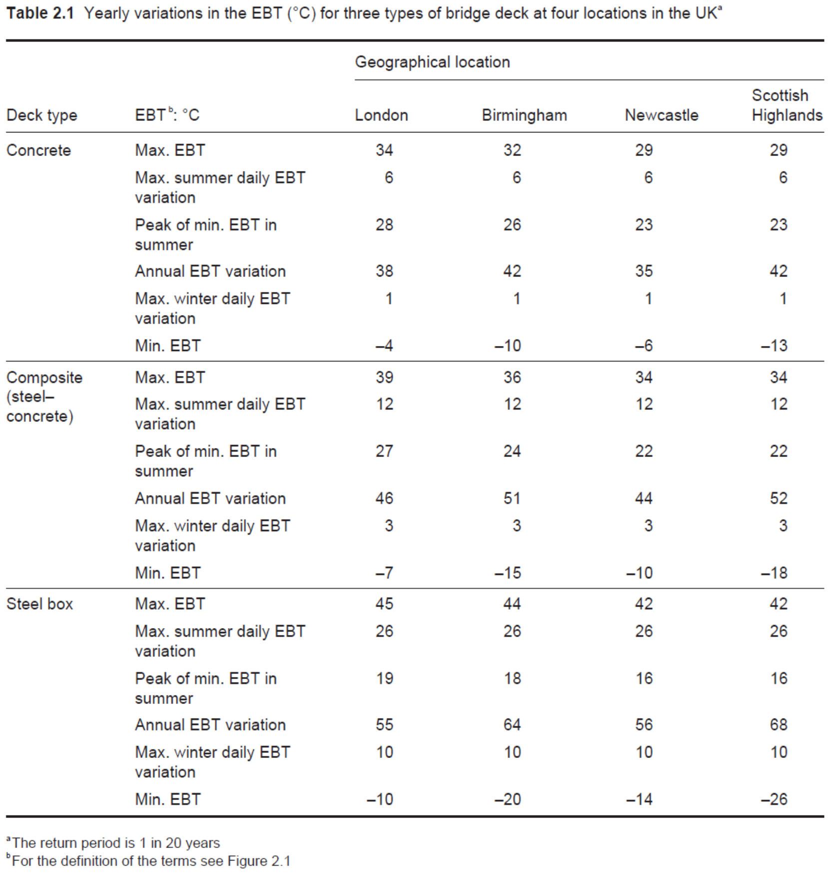

Table 2.1 Yearly variations in the EBT (°C) for three types of bridge deck at four locations in the UK[a]

Deck type	EBT[b]: °C	Geographical location: London	Birmingham	Newcastle	Scottish Highlands
Concrete	Max. EBT	34	32	29	29
	Max. summer daily EBT variation	6	6	6	6
	Peak of min. EBT in summer	28	26	23	23
	Annual EBT variation	38	42	35	42
	Max. winter daily EBT variation	1	1	1	1
	Min. EBT	−4	−10	−6	−13
Composite (steel–concrete)	Max. EBT	39	36	34	34
	Max. summer daily EBT variation	12	12	12	12
	Peak of min. EBT in summer	27	24	22	22
	Annual EBT variation	46	51	44	52
	Max. winter daily EBT variation	3	3	3	3
	Min. EBT	−7	−15	−10	−18
Steel box	Max. EBT	45	44	42	42
	Max. summer daily EBT variation	26	26	26	26
	Peak of min. EBT in summer	19	18	16	16
	Annual EBT variation	55	64	56	68
	Max. winter daily EBT variation	10	10	10	10
	Min. EBT	−10	−20	−14	−26

[a] The return period is 1 in 20 years

[b] For the definition of the terms see Figure 2.1

In addition, as per the research conducted by the Transport and Road Research Laboratory (Emerson, 1973, 1977), it was found that the EBT of a concrete bridge deck correlates strongly with the average environmental temperature observed over the preceding 2 days. In contrast, the EBT of a composite deck is notably associated with the average environmental temperature recorded over the previous 8 hours only.

As per the Eurocode classification (CEN, 2003a), the EBT is defined as a uniform temperature that includes both the minimum ($T_{e.min}$) and maximum ($T_{e.max}$) components for different bridge deck types. Specifically, the classification categorizes steel decks as Type 1, composite decks as Type 2, and concrete decks as Type 3. The recommended values for the EBT pertaining to each bridge deck type should be adjusted based on the site-specific shade air temperatures, both minimum (T_{min}) and maximum (T_{max}), as illustrated in the referenced Figure 2.32. These specific temperatures for the site are derived from isotherm maps.

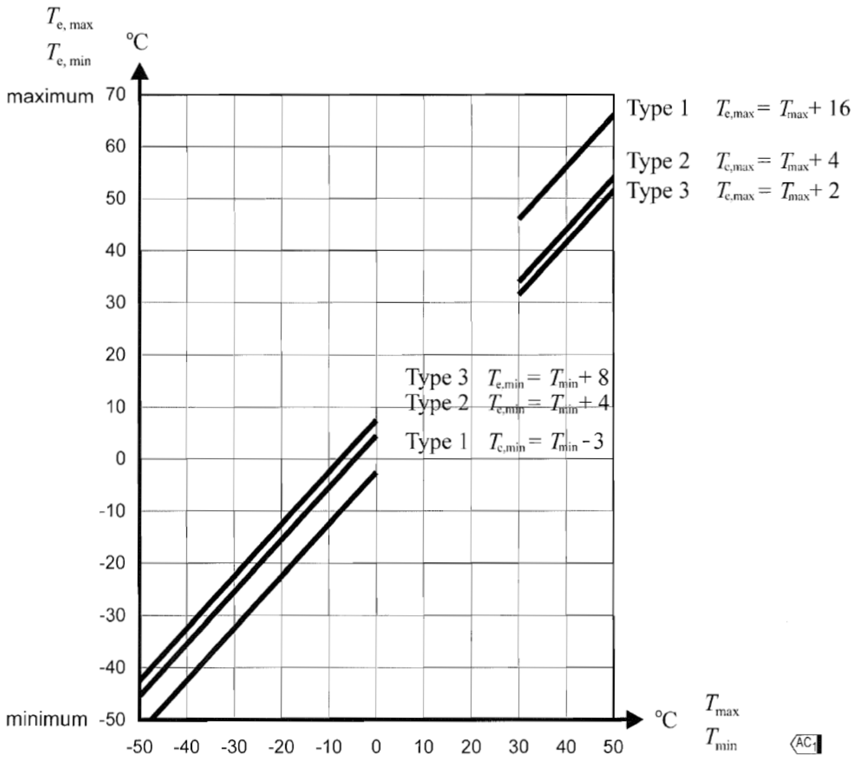

Figure 2.32. Correlation between minimum/maximum shade air temperature (T_{min}/T_{max}) and minimum/maximum uniform bridge temperature component ($T_{e.min}/T_{e.max}$) (EN 1991-1-5: 2003).

2.6. Temperature Variations in IABs

Two temperature-related phenomena contribute to structural forces: firstly, a uniform temperature range affecting the entire structure, and secondly, temperature gradients within the girder (Newmark et al., 1948). Variations in the average EBT (uniform temperature) result in dimensional changes within the bridge. The maximum permissible length for an IAB is determined by considering the thermal displacement of the superstructure of the bridge. The magnitude of these thermal displacements, as described in Equation (2.14), is a function of the level and values of thermal variation (Abendroth and Greimann, 2005). Additionally, non-uniform temperature distributions throughout the depth of a bridge superstructure, causing temperature gradients, may induce vertical plane curvature in the bridge. Subsequent sections aim to provide thorough academic descriptions and comparisons of uniform temperature ranges and vertical temperature gradients, drawing from various bridge design specifications.

2.6.1. Uniform Temperature Ranges

Bridge design specifications state that provisions must account for stresses or displacements arising from temperature variations. The fluctuations in temperature must be determined for the specific locality where the structure is erected and computed based on an assumed temperature at the construction time. The temperature variations are determined by the following Equations (2.15a) and (2.15b),

$$\Delta T\,(+) \;=\; T_{e.max} - T_{Const} \tag{2.15a}$$

$$\Delta T\,(-) \;=\; T_{Const} - T_{e.min} \tag{2.15b}$$

T_{Const} represents the construction temperature, while $T_{e.min}$ and $T_{e.max}$ denote the maximum and minimum extreme EBTs expected during the lifespan of the bridge, respectively. These two temperature differences are required as both expansion and contraction displacements occur within bridge girders. The following section will discuss the consideration of uniform temperature ranges according to different bridge design specifications in United States, Canada, and Europe.

In United States, American Association of State Highway Transportation Officials (AASHTO) advise a temperature range that define the change in temperature for the bridge superstructure, which based on climate conditions and the materials used in the superstructure. At times, bridge design specifications provide the temperature variation ($\Delta T\pm$) for a structure. Other times, these specifications provide a range from the maximum (T_{max}) to the minimum (T_{min}) temperatures. In such cases, the change in temperature ($\Delta T\pm$) is determined as the average value between the minimum and maximum design temperatures ($\Delta T\pm = \pm (T_{max} + T_{min})/2$). The tables below outline the temperature ranges specified by AASHTO for different years (1996, 1999, 2004, 2010, 2012, 2015). Table 2.4 details the ranges for steel IABs, while Table 2.5 covers those for concrete IABs.

Table 2.4. Temperature ranges according to AASHTO for steel IABs.

Bridge design specifications	Temperature Ranges for Steel Bridge °C (°F)	
AASHTO (1996)	Moderate climate	Cold climate
	Tmin -18°C (0°F) to Tmax 49°C (120°F)	Tmin -34°C (-30°F) to Tmax 49°C (120°F)
Massachusetts Highway Department Bridge Manual (1999)	ΔT (+) +40°C (+72°F) ΔT (-) -55°C (-99°F)	
Many states in the northern region of the United States, AASHTO (2010)	Tmin -34.4°C (-30°F) to Tmax 48.9°C (120°F)	
AASHTO, Procedure B (2012)	Temperature range 69.4°C (125°F), ΔT (±) ±34.7°C (± 62.5°F)	
AASHTO (2015)	Temperature range 66°C (120°F), ΔT (±) ± 33°C (± 60°F)	

Table 2.5. Temperature ranges according to AASHTO for concrete IABs.

Bridge design specifications	Temperature Ranges for Concrete Bridge °C (°F)	
AASHTO (1996)	Moderate climate	Cold climate
	ΔT (+) +16.7°C (+30°F) and ΔT (-) -22.2°C (-40°F)	ΔT (+) +35°F (+19.4°C) and ΔT (-)-25°C (-45°F)
AASHTO LRFD (2004)	Tmin -12°C (10°F) to Tmax 27°C (80°F)	Tmin -18°C (0°F) to Tmax 27°C (80°F)
AASHTO LRFD (2010), California	Tmin -1.1°C (30°F) to Tmax 46.1°C (115°F)	
AASHTO LRFD (2010), Pennsylvania	Tmin -12.2°C (10°F) to Tmax 26.7°C (80°F)	

The literature lacks studies validating bridge design specifications for temperature ranges. However, some studies in the section focus on validating AASHTO temperature ranges through field monitoring of IABs. In a study conducted by Girton et al. (1991), field testing was undertaken on two IABs in Iowa, aiming to monitor air and bridge temperatures along with other parameters. Their findings revealed that the temperature range specified by AASHTO was notably smaller than the measured values. Additionally, investigators at the University of Minnesota (Huang, 2004) examined the behavior of a prestressed concrete IAB in Rochester, Minnesota. Over the period from 1996 to 2004, these researchers monitored the behavior of the bridge along with weather conditions. Their observations indicated that the measured temperature range of 131°F exceeded the 80°F range specified by AASHTO. However, In the study by

Kim and Laman (2012) conducted through seven years of field monitoring on four IABs in central Pennsylvania, they concluded that the design temperature ranges recommended by AASHTO LRFD (2010) for concrete were conservative when compared to the measurements obtained in their study.

In Canada, the Canadian Highway Bridge Design Code (CHBDC) specifies different temperature variations to be considered for different types of bridges. The minimum average temperatures used for steel and concrete bridges are regarded as 10°C (18°F) and 5°C (9°F), respectively, below the minimum daily mean temperature. Conversely, the maximum average temperatures for steel and concrete are considered as 20°C (36°F) and 10°C (18°F) above the maximum daily mean temperature, respectively. The maximum and minimum daily mean temperatures are extracted from the provided maps in CHBDC. Table 2.6 illustrates the maximum and minimum temperature design for four major cities in Canada, adapted from CHBDC.

Table 2.6. Maximum and minimum effective temperature for big cities in Canada.

City	Minimum Temperature °C (°F)		Maximum Temperature °C (°F)	
	Steel Girder	Concrete Girder	Steel Girder	Concrete Girder
Toronto	-33°C (-27°F)	-23°C (-9°F)	50°C (122°F)	40°C (104°F)
Vancouver	-19°C (-2°F)	-14°C (7°F)	44°C (111°F)	34°C (93°F)
Ottawa	-39°C (-38°F)	-24°C (-11°F)	51°C (122°F)	41°C (106°F)
Montreal	-39°C (-38°F)	-24°C (-11°F)	50°C (122°F)	40°C (104°F)

In Europe, according to the Eurocode (CEN, 2003a), guidelines for temperature variation in bridges include defining uniform temperature components for both expansion ($\Delta T_{N,exp}$) and contraction ($\Delta T_{N,con}$), determined using the equations previously discussed as (2.15a) and (2.15b), respectively.

The following Equation (2.16) could determine the overall range of the uniform bridge temperature component,

$$\Delta T_N = T_{e.max} - T_{e.min} \tag{2.16}$$

$T_{e.max}$ and $T_{e.min}$ denote the maximum and minimum extreme EBTs expected during the lifespan of the bridge, respectively.

2.6.2. Vertical Temperature Gradient

Besides the uniform temperature affecting the entire structure, IABs encounter temperature gradients across the depth of their superstructure. The upper sections of the superstructure and exterior beams experience temperature fluctuations based on factors such as solar radiation, wind exposure, and the type and volume of precipitation. Conversely, the lower elements of the superstructure typically maintain a similar temperature to the surrounding air. Consequently, during sunlight exposure, the top of the deck slab tends to have a higher temperature than the superstructure's underside. This difference can lead to the top cooling faster than the girders when exposed to rain or snow. Such vertical-temperature gradients within an IAB have the potential to induce bending stresses in the bridge components and cause abutment rotations in a vertical plane parallel to the length of the bridge. The following section will discuss the consideration of vertical temperature gradient according to different bridge design specifications in United States, Canada, and Europe.

In the United States, AASHTO LRFD (2004) recommends a positive temperature gradient throughout the depth of the concrete deck slab and girder. This gradient is based on a model proposed in NCHRP Report 276, which originates from earlier work by Potgieter and Gamble (1983). The standard temperature gradient can be referenced from Figure 3.12.3-2 in the AASHTO LRFD (2004), as illustrated in the following Figure 2.33.

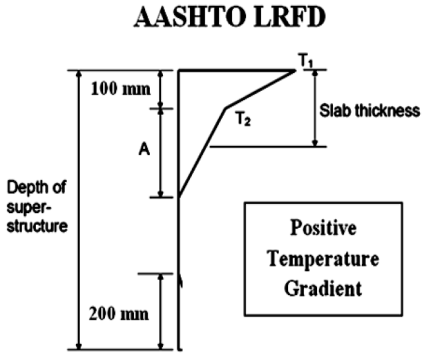

Figure 2.33. Code vertical temperature gradients according to AASHTO LRFD (2004).

In Canada, CHBDC (2006) recommends a positive linear temperature differential of ±15°C (±27°F) specifically through the concrete deck slab, without accounting for the girder. It is assumed that the temperature remains constant within the girder below the slab. Additionally, CHBDC (2006) does not consider negative temperature gradients. The CHBDC (2006) standard temperature gradient through the girder is illustrated in Figure 2.34.

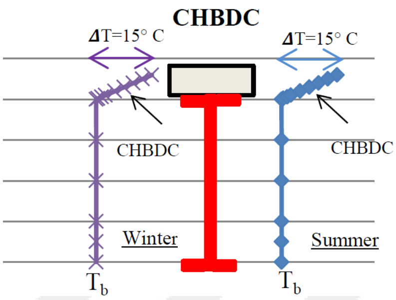

Figure 2.34. Code vertical temperature gradients according to CHBDC (2006).

In Europe, as per Eurocode (CEN, 2003a), addressing the effect of the vertical temperature gradient involves considering both linear and non-linear temperature difference components. The linear temperature difference component, referred to as $\Delta T_{M,heat}$ and $\Delta T_{M,cool}$, is applied between the top and bottom of the bridge deck. Figure 2.35. provides upper bound values of the linearly varying temperature difference component for representative bridge geometries.

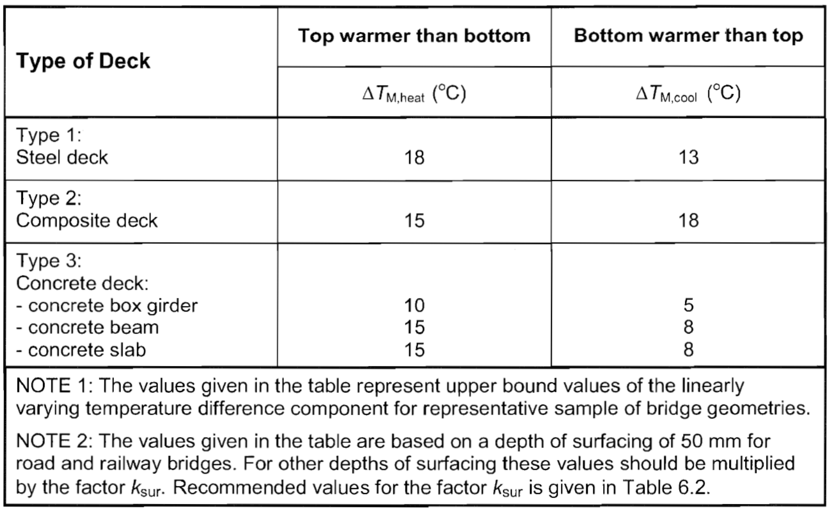

Type of Deck	**Top warmer than bottom**	**Bottom warmer than top**
	$\Delta T_{M,heat}$ (°C)	$\Delta T_{M,cool}$ (°C)
Type 1: Steel deck	18	13
Type 2: Composite deck	15	18
Type 3: Concrete deck: - concrete box girder - concrete beam - concrete slab	 10 15 15	 5 8 8

NOTE 1: The values given in the table represent upper bound values of the linearly varying temperature difference component for representative sample of bridge geometries.

NOTE 2: The values given in the table are based on a depth of surfacing of 50 mm for road and railway bridges. For other depths of surfacing these values should be multiplied by the factor k_{sur}. Recommended values for the factor k_{sur} is given in Table 6.2.

Figure 2.35. Recommended values of linear temperature difference component for different types of bridge decks for road, foot, and railway bridges (EN 1991-1-5: 2003).

The non-linear temperature difference component's recommended values are presented in Figure 2.36, where the temperature difference encompasses the non-linear temperature difference component, linear temperature difference component, and a small portion of the uniform bridge temperature component. In Figure 2.36, heating signifies conditions causing a heat gain through the top surface of the bridge deck due to solar radiation and other effects. Conversely, cooling refers to conditions leading to heat loss from the top surface of the bridge deck due to re-radiation and other effects.

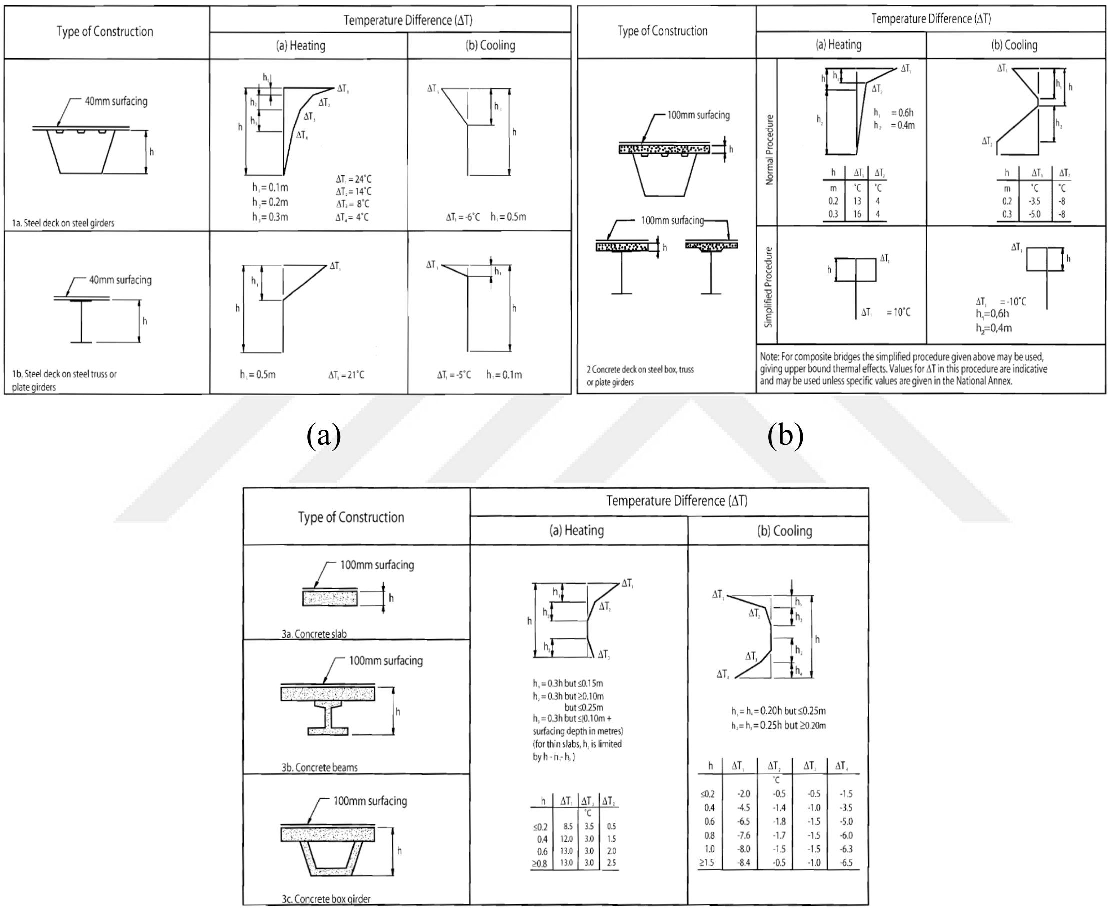

Note: For composite bridges the simplified procedure given above may be used, giving upper bound thermal effects. Values for ΔT in this procedure are indicative and may be used unless specific values are given in the National Annex.

h	ΔT_1	ΔT_2
m	°C	°C
0.2	13	4
0.3	16	4

h	ΔT_1	ΔT_2
m	°C	°C
0.2	-3.5	-8
0.3	-5.0	-8

h	ΔT_1	ΔT_2	ΔT_3
		°C	
≤0.2	8.5	3.5	0.5
0.4	12.0	3.0	1.5
0.6	13.0	3.0	2.0
≥0.8	13.0	3.0	2.5

h	ΔT_1	ΔT_2	ΔT_3	ΔT_4
		°C		
≤0.2	-2.0	-0.5	-0.5	-1.5
0.4	-4.5	-1.4	-1.0	-3.5
0.6	-6.5	-1.8	-1.5	-5.0
0.8	-7.6	-1.7	-1.5	-6.0
1.0	-8.0	-1.5	-1.5	-6.3
≥1.5	-8.4	-0.5	-1.0	-6.5

(a) (b)

(c)

Figure 2.36. Temperature differences for bridge deck Types: (a) Type 2: steel, (b) Type 2 composite, (c) Type 3 concrete (EN 1991-1-5: 2003).

In cases necessitating the consideration of both the temperature difference and the maximum range of the uniform bridge temperature component concurrently (e.g., in frame structures), the following Equations (2.17a) and (2.17b) may be utilized, to be interpreted as load combinations,

$$\Delta T_{M,heat} \left(\text{or } \Delta T_{M,cool}\right) + \omega_N \Delta T_{N,exp} \left(\text{or } \Delta T_{N,con}\right) \quad (2.17a)$$

$$\omega_N \; \Delta T_{M,heat} \left(\text{or } \Delta T_{M,cool}\right) + \Delta T_{N,exp} \left(\text{or } \Delta T_{N,con}\right) \quad (2.17b)$$

The most adverse effect should be chosen. the recommended values for ω_N and ω_M are 0.35 and 0.75, respectively.

2.6.3. Construction Temperature

construction temperature may be defined for IABs as the EBT when the integral connection between bridge deck and abutment is made. The time of integral connection can be defined as the time when connection is strong enough to handle thermal loadings and displacements, or when the interaction between bridge and soil begins. For jointed bridges, the construction temperature is the EBT of bridge immediately after girders have been set on bridge bearings. The following section will discuss the consideration of construction temperature for IABs according to different bridge design specifications in United States, Canada, and Europe.

In the United States, AASHTO procedures calculate thermal displacement based on temperature variation ($\Delta T\pm$), assuming that construction temperature is the mean value between the minimum and maximum design temperatures. This method does not consider potential variability in construction temperature during the construction phase.

In Canada, the CHBDC (2006) recommends assuming an effective construction temperature of 15°C (60°F) for both steel and concrete bridges when specific site data is unavailable.

In Europe, according to Eurocode (CEN, 2003a), the construction temperature refers to the initial temperature of the bridge (T_0). In cases where the initial temperature is unpredictable, the average temperature during the construction period is considered instead. This initial temperature value may be specified in the National annex or within a particular project. In the absence of available information, the initial temperature may be assumed as 10°C. In situations where uncertainty exists regarding the bridge's sensitivity to the initial temperature, it is advisable to consider both a lower and upper limit for expected initial temperature.

2.7. Structural Response of IABs to Varied Load Conditions:

IABs are subject to several load combinations including both primary and secondary loads. Primary loads, such as dead load and traffic load, are inherent to the structure and traffic conditions. Conversely, secondary loads, including changing earth pressure, temperature change load, time-dependent effects, and temperature gradient load, among others, arise from other external factors. Although numerous studies, including those involving field instrumentation, laboratory experiments, and numerical modeling, have been conducted, there is still a notable lack of understanding regarding the behavior of IABs. The following is a brief overview of research studies focusing on the behavior of IABs.

In a study conducted by Hemanth et al. in 2002, based on field testing and monitoring results of an IAB in West Virginia, it was found that dead load produces considerable tensile stresses at the superstructure top near abutments, as well as compressive stresses at the superstructure top and tensile stresses at the bottom flange of the girder at midspan. Their study concluded that earth pressure effects are negligible, leading to a recommendation to neglect earth pressure loads in the analysis and design of IABs.

According to a 2016 study by James et al., which was based on numerical simulations evaluating the behavior of IABs with composite steel I-girders subjected to temperature changes consistent with seasonal fluctuations in the state of Illinois, it was found that thermally induced girder stresses are significant for IAB superstructures. These stresses can increase overall girder demand, as superstructure contraction amplifies girder demands already created by gravity loads. Specifically, thermal contraction increases girder bottom fiber stresses in negative moment regions while relieving them in positive moment regions. Conversely, thermal expansion relieves girder bottom fiber stresses in negative moment regions and increases them in positive moment regions, as illustrated in Figure 2.37. However, the largest absolute magnitudes were observed in the positive thermal (expansion) load cases due to the additional resistance that the backfill force places on the abutment.

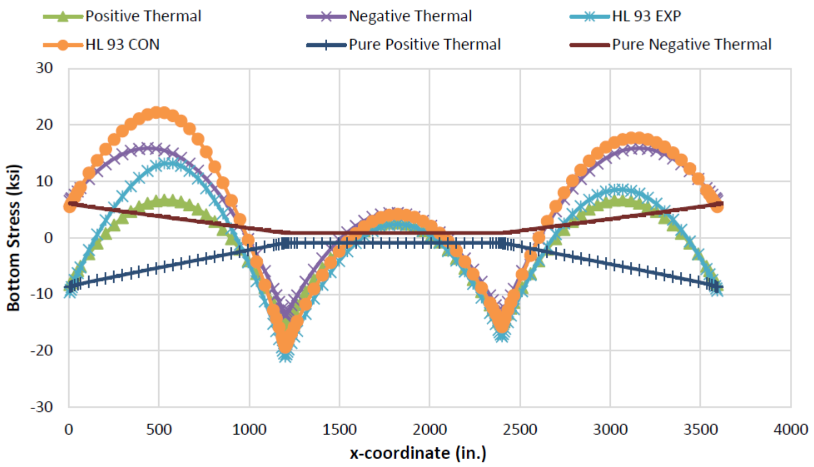

Figure 2.37. The bottom stress of girder for a three-span IAB (James et al., 2016).

The study clarified that the soil's resistance to thermal expansion is greater due to the additional overburden provided by the backfill. Consequently, the soil's resistance at the foundation is higher during thermal expansion compared to contraction. While the backfill acts to relieve demands placed on the pile during thermal expansion of the superstructure, the soil at the foundation is stiffer and may undergo higher forces compared to the abutment's response to thermal contraction. These opposing effects are influenced by various factors including backfill and foundation soil properties, abutment depth, and pile stiffness.

The interaction of these variables determines whether the thermal expansion or contraction load case governs the thermal structural demands, encompassing pile bending moments, girder axial force, and bending moments. Furthermore, the study highlighted that service load demands at critical points within the superstructure and pile are still primarily dictated by the load case including dead, live, and positive thermal loads. This is because thermal contraction acts to relieve stress induced by gravity loads, whereas thermal expansion thermal expansion acts to increase stress due to gravity loads at end span of the bridge girder.

For instance, the application of gravity loads to the bridge end span induces a clockwise rotation of the abutment, as depicted in Figure 2.38. This rotation contributes to expansion demands while mitigating contraction demands.

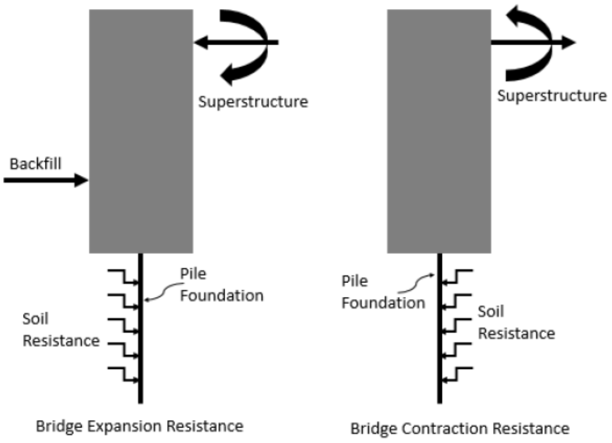

Figure 2.38. Free body diagram of the abutment under gravity and thermal loads (James et al., 2016).

In a study conducted by Peric´ et al. (2014), a full 3D finite element model of an existing three-span IAB was created and subjected to a combined thermal and gravity load. They found that the type of abutment movement is significantly affected by the magnitude of the temperature increase, the larger the temperature increases, the more dominant the translation of the abutment is compared to its rotation. The type of abutment movement directly relevant for the maximum bending moments in piles and the maximum negative bending moments of the superstructure.

According to Civjan et al. in 2007, based on numerical simulations evaluating the behavior of IABs, they found that the temperature increase assumed for design is not expected to result in pile yielding for this particular structure during bridge expansion. However, for bridge contraction, the design temperature decrease is expected to result in conditions approaching the onset of pile yielding.

In another study by Quinn et al. (2016), thermal analyses were conducted with temperature variations of ±41.7°C to investigate how both maximum temperature ranges affected bridge behavior. An illustrative case was provided to compare bridge expansion and contraction at the same temperature, both with and without backfill. The resulting weak-axis pile bending moment diagrams along the depth of the pile are illustrated in Figure 2.39. These findings indicate that in the absence of backfill, the behavior during bridge expansion closely mirrored that observed during bridge contraction.

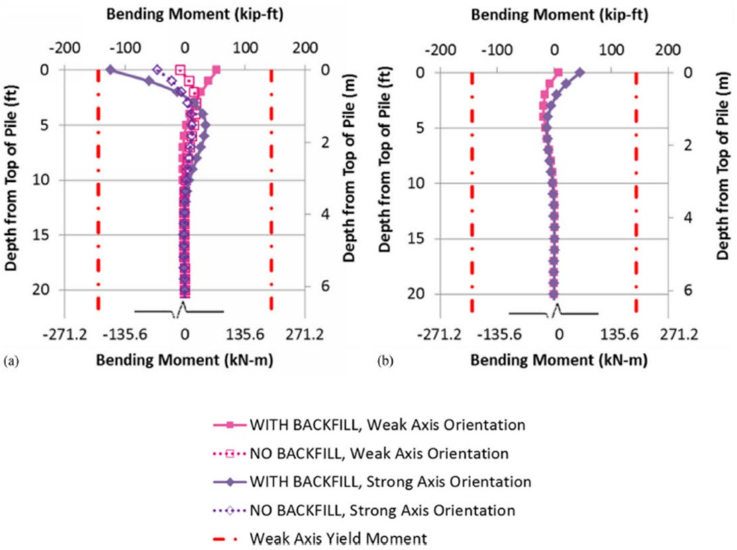

Figure 2.39. Bending moment diagrams along the depth of the pile comparing behavior with and without backfill present: (a) expansion case, (b) construction case. (Quinn et al., 2016).

2.8. Parameters Influencing the Response of IABs

Thermal displacement in the bridge deck can induce an elevation in the earth pressure behind the abutment, significantly affecting the bridge performance. This phenomenon has been observed in previous experimental (Kim and Laman (2012), and Peric et al. (2016)), and numerical studies (Kim and Laman (2012), Kim and Laman (2010a)), as well as damage observed in in-service bridges (Murphy and Yarnold (2018), and Lee et al. (2016)). The degree of elevation in the earth pressure relies on the magnitude of thermal displacements. The magnitude of thermal displacement is influenced by the coefficient of thermal expansion, a material-specific property of the superstructure. Additionally, it is affected by the length of the bridge superstructure, the maximum temperature changes experienced by the superstructure, and the construction temperature. Abutment height is important in bridge design due to its strong association with soil–structure interaction, while the stiffness of the foundation soil significantly affects the thermal behavior of IABs, particularly affecting the maximum thermal displacement observed at the top of the pile.

The following section summarizes the influence of these parameters on IAB response as reported in the literature.

2.8.1. Construction Temperature

In the existing literature, there is a noticeable lack of studies examining the effect of construction temperature on the response of IABs. However, Kim and Laman (2010a) conducted a study that involved a parametric analysis of 243 two-dimensional cases. This investigation aimed to understand the long-term response of IABs. The study investigated the influence of initial temperature at the completion of construction when the backwall is placed and integral behavior begins. Three cases were compared over a 75-year simulation, as illustrated in Figure 2.40: Case 1, during spring with a temperature of 7.5°C, (2) Case 2, during the summer with a temperature of 24.2°C, and (3) Case 3, during the fall with a temperature of 7.5°C. Kim and Laman's findings indicate that the initial temperature at the time of construction completion, referred to as the construction temperature in this context, significantly affects both the initial response and the long-term behavior of IABs. Moreover, they found that the initial abutment displacement difference between cases 1 and 2 or cases 3 and 2 due to the difference in construction temperature is maintained over the bridge life. The research further implies that the higher the construction temperature, the larger the abutment displacement the bridge experiences during bridge life because a higher construction temperature means a larger temperature decrease.

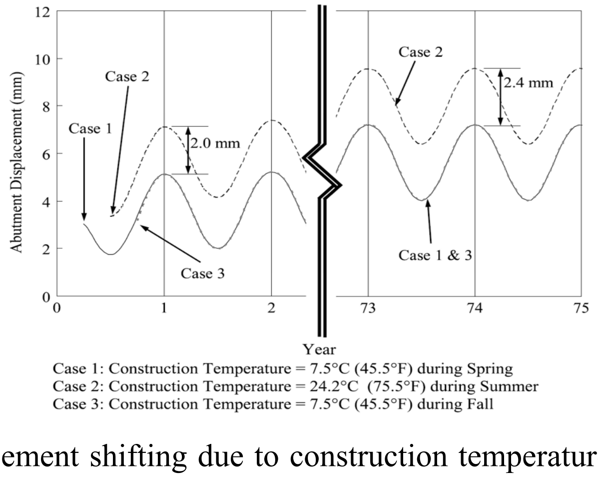

Figure 2.40. Displacement shifting due to construction temperature, (Kim and Laman, 2010).

In another study conducted by Quinn et al. (2016), a detailed parametric investigation of steel girder IABs was presented. This study utilized finite-element models to compare the effects of pile orientation on the response of IABs with varying lengths and skews. The thermal analyses were conducted with temperature variations of ±41.7°C, assuming bridge construction temperature at 7.2°C, which represented the mean between minimum and maximum design temperatures (-34.4°C and 48.9°C). Additionally, the study explored temperature ranges of +50°C and -66.7°C, assuming bridge construction temperature ranging from -1.1°C to 32.2°C. The primary objective was to investigate how both symmetric and non-symmetric maximum temperature ranges affected bridge behavior for different pile orientations. The results indicated that for symmetric temperature increases and decreases, the weak-axis pile orientation would be less likely to result in pile yielding; for the nonsymmetric values considered, there was no clear advantage to either pile orientation. For all cases, the strong-axis moment did not cause yielding of the pile.

However, R. J. Lock's study in 2002 indicated that varying the construction temperature had no lasting effect on the bridge's behavior over the long term.

2.8.2. Superstructure Material

The superstructure material property, i.e., thermal expansion coefficient α directly influences superstructure strain in response to material temperature changes and is the primary cause of the difference in response between steel and concrete girder IABs according to AASHTO (1989), therefore state agencies in different countries limit the length of IABs depending on girder material. For example Design Manual Part 4 by Pennsylvania Department of Transportation (PennDOT DM4) in united states limits the IAB bridge length to 180 m for concrete and 120 m for steel, Dicleli and Albhaisi (2003a) reported bridge length limitation for moderate climate at 260 m for concrete and 180 m for steel girder. Additionally, the materials used in the superstructure are used in defining the design temperature ranges as mentioned earlier (refer to Section 2.6.1) according to different bridge design specifications.

2.8.3. Bridge Length

The length of the bridge is the parameter that most significantly influences the performance of IABs, according to the AASHTO Guide Specifications (1989). A study by Kim et al. (2021) underlines this point by evaluating the effect of bridge length on bridge response. They concluded that the bridge length parameter, as provided in bridge design specifications, significantly influenced all considered responses of both the superstructure and substructure and should be regarded as a key design parameter. The results indicated that while the bridge responses were not linearly proportional to the bridge length, all responses increased with an increase in bridge length. To manage these effects, bridge design specifications provide limits on the length of IABs or allowable thermal displacement. Both methods control a structure's thermal displacement, but agencies controlling length usually allow larger displacements. Others have no limits on length. According to the departments of transportation in the USA and Canada, Table 2.7 lists the maximum length limits imposed by various transportation agencies for IABs.

Table 2.7. Maximum length limits imposed by various transportation agencies for IABs.

State or Province	Thermal displacement (cm)	Length (m)		
		Steel girder	Precast concrete girder	Cast-in-place concrete girder
Alaska	-	-	61	-
Arkansas	-	91.5	91.5	-
California	1.3	31.1	50.9	50.9
Colorado	10.2	91.5	183	152.5
Georgia	No limit	No limit	No limit	No limit
Illinois	No limit	83.9	114.4	114.4
Iowa	Limited by length	Undetermined	152.5	152.5
Kansas	5.1	91.5	152.5	152.5
Kentucky	No limit	91.5	122	122
Maine	9.5	90	150	150
Maryland	2.5	-	18.3	-
Massachusetts	Not defined	99.1	99.1	99.1
Michigan	No limit	No limit	No limit	No limit
Minnesota	No limit	61	61	61
Nevada	2.5	76.3	122	122
New York	Limited by length	140	140	140
North Dakota	Limited by length	122	122	48.8
Oklahoma	-	91.5	122	-
Oregon	No limit	No limit	No limit	No limit
Pennsylvania	5.1	91.5 to 122	122	Not used
Quebec	No limit	-	78.1	-

a Lesser value used with maximum skew.
b displacement is limited, not length.

Table 2.7. Maximum length limits imposed by various transportation agencies for IABs (Continued).

State or Province	Thermal displacement (cm)	Length (m)		
		Steel girder	Precast concrete girder	Cast-in-place concrete girder
South Dakota	Limited by length	106.8	213.5	213.5
Tennessee	5.1	130.8	244	244
Vermont	Limited by length	24.4	-	-
Virginia	3.8	91.5/46.8a	152.5/79.3a	-
Washington	No limit	Not used	106.8	61
West Virginia	5.1	-b	-b	-b
Wyoming	5	100	130	100

a Lesser value used with maximum skew.
b displacement is limited, not length.

Furthermore, numerous research studies attempt to suggest maximum bridge lengths. In the study by Dicleli and Albhaisi (2003a), using pushover analysis results and based on the cyclic displacement capacities of steel H-piles, the maximum length limits for IABs subjected to cyclic thermal variations are calculated. The study found that the maximum length limit for concrete IABs ranges from 150 to 265 m in cold climates and from 180 to 320 m in moderate climates. For steel IABs, the maximum length limit ranges from 80 to 145 m in cold climates and from 125 to 220 m in moderate climates.

In another study by Dicleli and Albhaisi (2004), the maximum length limits for IABs built on clay were determined using pushover analysis results. This study recommended that the maximum length of concrete IABs be limited to 210 m in cold climates and 260 m in moderate climates, while the maximum length of steel IABs should be limited to 120 m in cold climates and 180 m in moderate climates.

2.8.4. Foundation Soil Stiffness

The stiffness of the foundation soil plays a crucial role in the thermal behavior of IABs, significantly influencing the maximum thermal displacement at the top of the pile. As soil stiffness increases, thermal displacement decreases, thereby affecting the response of the bridge elements. These findings have been highlighted in several studies, which will be discussed further here. Specifically, in three studies conducted by Dicleli and Albhaisi (2003a, 2003b, 2004), analyses were performed on IABs to investigate the effects of various geometric, structural, and geotechnical parameters on their performance under temperature variations. They concluded that the displacement capacity of IABs considerably decreases with stiffer foundation soil, as illustrated in Figure 2.41.

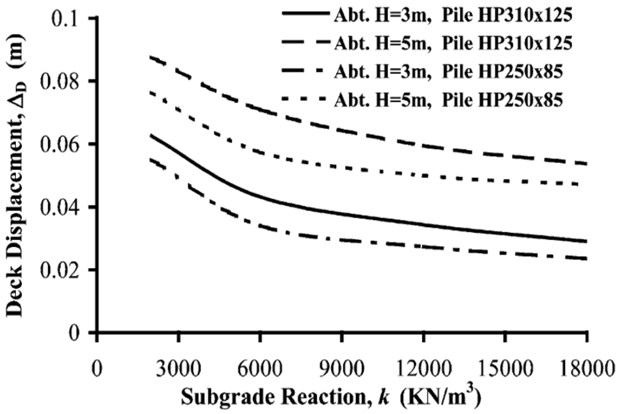

Figure 2.41. Deck displacement versus subgrade reaction modulus for different abutment heights and pile cross sections (Dicleli and Albhaisi, 2003).

In addition, a study conducted by Salman and Issa (2021) employed a parametric analysis to validate a field-monitored concrete IAB using a three-dimensional finite-element model. This study aimed to investigate various parameters affecting bridge response, including soil type. Their findings emphasized the influence of soil stiffness surrounding the pile on pile displacement. Furthermore, the study revealed that pile stresses were directly proportional to the soil stiffness, as illustrated in Figures 2.42, 2.43 and 2.44.

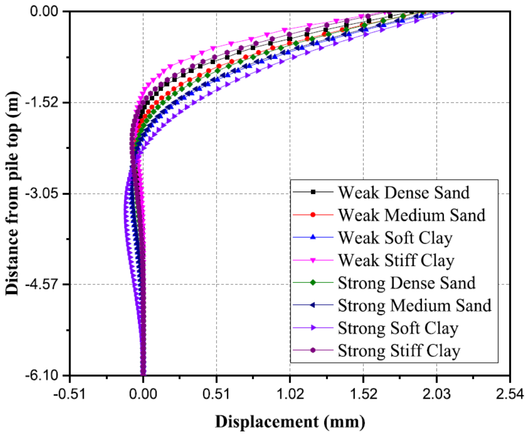

Figure 2.42. Displacement from pile top for various soil types (Salman and Issa, 2021).

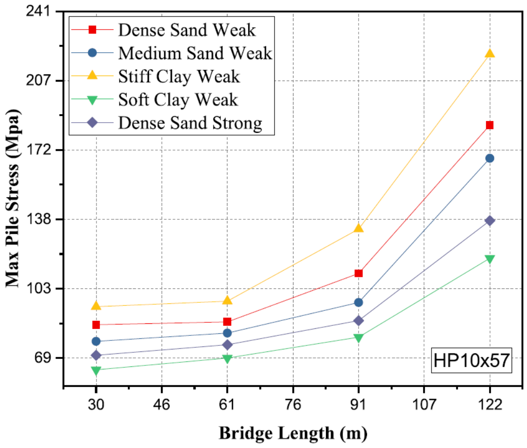

Figure 2.43. Maximum pile axial stress versus bridge length for different soil types in the bridge expansion case (Salman and Issa, 2021).

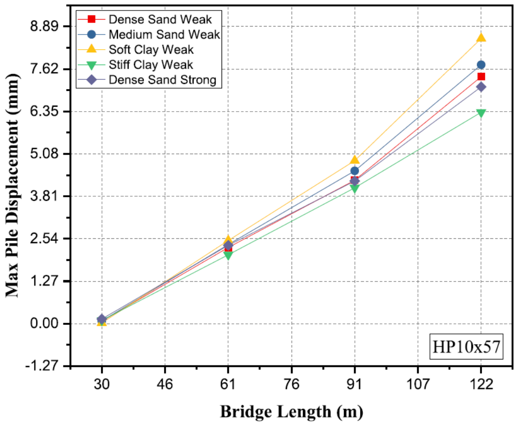

Figure 2.44. Maximum pile displacement versus bridge length for different soil types in the bridge expansion case (Salman and Issa, 2021).

In a study conducted by Firoozi et al. (2023), an investigation was carried out to determine the influence of structural and soil parameters on the response of IABs. Their findings revealed that as the combined stiffness of the soil behind the abutment and around piles increased, the maximum girder moments at the superstructure decreased. This trend was also observed in pile deflection and abutment displacement. However, they observed that the maximum abutment head moments decreased when the abutment backfill was dense and increased when piles were located in hard clay, similar to pile moments.

Additionally, Huang et al. (2008) conducted a parametric study with different design variables, including the type of soil surrounding the pile. Their research findings indicated that the behavior of IABs was significantly affected by the types of soil surrounding the piles. They observed that stiffer soils resulted in larger girder concrete stresses within the superstructure and higher levels of stress experienced by the piles, as illustrated in Figure 2.45.

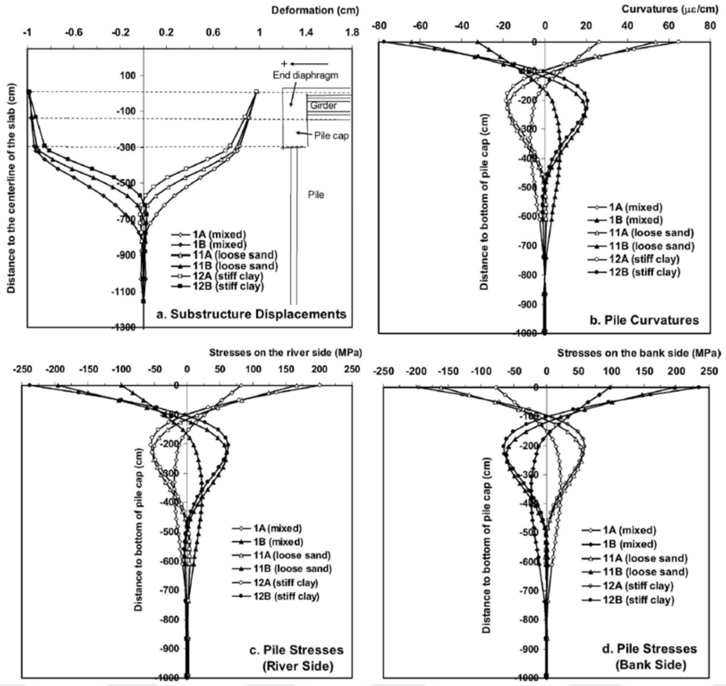

Figure 2.45. Effect of the soil surrounding the piles. (Huang et al, 2008).

Albhaisi et al. (2012) conducted an investigation into the effect of substructure stiffness on the performance of short and medium length steel IABs constructed on clay under thermal load effects. Their findings emphasized that soil stiffness significantly affected the displacement at the top of the pile and had a considerable influence on the rotation along the abutment and the piles.

In contrast, Baptiste et al. (2011) conducted a parametric study considering the effects of soil stiffness and other parameters. They noted that the influence of soil stiffness during contraction was generally more pronounced than during expansion. Additionally, their findings indicated that soil stiffness did not exert a significant influence on pile-head displacement under either expansion or contraction.

2.8.5. Abutment Height

The abutment height is a critical parameter in bridge design, strongly associated with soil-structure interaction, influencing both the backfill pressure (load) and passive pressure (resistance) of an IAB. Based on Ontario Ministry of Transportation (MTO) recommendations (Hussain and Bagnariol (1996)), bridges with abutment height more than 6 m should not be considered for integral abutment design. Abutment height plays a significant role in the performance of bridges, as shown by previous numerical studies and field monitoring of in-service bridges.

A study conducted by Kim et al. (2021) illustrates that the rotational stiffness of the substructure is directly linked to abutment height, which significantly affects the internal forces within bridge elements. An increase in abutment height means an increase in backfill resistance against bridge expansion consequently increasing abutment rotation. Conversely, a decrease of abutment height reduces backfill resistance, consequently increasing abutment translation. Therefore, both an increase and decrease in abutment height increase pile moment through pile rotation and translation, respectively. Regarding internal forces within girders, an increase in abutment height raises compressive girder axial forces and girder moment. Furthermore, their findings indicate that abutment height significantly influences pile head displacement, showing a decrease in pile head displacements as abutment height increases.

In another study conducted by Paul et al. (2008), which investigated the effects of abutment height and other parameters on thermally induced superstructure forces, it was established that bridge abutment height significantly influences these forces.

Furthermore, In a study conducted by Nikravan (2013), a parametric investigation analyzed the effect of key factors, including abutment height, on the performance of IABs under varying temperature conditions. The study noted a significant reduction in horizontal pile displacement with increased abutment height. Furthermore, their findings concluded that increasing the abutment height led to an extension in the allowable lengths of IABs.

Another study conducted by Baptiste et al. (2011) found that abutment height significantly influences various factors, including pile-head displacement, maximum pile moment, concrete stress at the abutment–pile connection, and girder stress.

In a seven-year field monitoring study of IABs conducted by Kim et al. (2012), it was observed that bridges with relatively shorter abutment heights experienced greater displacement at the abutment bottom compared to the top. Conversely, taller bridge abutments tended to result in reduced displacement at the abutment bottom. Additionally, shorter abutments led to smaller abutment rotations, while taller abutments showed larger rotations.

2.9. Finite Element Modeling of IABs

The finite element analysis technique is widely employed in the analysis of complex structures by dividing the structure into numerous smaller elements with appropriate section characteristics and properties. These elements are interconnected at discrete joints known as nodes. This method has been developed and refined for the analysis of two-dimensional elastic structures since the 1950s (Hambly, 1991).

The finite element method is widely regarded as the most powerful and versatile method of analysis available today. Recent advancements in the finite element method, coupled with the capabilities of high-speed computers, enable the modeling of bridges in a highly realistic manner and provide a comprehensive description of their structural response to various loadings. Finite element analysis software is employed to determine the structural behavior of IABs, which must be modeled to ensure full moment continuity between the girder and the supporting abutment. These software offers a variety of element types for structural analysis, including but not limited to:

Frame Element: The frame element is a two-node three-dimensional element that incorporates the effects of biaxial bending, tension, compression, axial deformation, and biaxial shear deformation. It is particularly suitable for modeling slender structural members like girders and piles.

Shell Element: The shell element is a four-node dimensional element that combines separate membrane and plate behavior. Each node of the four-node shell element has six degrees of freedom, including three displacements and three rotations The membrane behavior of the shell element includes translational in-plane stiffness components and rotational stiffness component in the direction normal to the plane of the element. Additionally, the plate bending behavior includes two-way, out-of-plane, plate rotational stiffness components in the direction normal to the plane of the element. This element type is suitable for representing thin-walled structures such as bridge decks and abutments. A detailed diagram of the shell element is presented in Figure 2.46.

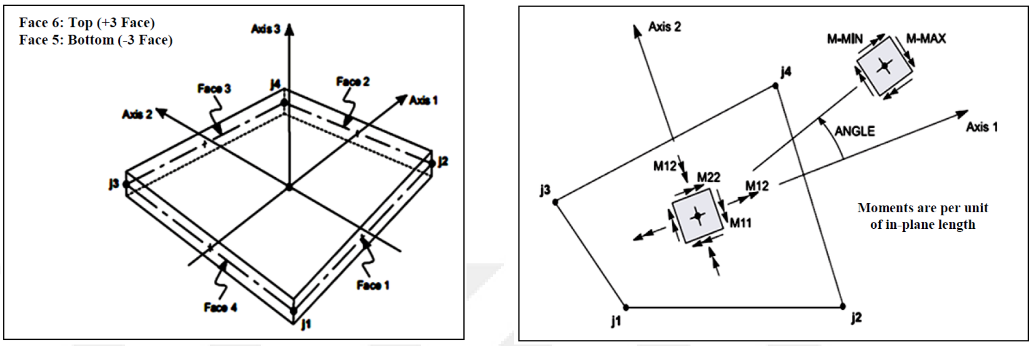

(a) (b)

Figure 2.46. Shell elements used in the analysis: (a) Four node shell element, (b) Plate bending moments.

Solid Element: The solid element is an eight-node three-dimensional element that includes nine optional incompatible bending modes. At each of its connected joints, the solid element contributes stiffness in all three translational degrees of freedom. This element type is used to model three-dimensional volumes and is often employed for simulating bridge piers and abutments.

Truss Element: A two-node one-dimensional element ideal for modeling truss structures subjected primarily to axial forces. It represents slender members connected at their ends and neglects bending, shear, and torsional effects, focusing solely on axial deformation. Suitable for analyzing the stability and load-carrying capacity of IABs with axial loads.

Link Element: The link element serves as a connector between other finite elements in a structural model, simulating joints or connections. It represents the behavior of connections like hinges or bearings, allowing for flexibility or nonlinearity. Typically one-dimensional, link elements are characterized by stiffness and damping properties, simplifying the modeling of complex connections in IABs while maintaining accuracy.

Soil springs: Soil springs possess stiffness and damping properties designed to replicate the response of the soil to applied loads. These properties are usually derived from soil mechanics principles and geotechnical data. Acting as virtual components, soil springs symbolize the mechanical behavior of the soil surrounding a structure. Soil springs can represent both linear and nonlinear springs and dampers, useful for modeling soil–structure interaction or bridge bearings.

2.9.1. Modelling of the Deck - Beam and Slab bridges

In the span range of 10m to 60m, the most commonly adopted bridge type is the slab-on-girder bridge. These bridges feature multiple longitudinal beams, often prestressed, spanning between the abutments, with a thin transversely spanning deck slab on top, as depicted in Figure 2.47. Load sharing among the longitudinal beams is facilitated by the presence of the top slab or a combination of the top slab and transverse diaphragm beams.

The extent of load sharing is primarily determined by the stiffness of the slab. Therefore, it is crucial to appropriately model or idealize the slab to avoid inaccurate predictions of load sharing between adjacent beams, which could lead to misleading load sharing scenarios. Additionally, incorporating wide diaphragms can enhance shear characteristics.

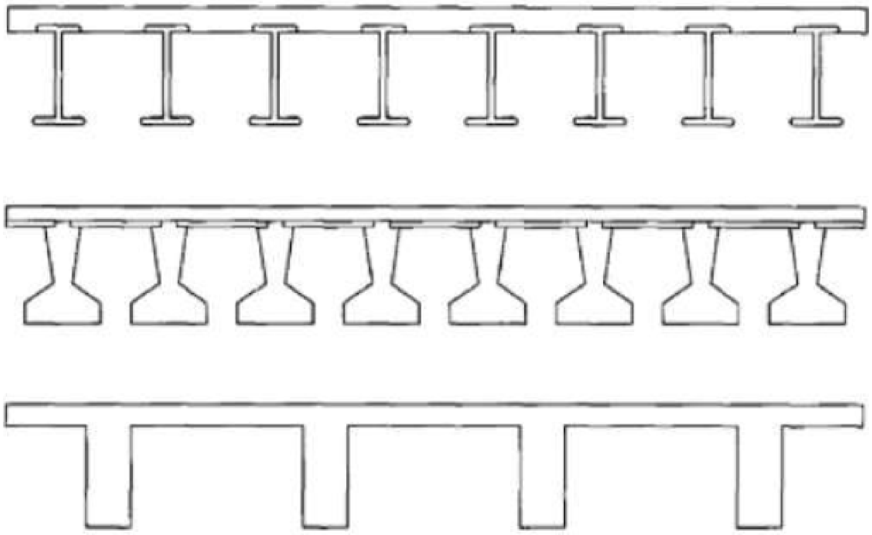

Figure 2.47. Beam and slab construction options (O'Brien and Keogh, 1999).

2.9.2. Pile Types and Considerations for Modelling

Piles for IABs are designed to possess both acceptable vertical resistance and low stiffness to minimize the flexural effects of thermal and other displacements. In the case of fully connected integral abutments, it is assumed that the superstructure will transmit all moments, as well as vertical and horizontal loads resulting from various factors such as dead loads, live loads, impact forces, temperature changes, creep, shrinkage, and seismic loads if applicable. The ability of the piles to withstand both vertical loads and cyclical temperature-induced displacements over numerous cycles is crucial in pile design for IABs. Lateral displacements tend to diminish the vertical-load carrying capacities of the piles (Greimann and Wolde-Tinsea, 1988). In fact, the maximum length achievable for an IAB is determined by the pile's capacity to accommodate lateral displacements. Piles are typically installed in a single row to support the abutment, with alignment ensuring that longitudinal bending occurs along the pile's weak axis. Figure 2.48 illustrates the pile types used for IABs (Featherston, 2022).

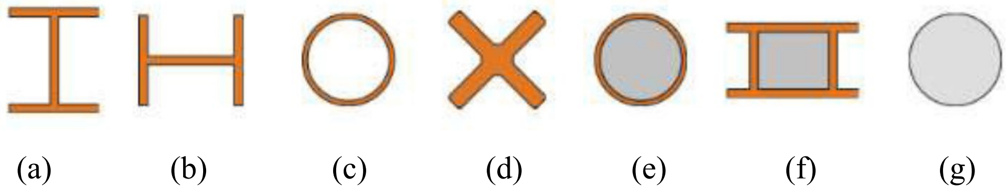

Figure 2.48. Pile types used for IABs, (a) H-pile strong axis bending, (b) H-pile weak axis bending, (c) Steel pipe pile, (d) X-pile rotated 45°, (e) Steel pipe filled with concrete (CIP), (F) Rectangular FRP pile filled with concrete, (g) Reinforced concrete pile (INTAB, 2010).

Horizontal displacements and rotations of the pile head cause bending moments in the pile, underscoring the need to accurately represent this behavior in the overall analysis model. The model may utilize either lateral springs located along the pile length or the 'equivalent cantilever' concept (refer to Section 24). If the piles are situated inside rings or pipes, the soil resistance over the length of the rings/pipes does not need to be included in the model. Figure 2.49 illustrates the equivalent spring and cantilever models for ends of the IAB. However, it is worth noting that the equivalent cantilever concept, sometimes used for modeling abutment piles, has shown inconsistent results, yielding either conservative or unconservative estimates of internal forces in IABs components, except for superstructure shear (Dicleli, 2009).

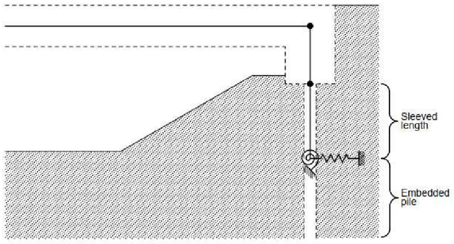

(a) Equivalent spring model

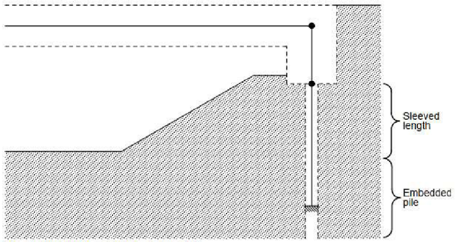

(b) Equivalent cantilever model

Figure 2.49. Equivalent spring and cantilever models for ends of the bridge (Iles, 2005).

2.9.3. IAB Structural Analysis Methods

The six general analysis methods for IABs are summarized as follows: (1) free expansion, which examines the bridge's response under different load conditions without constraints, (2) empirical approximate, which utilizes simplified methods or assumptions to estimate structural behavior, (3) two-dimensional static analysis (2D-SA), focusing on the structure's response to static loads in two dimensions; (4) two-dimensional time-history (2D-TH), assessing the dynamic response of the bridge over time in two dimensions; (5) three-dimensional static analysis (3D-SA), investigating the structure's response to static loads in three dimensions; and (6) three-dimensional time-history (3D-TH), evaluating the dynamic response of the bridge over time in three dimensions.

AASHTO LRFD (2013) includes a superstructure free expansion analysis method, applying displacements to determine substructure loads based on bridge length and design temperature range. This method overlooks important interactive effects like backfill pressure, concrete time-dependent effects, temperature gradient, and soil–structure interaction, limiting its ability to capture real-world bridge behaviors fully. Analyses (3) through (6) employ either 2D or 3D static or time-history analysis, focusing on loading related to temperature changes and thermal gradient. The structural numerical models encompass superstructure concrete time-dependent effects (creep and shrinkage), nonlinear behavior of the abutment construction joint, nonlinearity of soil-pile interaction, and backfill-abutment interaction (Kim and Laman, 2012).

While Thippeswamy et al. (2002) and Dicleli (2005) developed a simple 2D analysis approach based on design temperature ranges, these methods were limited in evaluating the simultaneous effects of concrete time-dependent effects and soil–structure interaction.

Conversely, Pugasap et al. (2009) and Kim and Laman (2010a, 2010b) introduced advanced 2D and 3D analysis methods, These methods underwent validation and calibration based on results obtained from a 7-year field measurement program conducted at four IABs ranging in lengths from 19 to 128 m (Kim and Laman, 2012, Laman and Kim, 2009, and Laman et al., 2006).

The nonlinear 3D-TH analysis represents an enhanced approach, building upon the foundation laid by Pugasap et al. (2009). This method offers a more detailed and precise simulation compared to the 3D-SA, akin to the approach outlined by Faraji et al. (2001). The 3D-TH analysis stands as the highest level of analysis assessed in this context, necessitating extensive computational resources and time. It enables the simultaneous consideration of time-varying temperature, concrete time-dependent effects, superstructure thermal gradient, as well as the nonlinearity of the construction joint, abutment-backfill interaction, and soil-pile interaction over a 75-year time period. Both the 3D-SA and 3D-TH analyses focus on individual bridge member responses, whereas both the 2D-SA and 2D-TH analyses include the superstructure (composite section of girder and deck slab) and pile responses in the transverse dimension. However, conducting a 3D, 75-year time-history simulation is currently impractical for design due to the extensive computational requirements it involves.

In a study conducted by Kim et al. (2016), the researchers investigated the accuracy and applicability of the IAB analysis approaches previously summarized. The study resulted in several conclusions:

Free expansion analysis is primarily useful for preliminary design of piles. It tends to underestimate pile shear force and pile head displacement while overestimating pile moment.

Both 2D and 3D static analyses serve as boundaries for time-history analysis, predicting only the initial response of girders and piles. Time-history analysis should be employed if the bridge's responses over time are required.

2D static analysis does not account for soil–structure interaction and time-dependent effects, making it unsuitable for predicting superstructure behavior. However, it may be acceptable for pile response predictions.

The 2D-TH is an advanced method that fully integrates soil–structure interaction and time-dependent effects over a specified period. In the study, stability in responses was observed within 15 years of simulated time. However, responses are averaged across the transverse dimension, and the approach doesn't provide maximum single member response. Except for girder axial force, responses closely match those of 3D-TH analysis.

Time-dependent effects are significant in IABs and should be considered in the analysis process, as indicated by comparisons between different analytical approaches.

Current design and analysis practices often assume a model without abutment rotation. However, findings from both 2D and 3D analyses indicate that abutment rotation does occur due to backfill pressure and time-dependent effects (which free expansion analysis fails to consider). This rotation can significantly affect the responses of IABs.

3. INVESTIGATING THE EFFECT OF VARIOUS LOADINGS ON THE STRUCTURAL BEHAVIOR OF IABs

IABs experience various load combinations, encompassing both primary and secondary loads. Primary loads, such as dead load and traffic load, are inherent to the structure and traffic conditions. In contrast, secondary loads, which include varying earth pressure, temperature change load, time-dependent effects, and temperature gradient load, originate from external influences. Despite extensive research through field instrumentation, laboratory experiments, and numerical modeling (Hemanth et al. (2002), James et al. (2016), Perić et al. (2014), Civjan et al. (2007), and Quinn et al. (2016)) (refer to Section 2.7), a significant gap remains in understanding how secondary loads, especially when combined with primary loads, effect the thermal behavior of IABs. It is essential to investigate the interactions between these secondary and primary loads to comprehensively evaluate their overall effect on IAB behavior.

The primary objective of this section is to conduct a comprehensive analysis of both primary and secondary loads, focusing on how secondary loads interact with the dead load and whether they amplify or mitigate the overall structural responses. This analysis aims to identify the beneficial or detrimental effects of these interactions, ultimately leading to a better understanding of their behavior.

To achieve this objective, a simple 3D finite element model is created using MIDAS CIVIL software. The model consists of a single span of 50 m with steel girders supported by an abutment, which is in turn supported by a single row of steel H-shaped piles oriented along their weak axes. The analysis focused on three distinct loads affecting the bridge: dead load (D) as a primary load, and temperature load (rising T_R, falling T_F) and earth pressure load (at-rest E_0, passive E_p, active E_a) as secondary loads. Three specific load combinations were evaluated: contraction ($D+T_F+E_a$), expansion ($D+T_R+E_p$), and a scenario without temperature loads ($D+E_0$). The response of the IAB elements was assessed by measuring the bending moment and displacement over the girder, pile, and abutment.

3.1. Development of 3D Numerical Model

This section discusses the development of a 3D finite-element model for IAB using MIDAS CIVIL software. The model was simplified to include only the primary components of the bridge to represent its general behavior. The superstructure was modeled as a slab-on-girder type (refer to Section 2.9.1), and the abutment was chosen as a frame abutment supported by piled foundations (refer to Section 2.2).

In this model, slabs and abutments are represented using shell elements, while girders and piles are modeled using beam elements, as shown in Figure 3.1. The girder boundary conditions at the abutment are rigidly connected to the backwall without bearings. The piles are rigidly connected to the bottom of the abutment.

Soil-pile interaction is modeled using the subgrade reaction approach (refer to Section (2.4.2), with the force-displacement (p-y) curves generated by the software. For the backfill-abutment interaction, the limiting equilibrium approach is employed, modeling the backfill soil as a load calculated using the Arsoy (2008) method (refer to Section 2.4.1). The finite-element model was implemented in a one-step 3D static analysis (refer to Section 2.9.3).

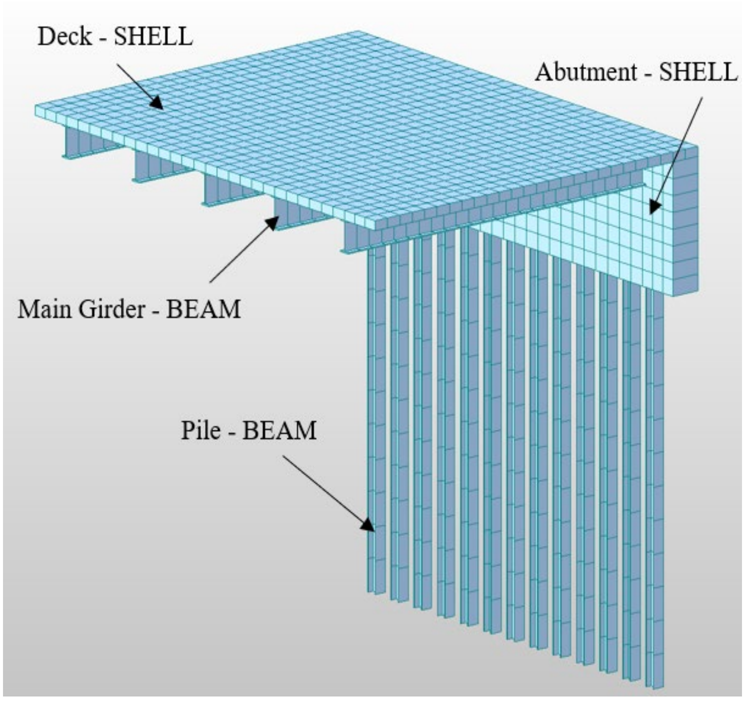

Figure 3.1. 3-D finite-element model of IAB.

3.1.1. Bridge Design Parameters and Description:

The IAB model comprises a single span with a length of 50 m. The superstructure consists of five steel plate girders with a yield strength of 355 MPa, complemented by a cast-in-place concrete deck with a strength of C30/37 MPa.

The thermal expansion coefficient of steel, a value that is both predictable and well-established, was set at 12 × 10^{-6}/°C. The range of thermal expansion coefficient for concrete exhibits considerable variability due to differences in concrete mixes include aggregate properties, water-to-cement ratio, relative humidity, concrete age, and other influencing factors. In instances where test data are unavailable, AASHTO LRFD (2014) suggests a thermal expansion coefficient for concrete of 10.8 × 10^{-6}/°C, within a range of 5.4 to 14.4 × 10^{-6}/°C. In this context, a value of 10.0 × 10^{-6}/°C has been chosen for concrete.

The I-shaped steel girders were designed in accordance with AASHTO LRFD (2014) standards. The main girders of the IAB are supported by a 4 m high reinforced concrete abutment, each with a thickness of 1 m. Each abutment is supported on 13 equally spaced HP 400×231 steel piles with a yield strength of 355 MPa, oriented with their weak axis resisting longitudinal bridge displacements.

Figure 3.2 illustrates the geometry of the IAB superstructure, while detailed cross-sections of the IAB elements are provided in the accompanying Table 3.1.

These specifications were implemented based on information obtained from Kim et al.'s (2021) finite element modeling study and another study conducted by Kim and Laman (2012) on seven-year field monitoring of four IABs located in the USA.

Table 3.1. Detailed cross sections of IAB elements.

Girder section (mm)	Pile web (mm) and pile flanges (mm)	Deck section (m)	Pile length (m)
(+): 508 × 31.7 × 1676.4 × 15.9 (–): 508 × 31.7 × 1676.4 × 15.9	372 × 26 402 × 26	0.30	12

(+): positive flexure, (-): negative flexure.

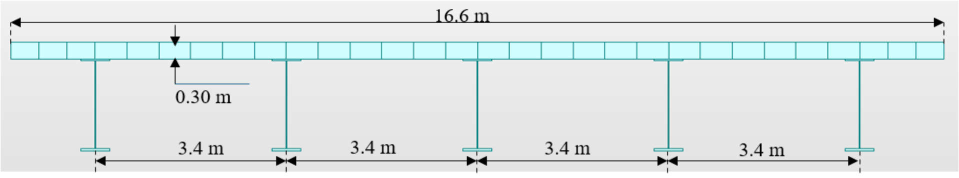

Figure 3.2. IAB superstructure geometry.

3.1.2. Thermal Loads Modeling

Concerning the thermal loadings affecting the IAB model, it was assumed that the structure is intended for construction in a northern region of the United States. According to AASHTO (2010), many states in this region specify minimum and maximum design temperatures of –34.4°C (–30°F) and 48.9°C (120°F), respectively, resulting in a thermal range of 83.3°C (150°F). For analysis purposes, a thermal load of 41.7°C (75°F) and a construction temperature of 7.2°C (45°F), representing the mean value between the minimum and maximum design temperatures, are used. This approach ensures balanced temperature variations during both expansion and contraction phases, allowing for a direct assessment of their effects.

3.1.3. Backfill–Abutment Interaction Modelling

For this model, typical properties of medium granular backfill soil were adopted, as variations in standard backfill materials are generally limited. The internal angle of friction (φ) and unit weight (γ) for medium granular backfills can vary depending on factors such as the specific type of soil, compaction, moisture content, etc. However, typical values for medium granular backfills usually fall within these ranges, the internal angle of friction (φ) ranges from 30° to 40°, the unit weight (γ) ranges from 16 kN/m³ to 20 kN/m³. For accurate design and analysis, it is recommended to conduct site-specific testing or refer to local standards and guidelines. The soil properties used in this study were selected based on previous field tests conducted by Kim and Laman (2012) and are detailed in Table 3.2.

Table 3.2. Medium granular backfill properties

Property	Values
φ Internal angle of friction (◦)	34
γ Unit weight (kN/m³)	18.7

For the abutment–backfill interaction, the limiting equilibrium approach is employed. In this section, the methodology used for calculating passive earth pressure behind the abutment follows the Arsoy (2008) method (refer to Section 2.4.1.1).

The resultant force at plastic equilibrium (E_{Pmax}), representing the point where full passive forces are mobilized, will be determined using the classical Rankine earth pressure theory (1857) and is calculated using Equation (2.5b) (refer to Section 2.4.1.1). The full passive earth pressure distribution is assumed to be a simple triangular distribution. Thus, the maximum lateral earth pressure (σ_{hmax}) occurs at bottom of the abutment, is calculated using Equation (2.3) (refer to Section 2.4.1.1, Figure 2.8), and the resultant force (E_{Pmax}) acts at one-third of the abutment height from the base and is determined by the total area of the triangular pressure diagram. These calculations are provided as follows, respectively:

$$K_{pR} = \tan^2\left(45 + \frac{\varphi}{2}\right) = \tan^2\left(45 + \frac{34}{2}\right) = 3.54$$

$$\sigma_{hmax} = K_{pR}\,\gamma\,H = 3.54 * 18.7 * 4 = 264.58\ \text{kN/m}^2$$

$$E_{pmax} = 0.5\,K_{pR}\,\gamma\,H^2 = 0.5 * 3.54 * 18.7 * 4^2 = 529.58\ \text{kN/m}$$

The resultant passive earth pressure force (E_P) for the determined relative abutment displacement in medium granular backfill soil, assuming the abutment displacement is purely translational, is obtained by multiplying the full passive force calculated (E_{Pmax}) by the values extracted from the chart illustrated in Figure 3.3. The displacement (Δ) will be calculated using Equation (2.14) (refer to Section 2.5), and the relative abutment displacement is defined as the ratio of the displacement to the abutment height (Δ/H). These calculations are provided as follows:

$$\Delta = \alpha\ L_b\,\Delta T(\pm) = 12 * 10^{-6} * \frac{50}{2} * 41.7 = 0.0125\ \text{m}$$

$$\Delta/H = 0.0125/4 = 0.0031\ \text{m}$$

$$\frac{E_P}{E_{Pmax}} = 50\% \quad \rightarrow \quad \frac{E_P}{529.58} = 0.50 \quad \rightarrow \quad E_P = 264.79\ \text{kN/m}^2$$

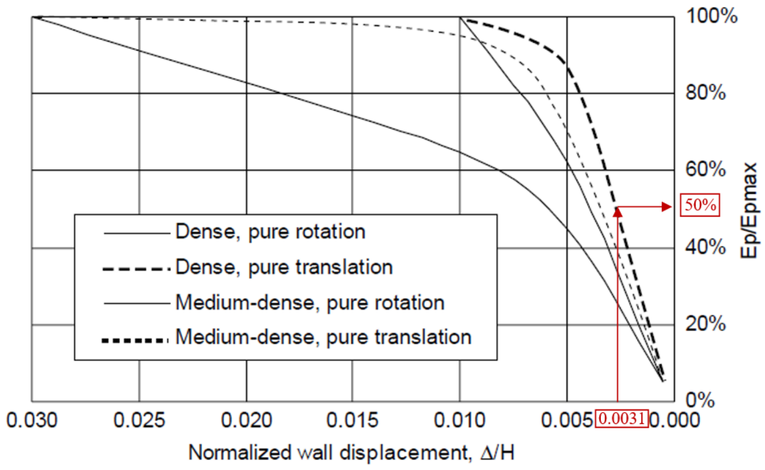

Figure 3.3. The resultant passive earth pressure force (E_P) for ($\Delta/H = 0.0031$).

For pure translation, it can be inferred from Figure (2.11) (refer to Section 2.4.1.1) that the abutment (y/H) ratio is equal to 1/3, indicating that the resultant force acts at one-third of the abutment height from the base. Thus, the earth pressure distribution is assumed to be a simple triangular distribution (refer to Section 2.4.1.1, Figure 2.8), as illustrated in Figure 3.4.

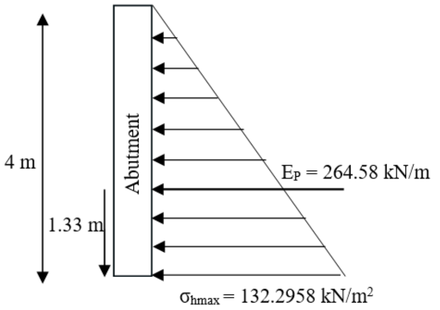

Figure 3.4. Passive earth pressure distribution according to Arsoy (2004) method.

To determine the active lateral earth pressure load, Rankine's theory (1857) will be applied, with the active earth pressure coefficient calculated using Equation (2.5a) (refer to Section 2.4.1.1). For calculating the at-rest lateral earth pressure coefficient, Jaky's equation (1944) will be used, as detailed in Equation (2.1) (refer to Section 2.4.1.1). These calculations are provided as follows:

$$K_{aR} = \left(45° - \frac{\varphi}{2}\right) = \left(45° - \frac{34}{2}\right) = 0.28$$

$$K_0 = 1 - \sin(\varphi) = 1 - \sin(34) = 0.44$$

The earth pressure distribution is considered as a simple triangle. Thus, the maximum active and at-rest lateral earth pressures (σ_a and σ_0), which occur at the bottom of the abutment, are calculated using Equation (2.3) (refer to Section 2.4.1.1, Figure 2.8).

$$\sigma_a = K\,\gamma\,H = 0.28 * 18.7 * 4 = 20.94\ \mathrm{kN/m^2}$$

$$\sigma_0 = K\,\gamma\,H = 0.44 * 18.7 * 4 = 32.91\ \mathrm{kN/m^2}$$

Figure 3.5. illustrates the modeling of backfill-abutment interaction within the software for passive, active, and at-rest earth pressure conditions, all of which have been modeled similarly.

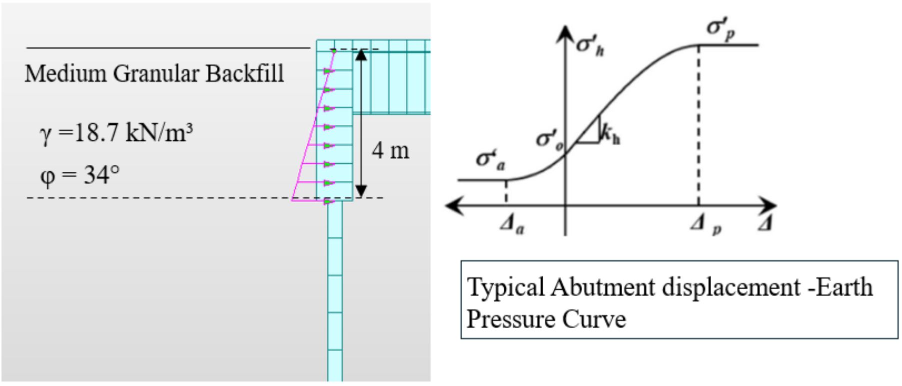

Figure 3.5. Backfill–abutment interaction modelling.

3.1.4. Soil–Pile Interaction Modelling

In this study, The soil surrounding the pile is regarded as a single layer of medium-density sand extending over a length of 12 m. The soil properties are defined as follows: (a) the unit weight of soil (γ) is 18 kN/m³, and (b) the internal friction angle of the sand (φ) is 35°.

The interaction between soil and piles is modeled using subgrade reaction approach (refer to Section 2.4.2.1), as a series of p-y curves distributed along the depths of the piles. Here, 'p' represents the soil force, while 'y' denotes the pile deflection. The p-y curves are generated using MIDAS CIVIL software, employing the sub-grade reaction

(k_h) calculated with the Vesic equation, as outlined in Bowles' 4th Edition (1998), as given in Equation (3.1),

$$K_h = \frac{0.65}{d} \sqrt[12]{\frac{E_S \, d^4}{E_{Pile} \, I_P}} \frac{E_S}{1 - \nu^2} \tag{3.1}$$

E_{Pile} denotes the modulus of elasticity of the pile, for steel piles according to EN1993-1-1, the modulus of elasticity is 210,000 MPa. I_p represents the moment of inertia of the pile, and for an HP 400×231 steel pile, the moment of inertia is 0.00028 m^4. Es signifies the modulus of elasticity of the medium sand, which will be assumed as 30 MPa. d represents the pile diameter, which will be taken as 0.402 m and ν denotes Poisson's ratio, taken as 0.30. Thus, the modulus of subgrade reaction (k_h) is calculated as follows:

$$K_h = \frac{0.65}{0.402} \sqrt[12]{\frac{30 * 0.402^4}{210000 * \; 0.00028}} \frac{30}{1 - 0.3^2} = 37.20 \text{ MPa}$$

Figure 3.6 illustrates the modeling of soil-pile interaction within the software.

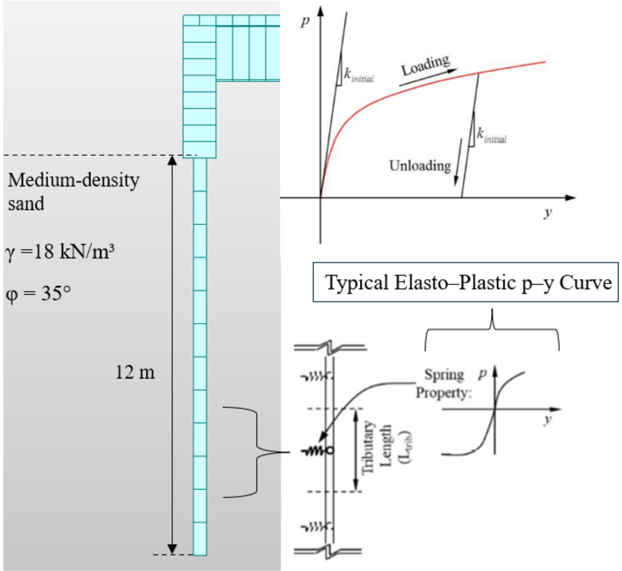

Figure 3.6. Soil–pile interaction modelling.

3.2. Summary of 3D Static Analysis Results

This section presents the results of 3D static analyses conducted to investigate the influence of various loads on the overall response of IABs, thereby enhancing our understanding of their behavior. The analysis results are categorized based on three distinct load conditions: dead load alone, backfill pressure alone, and temperature load alone. This approach allows for a direct comparison of the response of the bridge elements under each individual load condition. Additionally, results are provided for combined load scenarios to more accurately reflect real-world conditions. The load combinations considered in the IAB analysis are as follows:

Expansion Case: This combination includes the dead load (D), temperature rise (T_R), and the maximum possible passive pressure on bridge abutments (E_p), represented as $D+T_R+E_p$.

Active Case: This combination consists of the dead load (D), temperature fall (T_F), and the minimum active earth pressure on bridge abutments (E_a), represented as $D+T_F+E_a$.

At-Rest Case: A reference model is examined without temperature loadings, incorporating only the dead load (D), and the at-rest earth pressure on bridge abutments (E_0), represented as $D+E_0$.

The proportional value of the secondary load in comparison to the individual dead load (D) will be determined by calculating the ratio of the response due to each secondary load (T_R, T_F, E_p, E_a, and E_0) to the response due to the dead load. This comparison will provide insight into the magnitude and direction of the secondary load effects relative to the primary dead load. Furthermore, the proportional value of secondary load effects will also be determined for the load combinations relative to the at-rest case ($D+E_0$). Specifically, the proportional value of the responses from the expansion case ($D+T_R+E_p$) and the contraction case ($D+T_F+E_a$). This comparison will help in understanding how the secondary loads interact with the dead load and whether they amplify or mitigate the overall structural responses, thus identifying their beneficial or detrimental effect.

The response was evaluated by measuring the bending moment and displacement over the girder, pile, and abutment.

3.2.1. The Effect of Various Loading Conditions in Substructure Response:

3.2.1.1. Abutment and Pile Deformation

In examining abutment deformation, as shown in Figure 3.7 and Tables 3.3, 3.4 and 3.5, key observations are made. Initially, the effects of individual load conditions are discussed, followed by an analysis of secondary load effects in various load combinations.

Individual Load Conditions:

Dead Load (D): Causes buckling deformation in the substructure, moving the bottom of the abutment toward the backfill with minimal displacement at the top, leading to bending and rotational deformations.

Temperature loads (T_R, T_F): Rising or falling temperature leads to displacement of the top of the abutment toward or away from the backfill, respectively, causing translational and rotational deformations.

Earth pressure (E_p, E_a, E_0): Causes the bottom of the abutment to displace away from the backfill, while the top displacement is minimal. This results in bending deformations at the bottom, most pronounced with passive earth pressure and negligible with active and at-rest pressures.

Temperature loads significantly affect the top of the abutment, while earth pressures and dead load mainly affect the bottom. Dead load causes more pronounced bending at the bottom, in the opposite direction of earth pressure effects.

Combined Load Scenarios:

Expansion Case ($D+T_R+E_p$): Temperature rising load amplifies the deformation caused by the dead load, resulting in increased overall translation deformation. Although the effect of passive earth pressure is smaller compared to thermal expansion, it opposes the deformation caused by the dead load, slightly reducing the overall deformation of the abutment.

Contraction Case ($D+T_F+E_a$): Temperature falling load causes deformations that oppose those induced by the dead load, resulting in a decrease in overall translation deformation at the bottom of the abutment but an increase at the top. The effect of active earth pressure is minimal compared to the effects of the temperature loads.

At-rest Case ($D+E_0$): Since no temperature load is included, the total deformation closely mirrors that induced by the individual dead load. The effects of at-rest earth pressure are minimal and have a negligible effect on the overall deformation.

In examining pile deformation, as illustrated in Figure 3.7, the displacement at the top of the pile, which supports the abutment, is related to the displacement observed at the bottom of the abutment that is discussed above.

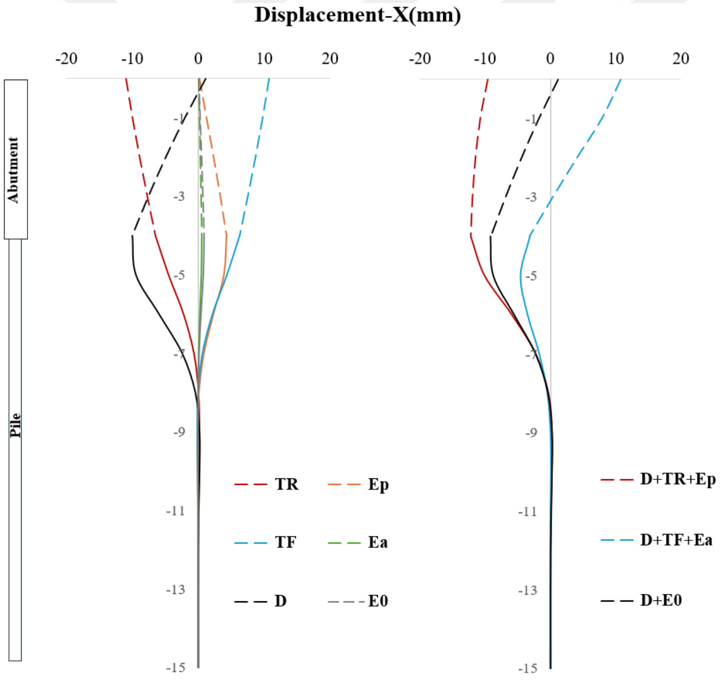

(a) (b)

Figure 3.7. Displacement diagrams of the abutment and pile: (a) individual loading, (b) load combinations.

Table 3.3. Reference values for displacement of the substructure for individual dead load and at-rest combination

Bridge element response		D	$D+E_0$
Displacement-X (m)	Abutment top	0.001106	0.001152
	Pile top	-0.010032	-0.009142

Table 3.4. Proportional values of secondary loads relative to the dead load for substructure displacement.

Bridge element response		D	T_R	E_p	T_F	E_a	E_0
Displacement-X (m)	Abutment top	1.00	-9.89	0.16	9.71	0.03	0.04
	Pile top	1.00	0.64	-0.43	-0.63	-0.06	-0.09

Table 3.5. Proportional values of expansion and contraction cases relative to the at-rest case for substructure displacement

Bridge element response		$D+E_0$	$D+T_R+E_p$	$D+T_F+E_a$
Displacement-X (m)	Abutment top	1.00	-8.38	9.35
	Pile top	1.00	1.33	0.34

3.2.1.2. Abutment and Pile Bending Moment

Regarding the bending moment in the abutment, as shown in Figures 3.8a and 3.8b and Tables 3.6, 3.7 and 3.8, the maximum moment occurs where the abutment connects with the main girder and gradually decreases downward. The dead load induces the largest bending moment due to its significant bending deformation effects. Combined load scenarios will be discussed to determine how secondary loads affect the resultant bending moment, either increasing or reducing it.

Expansion Case ($D+T_R+E_p$): The moment caused by rising temperature and passive earth pressure adds to the moment induced by the dead load, thus increasing the resultant moment.

Contraction Case ($D+T_F+E_a$): The moment caused by falling temperature opposes the moment from the dead load, thus reducing the resultant moment.

Regarding the bending moment in the pile, as observed in Figures 3.8c and 3.8d, and Tables 3.6, 3.7 and 3.8, the maximum moment occurs at the top of the pile and decreases progressively along its length, with the direction of the moment changing. This is because the middle portion of the pile bends in the opposite direction to the top. The combined effect of the loads determines whether the resultant moments are positive or negative.

Expansion Case ($D+T_R+E_p$): The moment caused by rising temperature adds to that induced by the dead load. However, the moment from passive earth pressure opposes the dead load moment, reducing the overall resultant moment. The combined effect of temperature and earth pressure loads determines whether the resultant bending moment at the top of the pile will be greater or smaller than the moment induced by the dead load alone.

Contraction Case ($D+T_F+E_a$): The moment caused by falling temperature opposes the dead load moment, leading to a reduction in the resultant moment.

The moments induced by active or at-rest earth pressures for both the abutment and pile are negligible compared to those from dead and thermal loads, unlike the more significant effects of passive pressures.

Finally, in the at-rest case ($D+E_0$), where no temperature load is present, the resultant bending moment for both the abutment and pile mirrors the individual moment induced by the dead load.

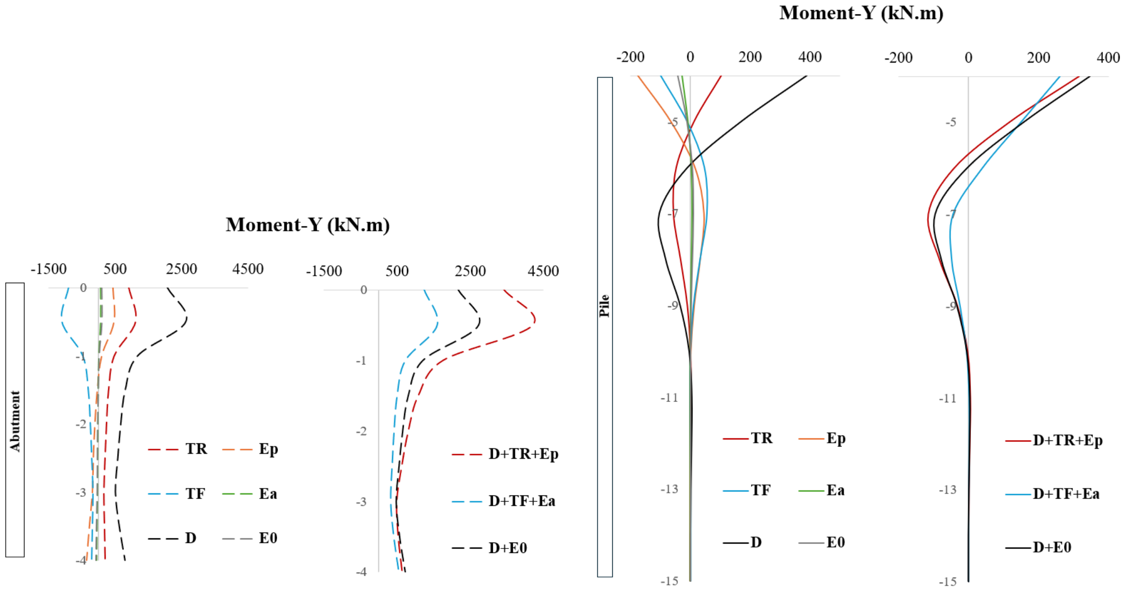

(a) (b) (c) (d)

Figure 3.8. Bending moment diagrams of the abutment: (a) individual loading, (b) load combinations; and the pile: (c) individual loading, (d) load combinations.

Table 3.6. Reference values for bending moment of the substructure for dead load and at-rest combination.

Bridge element response		D	$D+E_0$
Moment-Y (kN.m)	Abutment top	529.15	487.37
	Pile top	1136.88	1090.27

Table 3.7. Proportional values of secondary loads relative to the dead load for bending moment of the substructure.

Bridge element response		D	T_R	E_p	T_F	E_a	E_0
Moment-Y (kN.m)	Abutment top	1.00	0.44	0.21	-0.43	0.03	0.04
	Pile top	1.00	0.19	-0.33	-0.19	-0.05	-0.08

Table 3.8. Proportional values of expansion and contraction cases relative to the at-rest case for bending moment of the substructure

Bridge element response		$D+E_0$	$D+T_R+E_p$	$D+T_F+E_a$
Moment-Y (kN.m)	Abutment top	1.00	1.58	0.57
	Pile top	1.00	0.94	0.82

3.2.2. The Effect of Various Loading Conditions in Superstructure Response

3.2.2.1. Main Girder Bending Deformation

In examining main girder deformation, as shown in Figure 3.9 and Tables 3.9, 3.10 and 3.11, several observations are noted. The dead load causes the largest deformation due to bending in the main girder compared to temperature and earth pressure loads. Combined load scenarios will be discussed to determine how secondary loads affect the resultant deformation, either increasing or reducing it.

Expansion Case ($D+T_R+E_p$): The deformation caused by caused by rising temperature and passive earth pressure opposes the deformation caused by the dead load, leading to a reduction in total deformation.

Contraction Case (D+T_F+E_a): The deformation caused by falling temperature aligns with the deformation from the dead load, resulting in an increase in total deformation.

The deformation caused by active and at-rest earth pressures is relatively small and can be ignored compared to the effects of passive pressures. In the at-rest case (D+E_0), where no temperature load is present, the resultant deformation of the main girder mirrors the individual deformation caused by the dead load.

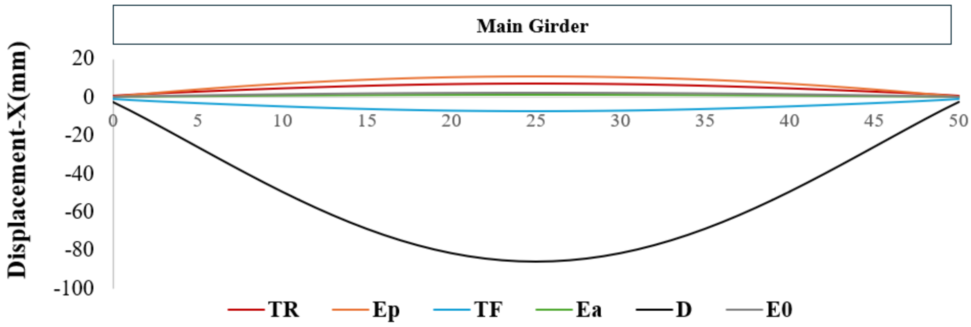

(a)

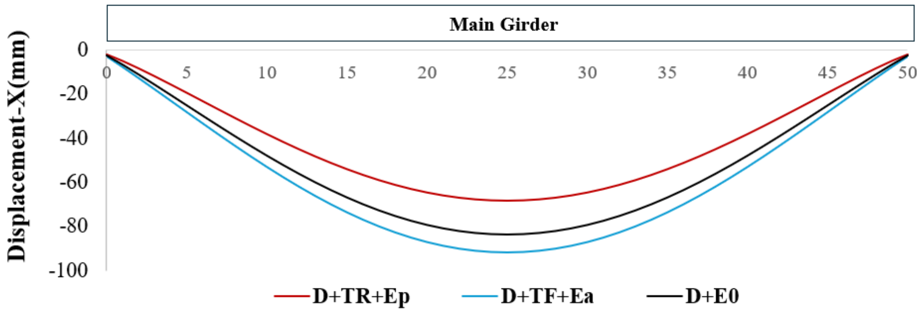

(b)

Figure 3.9. Displacement diagrams of the main girder: (a) individual loading, (b) load combinations.

Table 3.9. Reference values for displacement of the main girder for dead load and at-rest combination.

Main girder response		D	D+ E_0
Displacement-Z (m)	Midpoint	-0.085935	-0.083695

Table 3.10. Proportional values of secondary loads relative to the dead load for displacement of the main girder.

Main girder response		D	T_R	E_p	T_F	E_a	E_0
Displacement-Z (m)	Midpoint	1.00	-0.08	-0.13	0.08	-0.02	-0.03

Table 3.11. Proportional values of expansion and contraction cases relative to the at-rest case for displacement of the main girder.

Main girder response		$D+E_0$	$D+T_R+E_p$	$D+T_F+E_a$
Displacement-Z (m)	Midpoint	1.00	0.81	1.09

3.2.2.2. Main Girder Bending Moment

Regarding the bending moment in the main girder, as illustrated in Figure 3.10 and Tables 3.12, 3.13 and 3.14, several observations are noted. The bending moment induced by the dead load is the largest compared to secondary loads.

Combined load scenarios will be discussed to determine how secondary loads affect the resultant bending moment, either increasing or reducing it.

Expansion Case ($D+T_R+E_p$): The moment caused by rising temperature and passive earth pressure opposes the dead load moment, leading to a reduction in the resultant moment at the midpoint of the main girder.

Contraction Case ($D+T_F+E_a$): The moment caused by falling temperature aligns with the dead load moment, leading to an increase in the resultant moment at the midpoint of the main girder.

The situation is reversed for the moments at the end of the main girder for both expansion and contraction cases.

The moments induced by active and at-rest earth pressures are relatively small and can be ignored compared to the effects of passive pressures. In the at-rest case ($D+E_0$), where no temperature load is present, the resultant bending moment of the main girder mirrors the individual deformation caused by the dead load.

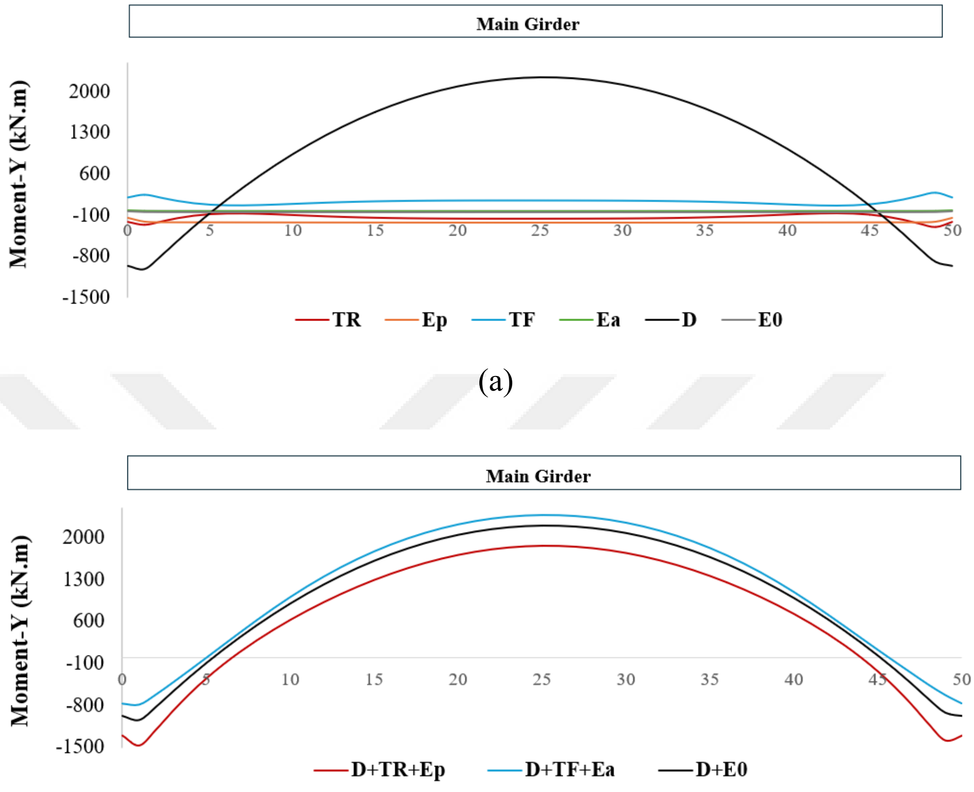

(a)

(b)

Figure 3.10. Bending moment diagrams of the main girder: (a) individual loading, (b) load combinations

Table 3.12. Reference values for bending moment of the main girder for dead load and at-rest combination

Bridge element response		D	D+E_0
Moment-Y (kN.m)	Midpoint	1136.88	1090.27
	Edge	-1354.55	-1383.84

Table 3.13. Proportional values of secondary loads relative to the dead load for bending moment of the main girder.

Main girder response		D	T_R	E_p	T_F	E_a	E_0
Moment-Y	Midpoint	1.00	-0.14	-0.20	0.13	-0.03	-0.04
	Edge	1.00	0.15	0.11	-0.15	0.01	0.02

Table 3.14. Proportional values of expansion and contraction cases relative to the at-rest case for bending moment of the main girder.

Bridge element response		$D+E_0$	$D+T_R+E_p$	$D+T_F+E_a$
Moment-Y	Midpoint	1.00	0.70	1.16
	Edge	1.00	1.23	0.84

3.3. Conclusion

This study, supported by various investigations including field instrumentation, laboratory experiments, and numerical modeling, highlighted the significant influence of secondary loads on the overall behavior of IAB elements. These secondary loads can have either beneficial or detrimental effects. The effects of secondary loads can be summarized for each element as follows:

For Abutment: Rising temperature and earth pressure increase the total moment, while falling temperature decreases the total moment. The maximum moment is achieved during the expansion case.

For Pile: Falling temperature and earth pressure decrease the total moment, while rising temperature increases the total moment. The combined effect of temperature and earth pressure loads determines whether the resultant bending moment at the top of the pile will be greater or smaller than the moment induced by the dead load alone.

For Main Girder: At the midpoint, rising temperature and earth pressure decrease the total moment, while falling temperature increases the total moment. The maximum moment occurs during the contraction case. While, At the end of the main girder, the effects are opposite to those at the midpoint, with the maximum moment being achieved during the expansion case.

The study notes that while earth pressure loads have a relatively minor effect compared to temperature effects, passive earth pressure loads have the most pronounced effect compared to active and at-rest earth pressures.

Therefore, secondary loads such as temperature and earth pressure can significantly affect IAB elements, either positively or negatively. Accurate assumptions for these loads during the design phase are critical to ensure the structural integrity and performance of the bridge.

It is noteworthy to acknowledge that the observed behavior is intricately tied to the specific design parameters and magnitudes employed within these analytical models. Consequently, any modifications to these parameters have the potential to exert a substantial influence on the overall response of the bridge structure.

4. COMPARATIVE ANALYSIS OF EARTH PRESSURE METHODS AND THEIR STRUCTURAL EFFECT ON IABs

The backfill soil behind abutments experiences horizontal cyclic displacements caused by thermal expansion and contraction of girders. Depending on the displaced position of the abutment, earth pressures can range from minimum active to maximum passive. If the limiting equilibrium approach is adopted for abutment-backfill interaction (refer to Section 2.4.1.1), classical earth pressure theories such as those by Rankine (1857), Coulomb (1776), and Broms and Ingelson (1971) can be used to predict the magnitude of the earth pressure behind the abutment. These theories assume that the soil mass experiences sufficient displacement for full mobilization of soil friction, leading to the earth pressure reaching its limiting active and passive values.

While traditional theories are generally applicable for active earth pressure, where limit values can occur under minimal displacement, passive earth pressure may not always fully mobilize soil friction due to insufficient displacement of the soil mass behind the abutment. Consequently, the resulting passive earth pressure may not reach the expected limiting values. The determination of the resulting passive lateral pressure behind the abutments for a specific displacement cannot be simply derived from static calculations alone.

Consequently, numerous experimental investigations were conducted by bridge engineers and geologists to establish empirical relationships between passive lateral pressure and the displacement of the abutment. These studies include those by Barker et al. (1991), England et al. (2000), MassDOT (2007), Arsoy (2004).

Several studies have highlighted significant variations in outcomes resulting from current methods used for calculating passive earth pressure and their significant influences on the overall behavior of the IAB (Huang et al., 2022, Liu et al., 2022, Huang et al., 2020, and Huntley et al.,2013) (refer to Section 2.4.1.2). Hence, it is worthwhile to investigate different methods for calculating passive earth pressure to highlight their varying outcomes and their subsequent effects on the overall response of IABs. To achieve this objective, seven different methods for calculating the passive earth pressure coefficient will be examined under various thermal displacement scenarios.

Additionally, six different methods were evaluated against the results of both long-term and short-term field monitoring of IABs.

Subsequently, a simple 3D finite element model is created using MIDAS CIVIL software. Within this model, five different methods for calculating the passive earth pressure behind the abutment will be investigated across different thermal displacement scenarios to assess their subsequent effects on the overall response of IABs. The response was evaluated by measuring the bending moment and displacement over the girder, pile, and abutment.

4.1. Assessment of Earth Pressure behind the Abutment Utilizing Various Calculation Methods

There are many theories, empirically based or analytically derived approaches, used for predicting the passive lateral earth pressure, which exerts the most significant influence on the IAB's response compared to active and at-rest pressures (refer to Section 3.2). While classical theories such as Rankine theory (1857) for active pressure and the equation developed by Jaky in 1944 for at-rest earth pressure are utilized to calculate these pressures, with the distribution typically considered as a simple triangle, different design standards worldwide recommend various methods to calculate passive earth pressure behind the abutment and suggest different distributions for it. Some of these methods depend on the abutment displacement, while others are independent of it.

This section aims to compare various methods for calculating the passive earth pressure coefficient using different methods across various displacements. Initially, a detailed explanation of the calculation process for the passive earth pressure coefficient using different methods across various displacements will be provided. Following this, graphical representations will illustrate the comparisons, followed by a discussion of the findings.

4.1.1. Calculation of Passive Earth Pressure behind the Abutment

In this section, seven different methods for calculating the passive earth pressure coefficient will be examined under different displacement scenarios. For these calculations, typical properties of medium granular backfill soil were utilized, as shown in Table 3.2 (refer to Section 3.1.3).

The methods and calculations are presented as follows:

- Coulomb Theory, (1776)

Coulomb's passive earth pressure coefficient (K_{pC}) can be obtained by Equation (2.2b) (refer to Section 2.4.1.1). In this context, the angle of friction between the backfill and the abutment (δ) is taken as half of the friction angle of the backfill (1/2 φ). The angle from the backfill surface to the horizontal (β) is 0, and the angle from the face of the wall to the vertical (θ) is 0. The calculated Coulomb's passive earth pressure coefficient is provided as follows:

$$K_{pC} = \frac{cos^2(\varphi+\theta)}{cos^2\theta cos(\delta-\theta)\left(1-\sqrt{\frac{sin(\delta+\varphi)sin(\varphi+\beta)}{cos(\delta-\theta)cos(\beta-\theta)}}\right)^2} = \frac{cos^2(34)}{cos^2 0 cos\left(\frac{34}{2}\right)\left(1-\sqrt{\frac{sin\left(\frac{34}{2}+34\right)sin(34)}{cos\left(\frac{34}{2}\right)cos(0)}}\right)^2} = 6.77$$

- Rankine Theory, (1857)

Rankine's passive earth pressure coefficient (K_{pR}), calculated using Equation (2.5b) (refer to Section 2.4.1.1), with the angle from the backfill surface to the horizontal (β) set to 0, is provided as follows:

$$\mathrm{K_{pR}} = \tan^2\left(45+\frac{\varphi}{2}\right) = \tan^2\left(45+\frac{34}{2}\right) = 3.54$$

- Burke–Chen method, (1993,1997)

Burke and Chen modified Rankine theory (1857) by multiplying Rankine's passive earth pressure coefficient by 2/3. Hence, the calculated Burke–Chen passive earth pressure coefficient (K_{BC}) is provided as follows:

$$K_{BC} = \frac{2}{3} K_{pR} = \frac{2}{3} * 3.54 = 2.36$$

- Barker Method (1991)

The Barker’s passive earth pressure coefficient (K_B) is calculated using Equation (2.6) (refer to Section 2.4.1.1). For the at-rest lateral earth pressure coefficient, Jaky's equation (1944) is used, as detailed in Equation (2.1) (refer to Section 2.4.1.1). The full passive earth pressure is assumed to be based on Rankine theory (1857). These calculations are provided as follows:

$$K_0 = 1 - \sin(\varphi) = 1 - \sin(34) = 0.44$$

$$K_B = K_0 + \phi\Delta \leq K_{pR} = 0.44 + 35\,\Delta \leq 3.54$$

The passive earth pressure coefficient curve according to Barker (1991) is presented in Figure 4.3 for various Δ/H values.

- NCHRP Method (Clough and Duncan, 1991)

For the medium granular sandy backfill soil with an angle of friction of 34°, the passive earth pressure coefficient (K_{NCHRP}) curve is approximated by using the intermediate curve between those for 30° and 37° angles of friction, as shown in Figure 4.1. The passive earth pressure coefficient curve according to NCHRP (1991) is presented in Figure 4.1 for various Δ/H values.

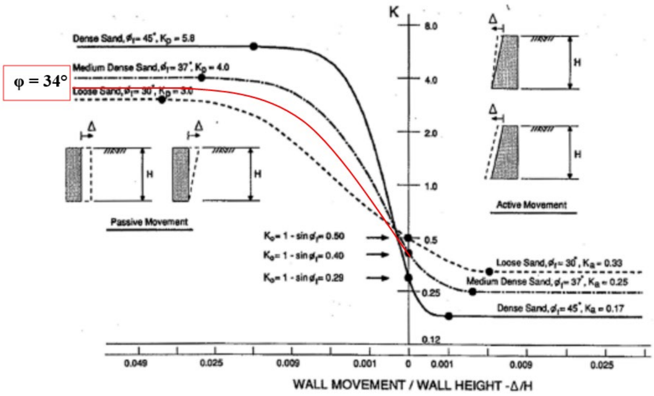

Figure 4.1. Relationship between wall displacement and earth pressure sand according to NCHRP for φ = 34°.

- England Method (2000), (PD6694-1, 2011)

England’s passive earth pressure coefficient (K*) is calculated using Equation (2.9) (refer to Section 2.4.1.1). For the at-rest lateral earth pressure coefficient, the same method used in the Barker method (1991) is employed. The full passive earth pressure coefficient, which should be derived from the design value of the triaxial test, will be taken as Coulomb’s passive earth pressure coefficient (K_{pC}). For a stiff abutment fixed at both the top and bottom, the parameter Δ' is approximately 0.5 times Δ. The elastic modulus of the subgrade (Es) is assumed to be 50 MPa, and the coefficient C_E, which depends on the elastic modulus of the subgrade in MPa, is determined by Equation (2.10) (refer to Section 2.4.1.1). The calculations are provided as follows:

$$C_E = 0.051E_S + 14.9 = 0.051\,(50) + 14.9 = 17.45$$

$$K^* = K_0 + \left(\frac{C_E\,\Delta'}{H}\right)^{0.6} K_{pC} = K_0 + \left(\frac{17.45 * 0.5\,\Delta}{H}\right)^{0.6} 6.77$$

The passive earth pressure coefficient curve according to England (2000) is shown in Figure 4.3 for various Δ/H values.

- Arsoy Method (2004)

The resultant force at plastic equilibrium (E_{Pmax}), representing the full passive earth pressure, is assumed using both Rankine (1857) and Coulomb (1776) theories.

The abutment movement is assumed to contribute equally to both translation and rotation. Consequently, the passive earth pressure coefficient curve is derived from the average of the resultant force curves for medium density in pure rotation and pure translation, as shown in Figure 4.2.

The passive earth pressure coefficient curve according to Arsoy (2004) for both Rankine and Coulomb theories, denoted as, K_{AC} and K_A respectively, is presented in Figure 4.3 for various Δ/H values.

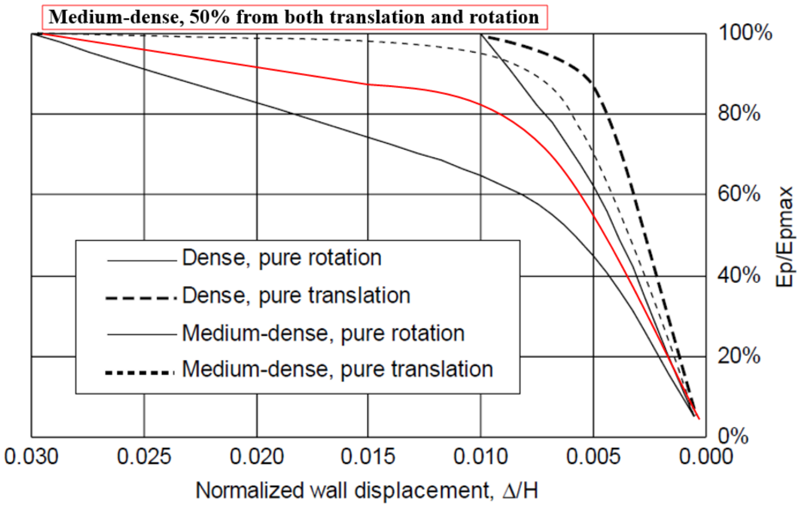

Figure 4.2. The resultant force curve for medium density, with the abutment movement contributing 50% from both translation and rotation, according to the Arsoy (2004) method.

4.1.2. Results and Conclusion of the Assessment

The investigation reveals significant differences in the estimation of the passive earth pressure coefficient across various methods, as shown in Figure 4.3.

Displacement-Independent Methods:

- Coulomb theory (1776): Compared to other displacement-independent methods, Coulomb theory produces the highest passive earth pressure coefficient (K_{pC}).
- Rankine theory (1857): This method tends to yield lower estimates of the passive earth pressure coefficient (K_{pR}) compared with Coulomb theory (1776), due to its assumption of negligible friction between the wall and the backfill.
- Burke and Chen method (1993, 1997): This method, modified from Rankine theory (1857), gives the lowest passive earth pressure coefficient (K_{BC}) among displacement-independent methods.

Displacement-Dependent Methods:

- Barker method (1991): This method proposes a passive earth pressure coefficient (K_B) that shows a linear increase from the at-rest earth pressure coefficient to Rankine passive earth pressure coefficient (K_{pR}). It underestimates the passive earth pressure under small displacements but approaches the results of other methods as displacement increases.

- NCHRP method (1991): The passive earth pressure coefficient (K_{NCHRP}) follows a non-linear path with larger values to reach Rankine passive earth pressure coefficient (K_{pR}) compared with the Barker method (1991). This method assumes an average value for the passive earth pressure coefficient (K_{NCHRP}) that falls between other methods, achieving full passive earth pressure at a displacement magnitude similar to that of the Barker method (1991).
- England method (2000): This method shows a relatively smaller increase in the passive earth pressure coefficient (K_E) with displacement, requiring larger displacements to reach its assumed full passive earth pressure, which is based on Coulomb theory (1776).
- Arsoy method (2004): Applicable to both Rankine and Coulomb full passive pressure assumptions. The passive earth pressure coefficients (K_{AC}, K_{AR}) in Arsoy method reach the full passive earth pressure coefficient under larger displacements for both assumptions compared to the other methods, excluding England method (2000).

In summary, displacement-independent methods tend to overestimate coefficients under minimal displacement, with Coulomb theory (1776) providing the highest estimates and Burke and Chen method (1993, 1997) the lowest.

Among displacement-dependent methods, the Barker method (1991) and the NCHRP method (1991) show varying paths to achieving full passive earth pressure at a lower displacement magnitude, while the England method (2000) and the Arsoy method (2004) require larger displacements to reach full passive values.

The choice of method significantly affects the estimated passive earth pressure coefficients, which in turn affects the IAB responses.

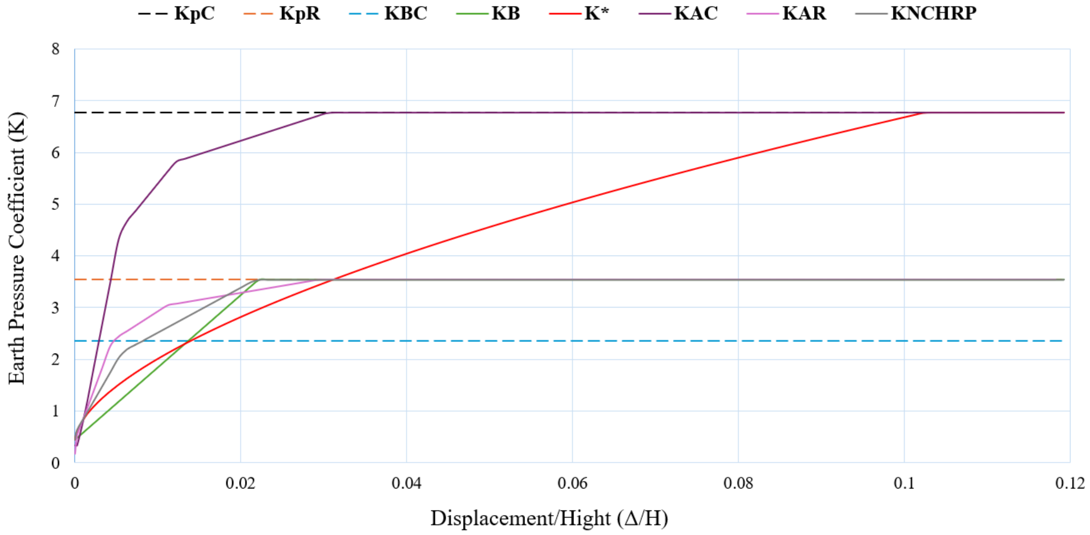

Figure 4.3. Comparison of passive earth pressure coefficient calculations obtained through various methods Among different abutment displacements.

4.2. Validation of Various Methods for Calculating Earth Pressure behind the Abutment

This section aims to verify six different methods by comparing their results with field monitoring results obtained from both short-term and long-term studies. Short-term monitoring includes studies by Civjan et al. (2013), which spanned approximately 2.5 years, and Nam and Park (2015), which examined data over about 3 years. For long-term monitoring, data from Kim and Laman (2012) covering approximately 7 years is included. These studies provide a comprehensive range of monitoring data for analysis.

The methods under consideration include Rankine theory (1957), Barker method (1991), Massachusetts method (2007), NCHRP method (1991), England method (2000), and Arsoy method (2004).

Note that some values were unavailable in the studies, necessitating assumptions during the calculations. Therefore, assumptions in earth pressure calculations for various methods are provided as follows:

- The angle of friction between the backfill and the abutment (δ) is assumed to be half of the friction angle of the backfill (1/2 φ). The angle from the backfill surface to the horizontal (β) is assumed to be 0, and the angle from the face of the wall to the vertical (θ) is assumed to be 0.

- For the England method (2000), the full passive earth pressure coefficient, which should be derived from the design value of the triaxial test, will be taken as Coulomb's passive earth pressure coefficient. The abutment is assumed to be fixed at both the top and bottom.
- For the Arsoy method (2004), the full passive earth pressure is assumed to be Rankine's passive earth pressure. The abutment movement is assumed to contribute equally to both translation and rotation.
- The earth pressure distribution is assumed to be a simple triangular distribution for Rankine theory (1957), Barker method (1991), NCHRP method (1991), Massachusetts method (2007), and for the field monitoring data of earth pressure.
- For the England method (2000), the earth pressure distribution is defined based on PD6694-1:2011, as illustrated in Figure 2.15 (refer to Section 2.4.1.1).
- Due to the lack of a defined earth pressure distribution for the Arsoy method, the magnitude of the earth pressure at the point of application of the resultant force is considered.

Additional assumptions specific to each study will be outlined separately.

Considering the last assumption above, the earth pressure calculated by the Arsoy method (2004) is expected to be higher in magnitude. Therefore, additional comparisons will be made regarding the resultant passive force, its application point, and the maximum bending moment at the top of the abutment.

Therefore, comparisons will include:

- The maximum earth pressure, resultant passive force with the point of application, and the maximum bending moment at the top of the abutment, as obtained from field monitoring versus those derived from various methods.
- Field monitoring results are taken as reference values, and the variations from different earth pressure methods are proportionally compared against these reference values.
- Passive earth pressure distributions from different methods (excluding Arsoy, 2004) compared to field monitoring results, assuming a simple triangular distribution.

4.2.1. Civjan et al. (2013) Study

The first study selected for the investigation was conducted by Civjan et al. in 2013. It involved short-term monitoring of two in-service IABs located in Vermont. The primary focus of this validation was on the Middlesex Bridge, a straight bridge with a length of 43 m and characterized as a single-span steel girder bridge. The study examines the substructure response over a span of 30 months. Data logging for the Middlesex Bridge began approximately six weeks after it was opened to traffic. The research analyzed variations in substructure displacements and backfill pressures under different ambient temperatures, including hot, cold, and moderate conditions. Detailed specifications of Middlesex Bridge can be found in Figure 4.4.

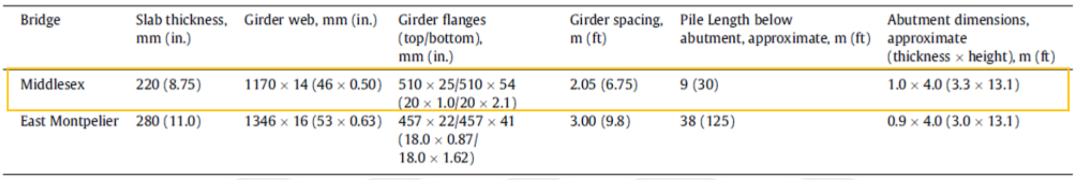

Bridge	Slab thickness, mm (in.)	Girder web, mm (in.)	Girder flanges (top/bottom), mm (in.)	Girder spacing, m (ft)	Pile Length below abutment, approximate, m (ft)	Abutment dimensions, approximate (thickness × height), m (ft)
Middlesex	220 (8.75)	1170 × 14 (46 × 0.50)	510 × 25/510 × 54 (20 × 1.0/20 × 2.1)	2.05 (6.75)	9 (30)	1.0 × 4.0 (3.3 × 13.1)
East Montpelier	280 (11.0)	1346 × 16 (53 × 0.63)	457 × 22/457 × 41 (18.0 × 0.87/ 18.0 × 1.62)	3.00 (9.8)	38 (125)	0.9 × 4.0 (3.0 × 13.1)

Figure 4.4. Bridges details of two in-service IABs located in Vermont (Civjan et al, 2013).

The abutments of the bridge were backfilled with compacted granular material. According to reports from the Vermont Agency of Transportation, the soil conditions at the site were defined to be medium dense, with an internal friction angle (φ) of approximately 35°.

Regarding the field monitoring data, Figure 4.5 presents average readings at each pressure cell depth, as well as the peak individual cell values (both minimum and maximum) for each abutment. The peak value was recorded in the middle row of pressure cells at the Middlesex Bridge in 2010 (Abutment 1), reaching approximately 33.75 KN/m^2 on the hottest day of the year.

Additionally, Figure 4.6 shows the daily substructure displacements for the Middlesex Bridge (Abutment 1), on the hottest day throughout the 2009-2010 year. The peak value observed was approximately 0.012 m.

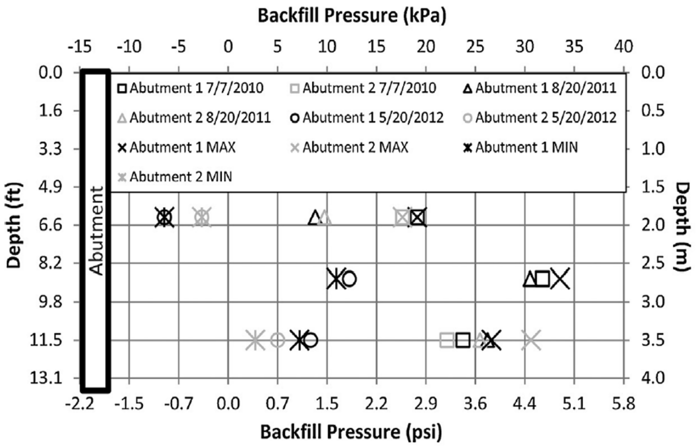

Figure 4.5. Middlesex Bridge abutments backfill earth pressures on hottest days of the year (Civjan et al, 2013).

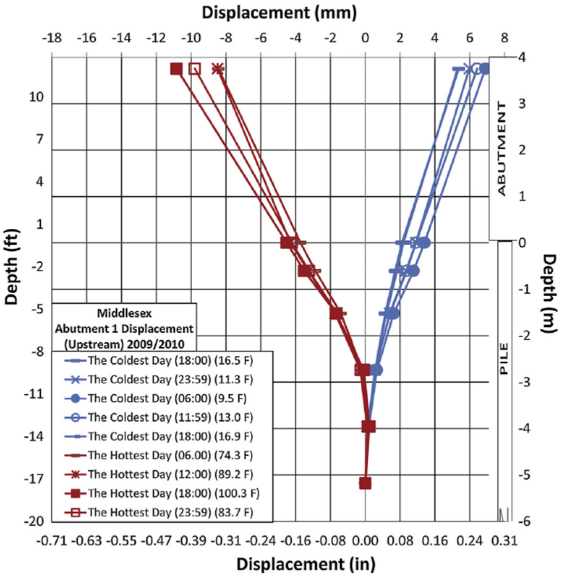

Figure 4.6. Daily bridge substructure displacements for the Middlesex Bridge (Abutment 1) on the hottest and coldest days of the year 2009-2010 (Civjan et al, 2013).

Assumptions:

- The unit weight (γ) of the backfill soil is assumed to be 18.7 kN/m³, and the elastic modulus of the subgrade (Es) is assumed to be 50 MPa, due to the absence of specific data.
- The maximum earth pressure was recorded on the hottest day in 2010, whereas the maximum displacement was recorded on the hottest day of the 2009-2010 period.

To proceed with the analysis, it will be assumed that these measurements were taken simultaneously, despite the lack of confirmation.

The earth pressure behind the abutment will be determined using various methods, taking into account the properties of the soil, the height of the abutment, and the maximum recorded displacement and earth pressure, as provided in the following Table 4.1.

Table 4.1. Properties of the soil and abutment, and maximum recorded data as reported by Civjan et al. (2013).

Abutment height (m)	φ Internal angle of friction (◦)	γ the unit weight (kN/m³)	Maximum earth pressure (kN/m^2)	Maximum Displacement (m)
4	35	18.7	33.75	0.012

The methodologies used for determining the earth pressure behind the abutment include the Rankine theory (1957), Barker method (1991), England method (2000), the NCHRP method (1991), and the Arsoy method (2004). The Massachusetts method (2007) is not included in this comparison as it is designed for dense backfill.

For the Rankine theory (1957) and the Barker method (1991), the passive earth pressure coefficient (K_{pR} and K_B) is determined using Equations (2.5b) and (2.6), respectively (refer to Section 2.4.1.1). The calculations are presented as follows:

$$\mathrm{K_{pR}} = \tan^2\left(45+\frac{\varphi}{2}\right) = \tan^2\left(45+\frac{35}{2}\right) = 3.69$$

$$K_B = K_0 + \phi\Delta \leq K_{pR} = (1-\sin(35)) + (35 * 0.012) = 0.85$$

For the NCHRP method (1991), the passive earth pressure coefficient for medium granular sandy backfill soil with an angle of friction of 35° is approximately determined using Figure 4.1 (refer to Section 4.1.1). For a relative abutment displacement, defined as the ratio of displacement to abutment height (Δ/H), K_{NCHRP} is as follows,

$$\Delta/\mathrm{H} = 0.012/4 = 0.003 \quad \rightarrow \quad K_{NCHRP} = 1.5$$

For the England method (2000), England's passive earth pressure coefficient (K^*) is calculated using Equation (2.9) (refer to Section 2.4.1.1). The calculations are provided as follows:

$$K_{pC} = \frac{cos^2(\varphi+\theta)}{cos^2\theta cos(\delta-\theta)\left(1-\sqrt{\frac{sin(\delta+\varphi)sin(\varphi+\beta)}{cos(\delta-\theta)cos(\beta-\theta)}}\right)^2} = \frac{cos^2(35)}{cos^2 0 cos\left(\frac{35}{2}\right)\left(1-\sqrt{\frac{sin\left(\frac{35}{2}+35\right)sin(35)}{cos\left(\frac{35}{2}\right)cos(0)}}\right)^2} = 7.36$$

$$\mathrm{C_E} = 0.051\mathrm{E_S} + 14.9 = 0.051(50) + 14.9 = 17.45$$

$$\mathrm{K}^* = \mathrm{K_0} + \left(\frac{\mathrm{C_E}\ \grave{\Delta}}{\mathrm{H}}\right)^{0.6} \mathrm{K_{pC}} = 0.43 + \left(\frac{17.45 * 0.5 * 0.012}{4}\right)^{0.6} 7.36 = 1.25$$

For the Arsoy method (2004), the resultant passive force (E_P) for a relative abutment displacement defined as the ratio of displacement to abutment height ($\Delta/H=0.003$) is determined using average of the resultant force curves for medium density in pure rotation and pure translation, as shown in Figure 4.2. (refer to Section 4.1.1). The full passive resultant force (E_{Pmax}) and the resultant passive force (E_P) is determined as follows:

$$\mathrm{E_{Pmax}} = 0.5\, \mathrm{K_{pR}}\, \gamma\, \mathrm{H}^2 = 0.5 * 3.69 * 18.7 * 4^2 = 552.02\ \mathrm{kN/m}$$

$$\frac{\mathrm{E_P}}{\mathrm{E_{Pmax}}} = 33\% \quad \rightarrow \quad \frac{\mathrm{E_P}}{552.02} = 0.33 \quad \rightarrow \quad \mathrm{E_P} = 182.17\ \mathrm{kN/m^2}$$

The point of application for the resultant force will be determined using Figure 2.11 (refer to Section 2.4.1.1). Accordingly, the abutment (y/H) ratio is found to be 0.4125.

The maximum lateral earth pressure is calculated using Equation (2.3) (refer to Section 2.4.1.1), and the resultant force is determined by the total area of the pressure diagram. The results are listed in Tables 4.2 and 4.3, where field monitoring results are used as reference values. Variations from different earth pressure methods are proportionally compared against these reference values.

Furthermore, Figure 4.7 illustrates passive earth pressure distributions from various methods (excluding Arsoy, 2004) alongside field monitoring results.

Table 4.2. Comparison of results from various earth pressure methods and field monitoring results as reported by Civjan et al. (2013) for earth pressure values.

	Earth passive pressure (kN/m^2)	Proportional changes
Field	33.75	1
Rankine (1857)	276.02	8.12
Barker (1991)	63.31	1.88
NCHRP (1991)	112.2	3.32
England (2000)	46.89	1.40
Arsoy (2004)	53.51	1.59

Table 4.3. Comparison of results from various earth pressure methods and field monitoring results as reported by Civjan et al. (2013) for resultant force, its point of application, and maximum bending moment.

	Resultant passive force (kN)	Application point (H-y) (m)	Bending moment (kN.m)
Field	101.50	2.67	271
Rankine (1857)	552.02	2.67	1473.9
Barker (1991)	126.63	2.67	338.10
NCHRP (1991)	224.20	2.67	598.61
England (2000)	125.67	2.34	294.07
Arsoy (2004)	182.17	2.35	428.10

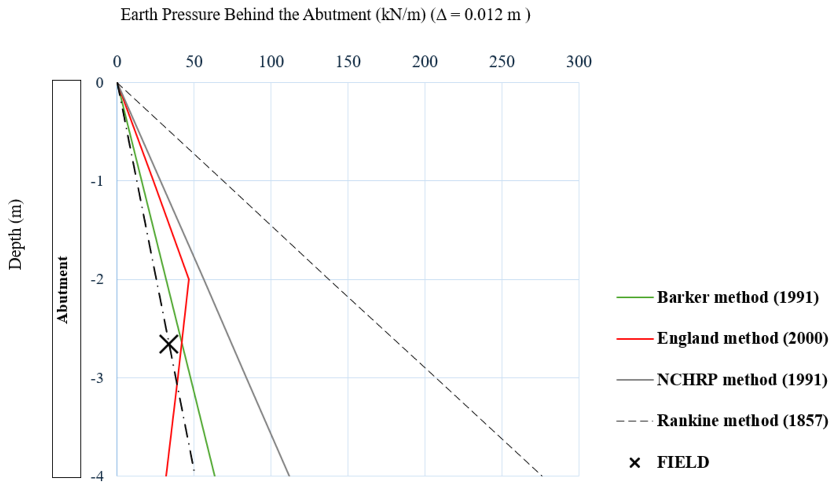

Figure 4.7. Comparison of results from various earth pressure methods and field monitoring results as reported by Civjan et al. (2013) for earth pressure distributions.

4.2.2. Nam and Park (2015) Study

The second study selected for the validation was conducted by Nam and Park (2015). This study involved short-term monitoring of an in-service IAB located on the Daejun-Tongyong Highway in Gyungsangnamdo, Korea. The bridge is characterized as a three-span continuous concrete slab bridge with a length of 90 m. The skew angle of the tested IAB is 30°, and the radius of curvature is 2 km.

The abutments have a height of 4 m. To minimize earth pressure on the abutments, earth pressure relief zones were installed with a width of approximately 1 meter behind the abutments and a height of 3.3 m from the bottom of the abutments.

The study noted that the materials in the earth pressure relief zones, denoted as SB-3, were subbase course materials with cohesive materials removed. According to the AASHTO soil classification system, SB-3 was classified as A-1-a(0). The elastic modulus of SB-3 was 14.7 MPa. The earth pressure relief zones were filled with SB-3 using a backhoe shovel without any compaction, resulting in a total unit weight of 15.3 kN/m^3. Direct shear tests conducted in accordance with ASTM D 3080 (ASTM 1999) revealed an internal friction angle of 53.1°.

The study examines the substructure response over a period from 1999 to 2002. The research analyzed variations in substructure displacements and backfill pressures under different ambient conditions.

Regarding the field monitoring data, Figure 4.8 presents the abutment displacement due to thermal loads measured from 2001 to 2002, showing a maximum passive displacement of 0.009 m.

Additionally, the maximum earth pressure due to thermal loads was recorded during the same period, as depicted in Figure 4.9. The peak value observed was approximately 45 KN/m^2.

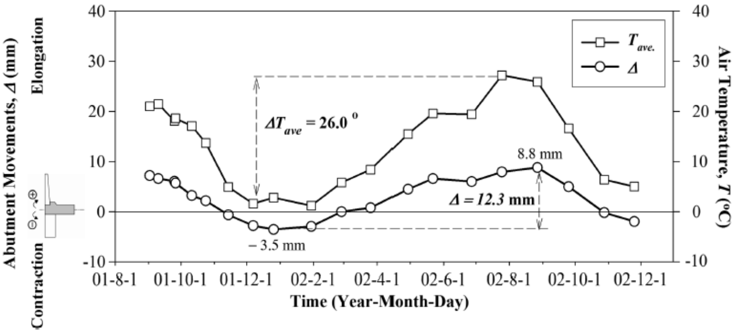

Figure 4.8. Abutment displacement and thermal exchange versus time as reported by Nam and Park (2015).

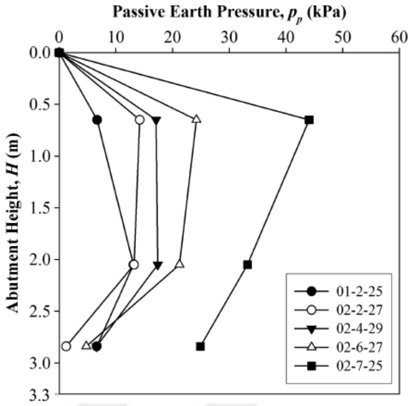

Figure 4.9. Changes in passive earth pressure distribution over time as reported by Nam and Park (2015).

The earth pressure behind the abutment will be determined using various methods, taking into account the properties of the soil, the height of the abutment, the maximum recorded displacement and earth pressure as provided in the following Table 4.4.

Table 4.4. Properties of the soil and abutment, and maximum recorded data as reported by Nam and Park (2015).

Abutment height (m)	φ Internal angle of friction (◦)	γ the unit weight (kN/m³)	Maximum earth pressure (kN/m²)	Maximum Displacement (m)
3.3	53	15.1	45	0.009

The methodologies employed to determine the earth pressure behind the abutment include the Rankine theory (1957), Massachusetts method (2007), Barker method (1991), England method (2000), and the Arsoy method (2004). The NCHRP method

(1991) is not considered in this comparison. This is because the NCHRP method (1991) lacks a curve corresponding to soil conditions with a friction angle of 53°.

It is important to highlight that the SB-3 has a high friction angle and a low unit weight. As a result, the coefficients of passive earth pressure obtained from some methods used to compute the passive earth pressure behind the abutment may not provide realistic estimates.

For the Rankine theory (1957) and the Barker method (1991), the passive earth pressure coefficient (K_{pR} and K_B) is determined using Equations (2.5b) and (2.6), respectively (refer to Section 2.4.1.1). The calculations are presented as follows:

$$\mathrm{K_{pR}} = \tan^2\left(45+\frac{\varphi}{2}\right) = \tan^2\left(45+\frac{53}{2}\right) = 8.93$$

$$K_B = K_0 + \phi\Delta \leq K_{pR} = (1-\sin(53)) + (35 * 0.009) = 0.52$$

For the England method (2000), England’s passive earth pressure coefficient (K^*) is calculated using Equation (2.9) (refer to Section 2.4.1.1). The calculations are provided as follows:

$$\mathrm{K_{pC}} = \frac{\cos^2(\varphi+\theta)}{\cos^2\theta\cos(\delta-\theta)\left(1-\sqrt{\frac{\sin(\delta+\varphi)\sin(\varphi+\beta)}{\cos(\delta-\theta)\cos(\beta-\theta)}}\right)^2} = \frac{\cos^2(53)}{\cos^2 0\cos\left(\frac{53}{2}\right)\left(1-\sqrt{\frac{\sin\left(\frac{53}{2}+53\right)\sin(53)}{\cos\left(\frac{53}{2}\right)\cos(0)}}\right)^2} = 101.07$$

$$\mathrm{C_E} = 0.051\mathrm{E_S} + 14.9 = 0.051\,(14.7) + 14.9 = 15.65$$

$$\mathrm{K^*} = \mathrm{K_0} + \left(\frac{\mathrm{C_E}\,\grave{\Delta}}{\mathrm{H}}\right)^{0.6}\mathrm{K_{pC}} = 0.20 + \left(\frac{15.65 * 0.5 * 0.009}{3.3}\right)^{0.6} 101.07 = 10.25$$

For the Arsoy method (2004), the resultant passive force (E_P) for a relative abutment displacement defined as the ratio of displacement to abutment height ($\Delta/H=0.0027$) is determined using average of the resultant force curves for dense density in pure rotation and pure translation, as could be Figure 4.10 .

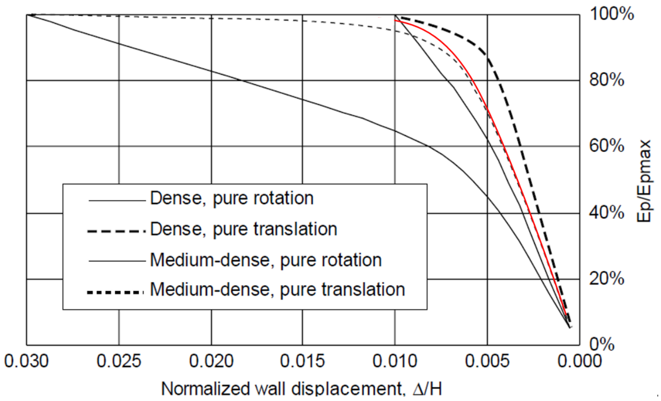

Figure 4.10. The resultant force curve for dense density, with the abutment movement contributing 50% from both translation and rotation, according to the Arsoy (2004) method.

The full passive resultant force (E_{Pmax}) and the resultant passive force (E_P) is determined as follows:

$$E_{Pmax} = 0.5\, K_{pR}\, \gamma\, H^2 = 0.5 * 8.93 * 15.1 * 3.3^2 = 734.22 \text{ kN/m}$$

$$\frac{E_P}{E_{Pmax}} = 67\% \quad \rightarrow \quad \frac{E_P}{734.22} = 0.67 \quad \rightarrow \quad E_P = 491.93 \text{ kN/m}^2$$

The point of application for the resultant force will be determined using Figure 2.11 (refer to Section 2.4.1.1). Accordingly, the abutment (y/H) ratio is found to be 0.4125.

Fore Massachusetts method (2007), the Massachusetts earth pressure coefficient (K_M) will be estimated using Equation (2.8) (refer to Section 2.4.1.1), as follows:

$$K_M = 0.43 + 5.7\left[1 - e^{-190\left(\frac{\Delta}{H}\right)}\right] = 0.43 + 5.7\left[1 - e^{-190\left(\frac{0.009}{3.3}\right)}\right] = 2.74$$

The maximum lateral earth pressure is calculated using Equation (2.3) (refer to Section 2.4.1.1), and the resultant force is determined by the total area of the pressure diagram. The results are listed in Tables 4.5 and 4.6, where field monitoring results are used as reference values. Variations from different earth pressure methods are proportionally compared against these reference values.

Furthermore, Figure 4.11 illustrates passive earth pressure distributions from various methods (excluding Arsoy, 2004) alongside field monitoring results.

Table 4.5. Comparison of results from various earth pressure methods and field monitoring results as reported by Nam and Park (2015) for earth pressure values.

	Earth passive pressure (kN/m^2)	Proportional changes
Field	45	1
Rankine (1857)	445.09	9.8
Massachusetts (2007)	136.34	3.03
Barker (1991)	25.73	0.57
England (2000)	225.39	5.01
Arsoy (2004)	175.31	3.90

Table 4.6. Comparison of results from various earth pressure methods and field monitoring results as reported by Nam and Park (2015) for resultant force, its point of application, and maximum bending moment.

	Resultant passive force (kN)	Application point (H-y) (m)	Bending moment (kN.m)
Field	105.36	1.7	179.11
Rankine (1857)	734.40	2.2	1615.7
Massachusetts (2007)	224.97	2.2	494.93
Barker (1991)	42.46	2.2	93.41
England (2000)	429.68	1.67	636.34
Arsoy (2004)	492.05	1.94	954.58

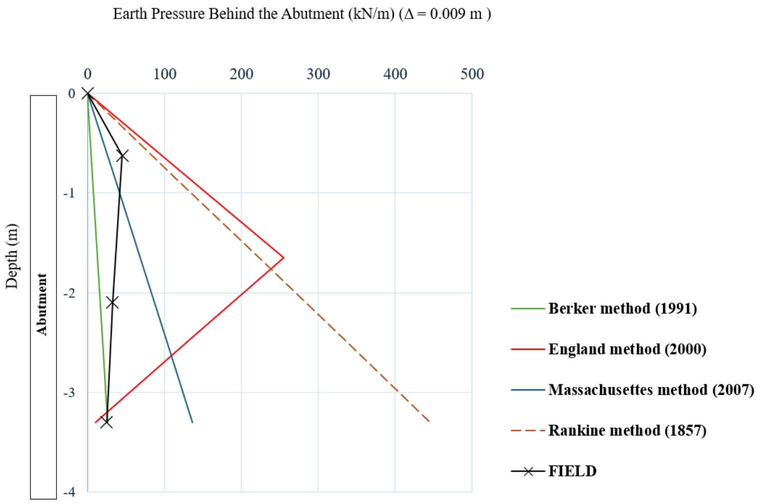

Figure 4.11. Comparison of results from various earth pressure methods and field monitoring results as reported by Nam and Park (2015) for earth pressure distributions.

4.2.3. Kim and Laman (2012) Study

The final study selected for validation was conducted by Kim and Laman (2012). This study involved long-term monitoring of four in-service IABs located in central Pennsylvania, named as 109, 203, 211, and 222. The primary focus of this validation was on the 109 Bridge. The research analyzed variations in substructure displacements and backfill pressures corresponding to daily and annual temperature fluctuations. The study examines the substructure response over a span of seven years. Detailed specifications of the bridges can be found in the table that is given in Figure 4.12. The properties of the backfill, unit weight, and internal friction were defined in Figure 4.13.

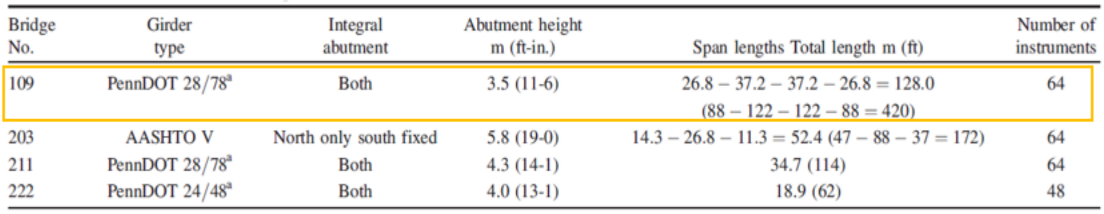

Bridge No.	Girder type	Integral abutment	Abutment height m (ft-in.)	Span lengths Total length m (ft)	Number of instruments
109	PennDOT 28/78[a]	Both	3.5 (11-6)	26.8 – 37.2 – 37.2 – 26.8 = 128.0 (88 – 122 – 122 – 88 = 420)	64
203	AASHTO V	North only south fixed	5.8 (19-0)	14.3 – 26.8 – 11.3 = 52.4 (47 – 88 – 37 = 172)	64
211	PennDOT 28/78[a]	Both	4.3 (14-1)	34.7 (114)	64
222	PennDOT 24/48[a]	Both	4.0 (13-1)	18.9 (62)	48

Figure 4.12. Field monitored IAB description as reported Kim and Laman (2012).

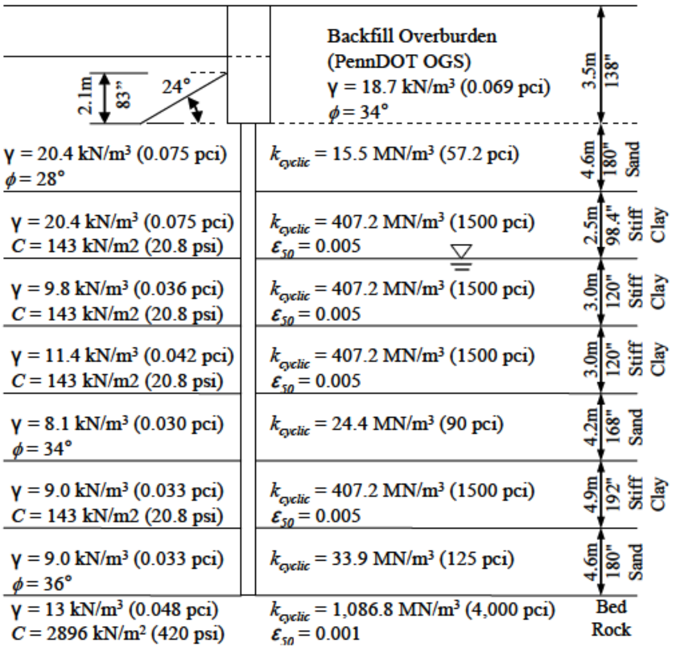

Figure 4.13. Bridge 109 soil properties as reported Kim and Laman (2012).

Regarding the field monitoring data provided in Figure 4.14, Present the measured maximum abutment displacement and maximum backfill pressure. Kim and Laman concluded that the maximum measured earth pressure was very close (±1%) to the design passive earth pressure.

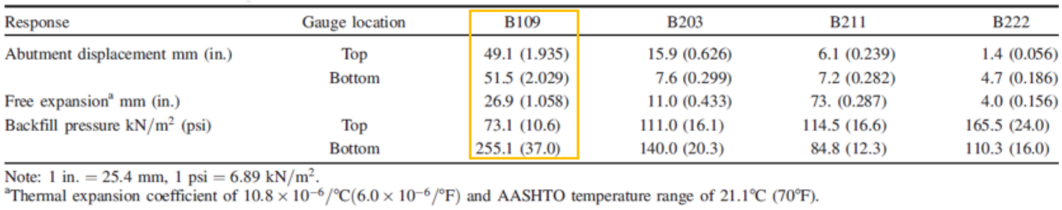

Response	Gauge location	B109	B203	B211	B222
Abutment displacement mm (in.)	Top	49.1 (1.935)	15.9 (0.626)	6.1 (0.239)	1.4 (0.056)
	Bottom	51.5 (2.029)	7.6 (0.299)	7.2 (0.282)	4.7 (0.186)
Free expansion[a] mm (in.)		26.9 (1.058)	11.0 (0.433)	73. (0.287)	4.0 (0.156)
Backfill pressure kN/m^2 (psi)	Top	73.1 (10.6)	111.0 (16.1)	114.5 (16.6)	165.5 (24.0)
	Bottom	255.1 (37.0)	140.0 (20.3)	84.8 (12.3)	110.3 (16.0)

Note: 1 in. = 25.4 mm, 1 psi = 6.89 kN/m^2.

[a] Thermal expansion coefficient of $10.8 \times 10^{-6}/°C(6.0 \times 10^{-6}/°F)$ and AASHTO temperature range of 21.1°C (70°F).

Figure 4.14. Maximum abutment displacement and backfill pressure as reported Kim and Laman (2012).

Assumptions:

- The specific locations of the earth pressure cells behind the abutment were not provided, the locations were simply identified as being at the top and bottom of the abutment. Given that the earth pressure distribution is assumed to be a simple triangular distribution, the measured earth pressure at the top of the abutment is assumed to be at 1 m from the top, and the measured earth pressure at the bottom of the abutment is assumed to be at the end of the bottom.
- The elastic modulus of the subgrade (Es) is assumed to be 50 MPa due to the absence of specific data.

The earth pressure behind the abutment will be determined using various methods, taking into account the properties of the soil, the height of the abutment, and the maximum recorded displacement and earth pressure, as provided in the following Table 4.7.

Table 4.7. Properties of the soil and abutment, and maximum recorded data as reported Kim and Laman (2012).

Abutment Hight (m)	φ Internal angle of friction (◦)	γ the unit weight (KN/m³)	Maximum earth pressure (kN/m^2)	Maximum Displacement (m)
3.5	34	18.7	255	0.049

The methodologies used for determining the earth pressure behind the abutment include the Rankine theory (1957), Barker method (1991), England method (2000), the NCHRP method (1991), and the Arsoy method (2004). The Massachusetts method (2007) is not included in this comparison as it is designed for dense backfill.

For the Rankine theory (1957) and the Barker method (1991), the passive earth pressure coefficient (K_{pR} and K_B) is determined using Equations (2.5b) and (2.6), respectively (refer to Section 2.4.1.1). The calculations are presented as follows:

$$\mathrm{K_{pR}} = \tan^2\left(45+\frac{\varphi}{2}\right) = \tan^2\left(45+\frac{34}{2}\right) = 3.54$$

$$K_B = K_0 + \phi\Delta \leq K_{pR} = (1-\sin(35)) + (35 * 0.049) = 2.16$$

For the NCHRP method (1991), the passive earth pressure coefficient for medium granular sandy backfill soil with an angle of friction of 34° is determined using Figure 4.1 (refer to Section 4.1.1). For a relative abutment displacement, defined as the ratio of displacement to abutment height (Δ/H), K_{NCHRP} is as follows,

$$\Delta/\mathrm{H} = 0.049/3.5 = 0.014 \quad \rightarrow \quad K_{NCHRP} = 3$$

For the England method (2000), England's passive earth pressure coefficient (K^*) is calculated using Equation (2.9) (refer to Section 2.4.1.1).The calculations are provided as follows:

$$K_{pC} = \frac{cos^2(\varphi+\theta)}{cos^2\theta cos(\delta-\theta)\left(1-\sqrt{\frac{sin(\delta+\varphi)sin(\varphi+\beta)}{cos(\delta-\theta)cos(\beta-\theta)}}\right)^2} = \frac{cos^2(34)}{cos^2 0 cos\left(\frac{34}{2}\right)\left(1-\sqrt{\frac{sin\left(\frac{34}{2}+34\right)sin(34)}{cos\left(\frac{34}{2}\right)cos(0)}}\right)^2} = 6.77$$

$$\mathrm{C_E} = 0.051\mathrm{E_S} + 14.9 = 0.051(50) + 14.9 = 17.45$$

$$\mathrm{K}^* = \mathrm{K_0} + \left(\frac{\mathrm{C_E}\,\grave{\Delta}}{\mathrm{H}}\right)^{0.6}\mathrm{K_{pC}} = 0.44 + \left(\frac{17.45 * 0.5 * 0.049}{3.5}\right)^{0.6} 6.77 = 2.36$$

For the Arsoy method (2004), the resultant passive force (E_P) for a relative abutment displacement defined as the ratio of displacement to abutment height (Δ/H=0.014) is determined using average of the resultant force curves for medium density in pure rotation and pure translation, as shown in Figure 4.2. (refer to Section 4.1.1). The full passive resultant force (E_{Pmax}) and the resultant passive force (E_P) is determined as follows:

$$E_{Pmax} = 0.5\, K_{pR}\, \gamma\, H^2 = 0.5 * 3.54 * 18.7 * 3.5^2 = 405.46\ \mathrm{kN/m}$$

$$\frac{E_P}{E_{Pmax}} = 87\% \quad \rightarrow \quad \frac{E_P}{405.46} = 0.87 \quad \rightarrow \quad E_P = 352.75\ \mathrm{kN/m^2}$$

The point of application for the resultant force will be determined using Figure 2.11 (refer to Section 2.4.1.1). Accordingly, the abutment (y/H) ratio is found to be 0.4125.

The maximum lateral earth pressure is calculated using Equation (2.3) (refer to Section 2.4.1.1), and the resultant force is determined by the total area of the pressure diagram. The results are listed in Tables 4.8 and 4.9, where field monitoring results are used as reference values. Variations from different earth pressure methods are proportionally compared against these reference values. Furthermore, Figure 4.15 illustrates passive earth pressure distributions from various methods (excluding Arsoy, 2004) alongside field monitoring results.

Table 4.8. Comparison of results from various earth pressure methods and field monitoring results as reported Kim and Laman (2012) for earth pressure values.

	Earth passive pressure (kN/m^2)	Proportional changes
Field	255	1
Rankine (1857)	231.51	0.91
Barker (1991)	141.09	0.55
NCHRP (1991)	196.35	0.77
England (2000)	77.15	0.30
Arsoy (2004)	201.41	0.89

Table 4.9. Comparison of results from various earth pressure methods and field monitoring results as reported Kim and Laman (2012) for resultant force, its point of application, and maximum bending moment.

	Resultant passive force (kN)	Application point (H-y) (m)	Bending moment (kN.m)
Field	446.25	2.33	1039.76
Rankine (1857)	405.13	2.33	943.95
Barker (1991)	246.92	2.33	575.32
NCHRP (1991)	343.61	2.33	800.61
England (2000)	160.25	1.93	309.28
Arsoy (2004)	352.47	2.06	726.09

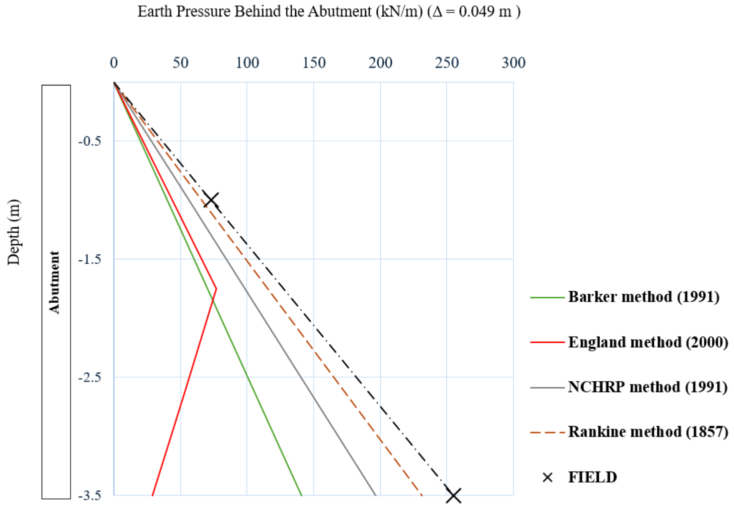

Figure 4.15. Comparison of results from various earth pressure methods and field monitoring results as reported Kim and Laman (2012) for earth pressure distributions.

4.2.4. Conclusion

The conclusions can be summarized as follows:

Short-Term Monitoring:

Civjan et al. (2013) study: The earth pressure behind the abutment was much smaller than the full passive Rankine earth pressure (1857) and closer to the Barker (1991), England (2000), NCHRP (1991), and Arsoy (2004) earth pressure values.

Nam and Park (2015) study: The earth pressure behind the abutment was much smaller than the full passive Rankine earth pressure (1857) and closer to Massachusetts (2007) and Barker methods. However, the England (2000) and Arsoy (2004) methods gave larger values close to the full passive earth pressure, likely due to the specific high-friction-angle materials used as backfill.

Long-Term Monitoring:

Kim and Laman (2012) study: The earth pressure behind the abutment was observed to be larger than even the full passive Rankine earth pressure (1857). This increase was attributed to the seasonal and daily cycles of expansion and contraction in the bridge deck, leading to an increase in earth pressure behind the abutment, a phenomenon known as soil ratcheting.

4.3. Evaluation of Various Passive Earth Pressure Methods on IAB Response Using a 3D Finite Element Model

To evaluate the effects of different methods for calculating passive earth pressure on the overall response of IABs, a 3D finite element model was developed using MIDAS CIVIL software. This model incorporates five different methods for determining the passive earth pressure behind the abutment, and their effects are analyzed across various thermal displacement scenarios. The finite element model was implemented using a one-step 3D static analysis.

All bridge design parameters, descriptions, cross-sections, and modeling techniques used in this model are consistent with those applied in the previous 3D model (refer to Section 3.1.1).

4.3.1. Thermal Loads Modeling

Regarding the thermal loadings affecting the bridge model, it was assumed that the structure is intended for construction in a northern region of the United States. According to AASHTO (2010), many states in this area specify minimum and maximum design temperatures of –34.4°C (–30°F) and 48.9°C (120°F).

For the analysis, three construction temperatures will be considered within the typical range of –1.1°C (30°F) to 32.2°C (90°F):

High construction temperature: 32.2°C (90°F).

Mean construction temperature: 15.5°C (60°F), representing the mean of the minimum and maximum design temperatures.

Low construction temperature: –1.1°C (30°F).

The temperature rise will be determined using Equation (2.15a) (refer to Section 2.6.1), as follows:

$$\Delta T_1(+) = T_{e.max} - T_{Const} = 48.9 - 32.2 = +16.7°C\ (+30°F)$$

$$\Delta T_2\ (+) = T_{e.max} - T_{Const} = 48.9 - 15.5 = +33.4°C\ (+60°F)$$

$$\Delta T_3\ (+) = T_{e.max} - T_{Const} = 48.9 - (-1.1) = +50°C\ (90°F)$$

4.3.2. Soil–Structure Interaction Modelling

For the abutment–backfill interaction, the limiting equilibrium approach is used (refer to Section 2.4.1.1). This section examines five different methods for calculating the passive earth pressure behind the abutment across three thermal displacement scenarios.

The displacements are calculated using Equation (2.14) (refer to Section 2.5) as follows:

$$\Delta_1 = \alpha\ L_b \Delta T_3\ (+) = 12 * 10^{-6} * \frac{50}{2} * 16.7 = 0.0005\,m$$

$$\Delta_2 = \alpha\ L_b\ \Delta T_2\ (+) = 12 * 10^{-6} * \frac{50}{2} * 33.4 = 0.010\,m$$

$$\Delta_3 = \alpha\ L_b\ \Delta T_1\ (+) = 12 * 10^{-6} * \frac{50}{2} * 50 = 0.015\,m$$

Following the procedures outlined in Section (4.1.1) for calculating the passive earth pressure coefficient and using the same assumptions and soil properties (refer to Section 4.1.1), the passive earth pressures for the Rankine (1857), Barker (1991), England (2000), NCHRP (1991), and Arsoy (2004) methods will be determined. The final calculations for the three different displacements are presented as follows:

For the Rankine theory (1957), which is a displacement-independent method, the passive earth pressure coefficients (K_{pR}) for all three displacements are calculated using Equation (2.5b) (refer to Section 2.4.1.1). The results are as follows:

$$K_{pR} = \tan^2\left(45 + \frac{\varphi}{2}\right) = \tan^2\left(45 + \frac{34}{2}\right) = 3.54$$

For the Barker method (1991), the passive earth pressure coefficient (K_B) is determined using Equation (2.6) (refer to Section 2.4.1.1). The coefficients have been determined for three displacements and are denoted as K_{B1}, K_{B2}, and K_{B3}. The calculations are presented as follows:

$$\mathrm{K_{B1}} = \mathrm{K_0} + \phi\Delta \le \mathrm{K_{pR}} = (1 - \sin(34)) + (35 \ * \ 0.005) = 0.62$$

$$\mathrm{K_{B2}} = \mathrm{K_0} + \phi\Delta \le \mathrm{K_{pR}} = (1 - \sin(34)) + (35 \ * \ 0.010) = 0.79$$

$$\mathrm{K_{B3}} = \mathrm{K_0} + \phi\Delta \le \mathrm{K_{pR}} = (1 - \sin(34)) + (35 \ * \ 0.015) = 0.97$$

For the NCHRP method (1991), the passive earth pressure coefficient (K_{NCHRP}) is determined using Figure 4.1 (refer to Section 4.1.1). For the three relative abutment displacements, defined as the ratio of displacement to abutment height, the calculations are presented as follows:

$$\Delta_1 /\mathrm{H} = 0.005/4 = 0.00125 \rightarrow K_{NCHRP} = 0.90$$

$$\Delta_2 /\mathrm{H} = 0.010/4 = 0.00250 \rightarrow K_{NCHRP} = 1.25$$

$$\Delta_3 /\mathrm{H} = 0.015/4 = 0.00375 \rightarrow K_{NCHRP} = 1.60$$

For the England method (2000), the passive earth pressure coefficient (K^*) is calculated using Equation (2.9) (refer to Section 2.4.1.1). The coefficients have been determined for three displacements and are denoted as K^*_1, K^*_2, and K^*_3. The calculations are presented as follows:

$$K_{pC} = \frac{cos^2(\varphi+\theta)}{cos^2\theta cos(\delta-\theta)\left(1-\sqrt{\frac{sin(\delta+\varphi)sin(\varphi+\beta)}{cos(\delta-\theta)cos(\beta-\theta)}}\right)^2} = \frac{cos^2(34)}{cos^2 0 cos\left(\frac{34}{2}\right)\left(1-\sqrt{\frac{sin\left(\frac{34}{2}+34\right)sin(34)}{cos\left(\frac{34}{2}\right)cos(0)}}\right)^2} = 6.77$$

$$\mathrm{C_E} = 0.051\mathrm{E_S} + 14.9 = 0.051(50) + 14.9 = 17.45$$

$$K_1^* = \mathrm{K_0} + \left(\frac{\mathrm{C_E}\ \grave{\Delta}}{\mathrm{H}}\right)^{0.6} \mathrm{K_{pC}} = 0.44 + \left(\frac{17.45 * 0.5 * 0.005}{4}\right)^{0.6} 6.77 = 0.89$$

$$K_2^* = \mathrm{K_0} + \left(\frac{\mathrm{C_E}\ \grave{\Delta}}{\mathrm{H}}\right)^{0.6} \mathrm{K_{pC}} = 0.44 + \left(\frac{17.45 * 0.5 * 0.010}{4}\right)^{0.6} 6.77 = 1.12$$

$$K_3^* = \mathrm{K_0} + \left(\frac{\mathrm{C_E}\ \grave{\Delta}}{\mathrm{H}}\right)^{0.6} \mathrm{K_{pC}} = 0.44 + \left(\frac{17.45 * 0.5 * 0.015}{4}\right)^{0.6} 6.77 = 1.31$$

For the Arsoy method (2004), the resultant passive force (E_P) for a given relative abutment displacement (Δ/H) is determined using Figure 4.2 (refer to Section 4.1.1).

The full passive resultant force (E_{Pmax}) and the resultant passive forces for three specific displacements, denoted as E_{p1}, E_{p2}, and E_{p3}, are calculated as follows:

$$E_{Pmax} = 0.5\, K_{pR}\, \gamma\, H^2 \; = 0.5 \, * \, 3.54 \, * \, 18.7 \, * \, 4^2 = \, 529.58\, \mathrm{kN/m}$$

$$\Delta_1\, /H \; = \; 0.005/4 = 0.00125 \; \rightarrow \; \frac{E_{P1}}{E_{Pmax}} = \; 15\% \; \rightarrow E_{p1} = 79.44 \;\; \mathrm{kN/m^2}$$

$$\Delta_2\, /H \; = \; 0.010/4 = 0.00250 \; \rightarrow \; \frac{E_{P2}}{E_{Pmax}} = \; 30\% \; \rightarrow E_{p2} = 158.87 \;\; \mathrm{kN/m^2}$$

$$\Delta_3\, /H \; = \; 0.015/4 = 0.00375 \; \rightarrow \; \frac{E_{P2}}{E_{Pmax}} = \; 45\% \; \rightarrow E_{p3} = 238.31\, \mathrm{kN/m^2}$$

The point of application for the resultant force will be determined using Figure 2.11 (refer to section 2.4.1.1). Accordingly, the abutment (y/H) ratio is found to be 0.4125.

The maximum lateral earth pressure for all methods will be calculated using Equation (2.3) (refer to Section 2.4.1.1).

Regarding the distribution of earth pressure behind the abutment:

England Method (2000): The earth pressure distribution is defined based on PD6694-1:2011, as illustrated in Figure 2.15 (refer to Section 2.4.1.1).

Arsoy Method (2004): The distribution of earth pressure behind the abutment is not specified. Therefore, the resultant force is modeled as a one-dimensional force applied at a determined point of application (refer to Section 2.4.1.1).

Other Methods: The earth pressure distribution is assumed to be a simple triangular distribution.

Figure 4.16 illustrates the earth pressure distribution behind the abutment for the various methods across three different abutment displacements.

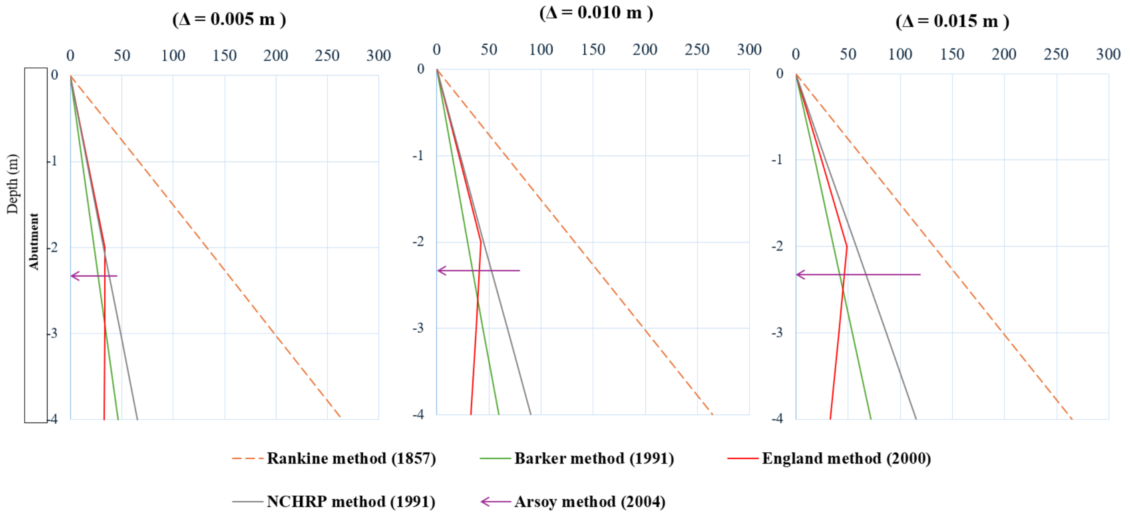

(a) (b) (c)

Figure 4.16. Earth pressure distribution behind the abutment for various methods across different displacements: (a) Δ = 0.005 m, (b) Δ = 0.010 m, and (c) Δ = 0.015 m.

For the soil-pile interaction, the subgrade reaction approach (refer to Section 2.4.2.1) will be used, employing p-y curves distributed along the depths of the piles.

These curves will be generated using MIDAS CIVIL software, with the subgrade reaction (kh) calculated using the Vesic equation, as outlined in Bowles' 4th Edition (1998) and given in Equation (3.1) (refer to Section 3.1.4).

All pile and soil parameters and properties in this model are consistent with those used in the previous 3D model (refer to Section 3.1.4).

4.3.3. Summary of 3D Static Analyses Results

This section presents the results of 3D static analyses aimed at comparing the outcomes derived from five passive earth pressure calculation methods on bridge element responses.

The results of these analyses included only backfill pressure to facilitate direct comparison of the effects of different methods used to calculate passive earth pressure on the bridge response.

Additionally, results are provided for combined load scenarios involving passive earth pressure and dead load ($D+E_p$) to more accurately reflect real-world conditions.

Furthermore, the proportional values of bridge response under dead load and passive earth pressure using various methods are compared to the responses from the at-rest case ($D+E_0$).

This comparison assesses how the methods used to calculate passive earth pressure affect the overall response of IABs and highlights the extent of their effect, thereby underscoring their significant effects on IAB design.

The findings derived from the analysis of 18 IAB models encompass critical internal forces, including the maximum bending moments and deformations experienced by the main girder, pile, and abutment.

4.3.3.1. IAB Response Under Passive Earth Pressure (Ep) Only

The investigation reveals significant differences in bridge element responses, such as bending moments and deformations, under various estimations of passive earth pressure, as illustrated in Figures 4.17, 4.18, 4.19, 4.20, and 4.21.

The following sections compare and summarize the effects of different methods for calculating passive earth pressure on bridge response:

- Barker (1991) and England (2000) methods: These methods exhibit relatively low earth pressure values with increasing displacements, resulting in less pronounced responses in bridge elements. Barker (1991) yields higher values compared to England (2000).
- Arsoy (2004) and NCHRP (1991) methods: These methods yield higher responses with increasing displacements, resulting in more pronounced effects on bridge elements. The NCHRP method (1991) produces the highest response, followed by the Arsoy method (2004), compared to other displacement-dependent methods.
- Rankine theory (1857): This approach assumes full passive earth pressure regardless of displacement magnitude, resulting in substantial and constant responses in bridge elements. This method shows the highest response compared to the others.

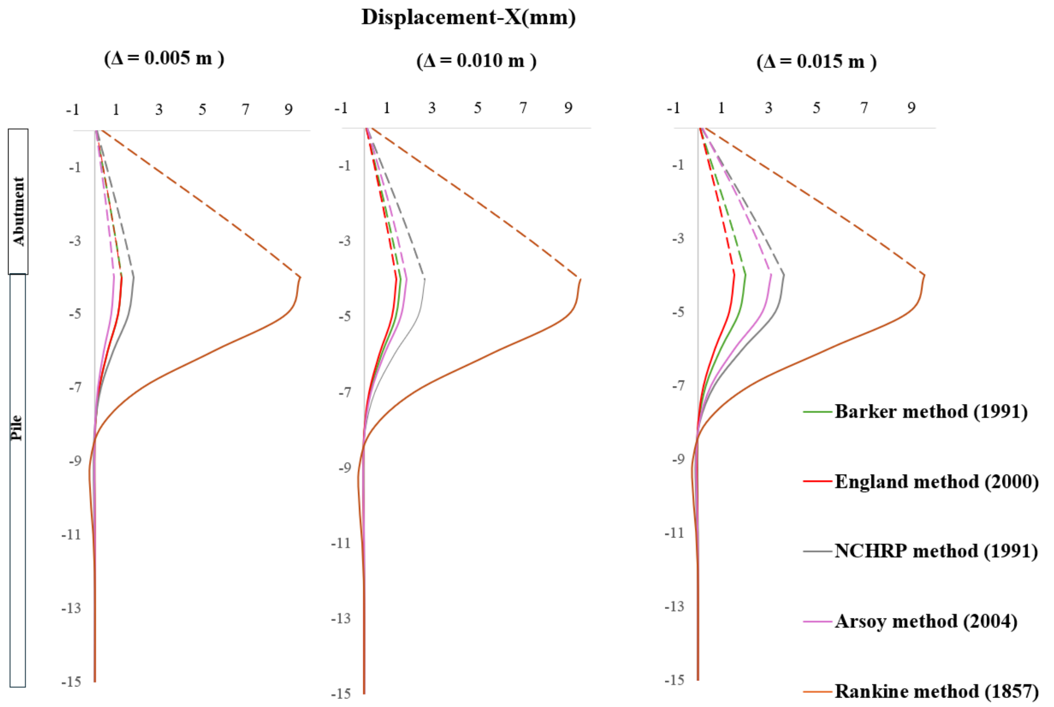

(a) (b) (c)

Figure 4.17. The displacement diagrams of the abutment and pile under individual earth pressure loading, utilizing various methods: (a) Δ = 0.005 m, (b) Δ = 0.010 m, and (c) Δ = 0.015 m.

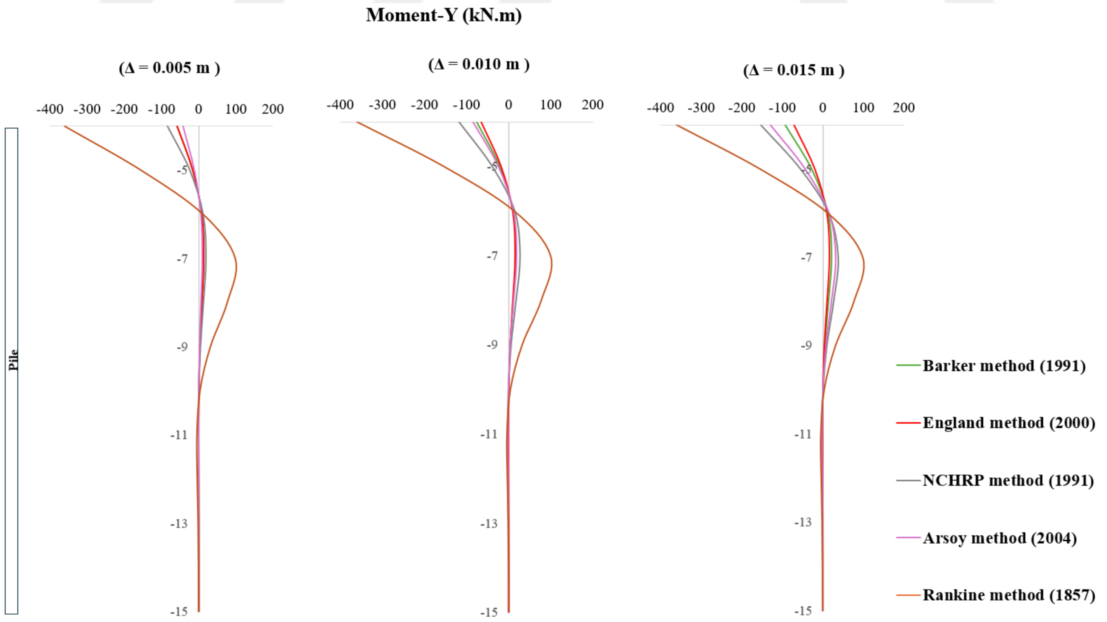

(a) (b) (c)

Figure 4.18. The bending moment diagrams of the pile under individual earth pressure loading, utilizing various methods: (a) Δ = 0.005 m, (b) Δ = 0.010 m, and (c) Δ = 0.015 m.

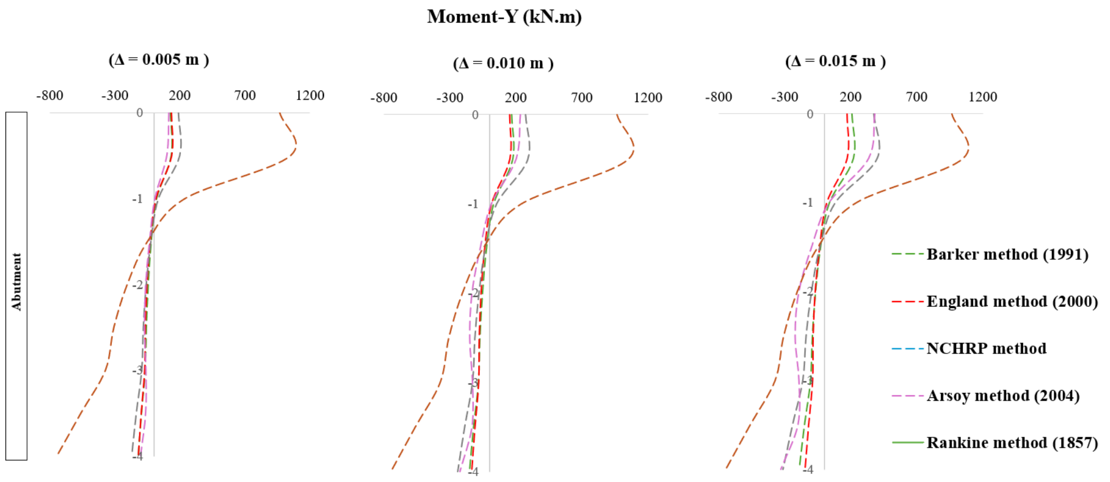

(a) (b) (c)

Figure 4.19. The bending moment diagrams of the abutment under individual earth pressure loading, utilizing various methods: (a) Δ = 0.005 m, (b) Δ = 0.010 m, and (c) Δ = 0.015 m.

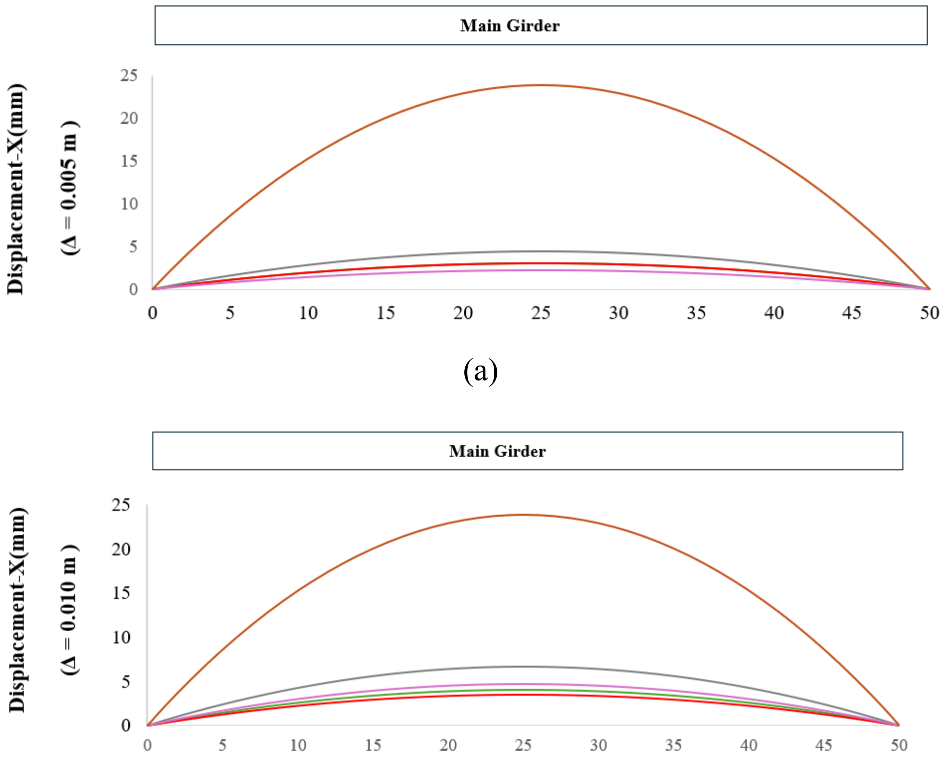

(a)

(b)

Figure 4.20. The displacement diagrams of the main girder under individual earth pressure loading, utilizing various methods: (a) Δ = 0.005 m, (b) Δ = 0.010 m, and (c) Δ = 0.015 m.

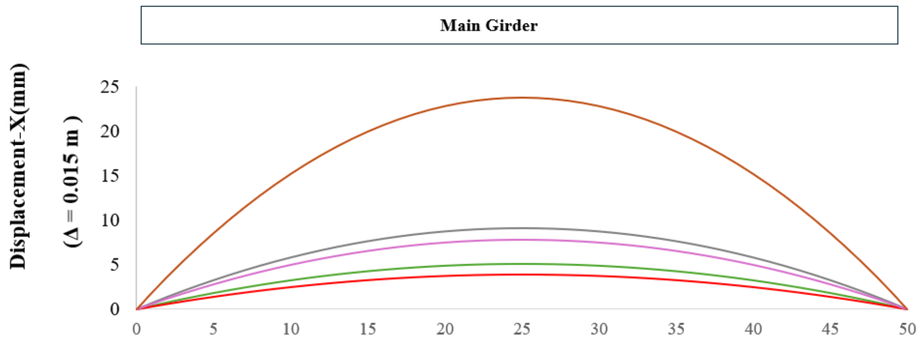

(c)

Figure 4.20. The bending moment diagrams of the main girder under individual earth pressure loading, utilizing various methods: (a) Δ = 0.005 m, (b) Δ = 0.010 m, and (c) Δ = 0.015 m. (Continued).

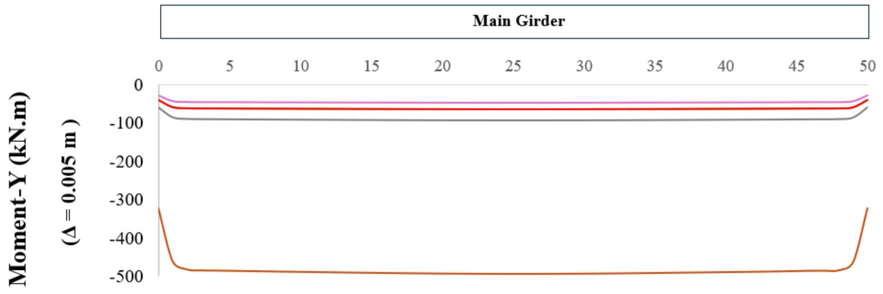

(a)

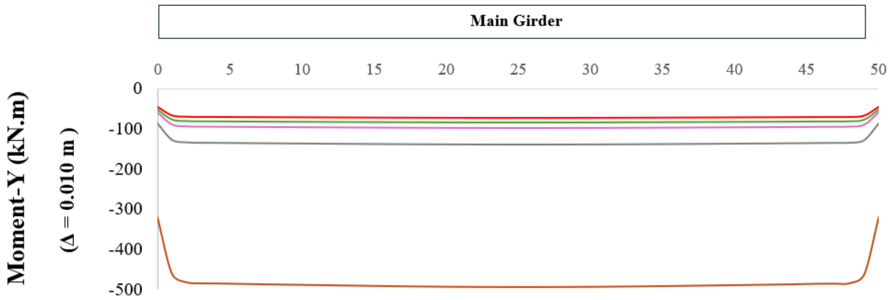

(b)

Figure 4.21. The bending moment diagrams of the main girder under individual earth pressure loading, utilizing various methods: (a) Δ = 0.005 m, (b) Δ = 0.010 m, and (c) Δ = 0.015 m.

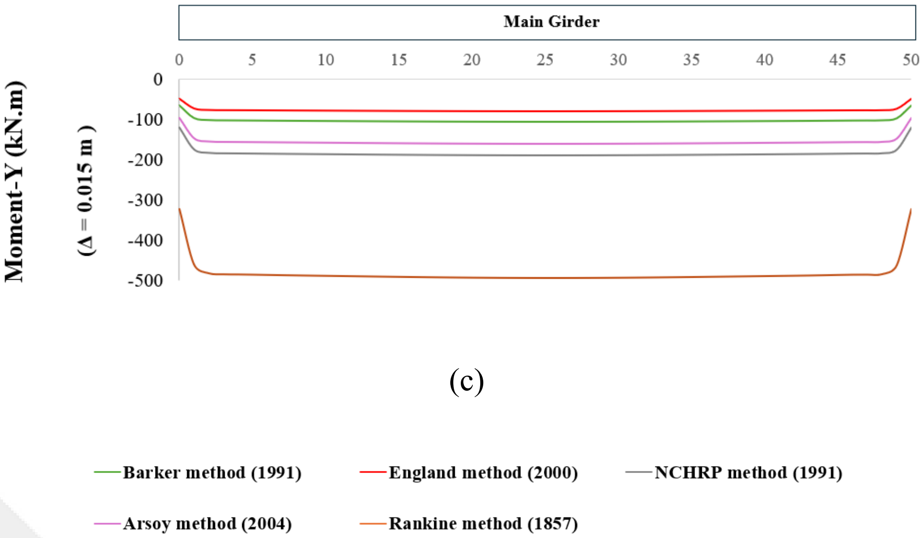

(c)

Figure 4.21. The bending moment diagrams of the main girder under individual earth pressure loading, utilizing various methods: (a) Δ = 0.005 m, (b) Δ = 0.010 m, and (c) Δ = 0.015 m. (Continued).

4.3.3.2. IAB Responses Under the Combination of Passive Earth Pressure and Dead Load (D+E$_p$)

- Main girder, Abutment, and Pile deformation:

As discussed in Section 3, the deformation induced by passive earth pressure counteracts the deformations caused by the dead load in the main girder, abutment, and pile, leading to an overall reduction in the resultant deformation (refer to Section 3.2). As illustrated in Figures 4.22 and 4.23 and Tables 4.10 and 4.11, when the method used to assume passive earth pressure introduces large values, the reduction in overall resultant displacement becomes significantly pronounced.

- Pile bending moment:

As discussed in Section 3, the bending moment induced by passive earth pressure is negative at the top of the pile, while the dead load induces a positive moment. Consequently, passive earth pressure counteracts the bending moment from the dead load, leading to an overall reduction in the resultant bending moment (refer to Section 3.2). As illustrated in Figures 4.24 and Tables 4.10 and 4.11, when the method used to estimate passive earth pressure introduces large values, the reduction in the overall resultant bending moment becomes significantly pronounced. Additionally, the increased passive earth pressure amplifies the positive moment in the near-middle portion of the pile and counteracts the negative moment induced by the dead load in that region. This results in a reduction in the overall resultant bending moment, similar to the effect observed at the top of the pile.

Depending on the method used for calculating earth pressure, it is possible to determine the extent of the reduction in the positive bending moment at the top of the pile and assess whether this reduction might shift the bending moment towards the negative side.

Abutment bending moment:

As discussed in Section 3, the bending moment induced by passive earth pressure aligns with the bending moment induced by the dead load at the top of the abutment and counteracts it at the bottom. This results in an overall increase in the resultant bending moment at the top of the abutment and a reduction at the bottom (refer to Section 3.2). As illustrated in Figures 4.25 and Tables 4.10 and 4.11, when the method used to estimate passive earth pressure introduces large values, the increase in the overall resultant bending moment at the top of the abutment and the reduction at the endpoints become significantly pronounced.

- Main girder bending moment:

As discussed in Section 3, the bending moment induced by passive earth pressure counteracts the bending moment induced by the dead load at the middle of the main girder and aligns with it at the endpoints. This results in an overall reduction in the resultant bending moment at the middle of the main girder and an increase at the endpoints (refer to Section 3.2).

As illustrated in Figures 4.26 and Tables 4.10 and 4.11, when the method used to estimate passive earth pressure introduces large values, the reduction in the overall resultant bending moment at the middle of the main girder and the increase at the endpoints become significantly pronounced.

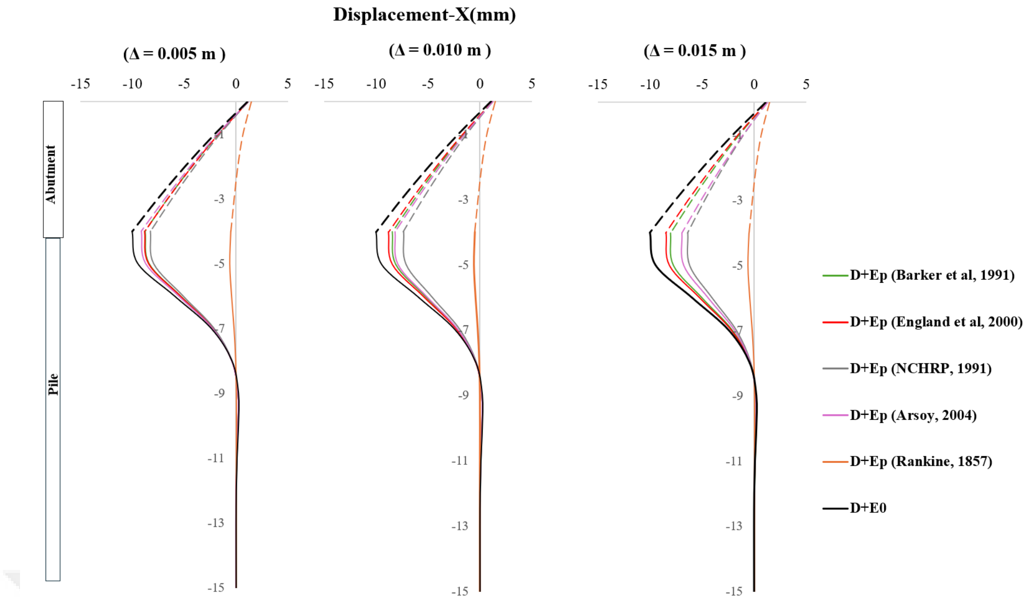

(a) (b) (c)

Figure 4.22. Displacement diagrams of the abutment and pile during expansion (D+E$_p$) state using various methods and the at-rest case (D+E$_0$): (a) Δ = 0.005 m, (b) Δ = 0.010 m, and (c) Δ = 0.015 m.

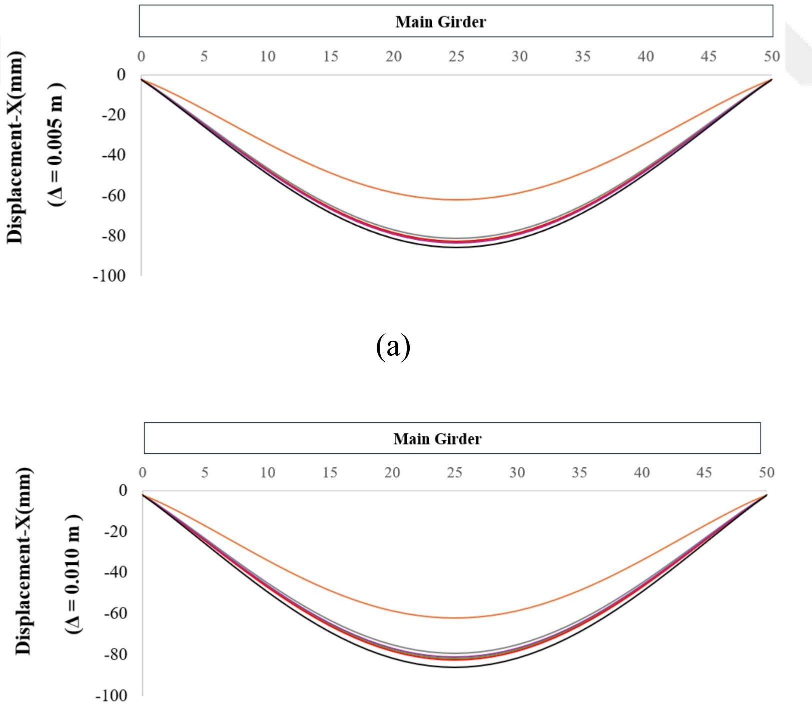

(a)

(b)

Figure 4.23. Displacement diagrams of the main girder during expansion (D+Ep) state using various methods and the at-rest case (D+E$_0$): (a) Δ = 0.005 m, (b) Δ = 0.010 m, and (c) Δ = 0.015 m.

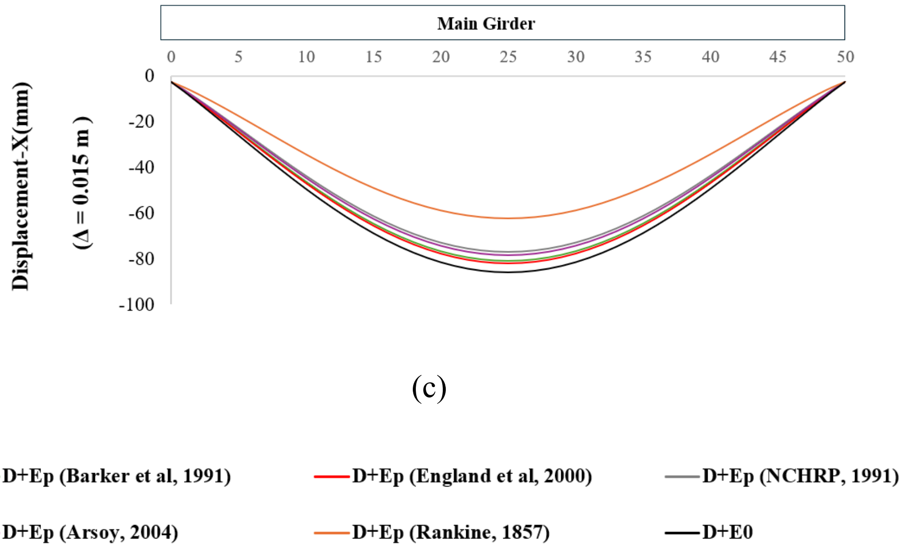

(c)

Figure 4.23. Displacement diagrams of the main girder during expansion (D+Ep) state using various methods and the at-rest case (D+E₀): (a) Δ = 0.005 m, (b) Δ = 0.010 m, and (c) Δ = 0.015 m. (Continued).

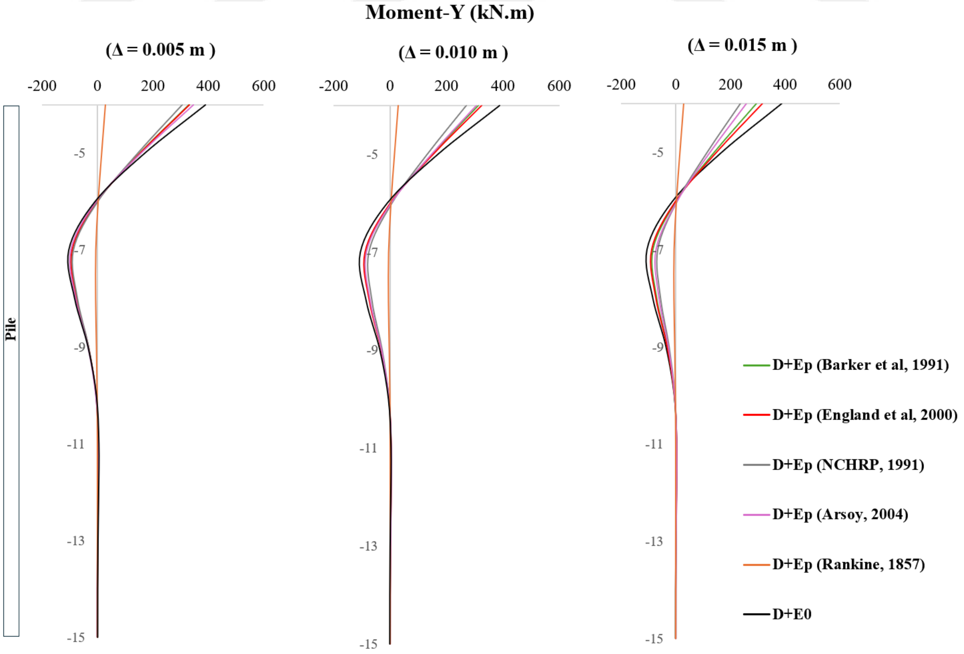

(a) (b) (c)

Figure 4.24. Bending moment diagrams of the pile during expansion (D+E_p) state using various methods and the at-rest case (D+E_0): (a) Δ = 0.005 m, (b) Δ = 0.010 m, and (c) Δ = 0.015 m.

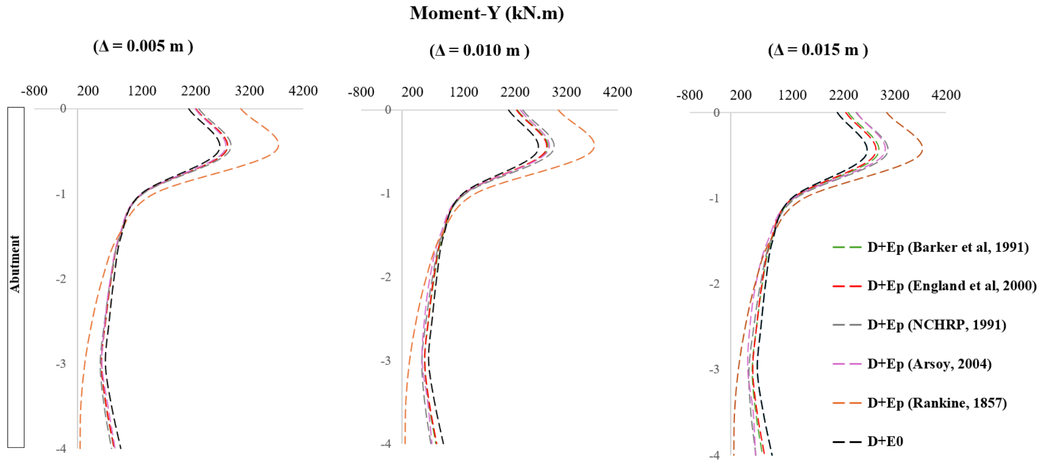

(a) (b) (c)

Figure 4.25. Bending moment diagrams of the abutment during expansion (D+Ep) state using various methods and the at-rest case (D+E₀): (a) Δ = 0.005 m, (b) Δ = 0.010 m, and (c) Δ = 0.015 m.

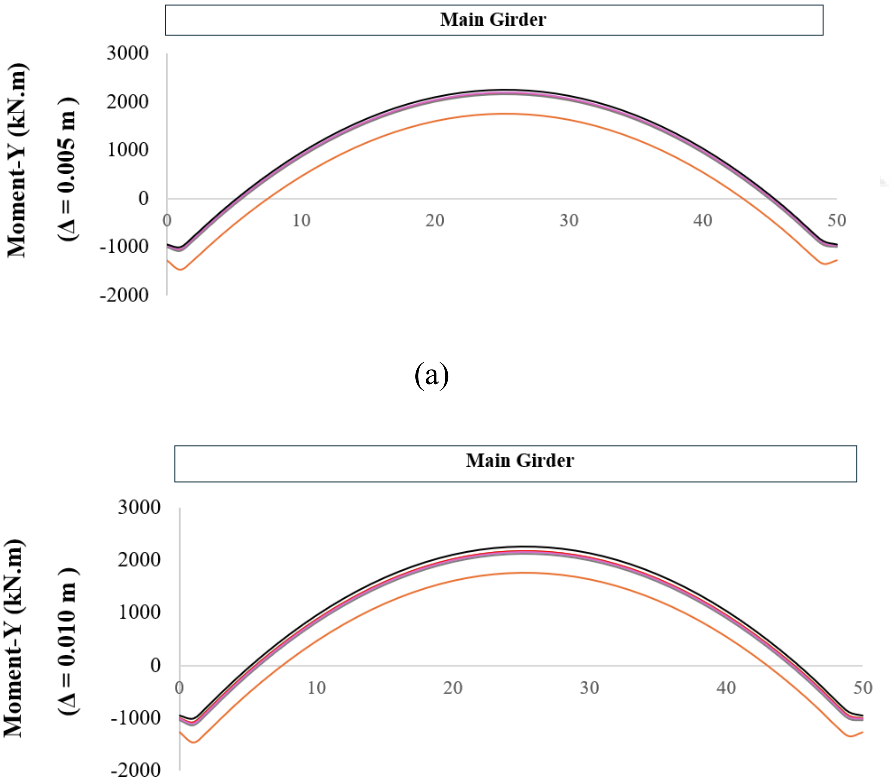

(a)

(b)

Figure 4.26. Bending moment diagrams of the main girder during expansion ($D+E_p$) state using various methods and the at-rest case (D+E₀): (a) Δ = 0.005 m, (b) Δ = 0.010 m, and (c) Δ = 0.015 m.

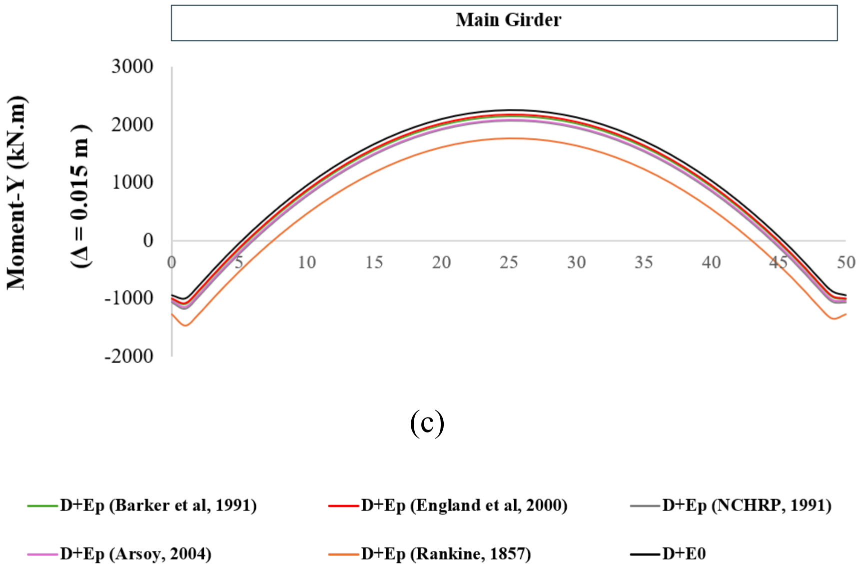

(c)

Figure 4.26. Bending moment diagrams of the main girder during expansion (D+E_p) state using various methods and the at-rest case (D+E_0): (a) Δ = 0.005 m, (b) Δ = 0.010 m, and (c) Δ = 0.015 m. (Continued).

Table 4.10. Reference values for bridge response under at-rest case.

Bridge Response	Bridge element	D+E_0
Displace-met (m)	Abutment	0.001152
	Pile	-0.00914
	Gir-mid	-0.0837
Bending moment (kN.m)	Abutment	2166
	Pile	346.83
	Gir-mid	2203.8
	Gir-edge	-979.67

Table 4.11. Proportional values of bridge response under dead load and earth pressure using various methods compared to the at-rest case for different displacement.

Δ (m)	Bridge Response	Bridge element	D+E_0	D+E_p Rankine	D+E_p Barker	D+E_p England	D+E_p NCHRP	D+E_p Arsoy
0.005	Displace-met (m)	Abutment	1.00	1.27	1.02	1.03	1.04	1.02
		Pile	1.00	0.05	0.96	0.96	0.90	1.00
		Gir-mid	1.00	0.74	0.99	0.99	0.97	1.00
	Bending moment (kN.m)	Abutment	1.00	1.40	1.02	1.02	1.04	1.01
		Pile	1.00	0.08	0.95	0.96	0.88	1.00
		Gir-mid	1.00	0.80	0.99	0.99	0.98	1.00
		Gir-edge	1.00	1.30	1.01	1.01	1.03	1.00

Table 4.11. Proportional values of bridge response under dead load and earth pressure using various methods compared to the at-rest case for different displacement (Continued).

Δ (m)	Bridge Response	Bridge element	D+E_0	D+E_p Rankine	D+E_p Barker	D+E_p England	D+E_p NCHRP	D+E_p Arsoy
0.010	Displace-met (m)	Abutment	1.00	1.27	1.03	1.05	1.07	1.08
		Pile	1.00	0.05	0.92	0.94	0.81	0.89
		Gir-mid	1.00	0.74	0.98	0.98	0.95	0.97
	Bending moment (kN.m)	Abutment	1.00	1.40	1.03	1.03	1.08	1.07
		Pile	1.00	0.08	0.90	0.93	0.78	0.88
		Gir-mid	1.00	0.80	0.98	0.99	0.96	0.98
		Gir-edge	1.00	1.30	1.02	1.02	1.06	1.03
0.015	Displace-met (m)	Abutment	1.00	1.27	1.05	1.06	1.10	1.14
		Pile	1.00	0.05	0.88	0.93	0.70	0.76
		Gir-mid	1.00	0.74	0.97	0.98	0.92	0.93
	Bending moment (kN.m)	Abutment	1.00	1.40	1.05	1.04	1.13	1.13
		Pile	1.00	0.08	0.85	0.91	0.68	0.75
		Gir-mid	1.00	0.80	0.97	0.98	0.94	0.95
		Gir-edge	1.00	1.30	1.04	1.02	1.09	1.07

4.4. Conclusion

This study, supported by various investigations, highlighted significant differences in the estimation of passive earth pressure across different methods and their substantial influences on the overall behavior of IABs.

Displacement-independent methods rely on traditional theories such as Rankine (1857) and Coulomb (1776), assuming full passive earth pressure regardless of displacement magnitude. This often leads to an overestimation of passive earth pressure under minimal displacement conditions. Conversely, displacement-dependent methods exhibit varying paths to achieving full passive pressure, resulting in different outcomes based on the magnitude of displacement. Some design specifications recommend full passive earth pressure theories, while others recommend displacement-dependent methods.

By evaluating these methods against field monitoring data, the study concludes that the earth pressure behind the abutment is initially lower than full passive values during the first few years after construction. However, due to soil ratcheting effects, these pressures eventually increase and reach their full passive values over time.

Notably, assuming maximum full passive pressures behind the abutment may not always represent the worst-case scenario for all bridge elements. In fact, earth pressure loads can reduce the bending moment in some bridge elements. Methods that result in significant earth pressure loads may lead to an unrealistic reduction in bridge element moments, potentially yielding unsafe results.

Therefore, during the design phase, it is crucial to consider the worst-case scenario for each element individually by accounting for all loading scenarios the bridge may encounter throughout its operational life, including the effect of soil ratcheting.

5. PROPOSED NEW CONSIDERATIONS FOR CONSTRUCTION TEMPERATURE IN IABs

The primary uncertainty in analyzing and designing IABs stems from predicting the soil response behind the abutment and around the piles, which depends on the abutment displacement resulting from changes in the bridge girder lengths due to temperature variations. Bridge design specifications typically recommend a uniform temperature range to account for variations in the bridge superstructure, based on climate, materials, and an assumed construction temperature (refer to Section 2.6.1). However, these specifications often overlook the potential variability in construction temperatures.

In this section, the focus is on evaluating how construction temperature is considered across different bridge design specifications, identifying gaps in these considerations, and proposing a new approach to incorporating construction temperature as a design parameter in construction practices. This approach involves defining an appropriate range for construction temperatures [$T_{Const.min}$, $T_{Const.max}$] during the design phase and ensuring it is managed and controlled throughout the construction phase. As a result, the accuracy of thermal displacement and internal force predictions can be improved, thereby enhancing overall design outcomes.

Although specifying an exact construction temperature range [$T_{Const.min}$, $T_{Const.max}$] poses challenges due to environmental variations, insights from the Arsoy model were utilized to address this issue.

5.1. Discussion about Construction Temperature Consideration in Different Bridge Design Specifications In United States, Canada, and Europe:

The construction temperature is typically linked to the construction timeline, making it a future event and an unknown factor during the design process. However, some bridge design specifications do not provide clear guidance for assuming the construction temperature. Instead, they recommend using a temperature range to account for variations in the length of the bridge superstructure based solely on climate and materials. This recommended range defines the expected temperature variation ΔT (±) for the bridge superstructure, while overlooking the value of the construction temperature. The temperature variations are determined by the Equations (2.15a) and (2.15b) (refer to Section 2.6.1). Consequently, the construction temperature may be indirectly inferred based on these temperature ranges, which can be mathematically represented as follows in Equation (5.1):

$$T_{Const} = T_{e.max} - \Delta T\,(+) = T_{e.min} + \Delta T\,(-) \qquad (5.1)$$

T_{Const} represents the construction temperature, while $T_{e.min}$ and $T_{e.max}$ denote the maximum and minimum extreme EBTs expected during the lifespan of the bridge, and ΔT (±) denotes the expected variation in temperature. Other specifications may provide direct recommendations for assuming the construction temperature.

The subsequent section will provide examples illustrating how the consideration of construction temperature varies across different bridge design specifications in the United States, Canada, and Europe, and will highlight the weaknesses in these considerations.

In accordance with the AASHTO Standard Specification (1996), steel bridges designed for moderate climates are intended for extreme design bridge temperatures ranging from –18°C (0°F) to +49°C (120°F). The total temperature range based on Equation (5.1), where the temperature rise is equal to the temperature fall, can be calculated as follows:

$$2\,\Delta T\,(\pm) = T_{e.max} - T_{e.min} = 49 - (-18) = 67°C\,(120°F).$$

Therefore, the temperature variation ΔT (±) can be calculated as follows:

$$\Delta T\,(\pm) = \frac{T_{e.max} - T_{e.min}}{2} = (\pm)\,33.5°C\,(\pm 60°F)$$

Consequently, the implied construction temperature derived from AASHTO's specifications using Equation (5.1) would be calculated as follows:

$$T_{Const} = 49 - 33.5 = -18 + 33.5 = 15.5°C\,(60°F)$$

For concrete bridges in moderate climates, the specifications suggest a rise in temperature ΔT (+) of +16.7°C (+30°F) and a fall in temperature of ΔT (–) of –22.2°C

(–40°F). The total temperature range considering these variations could be calculated as follows,

$$2\Delta \mathrm{T}\,(\pm) \;=\; \Delta \mathrm{T}\,(+) \;+\; \Delta \mathrm{T}\,(-) \;=\; 16.7 \;+22.2 \;=\; (\pm)\,38.9°\mathrm{C}\,(70°\mathrm{F}\,).$$

However, assuming the construction temperature for the concrete bridge to be the same as that for steel bridges, which is 15.5°C (60°F), would align with the AASHTO implication.

The potential deviation between the implied construction temperature derived from AASHTO and the actual variability in construction temperature might result in temperature changes (ΔT±) that exceed the design temperature variations specified by AASHTO. In this context, considering a pragmatic range of construction temperature variance spanning from –1.1°C (30°F) to 32.2°C (90°F), the maximum thermal differentials observed were:

For steel,

$$\Delta \mathrm{T}\,(\pm) \;=\; \mathrm{T}_{\mathrm{e.max}} - \mathrm{T}_{\mathrm{ConstMin}} =\; 49-(-1.1)=(\pm)\,50.1°\mathrm{C}\;\;(\pm 90°\mathrm{F})$$

For concrete,

$$\Delta \mathrm{T}\,(+) \;=\; \mathrm{T}_{\mathrm{e.max}} - \mathrm{T}_{\mathrm{ConstMin}} =\; 32.2-(-1.1)=(+)\,33.3\;°\mathrm{C}\;\;(+60°\mathrm{F})$$

$$\Delta \mathrm{T}\,(-) \;= \mathrm{T}_{\mathrm{ConstMax}} - \mathrm{T}_{\mathrm{e.min}} = 32.2-(-6.7)\;=(-)\,38.9°\mathrm{C}\;\;(-70°\mathrm{F})$$

It is clear that these variations exceed the prescribed design temperatures outlined by AASHTO when accounting for the variation in construction temperature. This is illustrated in Figures 5.1 and 5.2, which depict the variations in EBTs, showing both seasonal and daily fluctuations for steel and concrete decks within one thermal cycle of a year

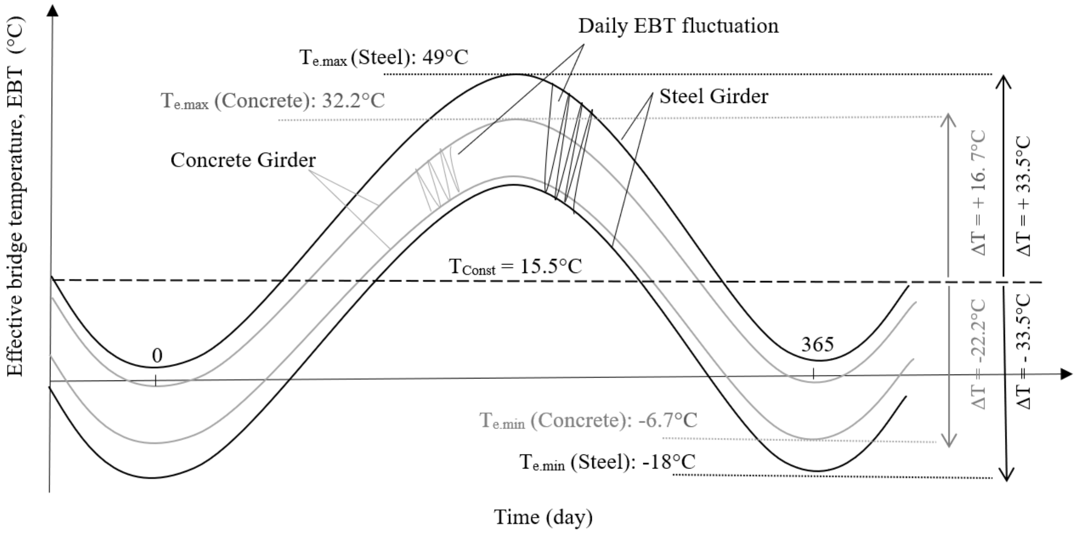

Figure 5.1. Variations in EBTs for steel and concrete decks over one thermal cycle of a year, based on an implied construction temperature of 15.5°C (60°F) derived from AASHTO.

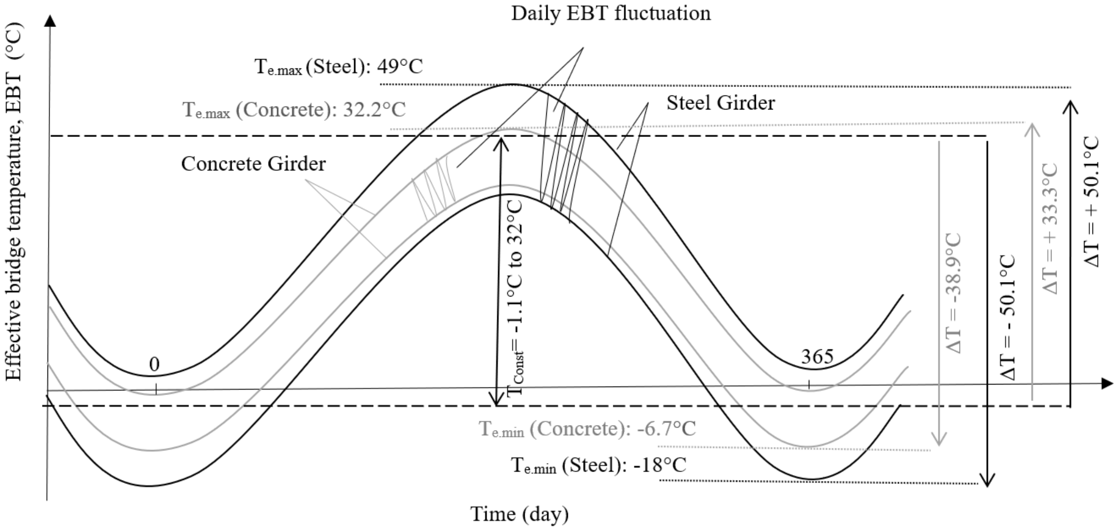

Figure 5.2. Variations in EBTs for steel and concrete decks over one thermal cycle of a year, considering range of construction temperature spanning from –1.1°C (30°F) to 32.2°C (90°F).

In general, different states in the USA adopt varying criteria and procedures concerning the consideration of construction temperature. The Iowa State Department of Transportation (DOT) recommends taking into account temperature variations during construction by applying setting factors of 1.50 for precast PSC bridges and 1.33 for continuous welded plate girder bridges. These factors aim to increase the calculated thermal movement for construction temperature ranging from 4 to 24 °C (25 to 75°F).

According to Canadian code (CHBDC), the observation that previously considered in AASHTO Standard Specification remains applicable as CHBDC adopt a specific construction temperature value of 15°C in the absence of site-specific data for both steel and concrete bridges (refer to Section 2.6.3). Considering the realistic variability in construction temperature, the resulting maximum temperature changes observed in both steel and concrete bridges could exceed the specified design temperatures.

According to Eurocode (CEN, 2003a), the recommended approach for determining the construction temperature is based on the predictable temperature, defined as the temperature of the element at its relevant stage of restraint (completion). If the construction temperature is unpredictable, the average temperature during the construction period is used instead. In the absence of such information, a construction temperature of 10°C is typically assumed. When there is uncertainty about the bridge's sensitivity to construction temperature, it is advisable to consider both lower and upper limits for the expected temperature (refer to Section 2.6.3). In the absence of specific information, Eurocode accounts for realistic variability in construction temperature only in scenarios where there is uncertainty about the bridge's sensitivity. Thus, the observation previously considered in AASHTO remains applicable, as Eurocode also adopts a specific construction temperature value of 10°C.

5.2. Proposed New Considerations for Construction Temperature

Some current bridge design specifications adopt an inaccurate approach by overlooking the potential variability in construction temperatures when estimating the temperature variations experienced by the bridge. Although construction temperature is generally assumed in the design process, it is not explicitly addressed in the recommendations, and specific upper or lower bounds for construction temperature during the construction phase are not provided. As a result, actual temperature changes in the bridge superstructure may exceed the assumed values, leading to potential inaccuracies in predicting thermal displacements, as observed in the previous Section (5.1.1).

This section proposes a new approach to incorporating construction temperature as a design parameter. The proposed approach involves defining an appropriate range for construction temperatures, denoted as [$T_{Const.min}$, $T_{Const.max}$], during the design phase and ensuring that this range is managed and controlled throughout the construction phase. By adopting this approach, the accuracy of thermal displacement and internal force predictions can be improved, thereby enhancing overall design outcomes. Moreover, by selecting the construction temperature to achieve symmetrical temperature variation during both expansion and contraction phases, the negative effects of thermal loading can be minimized.

However, Specifying an exact temperature range for construction can be challenging due to varying environmental conditions and project-specific factors. Achieving complete control over ambient temperatures might not be feasible. However, collaborating with structural engineers and employing appropriate construction techniques could be effective for managing temperatures within an acceptable range. For instance, monitoring weather conditions and scheduling construction activities during periods with more favorable temperatures can be beneficial. Implementing temporary heating or cooling systems in construction areas can regulate temperatures, particularly during extreme weather conditions, thereby ensuring that materials remain within the desired range. In addition, Seeking advice from experienced engineers, material specialists, and contractors who possess expertise in working within specific temperature ranges can offer valuable insights and guidance for managing temperatures within an acceptable range.

The followed sections will examine the feasibility of defining the construction temperature range using Arsoy (2008) mathematical model, which accounts for temperature difference patterns encompassing both seasonal and daily cycles of the EBT at specific locations.

5.2.1. Mathematical Model for Daily and Seasonal Thermal Bridge Displacements by Arsoy in 2008

In 2008, Arsoy introduced a mathematical model designed to predict temperature difference patterns for a specific location. This model is based on expected maximum and minimum shaded air temperatures and average daily temperature variations, which are determined from statistical analyses of historical data spanning a significant period, such as 40 years. The analysis includes record maximum and minimum temperatures, average maximum and minimum temperatures, and average values.

The proposed mathematical model accounts for both seasonal and daily fluctuations in the EBT, which exhibit time-dependent variations resembling a sine function. When considering only seasonal temperature variations, the EBT as a function of time (t) can be expressed by the following Equation (5.2):

$$\mathrm{T}_{e}(\mathrm{t}) \;=\; \mathrm{T}_{\mathrm{e.min}} \;+\; \mathrm{T}_{\mathrm{e.amp}}\left[1+\left(\sin\left(\frac{2\pi}{365}(\mathrm{t}+\mathrm{t}_0)\right)\right)\right] \tag{5.2}$$

T_{e} (t) represents the time-dependent EBT, while $\mathrm{T}_{\mathrm{e.min}}$ and $\mathrm{T}_{\mathrm{e.max}}$ denote the maximum and minimum extreme EBTs expected during the lifespan of the bridge, and $\mathrm{T}_{\mathrm{e.amp}}$ is the amplitude of the temperature variation, calculated as $(\mathrm{T}_{\mathrm{e.max}} - \mathrm{T}_{\mathrm{e.min}})/2$, t denotes the time in days (measured from the beginning of the calendar year), and t_0 is the time shift that defines the starting value of the EBT (t = 0) for a particular location.

If both daily and seasonal temperature variations are considered, the EBT as a function of time (t) can be expressed by the following Equation (5.3):

$$\mathrm{T}_{\mathrm{e}}(\mathrm{t}) = (\mathrm{T}_{\mathrm{e.min}} + \mathrm{A}(\mathrm{t})) + (\mathrm{T}_{\mathrm{e.amp}} - \mathrm{A}(\mathrm{t}))\left[1+\left(\sin\left(\frac{2\pi}{365}(\mathrm{t}+\mathrm{t}_0)\right)\right)\right] + \mathrm{A}(\mathrm{t})\sin(2\pi(\mathrm{t}+\mathrm{t}_{\mathrm{d}})) \tag{5.3}$$

To model the time-dependent daily temperature difference parameter, the variation of the parameter A(t) throughout the year could be effectively represented by the following sine function, as given in Equation (5.4),

$$\mathrm{A}(\mathrm{t}) = \mathrm{A}_{\mathrm{min}} + \left(\frac{\mathrm{A}_{\mathrm{max}}-\mathrm{A}_{\mathrm{min}}}{2}\right)\left[1+\left(\sin\left(\frac{2\pi}{365}(\mathrm{t}+\mathrm{t}_{\mathrm{a}})\right)\right)\right] \tag{5.4}$$

A(t) is the time-dependent daily temperature fluctuation. $\mathrm{A}_{\mathrm{max}}$ represents the maximum value of A(t), which is equal to half the maximum daily difference in EBT for a given year. Similarly, $\mathrm{A}_{\mathrm{min}}$ represents the minimum value of A(t), which is equal to half the minimum daily difference in EBT for a given year.

5.2.2. Defining Construction Temperature Range by Applying Arsoy Model

The Arsoy model provides a realistic perspective of potential daily and seasonal variations, offering valuable insights for defining the proposed construction temperature range. This section will present a numerical example to demonstrate the application of Arsoy (2008) model in defining the construction temperature range.

- Numerical Example:

The statistical evaluations of historical data spanning 72 years, chosen for use in Arsoy (2008) model, are derived from the T.C. Ministry of Environment, Urbanization, and Climate Change (General Directorate of Meteorology).

Table 5.1 presents the average maximum (Avg. Max) and minimum (Avg. Min) temperatures, average temperature (Avg), and the recorded maximum (Rec. Max) and minimum (Rec. Min) values of shaded air temperatures from 1950 to 2022 for each month in Istanbul, Turkey. This data is also illustrated graphically in Figure 5.3.

The shaded air maximum and minimum temperatures recorded over a span of 72 years are 40.6°C in July and -9°C in February, respectively. Considering the extreme environmental conditions that the bridge may encounter throughout its operational lifespan, these peak values will be adopted as design parameters.

For this example, the EBT for the bridge will be considered equivalent to the shaded air temperature.

Table 5.1. Temperature variation patterns in Istanbul, between (1950 - 2022).

Istanbul	Jan	Feb	Mar	Apr	May	Jun	Jul	Aug	Sep	Oct	Nov	Dec
Avg. Max °C	9.5	10.2	12.2	17.3	22.3	26.9	29.5	29.6	25.8	20.6	16.0	11.7
Avg. Min °C	4.1	4.2	5.4	9.2	13.6	18	20.4	20.7	17.6	13.7	9.8	6.4
Avg °C	6.7	6.9	8.4	12.8	17.6	22.2	24.6	24.6	21.1	16.6	12.5	8.9
Rec. Max °C	22.4	23.4	28.6	33.3	36.4	38.9	40.6	40.1	39.6	33.5	27.2	25.0
Rec. Min °C	-6.8	-9.0	-5.6	0.2	4.8	9.8	13.6	14.3	7.7	2.5	-2.0	-4.2

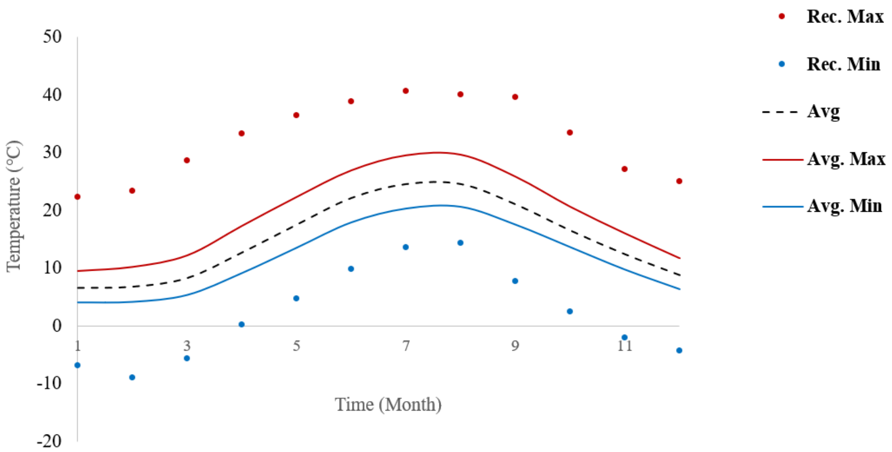

Figure 5.3. Temperature variation patterns in Istanbul, between (1950 – 2022).

In constructing this model to determine the maximum EBT ($T_{e.max}$) and the minimum EBT ($T_{e.min}$), it is more reasonable to consider the most frequent minimum and maximum EBTs ($T_{Freq.min}$ and $T_{Freq.max}$) rather than using the peak values of maximum and minimum temperatures recorded over 72 years (Rec. Min and Rec. Max). To define $T_{Freq.min}$ and $T_{Freq.max}$, it is advisable to select values between the recorded peak values and the average temperatures.

The following proposed approach could be used to determine $T_{Freq.min}$ and $T_{Freq.max}$,

To determine $T_{Freq.max}$, the process involves first assuming the minimum time-dependent daily temperature difference during summer (A_{min}), using the maximum temperature recorded over the 72-year span, which is 40.6°C in July, along with the average temperature for the same month and the corresponding minimum temperature recorded for that month, as shown in Figure 5.4. $T_{Freq.max}$ can then be calculated by adding A_{min} to the average temperature for the same month. The calculations are as follows:

$$A_{min} = 0.5\,\frac{|\text{Rec. Max} - \text{Avg}| + |\text{Rec. Min} - \text{Avg}|}{2} = 0.5\,\frac{|40.6 - 24.6| + |\,13.6 - 24.6|}{2} = 6.75°\text{C}$$

$$T_{Freq.max} = \text{Avg} + A_{min} = 24.6 + 6.75 = 31.35°\text{C}$$

Similarly, to determine $T_{Freq.min}$, the process involves first assuming the maximum time-dependent daily temperature difference during winter (A_{max}), using the minimum temperature recorded over the 72-year span, which is -9°C in February, along with the average temperature for the same month and the corresponding maximum temperature recorded for that month, as shown in Figure 5.4. $T_{Freq.min}$ can then be calculated by subtracting A_{max} from the average temperature for the same month. The calculations are as follows:

$$A_{max} = 0.5\,\frac{|\text{Rec. Min} - \text{Avg}| + |\text{Rec. Max} - \text{Avg}|}{2} = 0.5\,\frac{|-9 - 6.9| + |23.4 - 6.9|}{2} = 8.1°\text{C}$$

$$T_{Freq.max} = \text{Avg} - A_{min} = 6.9 - 8.1 = -1.2°\text{C}$$

Consequently, $T_{e.amp}$ is calculated as follows:

$$T_{e.amp} = \frac{T_{Freq.max} - T_{Freq.min}}{2} = \frac{31.5 - (-1.2)}{2} = 16.33°\text{C}$$

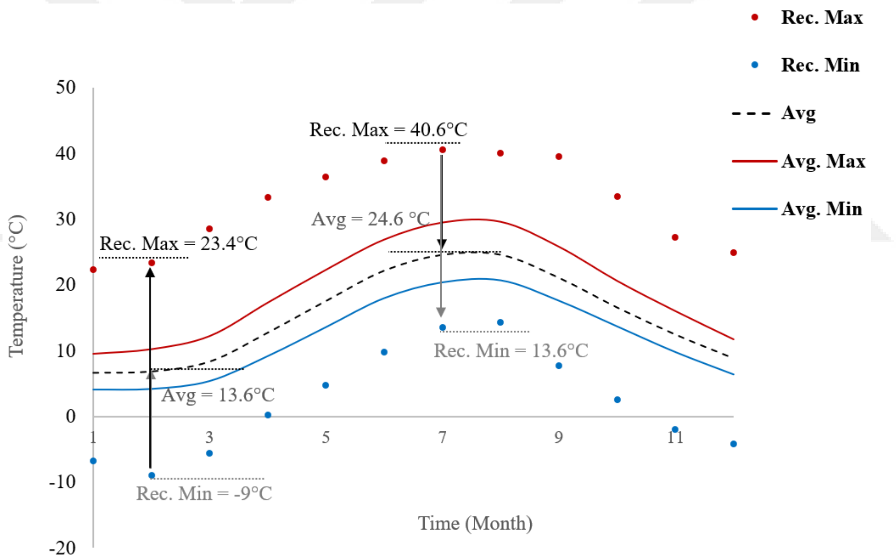

Figure 5.4. Determination of maximum and minimum temperatures recorded over a 72-year span, along with corresponding Rec. Min, Rec. Max, and Avg temperatures.

The sine function, as described in Equation (5.3), initiates from the average value of the range. To align the first value of the function with the temperature on January 1, a time shift of 244 days is required. This adjustment ensures that the function aligns accurately with the temperature data on the specified date. Therefore, t_0 = 244 is deemed appropriate. Disregarding hourly temperature variations, t_d = 0 is assigned. As the peak variation in daily temperatures occurs halfway through a period (183 days) from the sine function's beginning, the value of t_a is set at 61 days (t_a = 244 – 183 = 61), considering the starting value of the sine function has a time shift of 244 days. The proposed estimates the time-dependent temperature using Equation (5.3) as follows:

$$T_e(\mathrm{t}) = (\,-9 + \mathrm{A(t)}) + (16.33 - \ \mathrm{A(t)})\left[1 + \left(\sin\left(\frac{2\pi}{365}(\mathrm{t} + 244)\right)\right)\right] + \mathrm{A(t)}\sin(2\pi \mathrm{t}))$$

The approximate daily temperature difference in winter (A_{max}) is 8.1°C, and in summer (A_{min}) is 6.75°C, and between these values during other months. The parameter for daily temperature difference is presented using Equation (5.4) as follows:

$$\mathrm{A(t)} = \ 6.75 + \left(\frac{8.1-6.75}{2}\right) + \left[1 + \left(\sin\left(\frac{2\pi}{365}(\mathrm{t} + 61)\right)\right)\right]$$

Figure 5.5 displays the graphical variation of time-dependent temperature changes. To enhance graph clarity, every fifth daily cycle is presented.

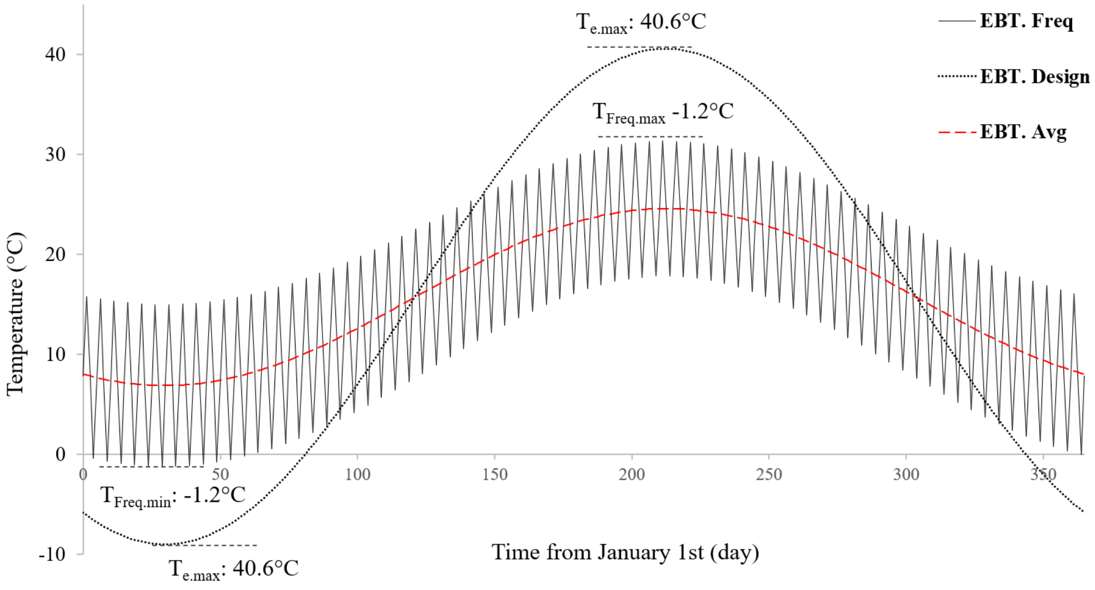

Figure 5.5. The variations in EBTs within one thermal cycle of a year based on Arsoy model (2008).

Based on this mathematical model, the recommended construction temperature range can be established to remain consistent throughout the year. For winter, the desired construction temperature could be set during the daytime, while in summer, it could be established during nighttime. This range is defined to ensure symmetrical temperature variation during both expansion and contraction phases, thereby minimizing the negative effects of thermal loading, as illustrated in Figure 5.6. The suggested range is [$T_{Const.min}$: 10°C, $T_{Const.max}$: 20°C].

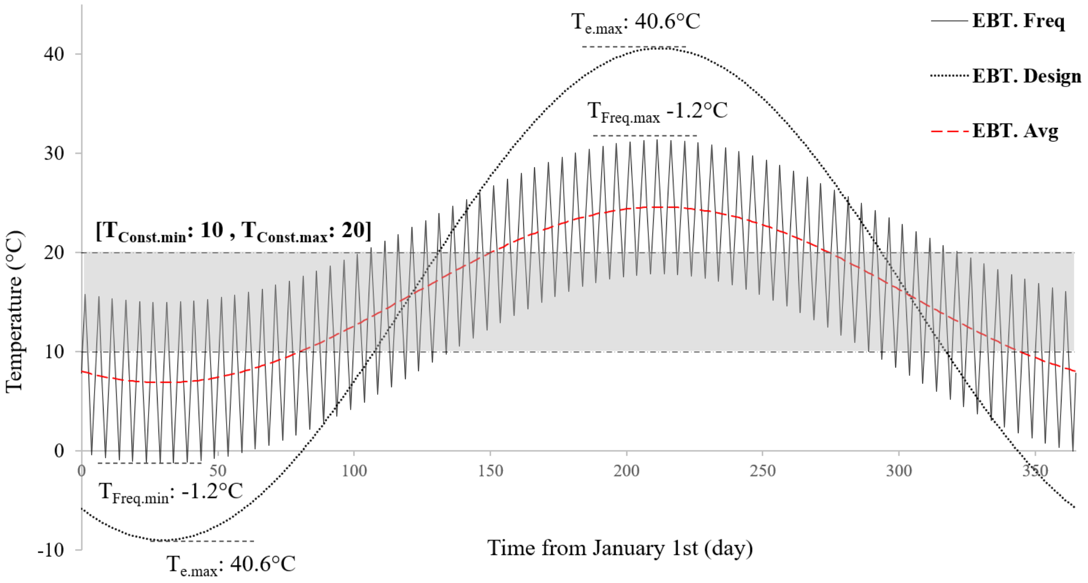

Figure 5.6. The selected construction temperature range [$T_{Const.min}$, $T_{Const.max}$], based on Arsoy model (2008).

5.3. Effective Construction Temperature

Construction temperature for IABs is defined as the EBT when the integral connection between the bridge deck and abutment is established. This time is characterized by the connection being strong enough to handle thermal loadings and displacements, marking the beginning of interaction between the bridge and the soil (refer to Section 2.3.6). Consequently, the construction temperature varies for different bridge superstructure materials due to differing times and the nature of this integral connection.

Construction temperature for steel bridges: Typically, the construction temperature for steel bridges is considered to be the ambient temperature at the time of final connection or welding of the steel components to the abutment.

Construction temperature for concrete bridges: For concrete bridges, the construction temperature is often taken as the ambient temperature at the time when the concrete has gained sufficient strength to form an integral connection with the abutment.

Therefore, the construction temperature used in the design to predict longitudinal displacements of the bridge will differ from the proposed or assumed ambient construction temperature.

A new parameter, termed effective construction temperature ($T_{e.Const}$), will be proposed to refer to the actual construction temperature. The effective construction temperature for both steel and concrete superstructures is defined as follows:

- Effective construction temperature for steel superstructure:

As mentioned above, the construction temperature for steel bridges is considered to be the ambient temperature at the time of final connection or welding of the steel components to the abutment. Thus, the effective construction temperature for steel will be assumed to be equivalent to the assumed or proposed ambient construction temperature.

- Effective construction temperature for concrete superstructure:

As previously noted, the construction temperature for concrete is the temperature recorded when the abutments and deck attain sufficient strength to provide girder-to-abutment continuity, thereby restraining the thermal displacement of the girders. It is crucial to account for the temperature variations resulting from the release of hydration heat during the initial hours following the casting of concrete when determining the construction temperature.

To estimate the rate of early temperature increase in the concrete deck due to hydration heat, several sets of experimental data were consulted. These datasets, sourced from studies by researchers such as Riding et al. (2009), Subramaniam et al. (2010), Choi et al. (2011), and Domski et al. (2015), focused on the temperature development within concrete decks during the hardening process. The experimental datasets show the changes in temperature within the concrete deck over time, making it worthwhile to determine when the concrete achieves adequate strength to restrict the displacement of the concrete girders. According to the typical strength development of concrete, it can be reasonably assumed that concrete attains about 40 percent of its strength within a 3-day period, equivalent to 72 hours. After analyzing the experimental data, it was concluded that the initial temperature increases in concrete due to hydration heat could be estimated at 5°C. Therefore, the effective construction temperature for concrete bridges will be the assumed or proposed ambient construction temperature plus 5°C.

5.4. Conclusion

Bridge design specifications generally recommend a uniform temperature range for thermal displacement calculations, considering factors such as climate, materials, and assumed construction temperatures. However, many specifications overlook the variability in construction temperatures. Neglecting accurate construction temperature assumptions during design can result in temperature variations that exceed specified limits, leading to potential inaccuracies in thermal displacement predictions.

Although construction temperature is assumed during the design process, it is not explicitly addressed in the recommendations, and no specific upper or lower bounds for construction temperatures are provided. This gap can result in design assumptions that may not align with actual field conditions.

The proposed approach involves defining a suitable construction temperature range, denoted as [$T_{Const.min}$, $T_{Const.max}$], during the design phase and ensuring that this range is managed and controlled throughout the construction phase. Adopting this approach can enhance the accuracy of thermal displacement and internal force predictions, thereby improving overall design outcomes.

Specifying an exact construction temperature range [$T_{Const.min}$, $T_{Const.max}$] is challenging due to environmental variations. However, insights from the Arsoy model (2008), which accounts for daily and seasonal temperature fluctuations, enable the selection of a suitable year-round range for local conditions. By applying this model, the recommended construction temperature range can be precisely defined to ensure balanced temperature variations during both expansion and contraction phases, thereby minimizing the negative effects of thermal loading.

Construction temperature for IABs is defined as the EBT when the integral connection between the bridge deck and abutment is established. This temperature varies with different bridge superstructure materials due to differences in timing and connection nature.

A new parameter, the effective construction temperature ($T_{e.Const}$), is proposed to represent the actual construction temperature. For steel bridges, the effective construction temperature equals the proposed construction temperature, while for concrete bridges, it is the proposed temperature plus 5°C to account for early hydration heat.

6. A PARAMETRIC STUDY UNDER VARIOUS CONSTRUCTION TEMPERATURE SCENARIOS

Although there has been a great deal of numerical and experimental IAB research performed, most have focused on bridge length, foundation soil stiffness, and abutment height effects (refer to Section 2.8). However, bridge response as a function of superstructure material and construction temperature has not been extensively investigated. the significance of construction temperature in IABs is important, as it directly influences the magnitude of thermal displacement of bridge girders.

However, effects of those design variables are still not fully understood. To minimize those uncertainties, a deeper understanding of bridge behavior is needed. Therefore, in this study, numerical modeling and parametric study were conducted to expand the results to general cases under different variables and to develop a rational basis for expanding the length limitations of IABs.

The primary objective of this study is to investigate the influence of construction temperature on the response of both steel and PSC IABs. This study also considered other factors influencing bridge response: (1) bridge length, (2) foundation soil stiffness, (3) abutment height. To achieve this objective, a series of Analyses were performed using MIDAS CIVIL software.

The results of the analysis are presented as the response of the bridge elements. The response was evaluated by measuring the bending moment and displacement over the girder, pile, and abutment.

6.1. Parameters Selection and Discussion for the Parametric Study

The parameters employed in the parametric study encompass construction temperature, superstructure material, bridge length, foundation soil stiffness, and abutment height.

This section provides a description of these parameters, including their respective magnitudes, intended for use in the parametric study of IABs.

6.1.1. Construction Temperature Selection and Discussion

A notable gap exists in the literature regarding the influence of construction temperature on the response of IABs (refer to Section 2.8.1). Consequently, construction temperature is incorporated into the parametric study.

The design extreme temperatures for this study will be based on historical statistical data utilized in the numerical example (refer to Section 5.1.2.2). The maximum and minimum design temperatures are set at 40.6°C and -9°C, respectively.

The proposed effective construction temperatures for IABs, depending on material type (refer to Section 5.3), are selected as follows and presented in Table 6.1.

Effective construction temperature for steel superstructure:

Since there are no specific limits for the construction temperature of steel superstructures, the minimum effective construction temperature is set at -9°C, and the maximum is 40.6°C. Additionally, two intermediate values within this range are selected based on the recommended construction temperature range of [10°C, 20°C] (refer to Section 5.2.2).

Effective construction temperature for PSC superstructure:

Concrete has specific temperature limits during casting to ensure its integrity and strength, which can vary by standard. According to the American Concrete Institute (ACI) code, fresh concrete should typically be maintained between 10°C and 32°C for optimal curing and setting. Additionally, the ACI specifies that the temperature during curing should not drop below 5°C to prevent diminished strength from freezing.

In this study, the selected minimum and maximum construction temperatures for PSC superstructures are 5°C and 32°C, respectively. Two intermediate values within this range are also chosen based on the recommended construction temperature range of [10°C, 20°C] (refer to Section 5.2.2). To account for the initial temperature rise due to hydration heat, an additional 5°C is added to the selected construction temperatures.

Table 6.1. Selected construction temperatures for steel and PSC girders.

Girder material	T_{Const} (°C)			
Steel	–9	10	20	40.6
PSC	5	10	20	32

6.1.2. Bridge Length Selection and Discussion

The analysis focuses on how different construction temperatures affect the stress experienced by both steel and PSC bridges across varying lengths. The goal is to determine how optimizing construction temperatures might mitigate negative thermal effects, especially in longer bridges, thereby addressing challenges associated with the limited length of IABs.

The chosen bridge lengths comprise one, two, and three spans: (1) 30 m, (2) 30 + 30 = 60 m, and (3) 40 + 40 + 40 = 120 m, as shown in Figure 6.1

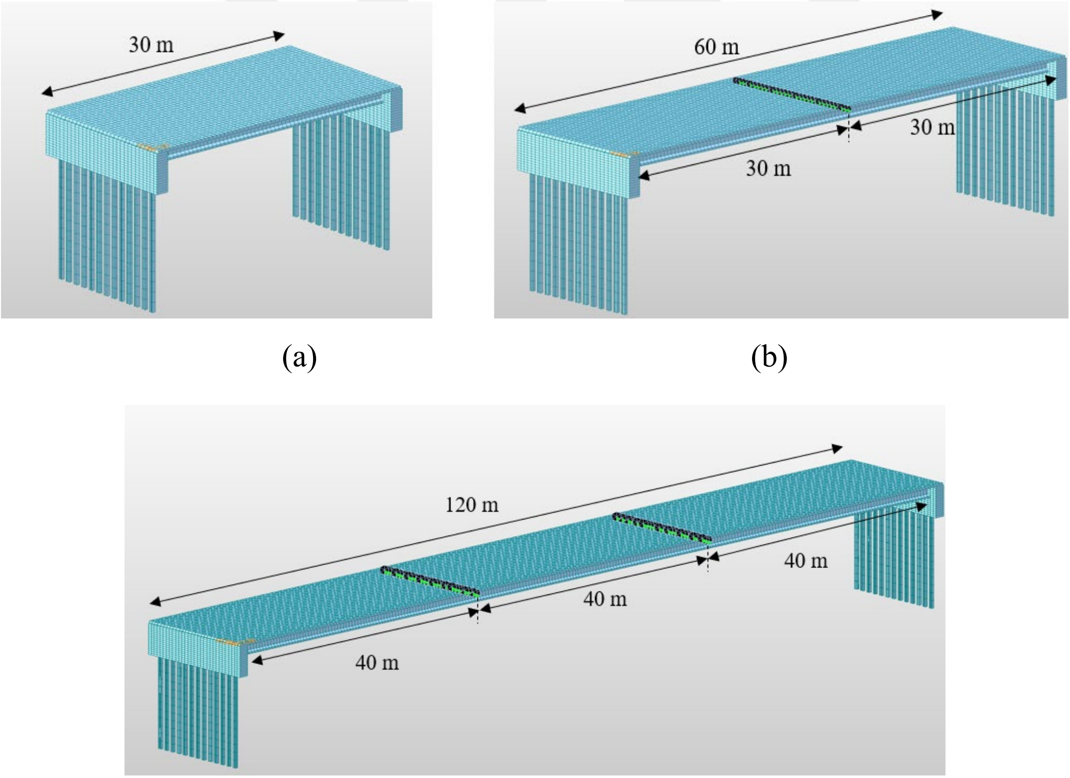

(a)

(b)

(c)

Figure 6.1. 3D finite element model of IAB for different lengths, (a) 30 m, (b) 30 + 30 = 60 m, and (c) 40 + 40 + 40 = 120 m.

6.1.3. Abutment Height Selection and Discussion

The selection of abutment heights is based on the most frequently observed heights documented in previous studies and the recommendations from the Ontario Ministry of Transportation (MTO) (Hussain and Bagnariol, 1996), which indicate that bridges with abutment heights exceeding 6 m are generally not suitable for integral abutment design. Consequently, three distinct abutment heights will be considered in this study: 3 meters, 4.5 meters, and 6 meters, as shown in Figure 6.2.

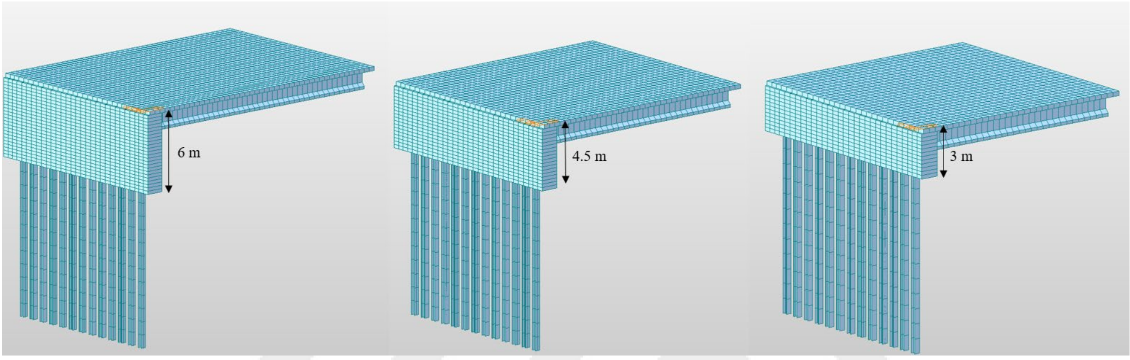

(a) (b) (c)

Figure 6.2. 3D finite element model of IAB for different abutment heights, (a) 3 m, (b) 4.5 m, and (c) 6 m.

6.1.4. Soil Foundation Type Selection and Discussion

The stiffness of the foundation primarily depends on the type of soil surrounding the piles, which is generally uncontrollable during the design stage. Therefore, based on the most commonly observed foundation soil types documented in previous studies, three types of sandy soil foundation with varying stiffness were selected.

The values for the unit weight (γ) of sandy soil chosen as the foundation for different relative densities will be sourced from Bowles (1996) and shown in Table 6.2.

The modulus of elasticity (Es) and Poisson's ratio (υ) of sandy soil can vary depending on factors such as grain size distribution, density, moisture content, and mineral composition. However, the typical ranges would be presented as follows:

(1) for loose sandy soil, the modulus of elasticity would range from 5 to 25 MPa, and Poisson’s ratio would range from 0.15 to 0.35.

(2) for medium sandy soil, the modulus of elasticity would range from 25 to 50 MPa, and Poisson’s ratio would range from 0.25 to 0.35.

(3) for dense sandy soil, the modulus of elasticity would range from 50 to 100 MPa, and Poisson’s ratio would range from 0.30 to 0.40.

The chosen values for the parametric study are presented in the following Table 6.2.

Table 6.2. Properties of sand used in the analyses:

Soil Property	Relative Density		
	Losse	Medium	Dense
φ Internal angle of friction (◦)	30°	35°	40°
γ Unit weight (kN/m^3)	16	18	20
E_S Modulus of elasticity (MPa)	10	30	60
υ Poison’s ratio	0.2	0.3	0.4

6.2. Summary of Selected Variables Considered in the Parametric Study

The parametric study aims to investigate the effect of construction temperature on the response of both steel and PSC IABs. Additionally, it considers the influence of three key parameters: (1) bridge length, (2) abutment height, and (3) foundation stiffness. The magnitudes for each of these parameters are presented in Table 6.3.

The effective construction temperatures for both steel and PSC are detailed in Table 6.4.

The three design parameters are listed in Table 6.3. were selected based on previous research ((Kim and Laman (2012), Kim and Laman (a2010)).

Table 6.3. Primary design parameters and ranges for the parametric study:

Variables	Description
Bridge span length, L (m)	30 m 30 + 30 = 60 40 + 40 + 40 = 120
Abutment height, H (m)	3, 4.5, 6
Sandy soil foundation stiffness	Loose ($\varphi = 30°$), Medium ($\varphi = 35°$), and Dense ($\varphi = 40°$).

Table 6.4. Effective construction temperatures for steel and PSC:

Girder material	$T_{e.Const}$ (°C)			
Steel	–9	10	20	40.6
PSC	10	15	25	37

6.3. Development of 3D Numerical Model

The study involves two primary groups of analyses: the first group focuses on steel IABs, and the second group examines PSC IABs. Each group of analyses is conducted using varying construction temperatures. The effects of three key parameters (1) bridge length, (2) abutment height, and (3) foundation stiffness is assessed for both groups.

The 3D finite element model used for these analyses is developed with MIDAS CIVIL software. A one-step 3D static analysis is employed for the finite element modeling. The bridge modeling techniques in this model are consistent with those used in the previous 3D model (refer to Section 3.1.1).

6.3.1. Bridge Design Parameters and Description:

Different bridge lengths and spans will be considered (30 m, 60 m, and 120 m). For the parametric study involving other parameters like abutment height and foundation stiffness, a bridge length of 120 m is used.

Each bridge girder, for varying bridge lengths and spans, was designed according to the AASHTO LRFD Bridge Design Specifications (2014). Both bridge types feature a superstructure with five girders and a cast-in-place concrete deck, which is 0.3 m thick with a compressive strength of C35/45 MPa.

The concrete girders also have a compressive strength of C35/45 MPa, while the steel girders have a yield strength of 450 MPa. Detailed cross-sections of each bridge are provided in Table 6.5 and Figure 6.3.

Table 6.5. Detailed of bridge girder sections:

Bridge length (m)	PSC girder	Steel girder (flange width × flange thickness × web depth × web thickness)
30	BT(72) (1372)	457.2× 31.7 × 1168.4 × 15.9
60	BT(72) (1372)	(+): 355.6 × 31.7 × 965.2 × 9.5 (–): 508 × 38.1 × 965.2 × 9.5
120	BT(81) (1600)	(+): 508 × 38.1 × 1371.6 × 12.7 (–): 508 × 50.8 × 1371.6 × 12.7

(+): positive flexure, (-): negative flexure.

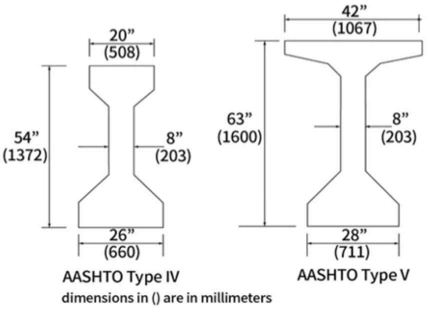

Figure 6.3. Detailed cross-sections of PSC girders.

The main girders of both steel and PSC bridges are supported by reinforced concrete abutments of varying heights (3 m, 4.5 m, and 6 m), each with a thickness of 1.4 m and a compressive strength of 35/45 MPa. For analyses related to bridge length and foundation stiffness, a height of 4 m was selected for the abutments.

Each abutment is supported by 13 equally spaced HP 400×231 steel piles with a yield strength of 450 MPa, oriented with their weak axis to resist longitudinal bridge movements. The detailed cross-section and length of the piles are provided in Table 6.6.

These specifications were implemented based on information from Kim et al. (2021) and Kim and Laman (2012), which include finite element modeling and field monitoring studies of IABs in the USA.

Table 6.6. Detailed of bridge pile and deck sections:

Pile web (mm) and pile flanges (mm)	Pile length (m)
372 × 26 402 × 26	12

6.3.2. Thermal Loads Modeling

Regarding the thermal loadings affecting the bridge model, the design extreme temperatures for this study will be based on historical statistical data utilized in the numerical example (refer to Section 5.1.2.2). The maximum and minimum design temperatures are set at 40.6°C and -9°C, respectively.

The effective construction temperatures detailed in Table 6.4, along with the maximum and minimum design temperatures mentioned above, will be used to determine the temperature rise and fall. These calculations, made using Equations (2.15a and 2.15b) (refer to Section 2.6.1), are presented in Table 6.7.

Table 6.7. Temperature rise and fall for both steel and PSC:

Girder material	$T_{e.Const}$ (°C)	–9	10	20	40.6
Steel	ΔT (+)	+49.6	+30.6	+20.6	0
	ΔT (–)	0	–19	–29	–49.6
PSC	$T_{e.Const}$ (°C)	10	15	25	37
	ΔT (+)	+30.6	+25.6	+15.6	+3.6
	ΔT (–)	–19	–24	–34	–46

6.3.3. Backfill–Abutment Interaction Modelling

The typical properties of medium granular backfill soil, as shown in Table 3.2 (refer to Section 3.1.3), were used in the analysis. For the abutment–backfill interaction, the limiting equilibrium approach was applied. The methodology for calculating passive earth pressure behind the abutment follows the Arsoy (2008) method (refer to Section 2.4.1.1). The abutment movement is assumed to contribute equally to both translation and rotation. Consequently, the resultant force curve is derived by averaging the resultant force curves for medium density under pure rotation and pure translation, as shown in Figure 4.2 (refer to Section 4.1.1).

The passive earth pressure will first be calculated for both steel and PSC bridges at different construction temperatures, for three bridge lengths (30 m, 60 m, and 120 m).

Following this, calculations will be performed for both bridge types at different construction temperatures, for three abutment heights (3 m, 4.5 m, and 6 m).

To determine the resultant force (E_P), the displacements for both steel and PSC bridge models at different construction temperatures, for three lengths (30 m, 60 m, and 120 m), are calculated as Δ_{30m}, Δ_{60m}, and Δ_{120m} respectively, using Equation (2.14) (refer to Section 2.5). These values are presented in Table 6.8. The thermal expansion coefficients for steel and PSC are selected as12×10^{-6}/°C and 10×10^{-6}/°C, respectively (refer to Section 3.1.1).

Table 6.8. Displacement for both steel and PSC bridge models at different construction temperatures, for three lengths (30 m, 60 m, and 120 m).

Girder material		ΔT (+)	+49.6	+30.6	+20.6	0
Steel	Displacement (m)	Δ_{30m}	0.009	0.006	0.004	0
		Δ_{60m}	0.018	0.011	0.007	0
		Δ_{120m}	0.036	0.022	0.014	0
PSC	Displacement (m)	ΔT (+)	+30.6	+25.6	+15.6	+3.6
		Δ_{30m}	0.005	0.004	0.002	0.0005
		Δ_{60m}	0.009	0.008	0.005	0.001
		Δ_{120m}	0.018	0.015	0.009	0.002

The passive earth pressure will first be calculated for both steel and PSC bridges at different construction temperatures, for three bridge lengths (30 m, 60 m, and 120 m), each with a 4 m abutment height.

The resultant force at plastic equilibrium (E_{Pmax}), representing the point where full passive forces are mobilized, will be determined using the classical Rankine earth pressure theory (1857). This will be calculated using Equation (2.5b) (refer to Section 2.4.1.1) for a 4 m abutment.

$$K_{pR} = \tan^2\left(45 + \frac{\varphi}{2}\right) = \tan^2\left(45 + \frac{34}{2}\right) = 3.54$$

$$E_{Pmax} = 0.5\, K_{pR}\, \gamma\, H^2 = 0.5 * 3.54 * 18.7 * 4^2 = 529.58\ \text{kN/m}$$

Following the procedures outlined in Section 4.1.1, the resultant passive force (Ep) for a given relative abutment displacement (Δ/H) and the point of application from the top of the abutment for the resultant force are determined using Figure 4.2 (refer to Section 4.1.1) and Figure 2.11 (refer to Section 2.4.1.1), respectively. If the resultant passive force (E_P) is found to be less than the at-rest force, the at-rest value will be used. The results are presented in Table 6.9.

Table 6.9. Resultant passive force (E_P) and its point of application for both steel and PSC bridge models at different construction temperatures, for three lengths (30 m, 60 m, and 120 m).

Girder material		Displacement (m)	$\Delta_{1,30m}$	$\Delta_{2,60m}$	$\Delta_{3,120m}$
Steel	resultant passive force (E_p)	$E_{P\,(+49.6)}$	142.40	286.45	405.72
		$E_{P\,(+30.6)}$	87.23	176.10	353.05
		$E_{P\,(+20.6)}$	65.94	118.01	237.66
		$E_{P\,(0)}$	65.94	65.94	65.94
	Application Point (m)	$(H\text{-}y)_{1\,(+49.6)}$	2.35	2.35	2.35
		$(H\text{-}y)_{2\,(+30.6)}$	2.45	2.35	2.35
		$(H\text{-}y)_{3\,(+20.6)}$	2.67	2.35	2.35
		$(H\text{-}y)_{4\,(0)}$	2.6	2.67	2.67
PSC		Displacement (m)	$\Delta_{1,30m}$	$\Delta_{2,60m}$	$\Delta_{3,120m}$
	resultant passive force (E_p)	$E_{P\,(+49.6)}$	72.41	146.47	294.58
		$E_{P\,(+30.6)}$	65.94	122.27	246.18
		$E_{P\,(+20.6)}$	65.94	73.87	149.37
		$E_{P\,(0)}$	65.94	65.94	65.94
	Application Point (m)	$(H\text{-}y)_{1\,(+30.6)}$	2.45	2.35	2.35
		$(H\text{-}y)_{2\,(+25.6)}$	2.67	2.35	2.35
		$(H\text{-}y)_{3\,(+15.6)}$	2.67	2.35	2.35
		$(H\text{-}y)_{4\,(+3.6)}$	2.67	2.67	2.67

Subsequently, the passive earth pressure will be calculated for both steel and PSC bridges at different construction temperatures, for three abutment heights (3 m, 4.5 m, and 6 m) and a bridge length of 120 m. The resultant force at plastic equilibrium (E_{Pmax}) for three abutment heights (3 m, 4.5 m, and 6 m) will be calculated using the classical Rankine earth pressure theory (1857) (refer to Section 2.4.1.1). These forces will be denoted as $E_{Pmax,3m}$, $E_{Pmax,4.5m}$, and $E_{Pmax,6m}$, respectively.

$$E_{Pmax,3m} = 0.5\ K_{pR}\ \gamma\ H^2\ = 0.5\ *\ 3.54\ *\ 18.7\ *\ 3^2 =\ 297.90\ kN/m$$

$$E_{Pmax,4.5m} = 0.5\ K_{pR}\ \gamma\ H^2\ = 0.5\ *\ 3.54\ *\ 18.7\ *\ 4.5^2 =\ 670.25\ kN/m$$

$$E_{Pmax,6m} = 0.5\ K_{pR}\ \gamma\ H^2\ = 0.5\ *\ 3.54\ *\ 18.7\ *\ 6^2 =\ 1191.65\ kN/m$$

Following the procedures outlined in Section 4.1.1, the resultant passive force (E_P) for a given relative abutment displacement (Δ/H) and the point of application from the top of the abutment for the resultant force are determined using Figure 4.2 (refer to Section 4.1.1) and Figure 2.11 (refer to Section 2.4.1.1), respectively. If the resultant passive force (E_P) is found to be less than the at-rest force, the at-rest value will be used. The results are presented in Table 6.10.

Table 6.10. Resultant passive force (E_P) and its point of application for both steel and PSC bridge models at different construction temperatures, for three abutment heights (3 m, 4.5 m, and 6 m).

Girder material		Displacement (m)	$H_{1,3m}$	$H_{2,4.5m}$	$H_{3,6m}$
Steel	resultant passive force (E_p)	$E_{P1\ (+49.6)}$	253.99	494.15	860.57
		$E_{P2\ (+30.6)}$	214.50	397.82	529.50
		$E_{P3\ (+20.6)}$	178.55	267.13	355.26
		$E_{P4\ (0)}$	37.10	83.46	148.38
	Application Point (m)	$(H\text{-}y)_{1\ (+49.6)}$	1.76	2.64	3.53
		$(H\text{-}y)_{2\ (+30.6)}$	1.76	2.64	3.53
		$(H\text{-}y)_{3\ (+20.6)}$	1.76	2.64	3.53
		$(H\text{-}y)_{4\ (0)}$	2.00	3.00	4.00
		Displacement (m)	$\Delta_{1,30m}$	$\Delta_{2,60m}$	$\Delta_{3,120m}$
PSC	resultant passive force (E_p)	$E_{P1\ (+30.6)}$	221.24	331.17	440.64
		$E_{P2\ (+25.6)}$	184.94	276.72	368.03
		$E_{P3\ (+15.6)}$	112.34	167.81	222.83
		$E_{P4\ (+3.6)}$	37.09	83.46	148.38
	Application Point (m)	$(H\text{-}y)_{1\ (+30.6)}$	1.76	2.64	3.53
		$(H\text{-}y)_{2\ (+25.6)}$	1.76	2.64	3.53
		$(H\text{-}y)_{3\ (+15.6)}$	1.76	2.64	3.53
		$(H\text{-}y)_{4\ (+3.6)}$	2.00	3.00	4.00

The distribution of earth pressure behind the abutment is not specified in this approach. Therefore, the resultant force is modeled as a one-dimensional force applied at a specified point of application (refer to Section 2.4.1.1).

To determine the active lateral earth pressure load, Rankine theory (1857) will be applied, with the active earth pressure coefficient calculated using Equation (2.5a) (refer to Section 2.4.1.1). For calculating the at-rest lateral earth pressure coefficient, Jaky's equation (1944) will be used, as detailed in Equation (2.1) (refer to Section 2.4.1.1). These calculations are provided as follows:

$$\mathrm{K}_{\mathrm{aR}} = \left(45^\circ - \frac{\varphi}{2}\right) = \left(45^\circ - \frac{34}{2}\right) = 0.28$$

$$\mathrm{K}_0 = 1 - \sin(\varphi) = 1 - \sin(34) = 0.44$$

The earth pressure distribution is modeled as a simple triangular shape for both active and at-rest earth pressures (σ_a and σ_0). Consequently, the maximum active and at-rest earth pressures at the bottom of the abutment, for heights of 3 m, 4.5 m, and 6 m, will be calculated using Equation (2.3) (refer to Section 2.4.1.1, Figure 2.8). These pressures will be denoted as $\sigma_{a,3m}$, $\sigma_{a,4.5m}$, and $\sigma_{a,6m}$ for active earth pressure, and $\sigma_{0,3m}$, $\sigma_{0,4.5m}$, and $\sigma_{0,6m}$ for at-rest lateral earth pressure, respectively, and will be presented in Table 6.11.

Table 6.11. Active and at-rest earth pressures, for three abutment heights (3 m, 4.5 m, and 6 m).

Case	Earth pressure (kN/m^2)	
Active	$\sigma_{a,3m}$	15.71
	$\sigma_{a,3m}$	23.56
	$\sigma_{a,3m}$	3.416
At-rest	$\sigma_{0,3m}$	24.68
	$\sigma_{0,3m}$	37.02
	$\sigma_{0,3m}$	49.37

6.3.4. Soil–Pile Interaction Modelling

In this study, three types of sandy soil foundations with varying stiffness were selected, as presented in Table 6.2. For the analyses of parameters such as abutment height and bridge length, a single layer of medium-density sand, as detailed in Table 6.2, was used.

For the soil-pile interaction, the subgrade reaction approach will be employed, using p-y curves distributed along the depths of the piles. These curves will be generated with MIDAS CIVIL software, and the subgrade reaction (k_h) will be calculated using the Vesic equation (Equation (3.1)), as outlined in Bowles' 4th Edition (1998) (refer to Section 3.1.4).

The subgrade reaction (kh) for the three types of sandy soil foundations, as presented in Table 6.2, will be calculated using Equation (3.1) and will be denoted as $k_{h,30°}$, $k_{h,35°}$, and $k_{h,40°}$, respectively. The results will be presented in Table 6.12.

Table 6.12. The subgrade reaction for the three types of sandy soil foundations.

The subgrade reaction (MPa)	
$k_{h,30°}$	85.38
$k_{h,35°}$	37.20
$k_{h,40°}$	10.72

6.4. Summary of 3D Static Analysis Results

This section presents the results of 3D static analyses for both steel and PSC bridge models, considering different construction temperatures and three key parameters: (1) bridge length, (2) abutment height, and (3) foundation soil stiffness. The response was evaluated by measuring the bending moment and displacement over the top of the abutment and pile and bending moment at the end of the main girder and the displacement at the middle of the span near the abutment.

The results are presented from two different perspectives: Firstly, the relationship between construction temperature and structural responses is illustrated considering various key parameters such as different bridge lengths, abutment heights, and foundation soil stiffnesses as shown in Figures 6.4, 6.5, 6.6, 6.7, 6.8, 6.9, 6.10, 6.11, and 6.12. Secondly, the relationship between various key parameters such as bridge length, abutment height, and foundation soil stiffness, and structural responses is illustrated considering different construction temperature s, as shown in Figures 6.13, 6.14, 6.15, 6.16, 6.17, 6.18, 6.19, 6.20, and 6.21. Both approaches are conducted under the combined effect of dead load, temperature load, and backfill pressure in both expansion ($D+T_R+E_p$) and contraction ($D+T_F+E_a$) conditions.

Furthermore, the proportional values of bridge response under expansion and contraction combinations, compared to the at-rest combination, across various construction temperatures and various key parameters will be presented. This comparison assesses the extent of the effect of construction temperature on different bridge elements, thereby highlighting their significant effects on IAB design.

6.4.1. Effect of Construction Temperature and Material of Superstructure

The finite element analyses for all models, varying in bridge lengths, abutment heights, and foundation soil stiffnesses, show significant differences in bridge element responses across different construction temperatures. This variation is expected, as construction temperature affects the thermal displacement of the superstructure.

As illustrated Figures 6.4, 6.5, 6.6, 6.7, 6.8, 6.9, 6.10, 6.11, and 6.12, and Tables 6.13, 6.14, 6.15, 6.16, 6.17, 6.18, 6.19, 6.20, and 6.21, it was observed that by considering the maximum construction temperature for both concrete and steel superstructures, the thermal displacement cycle would be governed by contraction, resulting in the maximum thermal responses of bridge elements achieved during the contraction case. Conversely, when considering the minimum construction temperature for both concrete and steel superstructures, the thermal displacement cycle would be governed by expansion, leading to the maximum responses of bridge elements achieved during the expansion case.

However, by considering the recommended construction temperatures [$T_{Const.min}$:10°C, $T_{Const.max}$:10°C] (refer to Section 5.2.2), which are selected to balance temperature variations during both expansion and contraction phases symmetrically, the thermal displacement cycle will be influenced by both expansion and contraction equally. Consequently, the thermal responses of bridge elements will achieve an intermediate level between the maximum responses observed in the contraction and expansion cases, thereby minimizing the negative effects of thermal loading.

It was observed that PSC superstructures exhibit less deformation compared to steel superstructures, resulting in greater moments and a more pronounced effect of construction temperature. This difference can be attributed to the fact that PSC superstructures experience lower thermal displacement due to their lower thermal coefficient and the lower minimum and maximum construction temperatures compared to steel superstructures.

Additionally, steel superstructures are more likely to experience rotational deformations in the abutment compared to PSC superstructures, a tendency that becomes more pronounced with higher abutments, as illustrated in Figures 6.8 and 6.17.

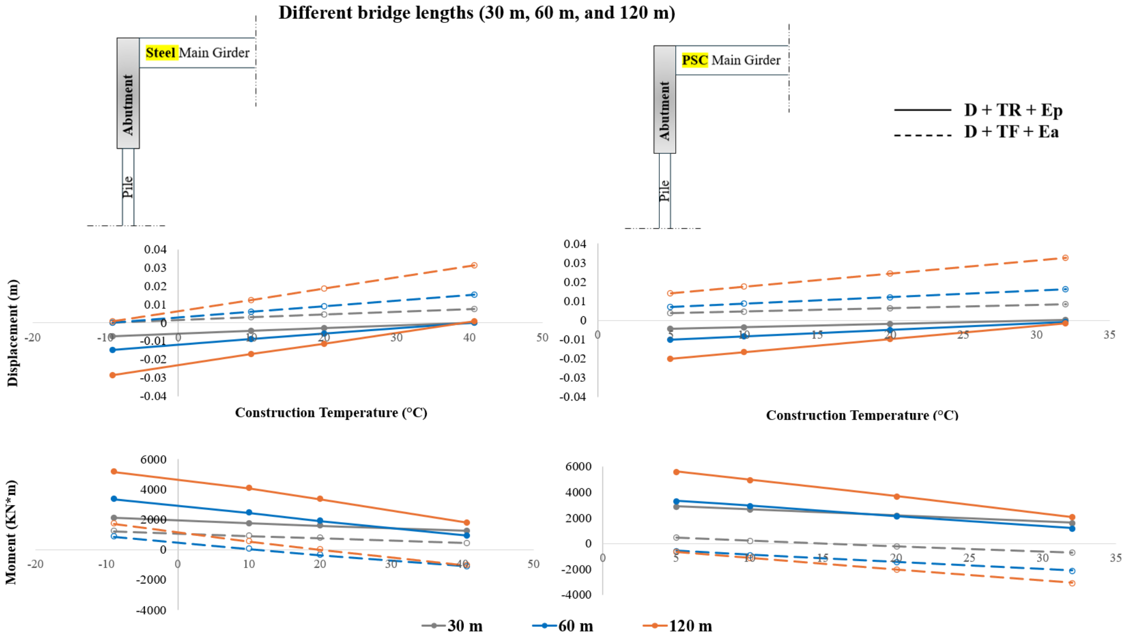

(a) (b)

Figure 6.4. Effects of construction temperature on abutment response across various bridge lengths; (a) Steel, (b) PSC.

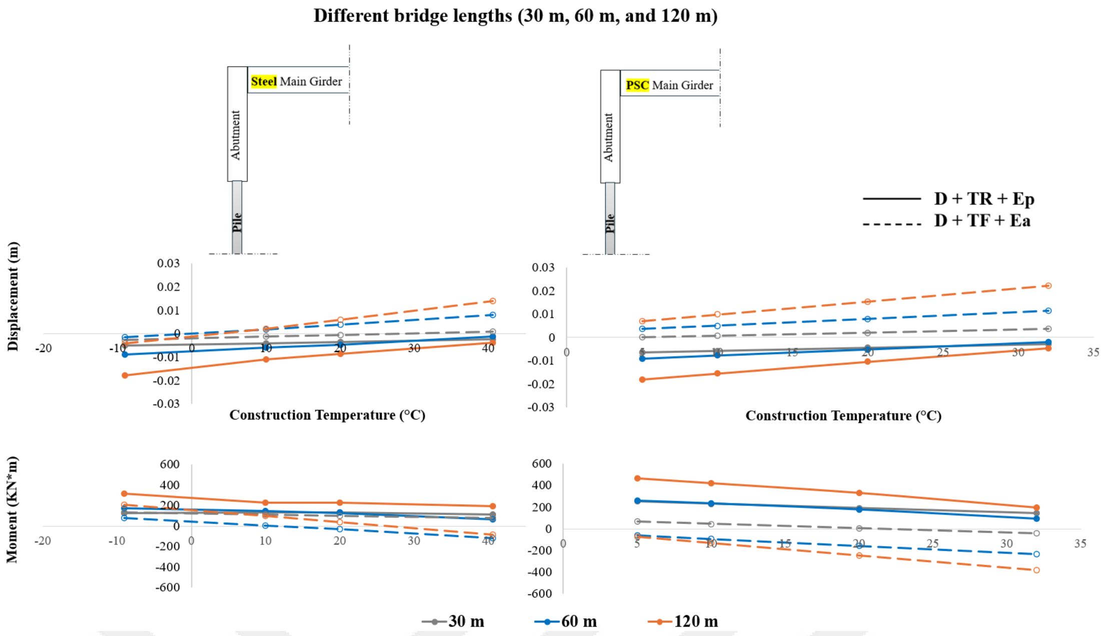

(a) (b)

Figure 6.5. Effects of construction temperature on pile response across various bridge lengths; (a) Steel, (b) PSC.

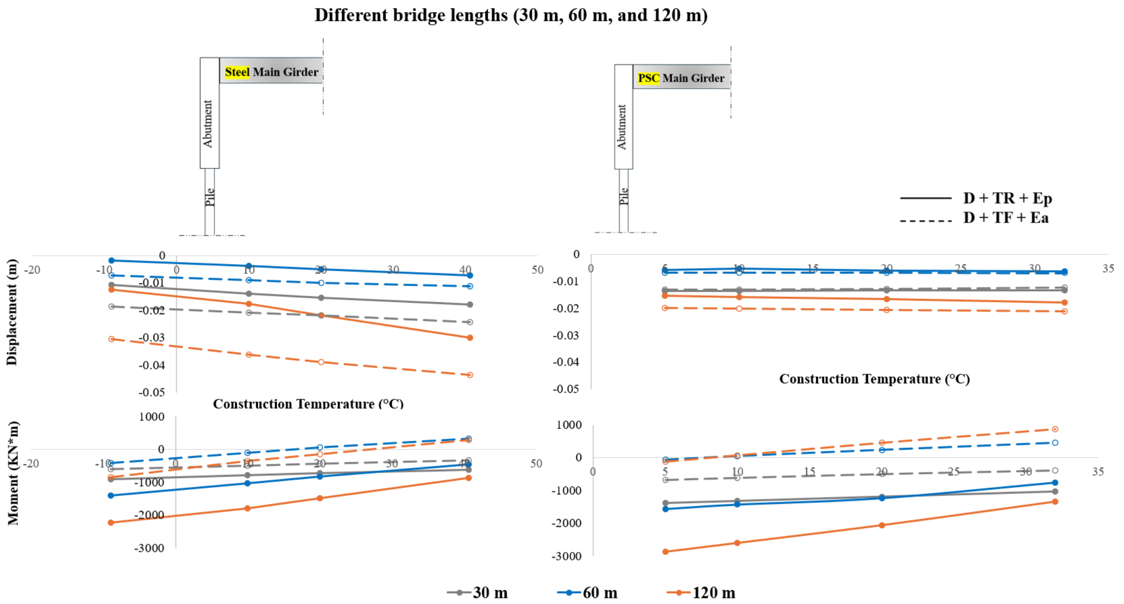

(a) (b)

Figure 6.6. Effects of construction temperature on main girder response across various bridge lengths; (a) Steel, (b) PSC.

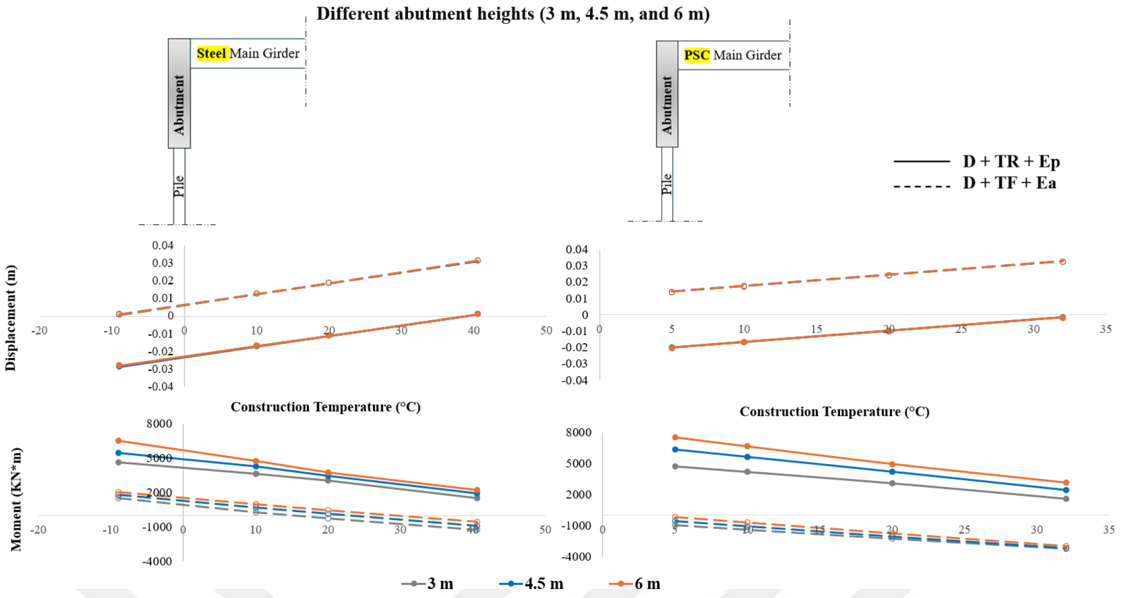

(a) (b)

Figure 6.7. Effects of construction temperature on abutment response across various abutment heights; (a) Steel, (b) PSC.

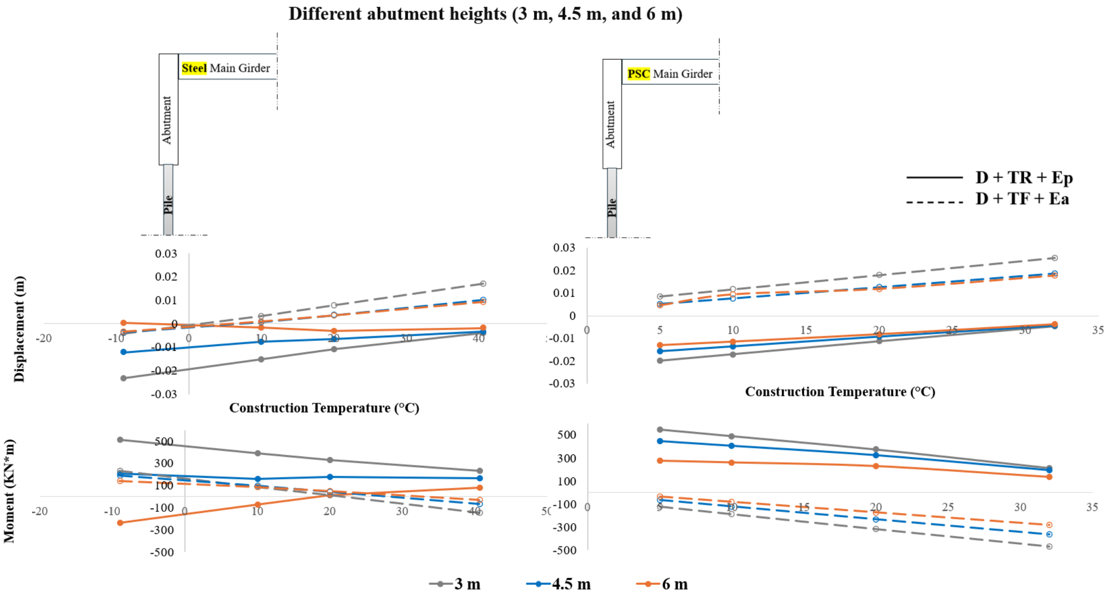

(a) (b)

Figure 6.8. Effects of construction temperature on pile response across various abutment heights; (a) Steel, (b) PSC.

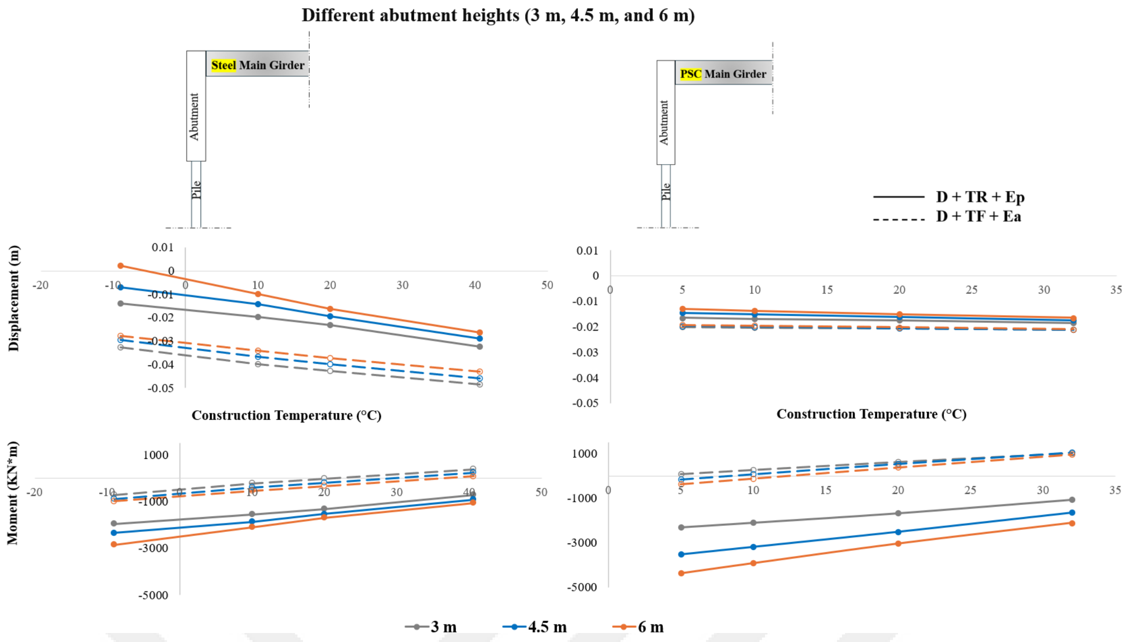

(a) (b)

Figure 6.9. Effects of construction temperature on main girder response across various abutment heights; (a) Steel, (b) PSC.

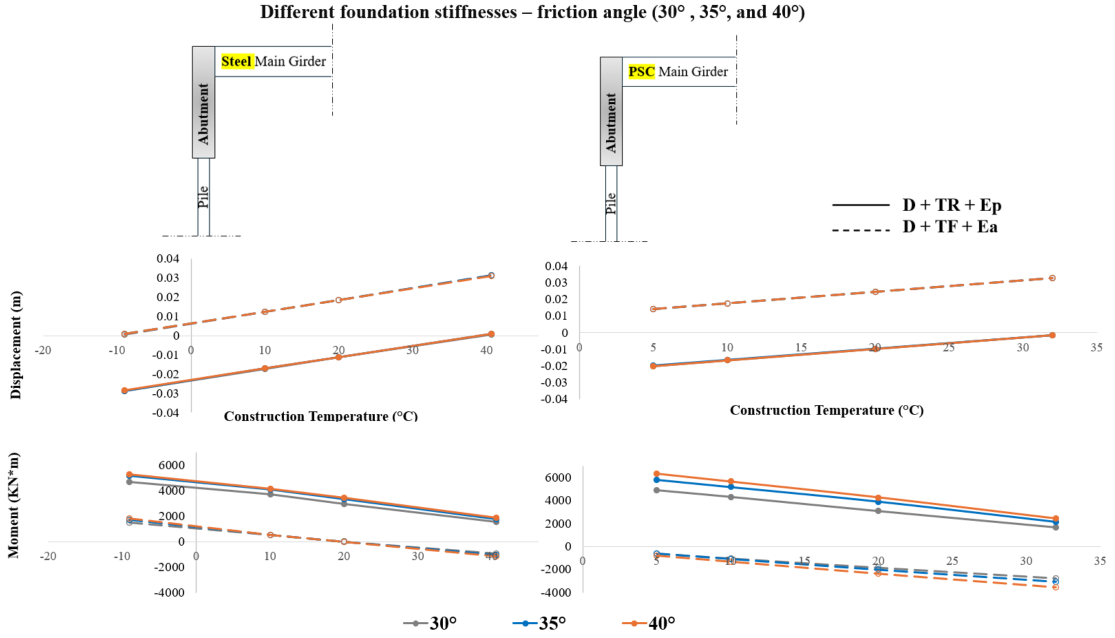

(a) (b)

Figure 6.10. Effects of construction temperature on abutment response across various foundation stiffnesses; (a) Steel, (b) PSC.

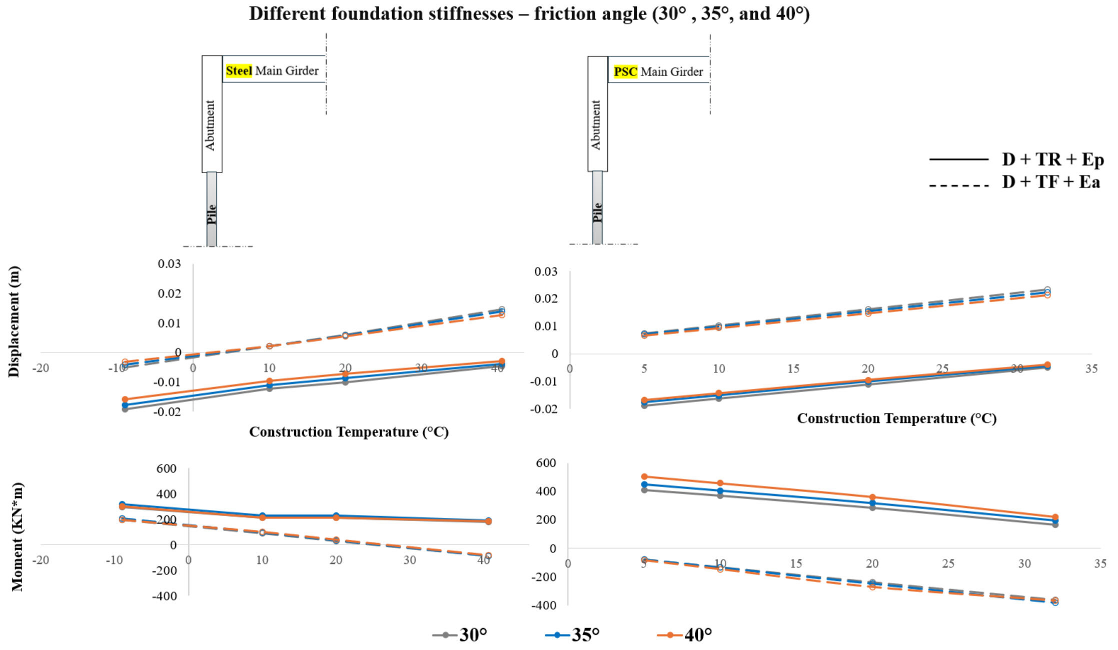

(a) (b)

Figure 6.11. Effects of construction temperature on pile response across various foundation stiffnesses; (a) Steel, (b) PSC.

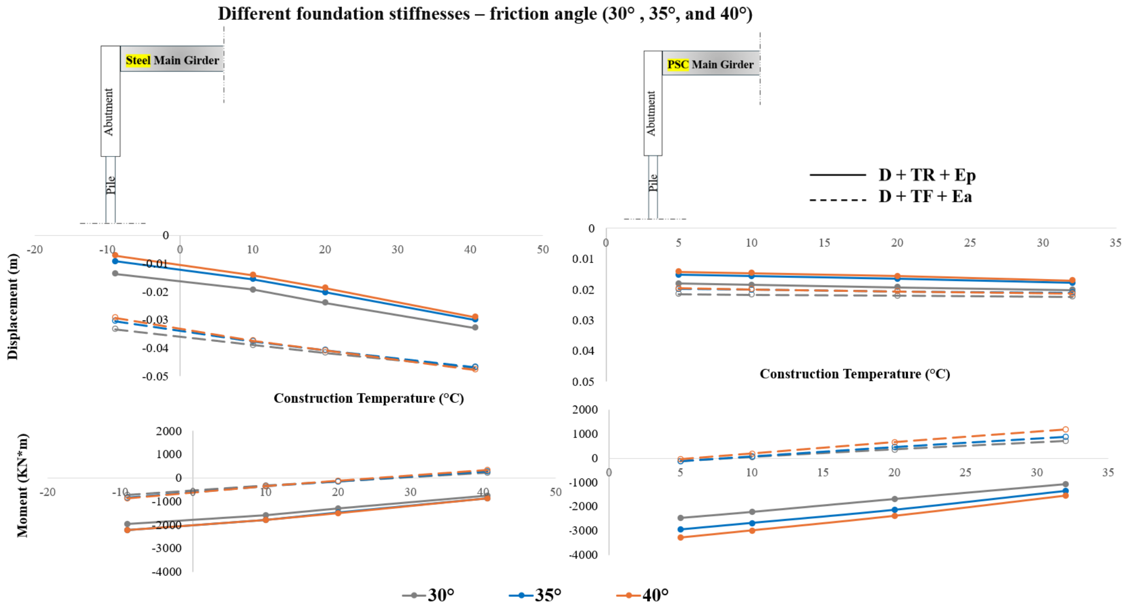

(a) (b)

Figure 6.12. Effects of construction temperature on main girder response across various foundation stiffnesses; (a) Steel, (b) PSC.

6.4.2. Effect of Bridge Length across Various Construction Temperatures

It is evident that the thermal responses of bridge elements, both for steel and prestressed superstructures, increase with the length of the bridge. Generally, the effects of construction temperature are most pronounced in long bridges. The same thermal effect observed in a medium-length bridge could be achieved in a long bridge if the recommended construction temperatures [$T_{Const.min}$:10°C, $T_{Const.max}$:10°C] (refer to Section 5.2.2) are considered, as illustrated in Figures 6.4, 6.5, 6.6, 6.13, 6.14, and 6.15, and Tables 6.13, 6.14, 6.15, and 6.16.

Additionally, it is noteworthy that the displacement of the girder in the 60 m bridge is less than that in the 30 m bridge, as illustrated in Figures 6.6 and 6.15, and Tables 6.13, 6.14, 6.15, and 6.16. This can be attributed to the fact that the 60 m bridge is multi-span while the 30 m bridge is single span, contributing to this difference in displacement.

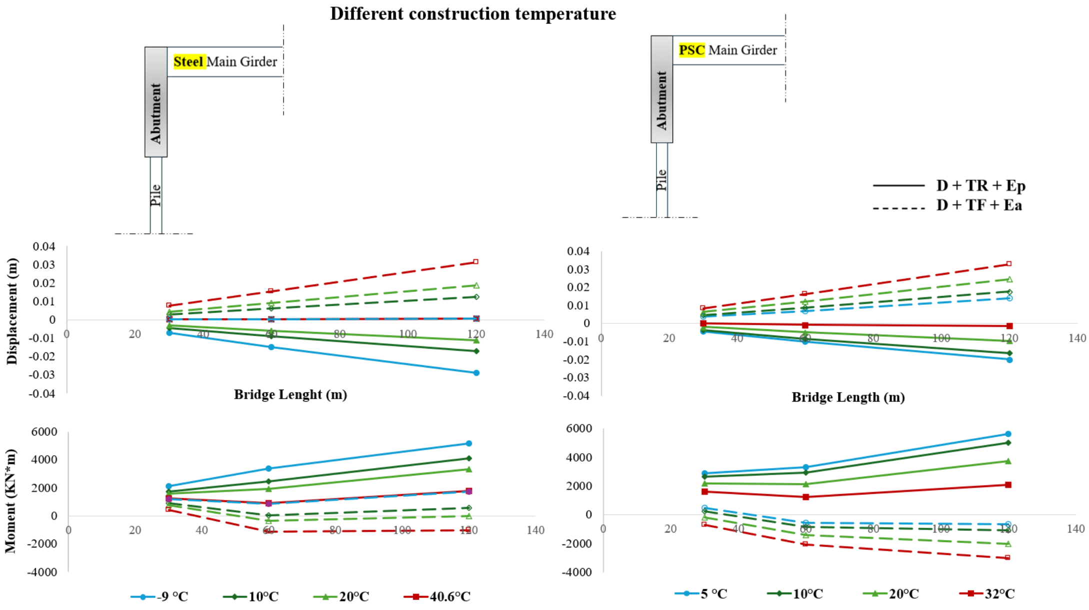

(a) (b)

Figure 6.13. Effects of bridge length on abutment response across various construction temperatures; (a) Steel, (b) PSC.

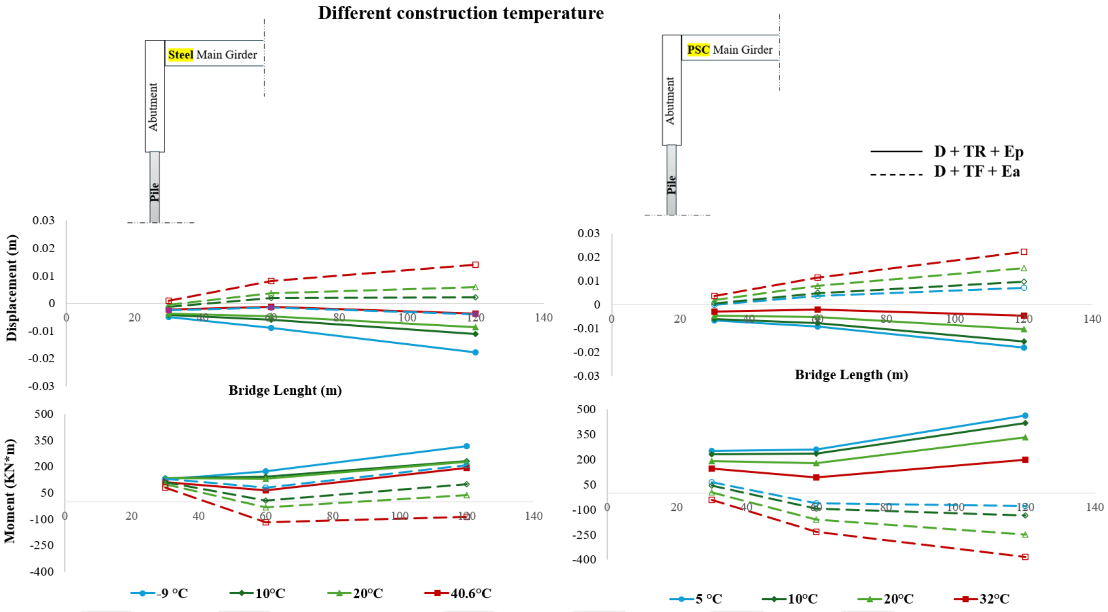

(a) (b)

Figure 6.14. Effects of bridge length on pile response across various construction temperatures; (a) Steel, (b) PSC.

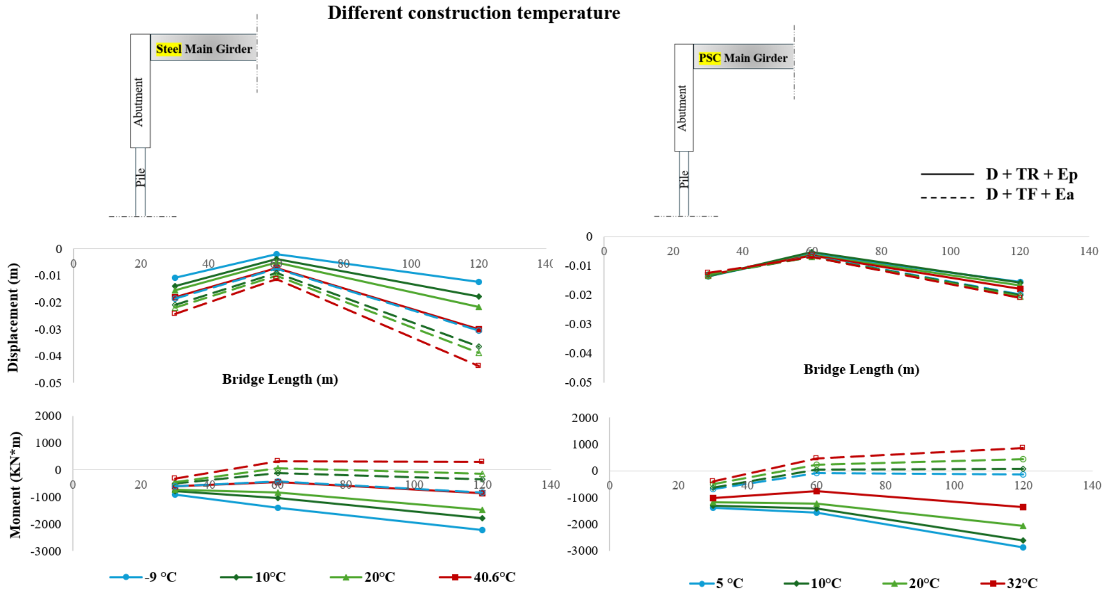

(a) (b)

Figure 6.15. Effects of bridge length on main girder response across various construction temperatures; (a) Steel, (b) PSC.

Table 6.13. Reference values for bridge response in the at-rest case across various lengths for Steel superstructure.

Steel Superstructure				
Bridge Response	Case	D+E_0		
	Length (m)	30	60	120
Displace-met (m)	Abutment	0.000129	0.000176	0.000697
	Pile	-0.003239	-0.002016	-0.004621
	Gir-mid	-0.019649	-0.007685	-0.031011
Bending moment (kN.m)	Abutment	1163	747	1650
	Pile	161.62	102.05	231.83
	Gir-end	-576.23	-374.71	-802.44
	Gir-mid	548.92	334.32	347.19

Table 6.14. Proportional values of expansion and contraction cases compared to the at-rest case across various lengths for Steel superstructure.

Steel Superstructure										
Length (m)	Bridge Response	Case	D+T_R+E_p				D+T_F+E_a			
		T_{Const} (°C)	–9	10	20	40.6	–9	10	20	40.6
30	Displace-met (m)	Abutment	-55.6	-33.9	-22.5	1.29	1.19	23.17	34.74	58.57
		Pile	1.54	1.30	1.14	0.69	0.81	0.39	0.17	-0.28
		Gir-mid	0.55	0.71	0.79	0.91	0.95	1.06	1.12	1.24
	Bending moment (kN.m)	Abutment	1.81	1.50	1.35	1.07	1.05	0.79	0.65	0.37
		Pile	0.79	0.84	0.83	0.70	0.81	0.69	0.62	0.49
		Gir-end	1.57	1.36	1.25	1.06	1.04	0.86	0.77	0.58
		Gir-mid	0.66	0.79	0.84	0.94	0.96	0.04	0.09	0.18
60	Displace-met (m)	Abutment	-83.6	-51.2	-34.1	1.42	1.28	34.47	51.97	88.06
		Pile	4.45	2.97	2.28	0.63	0.77	-0.93	-1.86	-4.02
		Gir-mid	0.25	0.50	0.66	0.93	0.95	1.18	1.29	1.47
	Bending moment (kN.m)	Abutment	4.51	3.26	2.55	1.24	1.15	0.06	-0.49	-1.48
		Pile	1.68	1.41	1.26	0.65	0.78	0.06	-0.33	-1.14
		Gir-end	3.72	2.77	2.21	1.20	1.13	0.28	-0.14	-0.9
		Gir-mid	-0.89	0.59	0.70	1.09	0.90	0.29	0.48	0.8

Table 6.14. Proportional values of expansion and contraction cases compared to the at-rest case across various lengths for Steel superstructure (Continued).

Steel Superstructure										
Length (m)	Bridge Response	Case	$D+T_R+E_p$				$D+T_F+E_a$			
		T_{Const} (°C)	–9	10	20	40.6	–9	10	20	40.6
120	Displace-met (m)	Abutment	-41.1	-24.5	-16.2	1.23	1.15	17.85	26.67	44.88
		Pile	3.85	2.40	1.87	0.81	0.88	-0.45	-1.26	-3.00
		Gir-mid	0.40	0.57	0.70	0.97	0.98	1.17	1.25	1.41
	Bending moment (kN.m)	Abutment	3.14	2.48	2.02	1.08	1.05	0.34	0.01	-0.63
		Pile	1.36	0.99	0.98	0.82	0.89	0.42	0.16	-0.38
		Gir-end	2.76	2.22	1.85	1.07	1.04	0.44	0.17	-0.36
		Gir-mid	-1.82	-1.51	0.17	1.03	0.92	0.78	1.15	1.84

Table 6.15. Reference values for bridge response in the at-rest case across various lengths for PCS superstructure.

PSC Superstructure				
Bridge Response	Case	$D+E_0$		
	Length (m)	30	60	120
Displace-met (m)	Abutment	0.000662	0.000369	0.000972
	Pile	-0.00294	-0.001609	-0.003246
	Gir-mid	-0.013788	-0.006554	-0.018456
Bending moment (kN.m)	Abutment	1199	668	1339
	Pile	155.27	85.04	173.96
	Gir-end	-864.42	-528.09	-998.5
	Gir-mid	3067.63	1799.54	1179.95

Table 6.16. Proportional values of expansion and contraction cases compared to the at-rest case across various lengths for PSC superstructure.

PSC Superstructure										
Length (m)	Bridge Response	Case	$D+T_R+E_p$				$D+T_F+E_a$			
		T_{Const} (°C)	5	10	20	32	5	10	20	32
30	Displace-met (m)	Abutment	-6.75	-5.50	-2.98	0.05	5.77	7.03	9.55	12.55
		Pile	2.24	2.00	1.54	0.99	0.02	-0.21	-0.69	-1.30
		Gir-mid	0.99	0.98	0.97	0.96	0.95	0.94	0.93	0.89

Table 6.16. Proportional values of expansion and contraction cases compared to the at-rest case across various lengths for PSC superstructure (Continued).

PSC Superstructure										
Length (m)	Bridge Response	Case	$D+T_R+E_p$				$D+T_F+E_a$			
		T_{Const} (°C)	5	10	20	32	5	10	20	32
30	Bending moment (kN.m)	Abutment	2.41	2.22	1.83	1.36	0.40	0.20	-0.17	-0.58
		Pile	1.62	1.48	1.23	0.93	0.41	0.29	0.03	-0.27
		Gir-end	1.60	1.53	1.38	1.19	0.80	0.72	0.58	0.44
		Gir-mid	1.01	1.00	0.98	0.96	0.94	0.93	0.91	0.88
60	Displace-met (m)	Abutment	-27.3	-22.7	-13.5	-2.33	18.66	23.29	32.55	43.66
		Pile	5.62	4.80	3.25	1.33	-2.23	-3.09	-4.88	-7.05
		Gir-mid	0.89	0.79	0.93	0.96	1.03	1.04	1.05	1.05
	Bending moment (kN.m)	Abutment	4.97	4.42	3.18	1.81	-0.83	-1.30	-2.15	-3.14
		Pile	3.03	2.73	2.08	1.08	-0.73	-1.13	-1.87	-2.74
		Gir-end	2.95	2.70	2.33	1.44	0.13	-0.08	-0.45	-0.86
		Gir-mid	1.15	1.18	1.12	1.01	0.89	-0.14	-0.18	-0.23
120	Displace-met (m)	Abutment	-20.5	-17.0	-9.98	-1.52	14.52	18.06	25.16	33.68
		Pile	5.55	4.77	3.21	1.40	-2.15	-3.02	-4.75	-6.88
		Gir-mid	0.83	0.86	0.90	0.96	1.07	1.08	1.11	1.14
	Bending moment (kN.m)	Abutment	4.20	3.72	2.78	1.56	-0.48	-0.82	-1.51	-2.27
		Pile	2.66	2.41	1.90	1.14	-0.44	-0.77	-1.42	-2.19
		Gir-end	2.88	2.61	2.07	1.35	0.13	-0.06	-0.45	-0.87
		Gir-mid	1.03	1.03	1.03	0.97	0.76	-0.29	-0.41	-0.53

6.4.3. Effect of Abutment Height across Various Construction Temperatures

The displacements and bending moments of the abutment of both steel and PSC superstructures are slightly affected by the abutment height, exhibiting only a slight increase with higher abutments, as illustrated in Figures 6.7 and 6.16, and Tables 6.17, 6.18, 6.19, and 6.20.

Conversely, the displacements and bending moments of the pile and main girder show a more significant effect with increasing abutment height, resulting in higher responses, as illustrated in Figures 6.8, 6.9, 6.17, and 6.18, and Tables 6.17, 6.18, 6.19, and 6.20.

In steel superstructures, the pile response shows a rotational deformation with increasing abutment height, leading to a converse moment at the top of the pile, especially when construction temperature reaches its limit values, as illustrated in Figures 6.8 and 6.17, and Tables 6.17 and 6.18.

Additionally, for PSC superstructures, the increased rotational deformation due to abutment height results in less bending moment at the top of the pile, as illustrated in Figures 6.8 and 6.17, and Tables 6.19 and 6.20.

Consequently, for piles, the effect of construction temperature is more pronounced in shorter abutments.

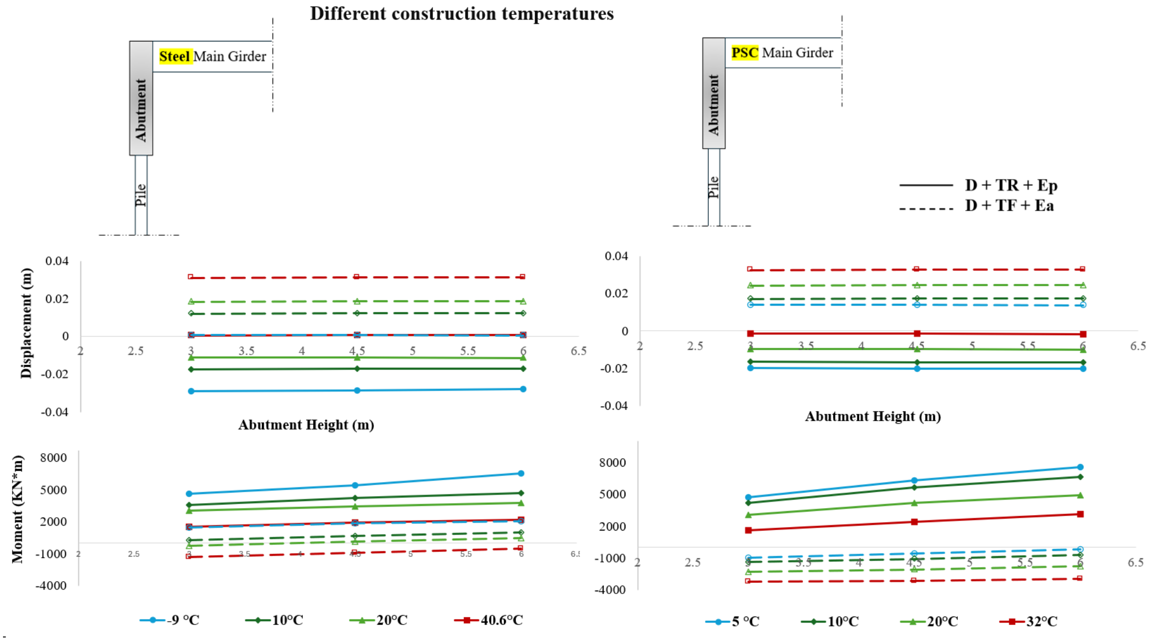

(a) (b)

Figure 6.16. Effects of abutment height on abutment response across various construction temperatures; (a) Steel, (b) PSC.

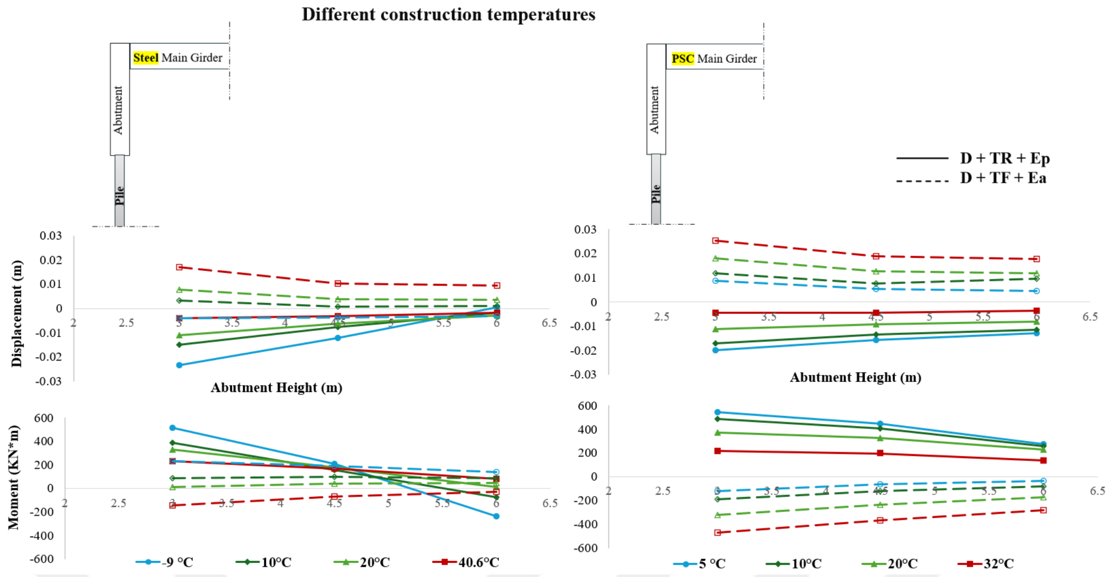

(a) (b)

Figure 6.17. Effects of abutment height on pile response across various construction temperatures; (a) Steel, (b) PSC.

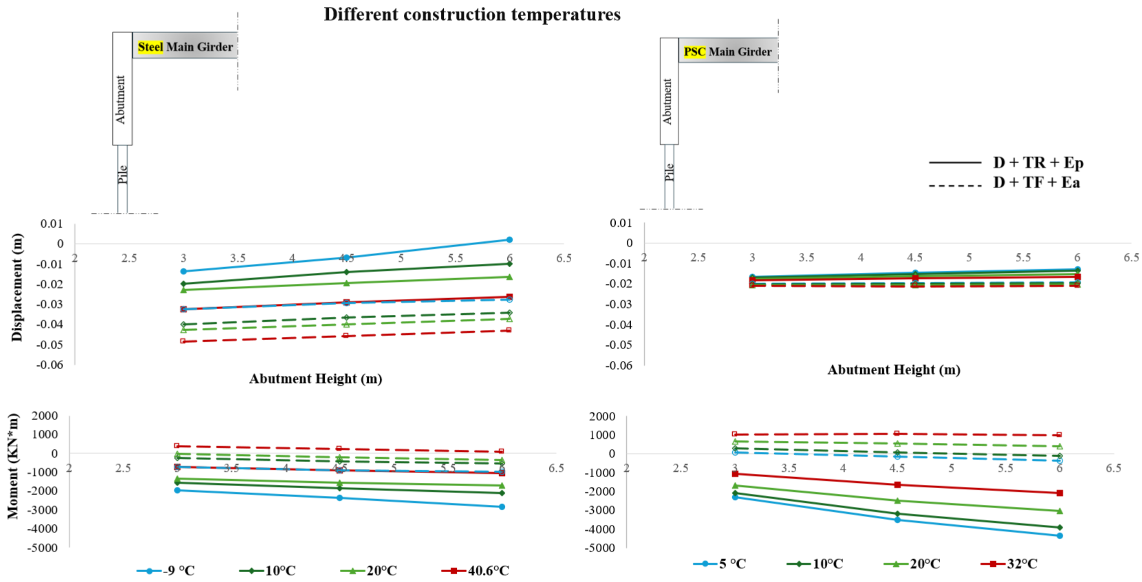

(a) (b)

Figure 6.18. Effects of abutment height on main girder response across various construction temperatures; (a) Steel, (b) PSC.

Table 6.17. Reference values for bridge response in the at-rest case across various abutment heights for Steel superstructure.

Steel Superstructure				
Bridge Response	Case	$D+E_0$		
	Abutment Height (m)	3	4.5	6
Displace-met (m)	Abutment	0.00075	0.000669	0.000587
	Pile	-0.004376	-0.0043675	-0.004346
	Gir-mid	-0.032973	-0.030252	-0.028626
Bending moment (kN.m)	Abutment	1431	1736	1918
	Pile	250.39	221.45	188.85
	Gir-end	-695.81	-844.58	-935.5
	Gir-mid	1055.7	989.79	949.64

Table 6.18. Proportional values of expansion and contraction cases compared to the at-rest case across various abutment heights for Steel superstructure..

Steel Superstructure										
Abutm-ent Height (m)	Bridge Response	Case	$D+T_R+E_p$				$D+T_F+E_a$			
		T_{Const} (°C)	–9	10	20	40.6	–9	10	20	40.6
3	Displace-met (m)	Abutment	-38.4	-23.1	-15	1.14	1.12	16.53	24.70	41.56
		Pile	5.31	3.44	2.49	0.91	0.93	-0.78	-1.80	-3.92
		Gir-mid	0.42	0.60	0.70	0.98	0.99	1.21	1.30	1.47
	Bending moment (kN.m)	Abutment	3.25	2.52	2.12	1.05	1.04	0.20	-0.16	-0.90
		Pile	2.06	1.56	1.32	0.93	0.94	0.35	0.05	-0.58
		Gir-end	2.83	2.24	1.91	1.04	1.04	0.34	0.04	-0.55
		Gir-mid	0.57	0.70	0.78	0.99	0.99	0.15	0.22	0.35
4.5	Displace-met (m)	Abutment	-42.6	-25.5	-169	1.29	1.17	18.61	27.82	46.82
		Pile	2.77	1.74	1.46	0.75	0.86	-0.19	-0.85	-2.34
		Gir-mid	0.23	0.47	0.64	0.96	0.98	1.21	1.32	1.51
	Bending moment (kN.m)	Abutment	3.14	2.45	1.99	1.10	1.06	0.39	0.07	-0.53
		Pile	0.94	0.72	0.81	0.76	0.86	0.44	0.20	-0.30
		Gir-end	1.00	1.00	1.00	1.00	1.05	0.48	0.22	-0.28
		Gir-mid	0.44	0.61	0.74	0.97	0.98	0.15	0.23	0.38

Table 6.18. Proportional values of expansion and contraction cases compared to the at-rest case across various abutment heights for Steel superstructure (Continued).

Steel Superstructure										
Abutment Height (m)	Bridge Response	Case	D+T_R+E_p				D+T_F+E_a			
		T_{Const} (°C)	–9	10	20	40.6	–9	10	20	40.6
6	Displacemet (m)	Abutment	-47.7	-29	-19.2	1.53	1.23	21.23	31.76	53.50
		Pile	-0.10	0.38	0.68	0.40	0.74	-0.23	-0.82	-2.18
		Gir-mid	-0.08	0.34	0.57	0.92	0.97	1.19	1.30	1.50
	Bending moment (kN.m)	Abutment	3.40	2.47	1.96	1.16	1.07	0.51	0.24	-0.29
		Pile	-1.26	-0.39	0.08	0.42	0.75	0.45	0.26	-0.16
		Gir-end	3.04	2.24	1.81	1.13	1.06	0.59	0.36	-0.08
		Gir-mid	0.23	0.53	0.69	0.94	0.98	0.14	0.22	0.37

Table 6.19. Reference values for bridge response in the at-rest case across various abutment heights for PSC superstructure.

PSC Superstructure				
Bridge Response	Case	D+E_0		
	Abutment Height (m)	3	4.5	6
Displacemet (m)	Abutment	0.001005	0.000953	0.000899
	Pile	-0.00268	-0.003419	-0.00391
	Gir-mid	-0.01883	-0.018213	-0.01777
Bending moment (kN.m)	Abutment	1041	1562	1908
	Pile	168.49	183.06	175.32
	Gir-end	-804.18	-1189.87	-1433.93
	Gir-mid	5672.6	5496.04	5367.3

Table 6.20. Proportional values of expansion and contraction cases compared to the at-rest case across various abutment heights for PSC superstructure.

PSC Superstructure										
Abutment Height (m)	Bridge Response	Case	D+T_R+E_p				D+T_F+E_a			
		T_{Const} (°C)	5	10	20	32	5	10	20	32
3	Displacemet (m)	Abutment	-19.8	-16.4	-9.60	-1.44	14.03	17.45	24.30	32.52
		Pile	7.42	6.34	4.19	1.68	-3.24	-4.39	-6.69	-9.49
		Gir-mid	0.88	0.89	0.93	0.98	1.06	1.07	1.10	1.12

Table 6.20. Proportional values of expansion and contraction cases compared to the at-rest case across various abutment heights for PSC superstructure (Continued).

PSC Superstructure										
Abutment Height (m)	Bridge Response	Case	$D+T_R+E_p$				$D+T_F+E_a$			
		T_{Const} (°C)	5	10	20	32	5	10	20	32
3	Bending moment (kN.m)	Abutment	4.55	4.03	2.98	1.56	-0.89	-1.32	-2.16	-3.11
		Pile	3.24	2.90	2.22	1.28	-0.71	-1.11	-1.89	-2.79
		Gir-end	2.87	2.61	2.08	1.32	-0.10	-0.34	-0.79	-1.29
		Gir-mid	0.90	0.92	0.94	0.98	1.05	1.06	1.08	1.09
4.5	Displace-met (m)	Abutment	-20.9	-17.4	-10.2	-1.57	14.80	18.42	25.67	34.36
		Pile	4.55	3.92	2.68	1.25	-1.55	-2.27	-3.71	-5.48
		Gir-mid	0.80	0.83	0.88	0.96	1.08	1.10	1.13	1.16
	Bending moment (kN.m)	Abutment	4.06	3.61	2.69	1.56	-0.36	-0.68	-1.31	-2.03
		Pile	2.44	2.22	1.78	1.08	-0.35	-0.66	-1.27	-1.99
		Gir-end	2.95	2.67	2.10	1.38	0.13	-0.07	-0.46	-0.88
		Gir-mid	0.84	0.86	0.91	0.96	1.07	1.08	1.11	1.14
6	Displace-met (m)	Abutment	-22.4	-18.6	-10.9	-1.74	15.67	19.52	27.22	36.45
		Pile	3.31	2.90	2.06	0.93	-1.20	-2.43	-3.04	-4.54
		Gir-mid	0.73	0.77	0.85	0.93	1.08	1.10	1.14	1.18
	Bending moment (kN.m)	Abutment	3.95	3.49	2.59	1.64	-0.10	-0.37	-0.91	-1.54
		Pile	1.57	1.49	1.30	0.77	-0.20	-0.46	-0.99	-1.61
		Gir-end	3.04	2.72	2.11	1.47	0.25	0.08	-0.27	-0.68
		Gir-mid	0.78	0.81	0.88	0.94	1.07	1.09	1.12	1.16

6.4.4. Effect of Foundation Soil Stiffness across Various Construction Temperatures

The displacements and bending moments of bridge elements for both concrete and steel superstructures are slightly affected by foundation soil stiffness, as illustrated in Figures 6.10, 6.11, 6.12. 6.19, 6.20, and 6.21, and Tables 6.21, 6.22, 6.23, and 6.24. This effect is more pronounced in PSC superstructures, which show less deformation associated with higher bending moments as the stiffness of the foundation soil increases.

The small effect observed could be attributed to the relatively minor differences in foundation soil stiffness used in the models. Consequently, the effects of the construction temperature are nearly consistent across different foundation stiffnesses.

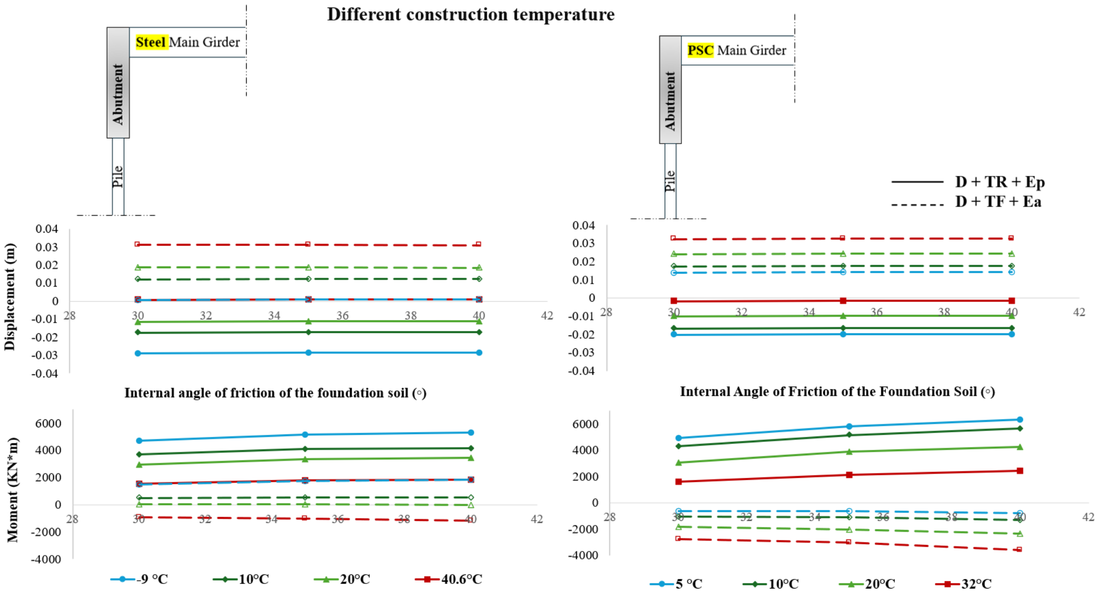

(a) (b)

Figure 6.19. Effects of foundation stiffnesses on abutment response across various construction temperatures; (a) Steel, (b) PSC.

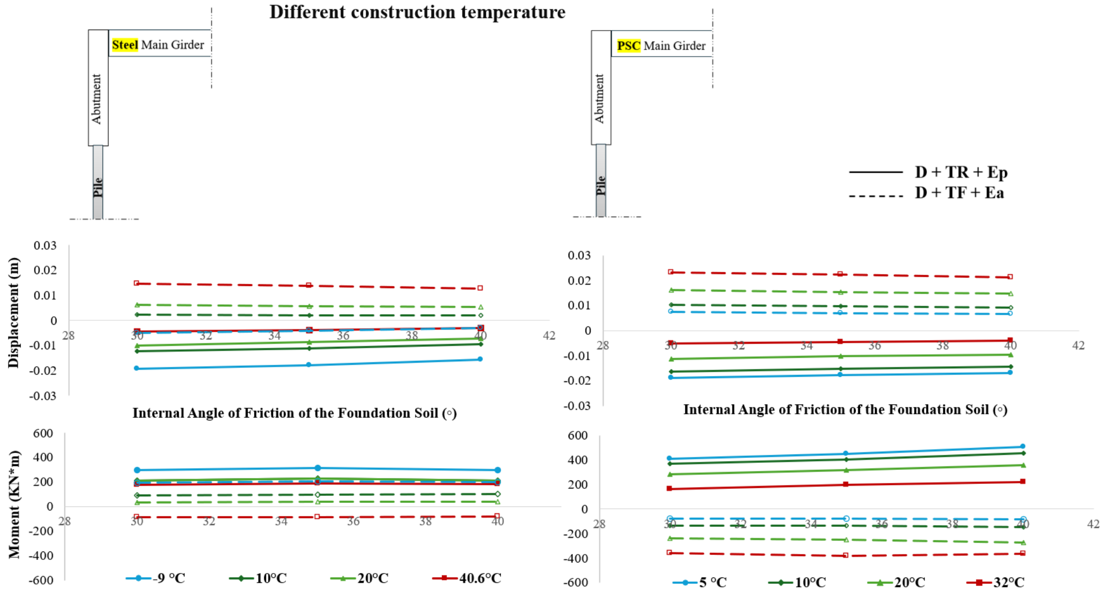

(a) (b)

Figure 6.20. Effects of foundation stiffnesses on pile response across various construction temperatures; (a) Steel, (b) PSC.

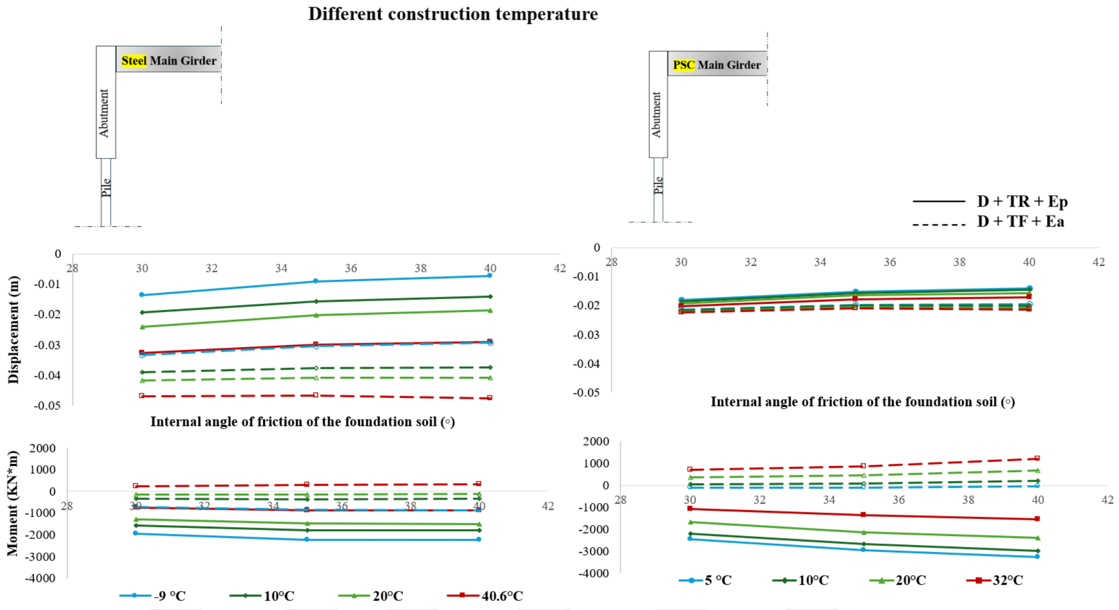

(a) (b)

Figure 6.21. Effects of foundation stiffnesses on main girder response across various construction temperatures; (a) Steel, (b) PSC.

Table 6.21. Reference values for bridge response in the at-rest case across various foundation stiffnesses for Steel superstructure.

Steel Superstructure				
Bridge Response	Case	D+E$_0$		
	Friction angle (°)	30°	35°	40°
Displace-met (m)	Abutment	0.000623	0.000697	0.000743
	Pile	-0.00568	-0.004621	-0.00357
	Gir-mid	-0.03417	-0.031017	-0.02973
Bending moment (kN.m)	Abutment	1376	1650	1757
	Pile	221.62	231.83	223.42
	Gir-end	-665.19	-802.44	-835.09
	Gir-mid	1053.95	1008.4	985.21

Table 6.22. Proportional values of expansion and contraction cases compared to the at-rest case across various foundation stiffnesses for Steel superstructure.

Steel Superstructure										
Friction angle (°)	Bridge Response	Case	$D+T_R+E_p$				$D+T_F+E_a$			
		T_{Const} (°C)	–9	10	20	40.6	–9	10	20	40.6
30°	Displace-met (m)	Abutment	-46.2	-27.6	-18.2	1.28	1.18	19.96	29.85	50.27
		Pile	3.38	2.14	1.75	0.79	0.87	-0.39	-1.08	-2.57
		Gir-mid	0.40	0.56	0.70	0.96	0.97	1.14	1.22	1.38
	Bending moment (kN.m)	Abutment	3.43	2.70	2.16	1.13	1.08	0.37	0.01	-0.68
		Pile	1.33	0.96	0.97	0.81	0.88	0.40	0.15	-0.39
		Gir-end	2.95	2.38	1.94	1.11	1.07	0.50	0.21	-0.34
		Gir-mid	0.54	0.67	0.77	0.97	0.98	1.11	1.17	1.29
35°	Displace-met (m)	Abutment	-41.1	-24.5	-16.2	1.23	1.15	17.85	26.67	44.88
		Pile	3.85	2.40	1.87	0.81	0.88	-0.45	-1.26	-3.00
		Gir-mid	0.30	0.50	0.65	0.97	0.98	1.21	1.31	1.51
	Bending moment (kN.m)	Abutment	3.14	2.48	2.02	1.08	1.05	0.34	0.01	-0.63
		Pile	1.36	0.99	0.98	0.82	0.89	0.42	0.16	-0.38
		Gir-end	2.76	2.22	1.85	1.07	1.04	0.44	0.17	-0.36
		Gir-mid	0.49	0.64	0.75	0.98	0.98	1.16	1.23	1.37
40°	Displace-met (m)	Abutment	-38.5	-22.9	-15.1	1.20	1.13	16.74	25.00	42.04
		Pile	4.40	2.67	2.02	0.81	0.88	-0.59	-1.54	-3.59
		Gir-mid	0.24	0.47	0.63	0.97	0.98	1.26	1.38	1.60
	Bending moment (kN.m)	Abutment	3.02	2.38	1.96	1.06	1.04	0.31	-0.01	-0.66
		Pile	1.34	0.96	0.96	0.82	0.89	0.45	0.18	-0.37
		Gir-end	2.67	2.14	1.80	1.05	1.03	0.41	0.14	-0.39
		Gir-mid	0.46	0.63	0.74	0.98	0.99	1.19	1.27	1.43

Table 6.23. Reference values for bridge response in the at-rest case across various foundation stiffnesses for PSC superstructure.

PSC Superstructure				
Bridge Response	Case	$D+E_0$		
	Friction angle (°)	30°	35°	40°
Displace-met (m)	Abutment	0.000913	0.000972	0.000982
	Pile	-0.00354	-0.00325	-0.00283
	Gir-mid	-0.02067	-0.01846	-0.017729

Table 6.23. Reference values for bridge response in the at-rest case across various foundation stiffnesses for PSC superstructure (Continued).

PSC Superstructure				
Bridge Response	Case	$D+E_0$		
	Friction angle (°)	30°	35°	40°
Displace-met (m)	Abutment	0.000913	0.000972	0.000982
	Pile	-0.00354	-0.00325	-0.00283
	Gir-mid	-0.02067	-0.01846	-0.017729

Table 6.24. Proportional values of expansion and contraction cases compared to the at-rest case across various foundation stiffnesses for PSC superstructure..

PSC Superstructure										
Friction angle (°)	Bridge Response	Case	$D+T_R+E_p$				$D+T_F+E_a$			
		T_{Const} (°C)	5	10	20	32	5	10	20	32
30°	Displace-met (m)	Abutment	-21.9	-18.2	-10.7	-1.69	15.38	19.16	26.72	35.78
		Pile	5.34	4.60	3.16	1.41	-2.09	-2.91	-4.56	-6.57
		Gir-mid	0.87	0.89	0.93	0.97	1.04	1.05	1.06	1.08
	Bending moment (kN.m)	Abutment	5.14	4.52	3.21	1.70	-0.66	-1.11	-1.93	-2.88
		Pile	2.81	2.54	1.95	1.14	-0.55	-0.92	-1.64	-2.48
		Gir-end	3.17	2.86	2.18	1.40	0.16	-0.07	-0.47	-0.91
		Gir-mid	0.88	0.90	0.94	0.98	1.04	0.05	0.06	0.08
35°	Displace-met (m)	Abutment	-20.5	-16.9	-9.95	-1.51	14.52	18.06	25.16	33.68
		Pile	5.46	4.68	3.12	1.39	-2.15	-3.02	-4.75	-6.88
		Gir-mid	0.82	0.85	0.89	0.96	1.07	1.08	1.11	1.14
	Bending moment (kN.m)	Abutment	4.33	3.85	2.91	1.59	-0.48	-0.82	-1.51	-2.27
		Pile	2.59	2.33	1.83	1.12	-0.44	-0.77	-1.42	-2.19
		Gir-end	2.96	2.69	2.15	1.37	0.11	-0.08	-0.46	-0.88
		Gir-mid	0.90	0.88	0.91	0.97	1.06	0.07	0.09	0.12
40°	Displace-met (m)	Abutment	-20.3	-16.8	-9.87	-1.49	14.38	17.90	24.92	33.36
		Pile	5.94	5.08	3.36	1.43	-2.35	-3.30	-5.19	-7.51
		Gir-mid	0.80	0.82	0.88	0.96	1.10	1.12	1.16	1.20
	Bending moment (kN.m)	Abutment	3.91	3.49	2.63	1.50	-0.48	-0.81	-1.47	-2.22
		Pile	2.67	2.41	1.90	1.15	-0.44	-0.77	-1.43	-1.94
		Gir-end	2.84	2.58	2.06	1.33	0.03	-0.17	-0.58	-1.03
		Gir-mid	0.84	0.86	0.91	0.97	1.08	0.10	0.13	0.16

6.5. Conclusion

The study highlights the substantial effects of construction temperatures on bridge element responses, as demonstrated by finite element analyses of various bridge lengths, abutment heights, and foundation soil stiffnesses. Key conclusions include:

- Maximum construction temperatures lead to peak thermal responses during contraction scenarios, while minimum temperatures result in maximum responses during expansion scenarios. Intermediate temperatures achieve a balance between these extremes, resulting in more moderate thermal responses.
- Thermal responses of both steel and PSC superstructures increase with bridge length, with the effects of construction temperature being most pronounced in longer bridges.
- For steel superstructures, higher abutments induce rotational deformation and reverse moments at the pile top, particularly under extreme construction temperatures. For PSC superstructures, increased rotational deformation leads to reduced bending moments at the pile top.
- Bridge element displacements and bending moments show slight sensitivity to foundation soil stiffness. Higher soil stiffness generally results in reduced deformations and increased bending moments. However, the minor variations in soil stiffness used in the models contribute to limited effect on bridge behavior.
- PSC superstructures exhibit less deformation compared to steel superstructures, resulting in greater moments and a more pronounced effect of construction temperature.

In conclusion, considering optimal construction temperatures that symmetrically balance expansion and contraction phases, the thermal displacement cycle is influenced equally by both. This approach effectively minimizes the negative effects associated with thermal loading across different design scenarios and provides a novel perspective on addressing challenges related to the limited length of IABs.

It is noteworthy to acknowledge that the observed behavior is intricately tied to the specific design parameters and magnitudes employed within these analytical models.

Consequently, any modifications to these parameters have the potential to exert a substantial influence on the overall response of the bridge structure.

7. CONCLUSIONS

Integral Abutment Bridges (IABs) face significant geotechnical challenges, particularly from thermal loads that cause cyclic displacements in backfill soil. This study addresses gaps in the literature by investigating assumptions related to secondary loads in current design practices, their interactions with primary loads, and proposing innovative solutions to improve these practices.

The research involved several critical tasks, leading to the following key conclusions:

A comprehensive analysis of both primary and secondary loads emphasized the significant influence of secondary loads on the overall behavior of IAB elements. These influences can be both positive and negative, as summarized below:

- Rising temperatures decrease the resultant bending moment at the midpoint of the girder while increasing it in the substructure and at the endpoint of the main girder.
- Falling temperatures have the opposite effect, increasing the resultant bending moment at the midpoint of the girder while decreasing it in the substructure and at the endpoint of the main girder.
- Although earth pressure loads have a relatively minor effect compared to temperature effects, passive earth pressure loads are the most pronounced when compared to active and at-rest earth pressures.
- Passive earth pressures increase the resultant bending moment at the endpoint of the girder and the top of the abutment while decreasing it at the pile and the midpoint of the girder.

Various methods for calculating earth pressure behind the abutment were explored and validated using field monitoring data, and their influence on the overall behavior of IABs has been highlighted. Key findings include:

- Passive earth pressure assumptions vary among design specifications, with some adopt for full passive earth pressure theories, while others reccomend displacement-dependent methods.
- Field monitoring data reveals that earth pressure behind the abutment is initially lower than full passive values in the first few years' post-construction, aligning

more closely with displacement-dependent methods. However, due to soil ratcheting effects, these pressures eventually rise to their full passive values over time.

- Assuming maximum full passive pressures behind the abutment may not always represent the worst-case scenario for all bridge elements. Methods that result in significant earth pressure loads may lead to an unrealistic reduction in bridge element moments, potentially yielding unsafe results.
- It is crucial to consider the worst-case scenario for each element individually during the design phase, accounting for all potential loading scenarios the bridge may encounter throughout its operational life, including soil ratcheting effects.

A primary focus was placed on integrating construction temperature considerations into design practices, with specific temperature ranges proposed. Key findings include:

- Bridge design specifications generally recommend a uniform temperature range for thermal displacement calculations, considering factors such as climate, materials, and assumed construction temperatures. However, many specifications overlook the variability in construction temperatures.
- Neglecting accurate construction temperature assumptions during design can lead to temperature variations that exceed specified limits, potentially resulting in inaccuracies in thermal displacement predictions.
- The proposed approach involves defining a suitable construction temperature range, denoted as [$T_{Const.min}$, $T_{Const.max}$], during the design phase and ensuring that this range is managed and controlled throughout the construction phase.
- Integrating construction temperature considerations into design practices can enhance the accuracy of thermal displacement and internal force predictions, thereby improving overall design outcomes.
- Insights from the Arsoy model (2008), which accounts for daily and seasonal temperature fluctuations, could be utilized to address challenges in specifying an exact construction temperature range [$T_{Const.min}$, $T_{Const.max}$] due to environmental variations.
- The Arsoy model (2008) can assist in selecting a suitable year-round range for local conditions and ensuring balanced temperature variations during both expansion and

contraction phases, minimizing the negative effects of thermal loading.

- Construction temperature for IABs is defined as the effective bridge temperature (EBT) when the integral connection between the bridge deck and abutment is established. This temperature varies with different bridge superstructure materials due to differences in timing and connection nature.
- A new parameter, the effective construction temperature ($T_{e.Const}$), is proposed to represent the actual construction temperature. For steel bridges, effective construction temperate equals the proposed construction temperature, while for concrete bridges, it is the proposed temperature plus 5°C to account for early hydration heat.

The study conducted a parametric analysis to evaluate the effects of construction temperature on steel and PSC IABs, considering factors such as bridge length, soil stiffness, and abutment height. Key findings include:

- Construction temperatures significantly affect bridge responses. Maximum temperatures cause peak thermal responses during contraction, while minimum temperatures lead to maximum responses during expansion. Intermediate temperatures result in more moderate responses.
- Thermal responses increase with bridge length, with effects being most pronounced in longer bridges.
- For steel superstructures, greater abutment height leads to increased rotational deformation and more pronounced converse moments at the pile during peak construction temperatures. In contrast, for PSC superstructures, increased height results in reduced bending moments at the pile top.
- Displacements and bending moments show slight sensitivity to soil stiffness. Higher stiffness generally reduces deformations and increases moments, but variations in soil stiffness have a limited overall effect.
- PSC superstructures exhibit less deformation, but greater moments compared to steel superstructures, making them more sensitive to construction temperature effects.

It is noteworthy to acknowledge that the observed behavior is intricately tied to the specific design parameters and magnitudes employed within these analytical models. Consequently, any modifications to these parameters have the potential to exert a substantial influence on the overall response of the bridge structure.

8. RECOMMENDATIONS FOR FURTHER RESEARCH

Future research should focus on several key areas to enhance the understanding and performance of integral abutment bridges (IABs).

- One important area is the examination of additional secondary loads, such as vertical temperature gradients, shrinkage, creep, differential settlement, and differential deflections. Assessing their effects on bridge behavior and evaluating current design assumptions will provide deeper insights into IAB performance.
- Utilizing finite element modeling to simulate the physical behavior of backfill soil, while incorporating soil stiffness, will be crucial for assessing the accuracy of existing earth pressure calculation methods. This approach is expected to enhance the precision of predictions and the reliability of these methods.
- Exploring the practical implications of integrating construction temperature considerations into design practices is essential. Research should address both theoretical benefits and practical challenges, including effects on scheduling and insights from on-site engineers.
- Further investigation is needed into advanced techniques for managing the temperature of the superstructure. Research should focus on effective methods for controlling temperatures during bridge construction, aiming to identify best practices for optimizing thermal conditions.
- Another significant area of study is the mechanism of soil ratcheting. Conduct comprehensive studies on the mechanism of soil ratcheting and develop methods to incorporate this phenomenon into the design phase. Understanding how soil properties evolve over time due to soil movement will enable more accurate predictions and facilitate the selection of conservative design parameters.
- Additionally, examining the effect of thermal expansion and contraction on pile fatigue is important. Research should focus on the extent of thermal expansion and contraction cycles and how maintaining a symmetrical balance between these cycles can enhance pile performance and overall bridge stability.
- Lastly, investigating the effects of different traffic load combinations, including bidirectional and unidirectional loads, on the overall behavior of IABs when combined with temperature and earth pressure loads is recommended.

Understanding these interactions will improve the accuracy of structural analyses and refine design practices.

These research directions are essential for advancing the understanding of IAB dynamics and for refining design and construction methodologies, ultimately leading to more reliable and efficient bridge infrastructure.

REFERENCES

Abdel-Fattah, M.T., Abdel-Fattah, T.T., Hemada, A.A., (2018). Nonlinear Finite-Element Analysis of Integral Abutment Bridges due to Cyclic Thermal Changes. *Journal of Bridge Engineering*. *23*(2), 04017134.

Abendroth, R. E., and Greimann, L. F., (2005). Field Testing of Integral Abutments. *Iowa Department of Transportation*, Report No. HR-399.

Abendroth, R.E., Greimann, Lowell F., and Patrick B.E., (1989*).* Abutment pile design for jointless bridges, *Journal of Structural Engineering*, *Journal of Structural Engineering, 115*(11), 2914-2929.

Albhaisi, S., Nassif, H., and Hwang, E.S., (2012). Effect of Substructure Stiffness on Performance of Steel Integral Abutment Bridges Under Thermal Loads. *Journal of the Transportation Research Board. 2313*(1), 22-32. DOI: 10.3141/2313-03.

American Association of State Highway and Transportation Officials (AASHTO LRFD), (2008). *Bridge Design Specifications AASHTO LRFD*. Washington, D.C, USA.

American Association of State Highway and Transportation Officials (AASHTO LRFD), (2014). *Bridge Design Specifications AASHTO LRFD*. Washington, DC. USA.

American Association of State Highway and Transportation Officials (AASHTO). (1996). *Standard Specifications for Highway Bridges,* (16th ed.), Washington. D.C, USA.

American Association of State Highway and Transportation Officials (AASHTO). (2010). *Bridge Design Specifications AASHTO LRFD,* Washington, D.C, USA.

American Association of State Highway and Transportation Officials (AASHTO), (1989). *AASHTO Guide Specifications Thermal Effects in Concrete Bridge Superstructures.* Washington. D.C, USA.

American Association of State Highway and Transportation Officials (AASHTO LRFD). (2013). *bridge design specifications AASHTO LRFD*, Washington, D.C, USA.

American Association of State Highway and Transportation Officials. (2004). *AASHTO LRFD Bridge Design Specifications (3rd ed.)*. Washington, D.C, USA.

American Association of State Highway and Transportation Officials (2012). *AASHTO.LRFD bridge design specifications (6th ed.).* Washington, DC, USA.

American Association of State Highway and Transportation Officials (2015*). AASHTO. LRFD bridge design specifications(7th ed.)*. Washington, D.C, USA.

American Association of State Highway Transportation Officials (1998). *AASHTO LRFD bridge design specifications, (2nd 13.).* Washington, DC, USA.

Arsoy S., (2004). Mobilization of passive earth pressures behind abutments of jointless bridges. *Transportation Research Record: Journal of the Transportation Research Board. 1868*(1), 199-204.

Arsoy, S., (2008). Proposed mathematical model for daily and seasonal thermal bridge displacements. *Journal of the Transportation Research Board. 2050*(1), 3-12. DOI: 10.3141/2050-01.

Arsoy, S., Duncan, J. M., Barker, R. M., (2004). Behavior of a Semi integral Bridge Abutment under Static and Temperature-Induced Cyclic Loading. *Journal of Bridge Engineering. 9*(2), 193-199. DOI: 10.1061/~ASCE!1084-0702~2004!9:2~193!.

Baptiste, K.T., (2009). Length limitations of prestressed concrete girder integral abutment bridges. Master Thesis, The Pennsylvania State University, Department of Civil and Environmental Engineering. Pennsylvania, USA.

Baptiste, K.T., Kim, W., Laman, J.A., (2011). Parametric Study and Length Limitations for Prestressed Concrete Girder Integral Abutment Bridges. *Structural Engineering International. 21*(2), 151-156. DOI: 10.2749/101686611X12994961034219.

Barker R.M., Duncan J.M., Rojiani K.B., Ooi P.S.K., Tan C.K., Kim S.G., (1991). Manuals for the design of bridge foundations, *Transportation Research Board, National Research Council.* NCHRP Report 343.

Barker, R.M., Kim, S.G., Duncan, J.M., and Rojiani, K.B., (1990). Application of LFRD to Design of an Integral Abutment. *Proceedings, Third International Conference on Short and Medium Span Bridges*. August 7-11, Toronto, Canada.

Boley, B.A., Weiner, J.H., (1960). *Theory of thermal stress*, Wiley, New York.

Bowles J.E., (1996). *Foundation analysis and design (3rd ed.).* McGraw-Hill. New York, USA.

British Standards Institution (2004). *BSI (2004) BS EN 1991-1-5:2003: Eurocode 1: Actions on structures General actions Thermal actions. BSI*, London, UK.

British Standards Institution (2020). *PD 6694-1:2011+A1:2020. Recommendations for the Design of Structures Subject to Traffic Loading to BS EN 1997-1:2004+A1:2013*. London, UK.

Broms, B., Ingleson, I., (1971). Earth Pressures Against Abutment of Rigid Frame Bridge. *Geotechnique*, *21*(1), 15-28.

Burke, M.P., (1993). Design of integral concrete bridges. *American Concrete Institute (ACI). 15*(6), 37-42.

Burke, M.P., (1996). An Introduction to the Design and Construction of Integral Bridges. *Presented at Workshop on Integral Abutment Bridges*, Pittsburgh, Pennsylvania, USA.

Canadian Standard Association, CSA. (2006). *Canadian Highway Bridge Design Code*, CHBDC. Etobicoke, ON, Canada.

Chen Y., (1997). Important considerations, guidelines, and practical details of integral bridges. *Journal of Engineering Technology.14*(1), 16–9.

Choi S., Cha S.W., Oh B.H., Kim I.H., (2011). Thermo-hygro-mechanical behavior of early-age concrete deck in composite bridge under environmental loadings. Part 1: temperature and relative humidity. *Materials and Structures*. (44), 1325–1346 DOI 10.1617/s11527-011-9751-8.

Civjan S., Kalayci E., Quinn B.H., Breña S.F., Allen C.A., (2013). Observed integral abutment bridge substructure response. *Engineering Structures*. *56*, 1177-1191.

Civjan, S.A., Bonczar, C., Breña, S.F., DeJong, J., Crovo, D., (2007). Integral Abutment Bridge Behavior: Parametric Analysis of a Massachusetts Bridge. *Journal of Bridge Engineering, 12*(1), 64-71. DOI: 10.1061/(ASCE)1084-0702(2007)12:1(64).

Clough, G., Duncan, J., (1991). *Foundation Engineering Handbook*, Van Nostrand Reinhold, New York, USA.

Coulomb, C.A., (1776). *Essay on the application of the rules of maximization and minimization to some problems of statics, related to architecture (Essai sur une application des règles de maximis et minimis a` quelques problèmes de statique, relatifs a` l'architecture. Mémoires de mathématique et de physique présentés a` l'Académie royale des sciences pardivers savants, et lus sans ses assemblées)*. De l'Imprimerie Royale, Paris, France.

Das, B., (1998), *Principles of Foundation Engineering (4th ed.).*Cole Publishing Company. California, USA.

David T.K., Forth J.P., (2011). Modelling of Soil Structure Interaction of Integral Abutment Bridges. *World Acad Sci Eng Technol, 78*, 769-774.

Dicleli, M. A, (2000). Rational design approach for prestressed-concrete-girder integral bridges. *Engineering Structure. 22*(3), 230-245.

Dicleli, M., (2005). Integral abutment-backfill behavior on sand soil - pushover analysis approach. *Journal of Bridge Engineering*. *10*(3), 354-364. DOI: 10.1061/(ASCE)1084-0702(2005)10:3(354).

Dicleli, M., Albhaisi, S.M., (2003a). Effect of cyclic thermal loading on the performance of steel H-piles in integral bridges with stub-abutments. *Journal of Constructional Steel Research*. *60*(2), 161-182. DOI: 10.1016/j.jcsr.2003.09.003.

Dicleli, M., Albhaisi, S.M., (2003b). Maximum length of integral bridges supported on steel H-piles driven in sand. *Engineering Structures*. *25*(12), 1491-1504.

Dicleli, M., Albhaisi, S.M., (2004). Estimation of Length Limits for Integral Bridges Built on Clay. *Journal of Bridge Engineering*. *9*(6), 572-581. DOI: 10.1061/(ASCE)1084-0702(2004)9:6(572).

Dicleli, M., and Erhan, S., (2009) Effect of superstructure-abutment continuity on live load distribution in integral abutment bridge girders. *Structural Engineering and Mechanics*, *34* (5).

Domski J., Katzer J., (2015). An example of monitoring of early-age concrete temperatures in a massive concrete slab. *Selected Practical and Theoretical Aspects of Contemporary Mechanics.* 94-105.

Emerson, M., (1973). The Calculation of the Distribution of Temperature in Bridges. *Transport and Road Research Laboratory (TRRL*). Report 561.

Emerson, M., (1977). Temperature Differences: Basis of Design Requirements. *Transport and Road Research Laboratory TRRL.* Report 765.

England G.L, Tsang N.C.M, Bush D.I. (2000). *Integral bridges: a fundamental approach to the time–temperature loading problem.* Thomas Telford. London, UK.

European Committee for Standardization. (2003). *EN 1991-5 (2003), Eurocode 1: Actions on Structures. Part 1.5: General actions - thermal actions,* Brussels, Belgium.

Fang Y. S., Chen T.J., Wu, B.F., (1994). Passive Earth Pressures with Various Wall Movements, *ASCE Journal of Geotechnical Engineering. 120*(8), 1307-1323.

Faraji, S., Ting, J.M., Crovo. D.S., (2001). Nonlinear Analysis of Integral Bridges: Finite Element Model. *Journal of Geotechnical and Geoenvironmental Engineering. 127*(5), 454-461.

Featherston. N. R., (2022). Parametric modelling of integral bridge soil spring reactions. Master Thesis, *Stellenbosch University, Department of Civil Engineering, Cape province*, South Africa.

Firoozi, A.A., Maryam, N.M., Firoozi, A.A., (2023). Effects of Soil–Structure Interaction on Performance of Bridges During Earthquakes. Case Study: Integral Abutment Bridge in Pennsylvania, USA. *Iranian Journal of Science and Technology, Transactions of Civil Engineering. 47*(6), 3487-3505.

Flener E.B., (2004), Soil-Structure Interaction for Integral Bridges and Culverts. PhD Thesis, Royal Institute of Technology, Stockholm, Sweden.

GangaRao, H., Thippeswamy, H., Dickson, B., Franco., J., (1996). Survey and Design of Integral Abutment Bridges. *Presented at Workshop on Integral Abutment Bridge.* Pittsburgh, Pennsylvania, USA.

Gerolymos, N., Escoffier, S., Gazetas, G., Garnier, J., (2009). Numerical Modelling of Centrifuge Cyclic Lateral Pile Load Experiments. *Earthquake Engineering and Engineering Vibration*. *8*(1), 61-76.

Girton, D.D., Hawkinson, T.R., Greimann, L.F., (1991). Validation of design recommendations for integral-abutment piles. *Journal of Structural Engineering. 117*(7), 2117–2134.

Greimann, L.F., Abendroth, R.E., Johnson, D.E., Ebner, P.B., (1987). Pile Design and Tests for Integral Abutment Bridges. *Iowa State University*. ERI Project 1780.

Greimann, L.F., Yang, P.S., Edmunds, S.K., Wolde-Tinsae, A. M., (1984). Design of Piles for Integral Abutment Bridges, *Department of Civil Engineering, Engineering Research Institute, Iowa State University.* Iowa DOT Project HR-252.

Griemann, L.F., Abendroth, R.E., Johnson, D.E., Ebner, P.B., (1987). Pile design and tests for integral abutment bridges. IOWA DOT Project HR-273.

Hambly, E.C. (1991). *Bridge Deck Behavior (2nd ed.).* Taylor & Francis, London And New York, UK and USA.

Hong J., (2006). Research on Simplified Calculating Model and Loaded Behavior of Integral Abutment Bridges, PhD Thesis, Fuzhou University, Fuzhou, China.

Hoppe, E.J., Gomez, J. P., (1996). Field Study of an Integral Backwall Bridge. *Virginia Transportation Research Council*. VTRC 97-R7.

Horvath, J.S., (1992). Modified Vlasov model for beams on elastic foundations, *Journal of geotechnical engineering*. *118*(9), 1482-1484.

Horvath, J.S., (2004). Integral-Abutment Bridges: A Complex Soil-Structure Interaction Challenge. *In Geotechnical Engineering for Transportation Projects; Geotechnical Special Publication*. 460–467. DOI: 10.1061/40744(154)31.Los Angeles, CA, USA.

Huang, F., Li, L., Javanmardi, A., Zhang, H., Izadifar, M., (2022). Modified calculation method of earth pressure and internal force of the abutment-pile in integral abutment jointless bridges. *Archives of Civil and Mechanical Engineering*. 22(4), 205.

Huang, F., Yulin, S., Chen, G., Lin, Y., Tabatabai, H., Briseghell, B., (2020). Experiment on Interaction of Abutment, Steel H-Pile and Soil in Integral Abutment Jointless Bridges (IAJBs) under Low-Cycle Pseudo-Static Displacement Loads. *Applied Sciences*. *10*(4), 1358.

Huang, J., French, C., Shield, C., (2004). Behavior of Concrete Integral Abutment Bridges. *St. Paul, Minnesota: Minnesota Department of Transportation,* Report No. MN/RC-43.

Huang, J., Shield, C.K., French, C.E.W., (2008). Parametric Study of Concrete Integral Abutment Bridges. *Journal of Bridge Engineering*. *13*(5), 511-526. DOI: 10.1061/(ASCE)1084-0702(2008)13:5(511).

Huntley, S.A., Valsangkar, A.J., (2013). Field monitoring of earth pressures on integral bridge abutments. *Canadian Geotechnical Journal. 50*(8), 841-857. DOI:10.1139/cgj-2012-0440.

Hussain, I., Bagnariol, D. (1996). Integral Abutment Bridges. *Ontario Ministry of Transportation*, Report No. SO-96-01.

Iles, D. C., (2005*). Integral Steel bridges: A summary of current practice in design and construction*. The Steel Construction Institute, SCI Publication P340. Berkshire, UK.

INTAB. (2010). INTAB Design Guide - Economic and Durable Design of Composite Bridges with Integral Abutments. *RWTH Aachen University*, Final report, INTAB Research Project RFSR-CT-2005-00041.

Jaky, J., (1944). The coefficient of earth pressure at rest. *Journal for Society of Hungarian Architects and Engineers*.

Kezdi, A., (1974). *Handbook of Soil Mechanics*. Elsevier. Amsterdam, Netherlands.

Kim, W., Laman, J.A., Zareian, F., Min, G., Lee, D., (2021). Influence of Construction Joint and Bridge Geometry on Integral Abutment Bridges. *Applied Sciences. 11*(11), 5031.

Kim, W., Laman, J.A., (2009). Monitoring of integral abutment bridges and design criteria development. *Pennsylvania Transportation Research Council*. Final criteria development 9-005-PSU002.

Kim, W., Laman, J.A., (2010a). Integral abutment bridge response under thermal loading. *Engineering Structures*. *32*(6), 1495-1508. DOI: 10.1016/j.engstruct.2010.01.004.

Kim, W., Laman, J.A., (2010b). Numerical analysis method for long-term behavior of integral abutment bridges. *Engineering Structures*. *32*(8), 2247-2257. DOI: 10.1016/j.engstruct.2010.03.027.

Kim, W., Laman, J.A., (2012). Seven-Year Field Monitoring of Four Integral Abutment Bridges. *Journal of Performance of Constructed Facilities*. *26*(1), 54-64. DOI: 10.1061/(ASCE)CF.1943-5509.0000250.

Kim, W., Laman, J. A., Jeong, Y., (2016). Comparative Study of Integral Abutment Bridge Structural Analysis Methods. *Canadian Journal of Civil Engineering*. *43*(4), 378-389.

LaFave, J. M., Fahnestock, L.A., Wright, B. A., Riddle, J. K., Jarrett, M. W., Svatora, J. S., An, H., Brambila, G., (2016). Integral abutment bridges under thermal loading numerical simulations and parametric study, *Illinois Center for Transportation*, Series No. 16-015; Research Report No. FHWA-ICT-16-014.

Laman, J.A., Pugasap, K., Kim, W., (2006). Field monitoring of integral abutment bridges. *Pennsylvania State University. Pennsylvania Transportation Research Council*. Final Report No. FHWA-PA-2006-006-510401-01.

Lee, J., Jeong, Y., Kim, W., (2016). Buckling Behavior of Steel Girder in Integral Abutment Bridges under Thermal Loadings in Summer Season during Deck Replacement*. International Journal of Steel Structure*. *16*, 1071-1082.

Liu, H., Hanand J., Parsons, R.L., (2022). Integral bridge abutments in response to seasonal temperature changes: State of knowledge and recent advances. *Frontiers in Built Environment*. *8*, 916-782. DOI: 10.3389/fbuil.2022.916782.

Lock, J., (2002). Integral Bridge Abutments. *University of Cambridge, Department of Engineering.* Project report CUED/D-SOILS/TR320.

Loveall, C., (1996). Integral Abutment Bridges. *Presented at Workshop on Integral Abutment Bridges*, Pittsburgh. Pennsylvania, USA.

Marx, S., Seidl, G., (2011). Integral Railway Bridges in Germany. *Structural Engineering International*. *21*(3), 332-340. DOI: 10.2749/101686611X12994961034534.

Massachusetts Department of Transportation (2020). *LRFD bridge design manual*. Massachusetts, USA.

Massachusetts Department of Transportation (MassDOT) (2007). *Bridge Manual (2005 Edition)*. Boston, USA.

Massachusetts Highway Dept., (1999). *Design guidelines and standard. Details for integral abutment bridges*, *Mass Highway Bridge Manual*, Boston, USA.

Matlock, H., (1970), Correlations for Design of Laterally Loaded Piles in Soft Clay. *Second Annual Offshore Technology Conference.* Houston, Texas, UAS.

Mitoulis, S. A., (2020). Challenges and opportunities for the application of integral abutment bridges in earthquake-prone areas: A review. *Soil Dynamics and Earthquake Engineering*. *135*, 106183.

Murphy, B., Yarnold, M., (2018). Temperature-driven structural identification of a steel girder bridge with an integral abutment. *Engineering Structures*. *155*, 209-221.

Nam, M. S., Park, Y. H., (2015). Relationship between Earth Pressure and Thermally Induced Movement of Integral Abutments. *Journal of Performance of Constructed Facilities. 29*(4), 04014093. DOI: 10.1061/(ASCE)CF.1943-5509.0000562.

National Standards Authority of Ireland (2004). EN 1992-1-1(2004). *Eurocode 2: Design of concrete structures. Part 1-1,* Ireland.

Newmark, N., Siess, C., Penman, R., (1948). Studies of slab and beam highway bridges: part III. *University of Illinois Bulletin, 396*, 115-133.

Nikravan. N., (2013). Structural Design Issues for Integral Abutment. PHD Thesis, Ryerson University, Toronto, Ontario, Canada.

O'Brien, E., Keogh, D. (1999). *Bridge Deck Analysis*. E & FN Spon, New York, USA.

Paul, M., Laman, J. A., Linzell, D. G., (2008). Thermally Induced Superstructure Stresses in Prestressed Girder Integral Abutment Bridges. *Journal of the Transportation Research Board.* 287–297.

Pennsylvania Department of Transportation (PennDOT DM4), (2015). *Design Manual Part 4, Structures: Procedures-Design-Plans Presentation, PennDOT Design Manual Part 4; Commonwealth of Pennsylvania*. Harrisburg, PA, USA.

Peric, D., Mietic, M. Shah, B.R., Esmaeily, A., Wang, H. (2016) Thermally induced soil structure interaction in the existing integral bridge. *Engineering Structures*. *106*, 484-494.

Potgieter, I., Gamble, W., (1983). Nonlinear Temperature Distributions in Bridges at Different Locations in the United States. *PCI Journal, Precast/Prestressed Concrete Institute. 34*(4), 80-103.

Prakash, S., Sharma, H. D., (1990). *Pile Foundations in Engineering Practice*, John Wiley & Sons, Inc., New York, USA.

Prat, M., Bisch, E., Millard, A., Mestat, P., Cabot, G. (1995). *The Modeling of Structures, La modélisation des ouvrages*. Hermes. Paris, France.

Pugasap ,K., Kim, W., Laman, J.A., (2009). Long-term response prediction of integral abutment bridges. *Journal of Bridge Engineering*. *14*(2), 129-139. DOI: 10.1061/(ASCE)1084-0702(2009)14:2(129).

Quinn, B., Civjan, S., (2016). Parametric Study on Effects of Pile Orientation in Integral Abutment Bridges. the Journal of Bridge Engineering. *22*(4), 04016132. DOI: 10.1061/(ASCE)BE.1943-5592.0000952.

Rankine W. J. M., (1857). On the stability of loose earth. *Philosophical transactions of the Royal Society of London*, (147), 9-27.

Reese L.C., Cox, W.R., Koop, F.D., (1974). Analysis of Laterally Loaded Piles in Sand. *Sixth Annual Offshore Technology Conference*, Houston. Texas, USA.

Reese, L.C., Cox, W.R., Koop F.D., (1975). Field Testing and Analysis of Laterally Loaded Piles in Stiff Clay. *The 7th Offshore Technology Conference*, Houston. Texas, USA.

Rhodes, S., Moses, J., (2014). Integral bridges and the modelling of soil-structure interaction. *International Bridge Conference,* Pittsburgh, Pennsylvania, USA.

Riding, K.A., Poole, J.L, Schindler A.K., Juenger M.C.G., Folliard K.J., (2009). Effects of Construction Time and Coarse Aggregate on Bridge Deck Cracking. *ACI Materials Journal*, *106*(5), 448-454.

Rowe, P. W., (1954). A Stress–Strain Theory for Cohesionless Soil with Applications to Earth Pressure at Rest and Moving Walls. *Géotechnique. 4*(2), 70-88.

Salman, N.N., Issa, M.A., (2021). Calibration and parametric investigation of integral abutment bridges. *Engineering Structures. 227*, 111381. DOI: 10.1016/j.engstruct.2020.111381.

Sandford, T.C., Elgaaly, M., (1993). Skew effects on backfill pressures at frame bridge abutments. *Transportation Research Record*, (1415).

Sherif, M.A., Ishibashi, I., Lee, C.D., (1982). Earth Pressures Against Rigid Retaining Walls. *Journal of Geotechnical Engineering, 108*(5), 679-695.

Soltani, A.A., Kukreti, A.R., (1992). Performance Evaluation of Integral Abutment Bridges. *Transportation Research Record* (1371), 17–25.

Subramaniam K.V., Kunin J., Curtis R., Streeter D., (2010). Influence of Early Temperature Rise on Movements and Stress Development in Concrete Decks. *Journal of Bridge Engineering, 15*(1), 108-116. DOI: 10.1061/(ASCE)1084-0702(2010)15:1(108).

Sullivan W.R., Reese, L.C., Fenske, C.W., (1979). Unified Method for Analysis of Laterally Loaded Piles in Clay. *Numerical Methods in Offshore Piling*, London, UK.

Swedish National Road Administration (Vägverket) Bro, A. T. B., (2002), General Technical Description for Construction and Improvement of Bridges (Vägverkets allmänna tekniska beskrivning för nybyggande och förbättring av broar), Sweden.

Terzaghi, K. A, (1936). Fundamental Fallacy in Earth Pressure Calculations. *Journal of Boston Society of Civil Engineers*, *23* (2). 71–88.

Thippeswamy, H.K., GangaRao, H.V.S., Franco, J.M., (2002). Performance evaluation of jointless bridges. *Journal of Bridge Engineering, 7*(5), 276-289. DOI: 10.1061/(ASCE)1084-0702(2002)7:5(276).

Tlustochowicz, G., (2005). Optimized Design of Integral Abutments for a Three Span Composite Bridge. Master's Thesis, Luleå University of Technology MSc Programs in Engineering, Department of Civil and Environmental Engineering Division of Steel Structures, Luleå and Kiruna, Sweden.

URL-1: https://resource.midasuser.com/en/solutions/integral-bridges#none (Access date: 30 November 2023).

URL-2: The American Concrete Institute https://www.concrete.org (Access date: 25th March 2024).

Vahedifard, F., Leshchinsky, B.A., Mortezaei, K., Lu, N., (2015). Active earth pressures for unsaturated retaining structures. *Journal of Geotechnical and Geoenvironmental Engineering*, *141*(11), 04015048. DOI: 10.1061/(ASCE)GT.1943-5606.0001356.

Vera, A., D., (2022). Integral Bridge Function in Midas Civil. MIDASIT Co., Ltd, https://www.midasbridge.com/en/blog/bridgeinsight/bearing-arrangement-for-curved-bridges-0-0 (Access date: 15th January 2024).

Wassermann, E. P., Walker, J. H., (1996) Integral Abutments for Continuous Steel Bridges. *Presented at Workshop on Integral Abutment Bridges*, Pittsburgh, Pennsylvania, USA.

Winkler, E., (1867). *The Theory of Elasticity and Stiffness (Die Lehre von Elastizität und Festigkeit)*. H. Dominicus. Prague, Czech.

Wolde-Tinsae, A. M., Greimann L., Yang P. S., (1988). End-Bearing Piles In Jointless Bridges. *Journal of Structural Engineering*. *114*(8), 1870-1884.

Wolde-Tinsea, A. M., Klinger, J. E., (1987). Integral Abutment Bridge Design and Construction, Final Report. *Maryland Department of Transportation*, FHWA/MD-87/04.

Yang, P., Wolde-Tinsae, A. M., Greimann, L. F., (1985). Effects of Predrilling and Layered Soils on Piles. *Journal of Geotechnical Engineering*, *111*(1), 18-31.

PUBLICATIONS AND WORKS

Rifai, H., Arsoy, S. (2023). The Thermal Response of Integral Abutment Bridges Using Different Assumptions for Earth Pressure Behind the Abutment. *6. International Marmara Scientific Research and Innovation Congress,* İstanbul, Turkey, 7 - 08 October 2023, pp. 584-595.

BIOGRAPHY

Completed her primary, secondary, and high school education in Damascus, the capital of Syria. Following her high school graduation, she began her bachelor’s degree in civil engineering at Damascus University in 2014. Due to the worsening conditions resulting from the civil war, she relocated to Turkey, where she continued her higher education journey at Kocaeli University. There, she dedicated two years to learning the Turkish and English languages before resuming her bachelor's degree studies in Civil Engineering in 2017, which she successfully completed in 2021. Following her graduation, she remained at the same institution to pursue a master's degree in Structural Engineering, which she accomplished in 2024.